UNIVERSITY OF
CANTERBURY
*Te Whare Wānanga o Waitaha*
CHRISTCHURCH NEW ZEALAND

# *In-Vitro* Analysis of Haemodynamics in Stented Arteries

Petra Nicole Williamson

A thesis submitted for the degree of
Doctor of Philosophy
in
Mechanical Engineering

Department of Mechanical Engineering
University of Canterbury
New Zealand

January 2022

# Acknowledgements

Getting to the final submission of this thesis would not have been possible without a whole team of people helping me. Please bear with me whilst I fumble through many ‘thank you’s.

First and foremost, I need to thank my supervisor, Dr Paul Docherty, for the mental and physical support he has provided going back as early as two weeks into my undergraduate degree when he told me “You’ll be fine,” in a time when I didn’t think I would be. I don’t know if I’d have made it to this point without our weekly chats and unlimited supply of sprite and cola whenever I wanted. A real heart on my sleeved moment… I didn’t doubt I had the intelligence to make it through a PhD. But I wasn’t so sure I would emotionally make it through. I have endless thanks for Paul, for making sure I got through.

I also have to thanks the Academic staff and technicians that made the experiments in this thesis possible. Specifically, I would like to thank Julian Philips, David Read, Garry Cotton, Tony Doyle, Dr Bill Mohs, Dr Natalia Kabaliuk and Dr Mark Jermy. All of whom have had to deal with some… sometimes not so intelligent questions… with patience and kindness and help me in many areas throughout my thesis. Thank you as well to Sina Yazdi, who basically jumpstarted my research. His help was invaluable throughout my thesis.

A huge thank you to my parents. Not only for their, unconditional love, encouragement and support throughout by thesis, but specifically during the month of April 2020, when I took over their conservatory so I could continue to work on my PhD even throughout a basically world-wide lockdown (A sarcastic thank you to COVID-19 for that). During that time, they discovered I knew a lot of… words… used when things went wrong. And thank you to my sister for caring and checking in every week. A special thank you to my partner, Ben for (I know I’m beginning to sound like a broken record) the constant assurances, the dinners, the love and general support he has offered me.

And finally, thank you to my friends. Of special note are Ella and Charles, you made flatting life exciting and fun. I will forever cherish the late-night drinks and daily conversations and basically just existing with you guys. Another special note to Obi AKA Ben (not the same one as before… I know I collect Bens). The coffee breaks are what got me to uni some days. I wouldn’t have made it without you all.

To everyone else that I have to thank and haven’t named. Thank you all. You have all dealt with smiles and tears and been there with me through it all.

# Abstract

Cardiovascular diseases (CVD) are the leading cause of death in the developed world. One of the most common management methods for CVD is through vascular implants such as stents to support arterial walls. However, determining the efficacy of stents can be difficult, particularly for high-risk stents, such as those used in the aorta. *In-vitro* modelling can provide safe insight into the haemodynamics changes within an artery due to specific stenting methods, without intrusive patient monitoring. The *in-vitro* studies presented in this thesis contribute to research on the haemodynamic changes within arteries using particle image velocimetry (PIV).

*In-vitro* modelling can be used to investigate haemodynamics of arterial geometry and stent implants. However, *in-vitro* model fidelity is reliant on precise matching of *in-vivo* conditions. Flow distribution and wall shear stress depend on the Reynolds and Womersley numbers. This thesis reviewed currently published Reynolds and Womersley numbers for 14 major arteries in the human body. The results were presented both in a table and graphically for ease of understanding and future use. The results identified a paucity of information in smaller distal arteries compared to major arteries such as the aorta.

Matching Reynolds and Womersley numbers for compliant *in-vitro* modelling may also be limited by model dimensional tolerances. A method for visualising the range of experimental conditions required for dynamic matching was developed and case studies for the ascending aorta and common carotid artery were presented. The assumed Sylgard 184 silicone would be used for phantom fabrication, and compared three working solutions: water/glycerine, water/glycerine/urea, and water/glycerine/sodium-iodide. To manufacture compliance matched silicone models of the ascending aorta and common carotid arteries, the models were scaled to 1.5x (ascending aorta) and 3x (common carotid) life scale, respectively. Modelling the ascending aorta with the comparatively high viscosity water/glycerine solution will lead to very high pump power demands. However, any of the working fluids considered could be dynamically matched with low pump demand for the common carotid model.

The Frozen Elephant Trunk (FET) stent is a hybrid endovascular device that may be implemented in the event of an aneurysm or aortic dissection of the aortic arch or superior descending aorta. However, the FET stent is a high risk stent. In particular, the Type 1B endoleak can lead to intrasaccular flow due to an incomplete distal fit between the stent and artery during systole. Chapter 5 developed an *in-vitro* modelling technique to enable the investigation of the known failure. Recirculation zones and an asymmetric endoleak were identified distal to the surrogate stent graft. The endoleak developed at the peak of systole and was sustained until the onset of diastole. The endoleak geometry indicated a potential variation in the phantom artery wall thickness or stent alignment. Recirculation was identified on the posterior dorsal line during late systole which may induce an inflammatory response in an artery. The identification of the Type 1B endoleak proved that *in-vitro* modelling can be used to investigate complex compliance changes and wall motions.

The kissing stent (KS) configuration is a low risk, stenting method often used to treat aorto-iliac occlusive disease (AIOD). However, long-term patency reduces by nearly 25% in the first five years potentially due to deleterious flow behaviour. The risk of harmful haemodynamics due to the KS configuration were investigated *in-vitro.* PIV experimentation identified peak proximal and distal velocity *in-vitro* was 0.71 $m \cdot s^{-1}$ and 1.90 $m \cdot s^{-1}$, respectively. A lumen wall collapse in the sagittal plane occurred during late systole to early diastole proximal the KS configuration. The collapse disturbed the flow proximal to the stented region producing potential recirculation zones and abnormal flow patterns. However, the systolic flow was as normal and undisturbed indicating the KS configuration is safe to use for repairing AIOD. The collapse had not been previously identified and would require further investigation.

Thoracic extra-anatomic bypasses (EAB) are grafted stents that may be used to prophylactically revascularize supra-aortic arteries that may require blockage during thoracic endovascular aortic repair (TEVAR) methods. However, prophylactic use of EAB may introduce a risk of failure due to abnormally low or disrupted flow, known as competitive flow, within the bypasses. Competitive flow

within the bypasses between supra-aortic arteries has not been captured previously. PIV was used to assess each model configuration for flow abnormalities and potential for flow competition. The investigation found potential for competitive flow in the bypasses when just the left subclavian artery (LSA), the left carotid artery (LCCA), or none of the arteries are blocked. In contrast, when the LSA and LCCA were both blocked, there was no evidence of competitive flow. Flow stagnated at the initiation of systole within the BC bypass in the 2 configurations with an unblocked LCCA, along with notable recirculation zones and reciprocating flow occurring throughout the rest of systolic flow. Flow stagnated in the CS bypass at early systole when only the LCCA was blocked. A large recirculation was identifiable in the CS bypass when just the LSA was blocked, particularly after peak systole. The potential of competitive flow indicated prophylactic used of EAB in the supra-aortic arteries may require location of proximal arteries to limit the number of pathways blood flow can take.

Deputy Vice-Chancellor’s Office
Postgraduate Research Office

UNIVERSITY OF CANTERBURY
*Te Whare Wānanga o Waitaha*
CHRISTCHURCH NEW ZEALAND

## Co-Authorship Form

This form is to accompany the submission of any thesis that contains research reported in co-authored work that has been published, accepted for publication, or submitted for publication. A copy of this form should be included for each co-authored work that is included in the thesis. Completed forms should be included at the front (after the thesis abstract) of each copy of the thesis submitted for examination and library deposit.

Please indicate the chapter/section/pages of this thesis that are extracted from co-authored work and provide details of the publication or submission from the extract comes:

WILLIAMSON, P. N., YAZDI, S. G., KHANAFER, A., DOCHERTY, P. D., GEOGHEGAN, P. H., KABALIUK, N. & JERMY, M. Particle Image Velocimetry (PIV) Analysis of Haemodynamics Distal of a Frozen Elephant Trunk Stent Phantom. *In:* MONTIEL, F., ed. Fluids in New Zealand, 31 Jan - 1 Feb 2019 Dunedin, New Zealand.

Please detail the nature and extent (%) of contribution by the candidate:

*The candidate contributed to ~80% of the final outcome based on the overall time and effort. The candidate developed and implemented all experimental work in consultation with the supervisors and co-authors.*

**Certification by Co-authors:**

If there is more than one co-author then a single co-author can sign on behalf of all

The undersigned certifies that:

- *The above statement correctly reflects the nature and extent of the Doctoral candidate’s contribution to this co-authored work*
- *In cases where the candidate was the lead author of the co-authored work he or she wrote the text*

Name: *Assoc. Prof. Paul Docherty* Signature: *Paul Docherty* Date: *27/01/2022*

Deputy Vice-Chancellor's Office
Postgraduate Research Office

UNIVERSITY OF CANTERBURY
Te Whare Wānanga o Waitaha
CHRISTCHURCH NEW ZEALAND

# Co-Authorship Form

This form is to accompany the submission of any thesis that contains research reported in co-authored work that has been published, accepted for publication, or submitted for publication. A copy of this form should be included for each co-authored work that is included in the thesis. Completed forms should be included at the front (after the thesis abstract) of each copy of the thesis submitted for examination and library deposit.

Please indicate the chapter/section/pages of this thesis that are extracted from co-authored work and provide details of the publication or submission from the extract comes:

WILLIAMSON, P. N., DOCHERTY, P. D., YAZDI, S. G., JERMY, M., KHANAFER, A., KABALIUK, N. & GEOGHEGAN, P. H. 2019. PIV Analysis of Stented Haemodynamics in the Descending Aorta. *In:* DÖSSEL, O. (ed.) *41st Annual International Conference of the IEEE Engineering in Medicine & Biology Society (EMBC).* Berlin, Germany.

Please detail the nature and extent (%) of contribution by the candidate:

*The contribution of the candidate to the work amounts to ~90% based on the overall time and effort dedicated to the final outcome. The candidate designed and implemented the experimental work with consultation from the supervisors and co-authors.*

**Certification by Co-authors:**

If there is more than one co-author then a single co-author can sign on behalf of all

The undersigned certifies that:

- *The above statement correctly reflects the nature and extent of the Doctoral candidate's contribution to this co-authored work*
- *In cases where the candidate was the lead author of the co-authored work he or she wrote the text*

Name: *Assoc. Prof. Paul Docherty* Signature: *Paul Docherty* Date: *27/01/2022*

Deputy Vice-Chancellor’s Office
Postgraduate Research Office

# Co-Authorship Form

This form is to accompany the submission of any thesis that contains research reported in co-authored work that has been published, accepted for publication, or submitted for publication. A copy of this form should be included for each co-authored work that is included in the thesis. Completed forms should be included at the front (after the thesis abstract) of each copy of the thesis submitted for examination and library deposit.

Please indicate the chapter/section/pages of this thesis that are extracted from co-authored work and provide details of the publication or submission from the extract comes:

WILLIAMSON, P.N., DOCHERTY, P.D., YAZDI, S.G., KABALIUK, N., JERMY, M., KHANAFER, A., GEOGHEGAN, P.H.: In-Vitro PIV Analysis of Pulsatile Flow Distal of a Frozen Elephant Trunk Stent Phantom. *1st International Conference of Thermal Fluid Dynamics and Control and the 2nd International Symposium of Combustion Instability and Control* 2019 Christchurch, New Zealand, 2-6 August. Becker S, Ed.

Please detail the nature and extent (%) of contribution by the candidate:

*The candidate contributed to ~90% of the resultant conference proceeding based on time and effort dedicated to the experiment design and data processing. The candidate produced the presentation.*

**Certification by Co-authors:**

If there is more than one co-author then a single co-author can sign on behalf of all

The undersigned certifies that:

- *The above statement correctly reflects the nature and extent of the Doctoral candidate’s contribution to this co-authored work*
- *In cases where the candidate was the lead author of the co-authored work he or she wrote the text*

Name: *Assoc. Prof. Paul Docherty* Signature: *Paul Docherty* Date: *27/01/2022*

Deputy Vice-Chancellor's Office
Postgraduate Research Office

UNIVERSITY OF CANTERBURY
Te Whare Wānanga o Waitaha
CHRISTCHURCH NEW ZEALAND

# Co-Authorship Form

This form is to accompany the submission of any thesis that contains research reported in co-authored work that has been published, accepted for publication, or submitted for publication. A copy of this form should be included for each co-authored work that is included in the thesis. Completed forms should be included at the front (after the thesis abstract) of each copy of the thesis submitted for examination and library deposit.

Please indicate the chapter/section/pages of this thesis that are extracted from co-authored work and provide details of the publication or submission from the extract comes:

WILLIAMSON, P.N., DOCHERTY, P.D., YAZDI, S.G., KHANAFER, A., KABALIUK, N., JERMY, M.: In-Vitro Analysis of Haemodynamics Distal of the Frozen Elephant Trunk Stent. *NZ Physics and Engineering in Medicine, 2020*, Hamilton, New Zealand, 8 – 10 March.

Please detail the nature and extent (%) of contribution by the candidate:

*The candidate contributed to ~90% of the outcome based on overall time and effort. The candidate developed and implemented the experimental work in consultation with the supervisors. The candidate also produced the and presented the research.*

**Certification by Co-authors:**

If there is more than one co-author then a single co-author can sign on behalf of all

The undersigned certifies that:

- *The above statement correctly reflects the nature and extent of the Doctoral candidate's contribution to this co-authored work*
- *In cases where the candidate was the lead author of the co-authored work he or she wrote the text*

Name: *Assoc. Prof. Paul Docherty* Signature: *Paul Docherty* Date: *27/01/2022*

Deputy Vice-Chancellor's Office
Postgraduate Research Office

UNIVERSITY OF
CANTERBURY
*Te Whare Wānanga o Waitaha*
CHRISTCHURCH NEW ZEALAND

# Co-Authorship Form

This form is to accompany the submission of any thesis that contains research reported in co-authored work that has been published, accepted for publication, or submitted for publication. A copy of this form should be included for each co-authored work that is included in the thesis. Completed forms should be included at the front (after the thesis abstract) of each copy of the thesis submitted for examination and library deposit.

| |
|---|
| Please indicate the chapter/section/pages of this thesis that are extracted from co-authored work and provide details of the publication or submission from the extract comes:<br>WILLIAMSON, P. N., DOCHERTY, P. D., YAZDI, S. G., KHANAFER, A., KABALIUK, N. & JERMY, M. 2021. PIV Analysis of Haemodynamics Distal to the Frozen Elephant Trunk Stent Surrogate. *Cardiovascular Engineering and Technology*. |

| |
|---|
| Please detail the nature and extent (%) of contribution by the candidate:<br>*The contribution of the candidate to the work was ~90% to the final outcome. The candidate developed and led all experimental work and data processing in consultation with the supervisors. The candidate drafted the initial manuscript. Co-authors contributed to the revision of the work and manuscript.* |

**Certification by Co-authors:**

If there is more than one co-author then a single co-author can sign on behalf of all

The undersigned certifies that:

- *The above statement correctly reflects the nature and extent of the Doctoral candidate's contribution to this co-authored work*
- *In cases where the candidate was the lead author of the co-authored work he or she wrote the text*

| |
|---|
| Name: *Assoc. Prof. Paul Docherty* Signature: *Paul Docherty* Date: *27/01/2022* |

Deputy Vice-Chancellor’s Office
Postgraduate Research Office

UNIVERSITY OF
CANTERBURY
*Te Whare Wānanga o Waitaha*
CHRISTCHURCH NEW ZEALAND

# Co-Authorship Form

This form is to accompany the submission of any thesis that contains research reported in co-authored work that has been published, accepted for publication, or submitted for publication. A copy of this form should be included for each co-authored work that is included in the thesis. Completed forms should be included at the front (after the thesis abstract) of each copy of the thesis submitted for examination and library deposit.

Please indicate the chapter/section/pages of this thesis that are extracted from co-authored work and provide details of the publication or submission from the extract comes:

WILLIAMSON, P. N., DOCHERTY, P. D., YAZDI, S. G., KHANAFER, A., KABALIUK, N., JERMY, M. & GEOGHEGAN, P. H. 2021. Review of the Development of Haemodynamic Modelling Techniques to Capture Flow Behaviour in Arteries Affected by Aneurysm, Atherosclerosis and Stenting *ASME Journal of Biomechanics*.

Please detail the nature and extent (%) of contribution by the candidate:

*The candidate gathered, reviewed, analysed, and prepared the manuscript, thereby contributing to ~90% of the final publication. The co-authors contributed to the revising and successful productions of the final work.*

**Certification by Co-authors:**

If there is more than one co-author then a single co-author can sign on behalf of all

The undersigned certifies that:

- *The above statement correctly reflects the nature and extent of the Doctoral candidate’s contribution to this co-authored work*
- *In cases where the candidate was the lead author of the co-authored work he or she wrote the text*

Name: *Assoc. Prof. Paul Docherty* Signature: *Paul Docherty* Date: *27/01/2022*

Deputy Vice-Chancellor's Office
Postgraduate Research Office

UNIVERSITY OF CANTERBURY
Te Whare Wānanga o Waitaha
CHRISTCHURCH NEW ZEALAND

# Co-Authorship Form

This form is to accompany the submission of any thesis that contains research reported in co-authored work that has been published, accepted for publication, or submitted for publication. A copy of this form should be included for each co-authored work that is included in the thesis. Completed forms should be included at the front (after the thesis abstract) of each copy of the thesis submitted for examination and library deposit.

Please indicate the chapter/section/pages of this thesis that are extracted from co-authored work and provide details of the publication or submission from the extract comes:

WILLIAMSON, P.N., DOCHERTY, P.D., YAZDI, S.G., KHANAFER, A., JERMY, M., KABALIUK, N., MURTON, B.: PIV evaluation of haemodynamics proximal to the kissing stent configuration in the aorto-iliac bifurcation. *Submitted to Journal of Endovascular Therapy* (IN REVIEW)

Please detail the nature and extent (%) of contribution by the candidate:

*The contribution of the candidate to the paper amounts to ~95% based on the overall work and final outcome. The candidate designed, implemented and analysed all the experimental work in consultation with the co-authors. The manuscript was prepared by the first author and edited by co-authors.*

**Certification by Co-authors:**

If there is more than one co-author then a single co-author can sign on behalf of all

The undersigned certifies that:

- *The above statement correctly reflects the nature and extent of the Doctoral candidate's contribution to this co-authored work*
- *In cases where the candidate was the lead author of the co-authored work he or she wrote the text*

Name: *Assoc. Prof. Paul Docherty* Signature: *Paul Docherty* Date: *27/01/2022*

Deputy Vice-Chancellor's Office
Postgraduate Research Office

UC
UNIVERSITY OF
CANTERBURY
*Te Whare Wānanga o Waitaha*
CHRISTCHURCH NEW ZEALAND

# Co-Authorship Form

This form is to accompany the submission of any thesis that contains research reported in co-authored work that has been published, accepted for publication, or submitted for publication. A copy of this form should be included for each co-authored work that is included in the thesis. Completed forms should be included at the front (after the thesis abstract) of each copy of the thesis submitted for examination and library deposit.

Please indicate the chapter/section/pages of this thesis that are extracted from co-authored work and provide details of the publication or submission from the extract comes:

WILLIAMSON, P.N., DOCHERTY, P.D., JERMY, M., STEVEN B.M.: Literature survey for in-vivo Reynolds and Womersley Numbers of various arteries and implications for compliant in-vitro modelling. *Submitted to Annals of Biomechanical Engineering* (IN REVIEW)

Please detail the nature and extent (%) of contribution by the candidate:

*The contribution of the candidate to the paper amounts to ~90% based on the overall work and final outcome. The candidate reviewed and analysed existing data and formed the case studies with assistance from co-authors. The manuscript preparation was carried out by the first author. All co-authors edited the manuscript.*

**Certification by Co-authors:**

If there is more than one co-author then a single co-author can sign on behalf of all

The undersigned certifies that:

- *The above statement correctly reflects the nature and extent of the Doctoral candidate's contribution to this co-authored work*
- *In cases where the candidate was the lead author of the co-authored work he or she wrote the text*

Name: *Assoc. Prof. Paul Docherty* Signature: *Paul Docherty* Date: *27/01/2022*

Deputy Vice-Chancellor's Office
Postgraduate Research Office

UC
UNIVERSITY OF
CANTERBURY
*Te Whare Wānanga o Waitaha*
CHRISTCHURCH NEW ZEALAND

# Co-Authorship Form

This form is to accompany the submission of any thesis that contains research reported in co-authored work that has been published, accepted for publication, or submitted for publication. A copy of this form should be included for each co-authored work that is included in the thesis. Completed forms should be included at the front (after the thesis abstract) of each copy of the thesis submitted for examination and library deposit.

Please indicate the chapter/section/pages of this thesis that are extracted from co-authored work and provide details of the publication or submission from the extract comes:

WILLIAMSON, P.N., DOCHERTY, P.D., KHANAFER, A., STEVEN, B.M.: Analysis of flow through extra-anatomic bypasses between supra-aortic branches using PIV. *Submitted to PLoS ONE* (SUBMITTED)

Please detail the nature and extent (%) of contribution by the candidate:

*The contribution of the candidate to the paper was ~95% of the final outcome. The candidate designed, experimented and analysed all the data in consultation with the co-authors. The manuscript was prepared by the first author and edited by co-authors.*

**Certification by Co-authors:**

If there is more than one co-author then a single co-author can sign on behalf of all

The undersigned certifies that:

- *The above statement correctly reflects the nature and extent of the Doctoral candidate's contribution to this co-authored work*
- *In cases where the candidate was the lead author of the co-authored work he or she wrote the text*

Name: *Assoc. Prof. Paul Docherty* Signature: *Paul Docherty* Date: *27/01/2022*

# Publications Arising from this Research

## Published:

1. **Williamson PN**, Docherty PD, Yazdi SG, Khanafer A, Kabaliuk N, Jermy M, Geoghegan PH: Review of the Development of Haemodynamic Modelling Techniques to Capture Flow Behaviour in Arteries Affected by Aneurysm, Atherosclerosis and Stenting. *ASME Journal of Biomechanical Engineering*. 2021, DOI: 10.1115/1.4053082.

2. **Williamson PN**, Docherty PD, Yazdi SG, Khanafer A, Kabaliuk N, Jermy M: PIV Analysis of Haemodynamics Distal to the Frozen Elephant Trunk Stent Surrogate. *Cardiovascular engineering and Technology*, 2021 DOI: 10.1007/s13239-021-00521-2

3. Yazdi SG, Docherty PD, Khanafer A, Jermy M, Kabaliuk N, Geoghegan PH, **Williamson PN**: In-vitro assessment of endovascular aortic repair grafts influence on limb occlusion and ischemia using particle image velocimetry, *Journal of the Royal Society of New Zealand*, 2020 DOI: 10.1080/03036758.2020.1826988

4. Yazdi SG, Hütter L, Docherty PD, **Williamson PN**, Clucas D, Jermy M, Geoghegan PH: A Novel Fabrication Method for Compliant Silicone Phantoms of Arterial Geometry for Use in Particle Image Velocimetry of Haemodynamics. *Applied Sciences (MDPI) Special Issue on Biofabrication: From Additive Bio-Manufacturing to Bioprinting*. 2019;9(18):3811

5. Yazdi SG, Docherty PD, **Williamson PN**, Jermy M, Kabaliuk N, Khanafer A, Geoghegan PH: In vitro pulsatile flow study in compliant and rigid ascending aorta phantoms by stereo particle image velocimetry. *Medical Engineering & Physics*, 96, 81-90. 2021

## In Review:

1. **Williamson PN,** Docherty PD, Yazdi SG, Khanafer A, Jermy M, Kabaliuk N, Murton B: PIV evaluation of haemodynamics proximal to the kissing stent configuration in the aorto-iliac bifurcation. *Submitted to Journal of Endovascular Therapy*
2. **Williamson PN,** Docherty PD, Jermy M, Steven BM: Literature survey for in-vivo Reynolds and Womersley Numbers of various arteries and implications for compliant in-vitro modelling. *Submitted to Annals of Biomechanical Engineering*

## Conference Proceedings:

1. **Williamson PN**, Docherty PD, Khanafer A: In Vitro Analysis of Competitive Flow in Extra-Anatomic Bypasses of the Arteries of the Aortic Arch. Queenstown Research Week: MedSci NZ, 2022, Queenstown, New Zealand, 31 August – 2 September.
2. **Williamson PN**, Docherty PD, Yazdi SG, Khanafer A, Kabaliuk N, Jermy M: In-Vitro Analysis of the Kissing Stent Configuration Haemodynamics in the Aorto-Illiac Bifurcation. Queenstown Research Week: MedSci NZ, 2022, Queenstown, New Zealand, 31 August – 2 September.
3. **Williamson PN,** Docherty PD, Yazdi SG, Khanafer A, Kabaliuk N, Jermy M: In-Vitro Analysis of Haemodynamics Distal of the Frozen Elephant Trunk Stent. NZ Physics and Engineering in Medicine, 2020, Hamilton, New Zealand, 8 – 10 March.
4. **Williamson PN**, Docherty PD, Yazdi SG, Kabaliuk N, Jermy M, Khanafer A, Geoghegan PH: In-Vitro PIV Analysis of Pulsatile Flow Distal of a Frozen Elephant Trunk Stent Phantom. 1st International Conference of Thermal Fluid Dynamics and Control and the 2nd International Symposium of Combustion Instability and Control 2019 Christchurch, New Zealand, 2-6 August. Becker S, Ed.

5. **Williamson PN**, Docherty PD, Yazdi SG, Jermy M, Khanafer A, Kabaliuk N, Geoghegan PH: PIV Analysis of Stented Haemodynamics in the Descending Aorta. 41st Annual International Conference of the IEEE Engineering in Medicine & Biology Society (EMBC) 2019 Berlin, Germany, 23-27 July. Dössel O, Ed.

6. **Williamson PN**, Yazdi SG, Khanafer A, Docherty PD, Geoghegan PH, Kabaliuk N, Jermy M: Particle Image Velocimetry (PIV) Analysis of Haemodynamics Distal of a Frozen Elephant Trunk Stent Phantom. *Fluids in New Zealand* 2019 Dunedin, New Zealand, 31 Jan - 1 Feb. Montiel F, Ed.

7. Docherty PD, Sellier M, Geoghegan PH, Yazdi S, **Williamson PN**, Khanafer A, Kabaliuk N, Jermy M: Integral-based reconstruction of static pressure in a compliant axisymmetric vessel using velocity field data from particle image velocimetry (PIV) analysis. *Fluids in New Zealand (FiNZ)* 2019 Dunedin, New Zealand, 31 Jan - 1 Feb. Montiel F, Ed.

8. Yazdi SG, Docherty PD, Khanafer A, Jermy M, Geoghegan PH, Kabaliuk N, **Williamson PN**: In-vitro measurement of hemodynamics in rigid and compliant silicone replicas of aortic arch using stereoscopic particle image velocimetry *Fluids in New Zealand (FiNZ)* 2019 Dunedin, New Zealand, 31 Jan - 1 Feb. Montiel F, Ed.

9. Yazdi SG, Docherty PD, Khanafer A, Jermy MC, Geoghegan PH, Kabaliuk N, **Williamson PN**: The flow field in compliant and rigid models of the human aortic arch. 19th International Symposium on Applications of Laser and Imaging Techniques to Fluid Mechanics 2018 Lisbon, Portugal, 16-19 July. Hishida K, Ed.

10. Docherty PD, Chase JG, Fox WH, Naswall K, **Williamson PN**: Where do New Zealand Female Engineers come from? Insights from a quantitative analysis. 29th Australasian Association for Engineering Education Conference 2018 Hamilton Waikato, 9-12 December. Armstrong P, Ed.

# Foreword

This thesis presents *in-vitro* measurements of haemodynamic changes as a result of various stenting methods performed within the aorta and its immediate distal branches.

**Chapter 1** introduces the physiology of the cardiovascular system with specific consideration of the regions pertinent to the content of this thesis. The chapter also provides a brief description of cardiovascular diseases and the mechanics of stents used to restore healthy blood flow.

**Chapter 2** describes modern PIV modelling methods. Chapter 2 gives an overview on optical PIV techniques used for visualisation and measurement of fluid flow behaviour through the phantoms and stents analysed in this thesis. The pre- and post- processing methods used for analysis of the PIV images were defined as well as the software and hardware used. Then flow circuit designs and methods for preserving dynamic similarity are provided. Finally, an in-depth description of the design and fabrication process for making thin-walled silicone phantoms of arterial models.

**Chapter 3** evaluates previous literature on non-invasive *in-silico* and *in-vitro* modelling, such as CFD and PIV, respectively, of arteries and stents. CFD and PIV have been used with varying degrees of success to determine haemodynamics in arteries and how implementing stents can improve flow. CFD and PIV approaches are able to examine the effects of stenting without risk to human life, allowing for safer design investigation before deployment. A review of the benefits and deficits of each modelling approach with specific reference to the boundary conditions was undertaken. Chapter 3 also investigates gaps in the literature to be considered in this thesis.

**Chapter 4** provides a survey of the dynamic fluid parameters that are critical for precise *in-vivo* and *in-vitro* modelling. The chapter identifies some major difficulties for design *in-vitro* experiments. The chapter also provides a potential setup for experimentation of a compliance match artery.

**Chapter 5** investigates the effects of the Frozen Elephant Trunk hybrid stent on the haemodynamics within the descending aorta. A surrogate prosthetic stent was designed and implemented within a compliant phantom of the aorta. The research identified a Type 1B endoleak occurring at the distal friction fixing of the stent which may lead to blood leaking into the diseased portion of aorta. This chapter suggests that further research should be carried out on the mismatch in compliance between stents and arteries, particularly for stents implanted in the aorta.

**Chapter 6** investigates the area mismatch of kissing stent geometry used to reconstruct the aorto-iliac bifurcation. Two surrogate stents were produced and installed within a compliant model of the aorto-iliac bifurcation. The stents were designed to protrude significantly into the aorta. This chapter suggests that the kissing stents had little effect on the flow through the iliac arteries. However, a transverse collapse occurred within the abdominal aorta. The collapse has not previously been identified but may be a cause for the reduction of long-term patency.

**Chapter 7** presents a method to determine the presence of competitive flow through extra-anatomic bypasses between the supra-aortic arteries. The purpose is to evaluate the necessity to ligate or embolise proximal supra-aorta arteries. A compliant phantom of the aorta with bypasses was designed and four model setups investigated. The four setups were achieved via purposely occluding the proximal left carotid and/or subclavian artery. The haemodynamic differences between the models indicate that ligation or embolising the proximal supra-aorta arteries may be required to prevent competitive flow. However, ligating both the left carotid and the subclavian arteries also resulted in a notably lower flow through the supra-aortic arteries which may cause other complications.

**Chapter 8** draws general conclusions from the research carried out within the thesis and presents potential future work that may be carried out to advance the research further.

# Contents

# Figure List

# Table List

# Nomenclature

| | |
|---|---|
| AAA | Abdominal aortic aneurysm |
| ABS | Acrylonitrile butadiene styrene |
| AIOD | Aorto-iliac occlusive disease |
| BC bypass | Brachiocephalic-Carotid bypass |
| BCA | Brachiocephalic artery |
| CAD | Computer aided design |
| CCD | Charge coupled device |
| CERAB | Covered endovascular reconstruction of aortic bifurcation |
| CFD | Computational fluid dynamics |
| CMM-FSI | Coupled momentum method for fluid–solid interaction |
| CT | Computer tomography |
| CVD | Cardiovascular disease |
| $De$ | Deans Number |
| EAB | Extra-anatomic bypass |
| FDM | Fuse deposition modelling |
| FET | Frozen elephant trunk |
| FFT | Fast fourier transform |
| FSI | Fluid-structure interactions |
| KS | Kissing stent |
| LCCA | Left common carotid artery |
| LDL | Low density lipoproteins |
| LED | Light emitting diodes |
| LSA | Left subclavian artery |
| LV | Left ventricle |

| | |
|---|---|
| MRI | Magnetic resonance image |
| MRV | Magnetic resonance velocimetry |
| Nd:YAG | Neodymium-doped yttrium aluminium garnet |
| NO | Nitric oxide |
| OSI | Oscillatory shear index |
| ox-LDL | Oxidized-LDL |
| PC-MRI | Phase contrast MRI |
| PDMS | Polydimethylsiloxane |
| $PGI_2$ | Prostaglandin $I_2$ |
| PIV | Particle image velocimetry |
| PMMA | Polymethyl methacrylate |
| PPE | Personal protection equipment |
| PTFE | Polytetrafluoroethylene |
| PTV | Particle tracking velocimetry |
| PVA | Polyvinyl alcohol |
| PVC | Polyvinyl chloride |
| RCCA | Right common carotid artery |
| *Re* | Reynolds Number |
| RI | Refractive index |
| RSA | Right subclavian artery |
| CS bypass | Carotid-Sunclavian bypass |
| TAWSS | Time averaged WSS |
| TEVAR | Thoracic endovascular aortic repair |
| TVWSS | Time varying WSS |
| *Wo* | Womersley Number |

| | |
|---|---|
| WSS | Wall shear stress |
| WSSG | Wall shear stress gradient |

# *1. Introduction*

This chapter provides an overview of the cardiovascular system physiology and concepts related to cardiovascular diseases and vascular treatments. The chapter will focus on arteries investigated in later chapters of this thesis as well as arterial structures and mechanical properties relevant to the research. The potential causes of cardiovascular diseases, particularly those relating to haemodynamic changes will also be introduced. Finally, this chapter will introduce vascular implants, with a focus on covered stents.

## 1.1. Cardiovascular System

The cardiovascular system has two major components, the heart and the blood vessels [1]. A third component, the lymphatic vessels, play an important role in cardiovascular functions. However, they do not contain blood and hence was not relevant to this thesis. The purpose of the cardiovascular system is to pump oxygenated blood, hormones and nutrients throughout the body and allow gas exchange in the lungs [1]. The cardiovascular system helps the body regulate body temperature and to meet the demands of activity, exercise, and stress.

Three subsystems make up the cardiovascular system:

1) Systemic Circulation is supplied via the aorta and branching arteries to the systemic capillaries.
2) Pulmonary Circulation is supplied by the pulmonary artery and feeds the pulmonary capillaries. Pulmonary Circulation allows the exchange of gases within the alveoli of the lung.
3) Coronary Circulation is a specialized blood supply that perfuses blood to the cardiac muscles.

A stylized representation of the systematic and pulmonary circulation is shown in Figure 1.1.

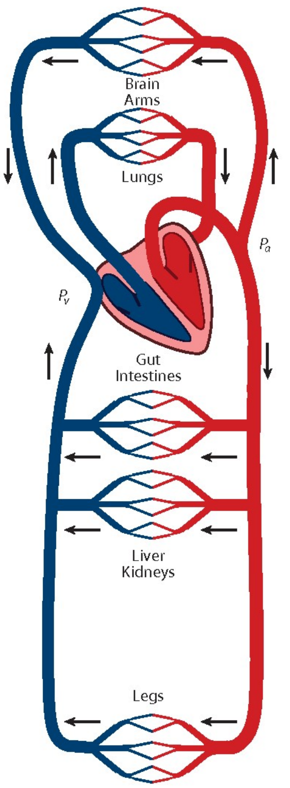

*Figure 1.1: The cardiovascular system showing the systematic (red) and pulmonary (blue) circulation, reproduced with permission from [2]*

The heart can be considered to function as two pumps, left and right, that feed the systemic and pulmonary circulation systems, respectively [1]. The pumps are connected in series. Thus, the output of one eventually becomes the input of the other. The right side of the heart comprises of the right atrium and right ventricle. The right atrium receives deoxygenated (venous) blood from the systemic circulation. The right ventricle then pumps this blood through the pulmonary circulation to allow gas exchange [1]. The left side of the heart is structured similar to the right side. However, the left atrium receives oxygenated blood from the pulmonary circulation, which the left ventricle then pumps through the systemic circulation to perfuse through the aorta to the rest of the body [1]. Cardiac output is a measure of the volume of blood output by the left ventricle and is dependent on arterial pressure and stroke volume [3].

### 1.1.1. Systematic circulation

The systematic circulation begins with oxygenated blood being pumped from the heart [1]. Oxygenated blood is passed through the arteries, then arterioles, then capillaries where gas exchange occurs to tissues [2]. Deoxygenated blood then continues through the venules and veins back to the heart [2]. This thesis focuses on modelling of the effects of stenting on regions of the aorta and its immediately distal arteries.

Arteries can be classed as elastic or muscular depending on their size and structure [3]. Elastic arteries have a large diameter and high percentage of elastin fibers, resulting in an overall low Young's Modulus. The largest and most elastic artery in the human body is the aorta [3]. Most of the stroke volume passes through the aorta. The aorta has a large proximal diameter and tapers into a smaller diameter as other arteries branch off distally. Due to its size, the aorta is separated into multiple sections, beginning with the ascending aorta at the heart. The ascending aorta leads into the aortic arch, then the descending thoracic aorta and finally the abdominal aorta [4]. The major arteries branching off the aorta are shown in Figure 1.2. This thesis primarily looked at the aorta and its branches. Further distal branching was not a focus of this thesis and therefore has not been discussed further. There are many different stenting methods that may be used in the aorta due to its size and geometry [5-9]. Failure of these stents can be fatal. Stenting in the smaller distal arteries such as the femoral arteries can have a lower mortality risk and tend to utilise simpler geometries [10]. Hence, this thesis focused on stents that had a higher associated risk.

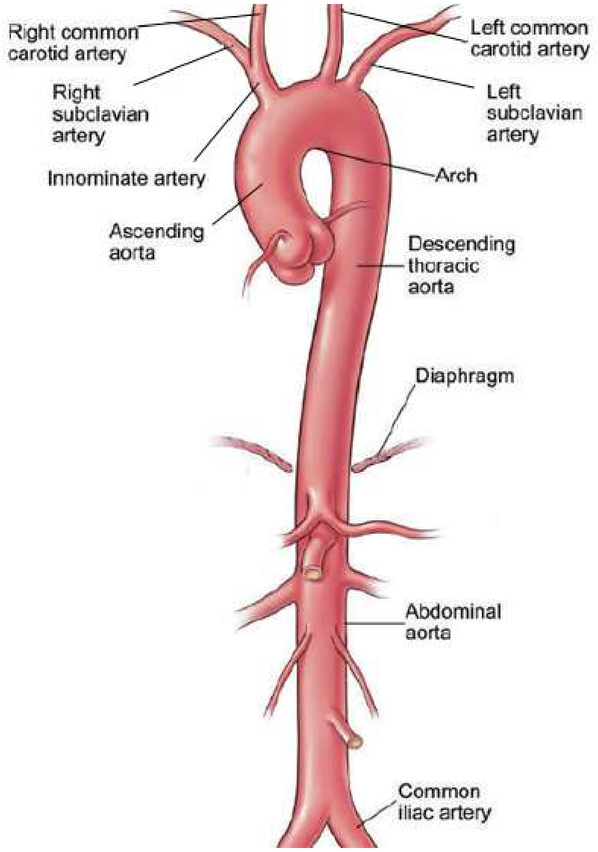

*Figure 1.2: The aorta and its major branches. Retrieved from [11]*

#### *1.1.1.1. Aortic Valve*

The aortic valve is the located at the outlet of the left ventricle into the ascending aorta [12]. The aortic valve is comprised of three semi-circular cusps [12]. The aortic valves acts as a one way flow valve. The valve opens when the pressure within the left ventricle exceeds the pressure in the ascending aorta, initiating systole, and propelling fluid forward into the aorta [13]. The valve then closes when the ascending aorta pressure exceeds the left ventricle, thereby preventing backflow into the heart [13]. The aortic valve ensures anterograde flow through the arteries.

#### *1.1.1.2. Aortic Arch*

The aortic arch connects the ascending aorta and descending aorta through an approximately $180^o$ curve. The supra-aortic arteries branch from the top of the arch and feed blood to the upper limbs and head. For most of the human population these branches are the brachiocephalic artery (BCA), the left common carotid (LCCA) and the left subclavian artery (LSA). However, there are common mutations that may result in more or less arteries branching off the arch [14]. Some common mutations are the bovine arch, additional left vertebral (LV) branch, bovine and LV arch, joined common carotid, aberrant right subclavian and the 'mirrored' or right arch (Figure 1.3). The combined incidence of these mutations is approximately 20% [14]. The normal aortic arch has a tortuous geometry [6]. Along with its many branches, the complex geometry can make vascular intervention difficult. Hence, the aortic arch can be one of the most complicated, as well as one of the most important, arteries.

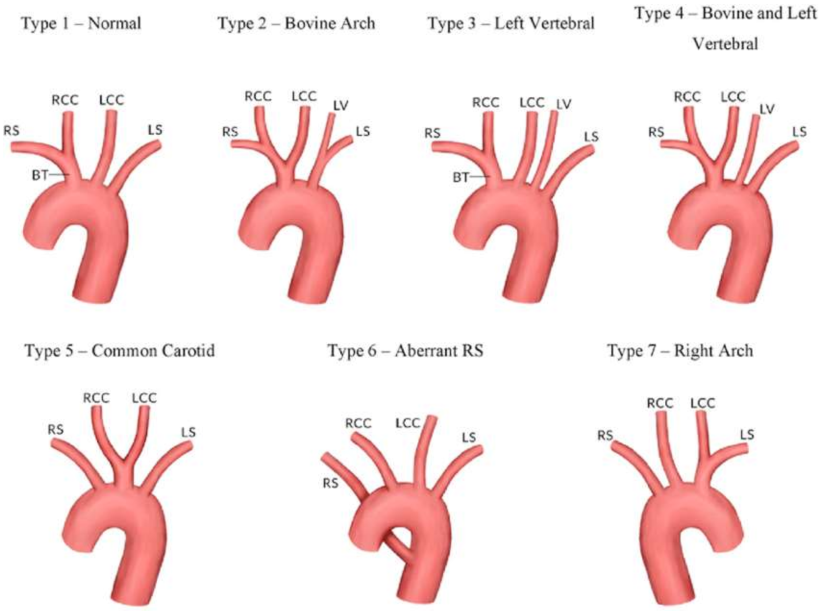

*Figure 1.3: Variations of the aortic arch. Reproduced with permission from Popieluszko, et al. [14]*

### *1.1.1.3. Brachiocephalic*

The BCA (also referred to as the innominate artery or brachiocephalic trunk) is generally the first and largest of the arteries to branch off the aortic arch [12]. It is a short segment of artery that feeds the right subclavian artery (RSA) and the right common carotid artery (RCA) [12]. The BCA provides the main blood supply to the right arm (*brachio*) and head (*cephalic*).

#### *1.1.1.4. Common Carotid Artery*

The LCCA is typically the second branch off the aortic arch immediately following the BCA branch [12]. The common carotid arteries are the primary blood supply for the neck and head [15]. The common carotid arteries branch downstream into the internal and external carotid. The external carotid supplies blood to the face and skull [15]. The internal carotid arteries connect with the basilar artery (feed by the vertebral arteries) in a ring to form the Circle of Willis in the cranial cavity [15].

#### *1.1.1.5. Subclavian Artery*

The LSA is the third branch off the common aortic arch [12]. The subclavian arteries provide blood flow to the axillary and vertebral arteries on the left and right side of the body [16]. The subclavian arteries primarily supply blood to the upper limbs of the body and the thorax. However, they also contribute to blood flow to the head through the vertebral arteries [15].

#### *1.1.1.6. Descending Thoracic Aorta*

The descending thoracic aorta begins at the aortic arch and passes down through the chest connecting to the abdominal aorta at the diaphragm [12]. There are many small arteries that branch off the descending thoracic aorta to provide blood to the ribs and some chest structures [12]. However, the descending thoracic aorta primarily transports blood to the abdominal aorta. The descending thoracic aorta transports a large portion of the stroke volume through to the abdominal aorta.

#### *1.1.1.7. Abdominal Aorta*

The abdominal aorta is the final segment of the aorta. It begins at the diaphragm and continues down through the abdomen until finally bifurcating into the two common iliac limbs. Notable arteries branching off the abdominal aorta, are the iliac limbs, celiac trunk, superior and inferior mesenteric arteries, and renal arteries [12]. The celiac trunk is the first major branch off the abdominal aorta. It is main blood supply for the distal esophagus, stomach and part of the duodenum [12]. The superior mesenteric is the second branch from the abdominal aorta, and supplies blood to the midgut. The midgut starts with the duodenum and continues through the intestines to the proximal region of the colon [12]. The inferior mesenteric is the primary blood supply of the descending colon and pelvic brim. The renal arteries are the only blood supply to the kidneys [12]. They branch from abdominal aorta from between the superior and inferior mesenteric arteries.

#### *1.1.1.8. Common Iliac Arteries*

The common iliac arteries bifurcate off the distal abdominal aorta. They provide blood to the lower extremities of the human body. The common iliac artery is a section typically average 50 – 60 mm in length [17]. The left and right common iliac limbs are usually asymmetric, with slight variances in lengths and take-off angles [18]. The distal common iliac arteries branch into the internal iliac and external iliac arteries. The internal iliac arteries supply the sphincters, pelvic viscera, and reproductive organs with blood [19]. However, the external iliac arteries proceed inferiorly along the medial border of the psoas major muscles and pass deep to the inguinal ligament [20]. At this region, the arteries are known as femoral arteries and continue down the legs.

## 1.2. Blood

Blood is a suspension consisting largely of plasma with solid (cells) and liquid (chylomicrons) particles [4]. Plasma is a pale-yellow fluid that is 90% water with the remainder being made from vital proteins and minerals [4]. Plasma makes up around 55% of the total blood volume. The remaining 45% solid particles include red blood cells, white blood cells and platelets. Red blood cells (or erythrocytes) carry oxygen through arteries and have the largest effect on the mechanical properties of blood due to their high concentration [4]. For comparison there are only a few white blood cells and 50-100 platelets per 1000 red blood cells. White blood cells are mainly involved in the human body immune response and platelets aid the clotting of blood. Blood accounts for approximately 6-10% of the body’s mass and has a density of approximately 1060 $kg{\cdot}m^{-3}$ [3].

For blood to flow, there must be a pressure gradient driving the fluid. Blood flow rate is determined by the pressure gradient and the resistance of flow. Hence, one of the most important mechanical properties of blood is the viscosity. Viscosity is defined as the ratio of shear stress to shear rate, measured in Pascal-seconds [Pa·s] [21] and is one of the most important characteristics to determine flow resistance, along with vessel diameter and length (Equation 1.1) [1].

$$R \propto \frac{\mu L}{r^4} \qquad \text{(Eq. 1.1)}$$

where $R$ is the flow resistance, $\mu$ is the dynamic viscosity [Pa·s], $L$ is the vessel length [m] and $r$ is the radius of the vessel [m]. The viscosity of blood at body temperature (37°C) has been reported between 0.003 and 0.006 Pa·s [3].

Viscosity is also used to class fluid types. Plasma is a Newtonian fluid. Newtonian fluids have a constant viscosity with respect to the rate of shear straining [3]. Hence, Newtonian fluids have a linear relationship between shear stress and shear rate (Equation 1.2). However, the viscosity of Newtonian fluids can still be affected by temperature.

$$\tau = \mu\dot{\gamma} \qquad \text{(Eq. 1.2)}$$

where $\tau$ is the shear stress [Pa], $\mu$ is the dynamic viscosity [Pa·s] and $\dot{\gamma}$ is the shear strain [$s^{-1}$]. While plasma is Newtonian, the solid substrates within blood (such as red blood cells) result in whole blood behaving like a non-Newtonian fluid. Hence, true blood viscosity is dependent on both the shear rate and temperature. Since the human body is generally maintained at 37°C, temperature dependence of blood is not generally considered significant [3].

Viscosity of blood can be dependent on the geometry of the vessel it flows through. As blood flows through a tube, red blood cells tend to 'tumble' and move towards the centre of the lumen. As such, a layer near the wall is produced with very few cells present, known as the free-cell layer [15]. Blood flow through vessels smaller than 1.5 mm in diameter have a lower apparent viscosity than through large diameter arteries. This effect is called the 'Fahraeus-Lindqvist effect' [15]. For blood flow through tubes less than 1 mm in diameter, the free-cell layer has a large effect on the overall flow and causes the effective viscosity to change with respect to diameter. As the diameter of arteries increases, the effect of the free-cell-layer reduce and the viscosity reaches an apparent asymptotic viscosity value that is unaffected by shear stresses. Hence, it may be safely assumed blood behaves as a non-Newtonian fluid through small blood vessels, such as capillaries [3]. However, as McDonald [22] noted, blood flow through large arteries, such as the aorta, can be assumed to behave as a Newtonian fluid as the concentration of red blood cells is typically lower than 10%. This occurs as the free-cell layer has little effect on larger arteries.

## 1.3. Arterial Wall Structure

The arterial walls are made up of three layers. The innermost is the internal tunica intima, which is surrounded by the tunica media and finally the tunica adventitia (Figure 1.4) [4]. Each layer has a unique make-up. The intima has two key components. The innermost component is a single layer of endothelial cells called the endothelium. This layer is in contact with the blood as it passes through the arteries. Surrounding the endothelium is a sub-endothelial layer comprised largely of collagen fibers and some collagen producing cells [4]. A layer of elastic fibers forms a boundary between the intima and the media layer. The media layer is typically the thickest of the three layers [4]. The media layer typically defines whether the artery is an elastic artery or muscular vessel. These definitions arise dependent on the ratio of elastic fibers present. Large elastic arteries, such as the aorta, have a large percentage of concentrically layered elastic fibers separated by thin layers of connective tissues, collagen and smooth muscle cells [4]. Arteries further from the heart are smaller and have a larger percentage of smooth muscle cells. Smooth muscle cells are also layered, however, the number of layers decreases with the size of the vessel. Smooth muscle cell layers in muscular arteries are interspersed with small amounts of connective tissues, collagen and elastin fibers [4]. The adventitia is the outermost layer. The main component of the adventitia is loose connective tissues with sparse amounts of elastin and collagen fibers [4]. The adventitia may be as thick as, or even thicker, than the media layer.

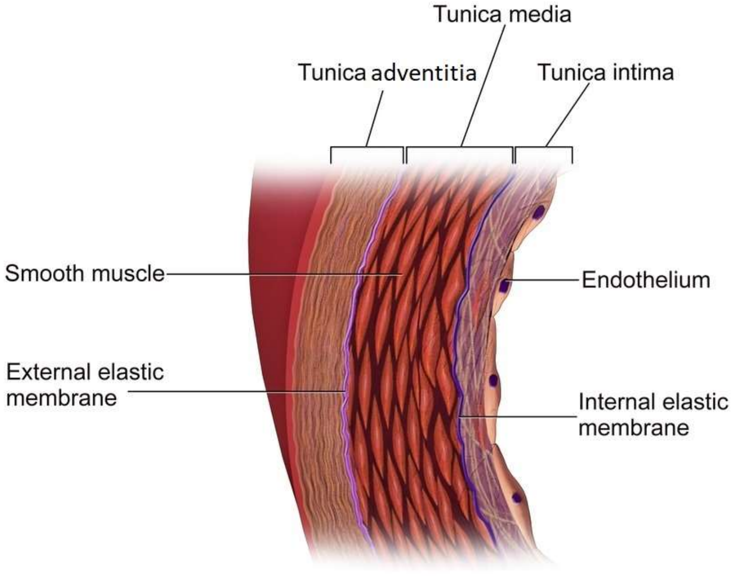

*Figure 1.4: Arterial wall layers. Reproduced with permission from [23]*

### 1.3.1. Endothelial Cells

Endothelial cells are a single layer of cells that line the internal wall of all arteries and veins, irrespective of the vessel size [24]. They are in constant contact with blood flow. Endothelial cells are highly sensitive to wall shear stresses (WSS) and can be quite fragile in the presence of disturbed flow [4]. The mechanics of WSS are provided in detail in Section 3.1. Physiology and Mechanics of Arteries and Stents. Despite the fragility of endothelial cells, they also have a strong regenerative ability. Endothelial cells can continuously regenerate, even growing through synthetic materials implanted into the vessels [4]. Endothelial cell behaviour in straight arteries is relatively simple. In straight arteries the cells align in the direction of the blood flow as the shear stresses at the wall are well defined. However, the flow at branch points and curves is less simple. When blood velocity increases, as on the outer curves of a bending artery, the WSS increases and endothelial cells become flatter, also aligning with the direction of flow [25]. However, as blood flow decreases, as along the internal curve of a bending artery or branch point, the WSS decreases and the endothelial cells increase in volume and lose their alignment [25]. Low WSS can also result from recirculating or stagnating flow.

Endothelial cells maintain the fluidity of blood, regulate flow, control the permeability of vessel walls and mediate white blood cells within healthy arteries [26]. Endothelial cells are involved in mechanisms that prevent coagulation of blood within the vascular network, thereby assisting with blood fluidity [26]. They produce Nitric Oxide (NO) and prostaglandin $I_2$ ($PGI_2$) which inhibit platelet aggregation and adhesion [26]. NO is beneficial to the overall heart health as it aids blood pressure control. NO is a molecule that is the principal vasorelaxant involved in relaxing the smooth muscle cells and mediating the blood flow [26]. Vasorelaxation means the cells of the inner wall relax and cause the vessel to dilate. NO may also be the primary inhibitor to white blood cell activation. Endothelial cells create a permeability barrier that prevents plasma passing from the bloodstream into tissues within the capillaries. NO production is influenced by shear stresses in the proximal blood flow [26].

Endothelial cell dysfunction is one of the principal causes for atherosclerotic lesion formation. Endothelial cells are the primary cells involved in the inflammatory response of the arterial vessel walls [26]. Whilst the primary role of thrombosis is to exclude infected or damage cells from the surrounding cells, it can also cause further damage to the vessel walls and induce haemorrhaging. Changes in endothelial cell function may lead to the loss of anti-coagulant functions, allowing platelets to adhere more to vessel walls and each other. Changes may also alter the cell wall permeability [25]. Altered hormone production and cell activation has been linked to both initial plaque formation within arteries and plaque growth [25].

Fluid shear stresses and forces on the endothelial cells are important to the health and longevity of the arterial vessels. Changes in blood flow can induce abnormal WSS and oscillations that alter the structure and function of endothelial cells and thus NO production and consequently, alter the endothelium response. Reduced NO production may contribute to constriction of vascular vessels and aggregation/adhesions of platelets and activate white blood cells. Concomitant with NO production changes, low velocities may promote the presence of oxidized-low density lipoproteins (ox-LDL). Ox-

LDL molecules that enter the arterial walls may be consumed by macrophages, turning the macrophages into “foam cells” that promote inflammation and exacerbate atherosclerotic development. A detailed description of atherosclerotic formation is provided in Section 1.3.1. Atherosclerosis.

### 1.3.2. Mechanical Properties of Arteries

All arteries have a level of compliance. Compliance is the inverse of elastance. Compliant arteries deform under pressure changes due to their high elastin content. The ability to deform enables compliant arteries to accommodate large bursts of blood and dampen fluctuations in flow [27]. The blood is distributed in two phases. The first phase is the ‘systolic period’. During the systolic phase, the aortic valve opens, and blood is ejected from the left ventricle into the aorta. The aorta is the most compliant (and therefore elastic) artery in the human body and can dampen the pulsatile pressure that results from the intermittent ejection of blood from the left ventricle [1]. The aorta can dilate to accommodate up to 50% of the blood ejected from the left ventricle [28]. When the aortic valve closes, terminating flow from the heart, the aorta contracts, thereby forcing flow to continue flowing through the arteries and preventing flow reversal in smaller arteries (Figure 1.5). The second pressure phase is called the ‘diastolic period’ and begins with the aortic valve closing. The flow through the dilating and contracting vessel is known as Windkessel motion.

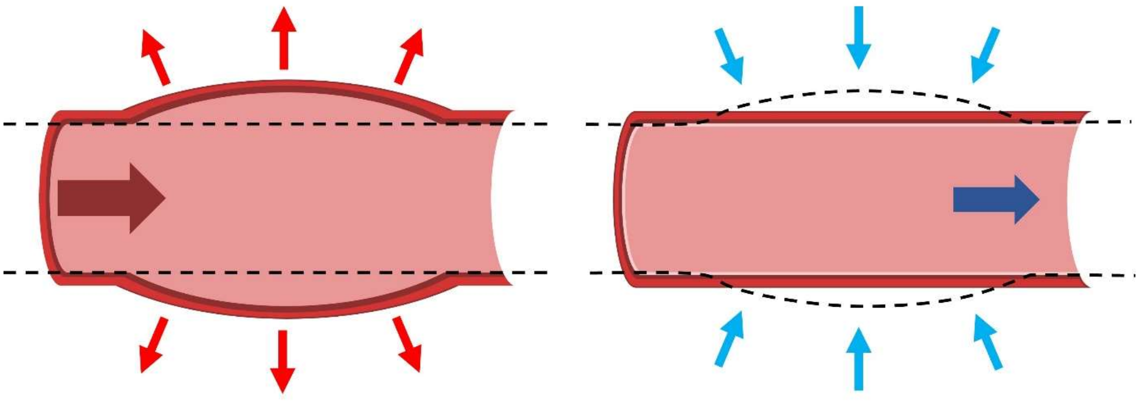

*Figure 1.5: (left) Systolic inflation of elastic artery, (right) diastolic return to original diameter*

Pulse pressure is the difference between the peak systolic pressure and peak diastolic pressure [1]. The deformation of the aorta reduces the arterial pulse pressure experienced by distal arteries. If the aorta was rigid, the pulse pressure within the distal arteries and the capillaries may be too high, resulting in damage [29]. Normal pulse pressure ranges 40 to 45 mmHg in heathy people [1]. However, cardiovascular diseases (CVD) and age can affect this range and it is not uncommon elderly patients to have a pulse pressure up to 60 mmHg [1].

## 1.4. Cardiovascular Diseases

CVD are the leading cause of death in the developed world [30]. There are many different types of CVD, though this thesis focuses on three main forms:

1) Atherosclerosis,

2) Aneurysm,

3) Dissection of the arterial wall.

Medication and life-style changes can help mitigate early stages of CVD. However, in more severe cases, open surgical repair or endovascular intervention may be necessary.

### 1.4.1. Atherosclerosis

Atherosclerosis is the most common type of CVD [31]. Atherosclerosis is characterized by the deposition of fatty lipids both within and on arterial walls [31]. This deposition results in the hardening and narrowing of vessel [31]. The depositions on the arterial walls are known as plaque. Plaque significantly reduces arterial compliance [15]. Atherosclerosis can range in severity from small lesions to total occlusion of the artery, entirely preventing blood perfusion, and can thus prevent oxygen reaching distal tissue [15]. Total occlusion of the artery can lead to downstream organ necrosis. Coronary arteries supply blood to the heart. If occlusion occurs within the coronary arteries, the patient may suffer from potentially fatal myocardial infarction [31].

Atherosclerosis has high incidence within large arteries. However, it is also prone to develop at branching or bifurcation regions. This is because lesions tend to initiate within the endothelial cells. As noted in Section 1.3.1, cells at junctions or curves tend to have a larger volume to surface area ratio and are not well aligned due to poorly defined WSS. This can lead to increased permeability of macromolecules such as LDL [32]. The primary cause for atherosclerosis initiation is an accumulation of sub-endothelial LDL molecules [32]. Genetics, lifestyle and trauma can also have a significant impact on a patients likelihood to develop stenotic (narrowed) or occluded (blocked) arteries [15].

Atherosclerosis can form in a vicious cycle. The build-up of LDL molecules in the endothelium causes inflammation in the damaged cells. Monocytes along with platelets pass through the endothelium due to the increased permeability. The platelets adhere to the damaged region. Monocytes in the endothelium consume the LDL and form “foam cells” which eventually die and further propagate the inflammatory response [15]. In addition, smooth muscle cells from within the tunica media migrate to the intima layer of the vessel wall and produce a fibrous layer. As LDL proteins continue to accumulate, a fibrous scar tissue is formed and the intima layer of the vessel and begins to thicken [15]. This formation of fibrous scar tissue is called intimal hyperplasia. The changes in local fluid dynamics can encourage further abnormal cell behaviour, permeation of LDL molecules and organ necrosis, resulting atherosclerotic plaque growth  [25]. The stages of atherosclerosis formation are shown in Figure 1.6.

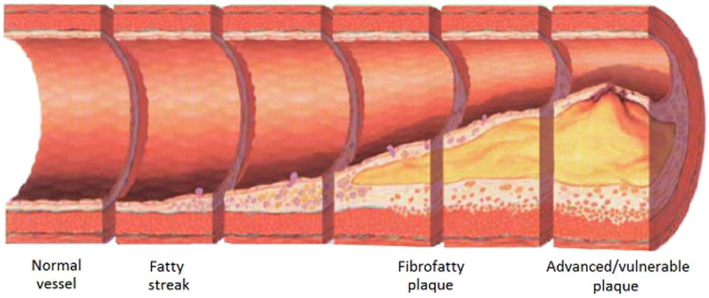

*Figure 1.6: Atherosclerotic formation process. Adapted with permission from Patchett [33]*

To compensate for the lesions, arterial walls may remodel and grow thinner to maintain the lumen diameter [34]. When the remodelling limit is reached, atherosclerosis begins to protrude into the artery lumen produce a stenosis. In advanced stenosis, cells may begin to die resulting in calcified scar tissue [15]. The scar tissue has a much lower compliance. If the surface cells are rough or the atherosclerotic lesions rupture, platelets will adhere to the damaged regions and form a thrombus [15]. Atherosclerosis often doesn’t present with any symptoms until either the lesions rupture or grow to fully preclude blood flow [31]. Advanced atherosclerosis frequently requires surgical intervention to repair the artery wall and restore healthy perfusion of blood.

Some of the most common initiation zones for atherosclerotic lesion formations are the inner curve of the aorta, the leading edge of the take-off locations for supra-aortic locations (such as the BCA, LCCA and LSA) and the aorto-iliac bifurcation [15]. This does not mean that these are the only locations. Atherosclerotic lesions can develop within any medium-large arteries [2].

### 1.4.2. Aneurysm

Aneurysms are defined as the permanent dilation of an artery beyond 150% of its original diameter (Figure 1.7) [35]. Aneurysms may occur within any artery. However, they predominantly occur within the aorta or the brain. If left untreated, aneurysms may continue to expand until they rupture, which can be fatal. In 2015, approximately 168,200 of deaths were due to aortic aneurysm globally [36]. The ultimate cause for aneurysm initiation is not well understood. It is believed that aneurysms form due to malfunction of the connective tissues in the arterial wall. However, lifestyle, genetics, or underlying health complications such as high blood pressure are known to increase the risk of aneurysm.

There are two main types of aneurysms: saccular, and fusiform [15] (Figure 1.7). Saccular aneurysms are most common in cerebral arteries [37]. They appear as a bulge on the side of an artery. They have a “neck” that connects then to the artery and a dome that creates the bulge [37]. Fusiform aneurysms are a dilation involving the entire arterial circumference dilating, typically over a short distance. Fusiform aneurysms are more common within sections of the aorta [37].

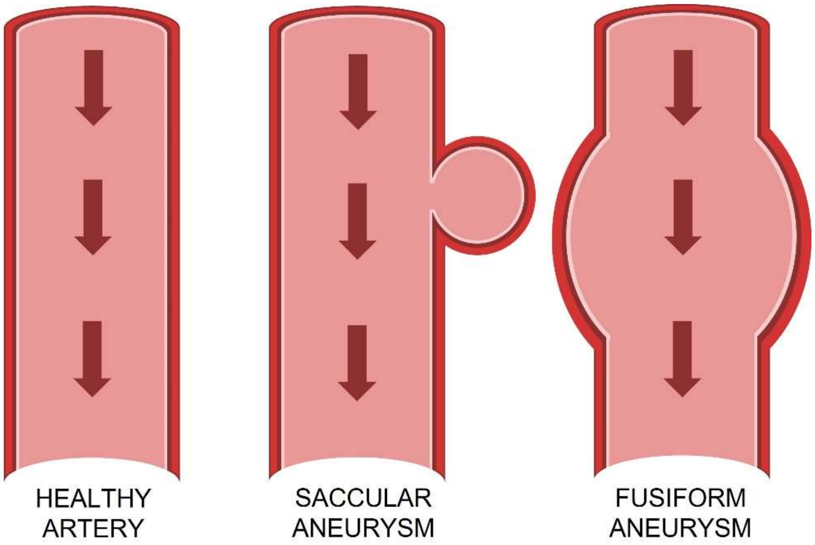

*Figure 1.7: Forms of aneurysms*

The most common aneurysms in the human body are abdominal aortic aneurysms (AAA). However, thoracic aortic aneurysms and intracranial aneurysms are also common [15]. AAA may have no noticeable symptoms. The most common identification method for AAA is through screening for unrelated health problems [38]. Aneurysms typically have a threshold value for which medical practitioners will intervene. In the case of AAA, aneurysms below 5 cm in diameter will be closely observed, but intervention is unlikely unless the aneurysm grows suddenly. However, when the aneurysm is over 5 cm, it is considered to be at high risk of rupture and therefore surgical repair methods are used. Ruptured aneurysms, particularly within the aorta, have a high fatality rate. 30-50% of patients with ruptured AAA will die before hospitalization, and there remains a 50-70% mortality rate after surgical repair [38]. Aneurysms can change the haemodynamic behaviour through an artery resulting in stagnating or recirculating flow. The abnormal flow can change flow of blood to distal organs and may exacerbate disease propagation [39, 40].

### 1.4.3. Dissection

Arterial dissection is a tear in the lining of the vessel wall that may propagate through the layers of the artery (Figure 1.8). Dissection occurs often as a result of trauma or injury. However, spontaneous dissection may also occur. The most common, non-traumatic cause for dissection is weakened arterial walls due to atherosclerotic plaque build-up [41]. Dissections initiate within the intima layer of the arterial wall, but the flap produced can be as thick as 66% of the media layer [41]. The tear provides and alternate pathway for blood to flow resulting in the wall dissecting into two lumens. The tear can propagating distally within intima and media layers. Tears may propagate back into the true lumen or out through the adventitia layer, referred to as a rupture. Dissections are particularly important to identify in the aorta due to the high volume of blood they transport. A dissected aorta may not enable blood to effectively perfuse through branching arteries [42]. This can result in ischemia and organ necrosis. Dissections can be fatal if not identified and treated quickly.

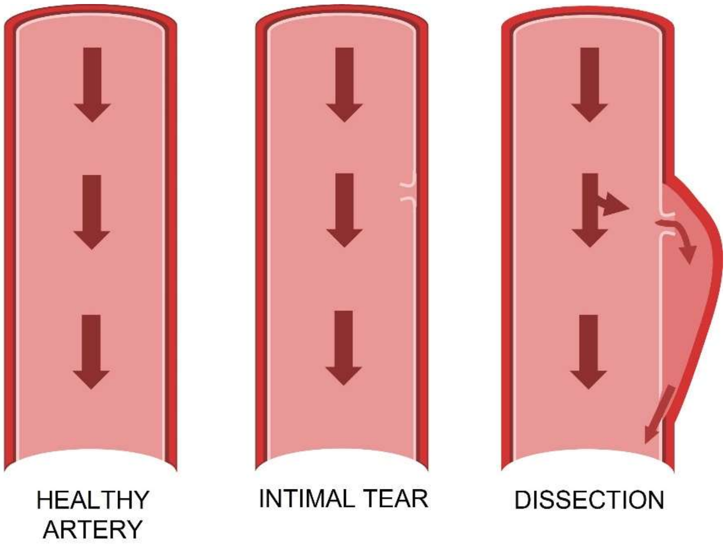

*Figure 1.8: Evolution of arterial dissection*

Aortic dissection will lead to two or more lumens (depending on the number of times it dissects) of which only one is the true lumen. False lumens may encroach on branched arteries, acting to narrow the branches and prevent or significantly reduce flow [41]. The true lumen can generally be identified as it is the smallest of the potential lumens [43]. For pressure within the lumens to be at equilibrium the false lumens will have a greater expansion as they have thinner walls, thereby causing the true lumen to collapse [43].

There are two main types of aortic dissection according to the Stanford classification system [35]. Stanford Type A Aortic dissections occur typically within the ascending aorta. Though less common, Type A dissections require immediate treatment, often requiring open surgery to identify the damaged artery and replace it with a synthetic prosthetic [35, 42]. The more common aortic dissection is the Stanford Type B Aortic dissection. This form of dissection typically initiates distal of the aortic arch. Type B dissections have a much lower risk and may be repaired by either open surgery or endovascular repair, so long as blood flow to the branching arteries is not inhibited [42]. Whilst immediate surgical intervention is not always necessary, there is still a risk of the dissection propagating through the vessel wall and rupturing. Furthermore, specific selection and precise positioning of the stent-graft is pivotal to prevent a Type I endoleak. A Type I endoleak occurs when the graft insufficiently seals against the artery wall and blood flow still seeps outside the proximal or distal graft into the aortic wall tear. This leak allows a new fluid entry (i.e. a new tear) or retrograde Type A dissection [44]. Type I endoleaks require re-intervention to repair.

## 1.5. Treatment of CVD

The three types of CVD outlined in Section 1.3 are often treated using vascular implants. Vascular implants are typically stents or stent grafts and are manufactured from biocompatible metals or polymers (Figure 1.9) [28]. Stents are tubular components that are deployed within the lumen of a vessel to open the vessels and support arterial walls, thereby maintaining healthy blood flow. There are three main types of stents: bare metal stent, drug-eluting stents, and grafted/covered stents. Bare metal stents are the most basic stents. They are a mesh-like tube made from thin wires [45]. The mesh patterns may vary between manufacturers and intended purpose of the stent. Stents were first introduced in the mid-1980’s to treat coronary artery disease [45]. In 1986, a self-expanding, stainless steel wire mesh structure stent was implemented for the first time in the human body [45]. More recently though, biocompatible materials such as platinum, chromium and cobalt have been preferred over stainless steel [45]. Bare metal stents were introduced in the 1990s, however, their prevalence in surgical repair is reducing due to a higher risk of restenosis [45]. Restenosis occurs when atherosclerotic legions continue to grow through the mesh of the stent, resulting in a re-narrowing of the arterial lumen. Drug-eluting stents are similar to bare metal stents in geometry. However, they are coated with slow-release medication to block cell proliferation and hence prevent blood clotting and restenosis [45]. Covered stents are stents with a fabric/graft material covering the metal [46]. Covered stents were initially designed to repair aneurysmal arteries as they can purposely exclude blood flow from an aneurysm or dissected wall [46, 47]. They are now frequently used to treat long segments of occlusive disease as they can inhibit the ability for intima to grow through the wire mesh [47].

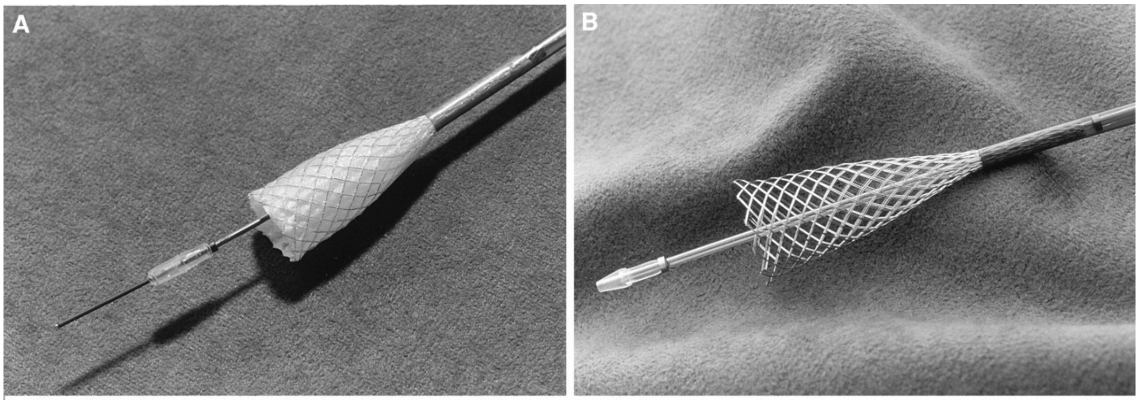

*Figure 1.9: Covered stent (left) and bare metal stent (right) being deployed. Note drug eluting stents look similar to bar metal stents Image reproduced with permission from [48]*

### 1.5.1. Covered Stents

Covered stents, and their use in specific CVD repair were the focus of this thesis. The grafts are typically made from PTFE (polytetrafluoroethylene) or Dacron [28]. The manufacture methods of these stent graft materials preclude flow between the stent graft lumen and the native artery wall. This makes them ideal for repair of dissection or aneurysms [46]. Covered stents also have a low risk of in-stent restenosis [49]. Resultantly, they have a higher patency for repair of atherosclerosis than bare metal stents.

Another use of covered stents is in bypassing arteries. Due to the lack of blood flow across the graft surface, covered stents are suitable for extra-anatomic bypasses to revascularize arteries that would otherwise not receive sufficient blood flow [8, 50, 51]. Extra-anatomic bypasses do not follow the natural geometry of the artery and therefore are ubiquitous with altered haemodynamics. Furthermore, they introduce a risk of competitive flow which may exacerbate CVD progression. Competitive flow occurs when the bypasses artery is not total blocked, thereby resulting in abnormally low flow through the extra-anatomic bypass [52]. However, extra-anatomic bypasses are often implemented when other methods of delivering blood to the distal arteries has failed or is not possible [53].

### 1.5.2. Mechanics of stents

Stents are generally compressed prior to deployment and dilate into their desired position during implant. Stent dilation may be driven by elastic self-expansion, or balloon expansion [54]. The key differences between the two is largely their deployment method and intended use. Self-expanding stents are compressed and constrained within a delivery catheter [54]. At the location of CVD repair the self-expanding stents are unsheathed and will conform to their original unconstrained state. Self-expanding stents have good radial forces and hoop stresses. They are resistant to crushing as they will always try to return to their nominal geometry [47]. As such, they are beneficial in curved geometries or flexural arteries [47]. Self-expanding stents require a high level of surgeon skill to place accurately within the diseased artery.

Balloon expanded stents are crimped down onto a deflated balloon [54]. They are deployed within the artery by inflating the balloon until the final diameter is achieved. Following this the balloon is deflated and removed. Balloon expanded stents can be located within the artery more accurately, compared to self-expanding stents [47]. Balloon-expandable stents also have a great hoop strength and hence are more resistant to elastic recoil within an artery [47]. However, balloon expanded stents are more at risk of being crushed. Balloon expandable stents have a specific yield stress, beyond which they will plastically deform. Hence, balloon-expandable stents are most suitable in short straight segments of arteries.

Stents can change the fluid behaviour through a vessel. Many studies on the fluid dynamics of stents have been carried out with a focus on the effects of different mesh patterns and strut size of the stents on the WSS of the arterial walls [54-59]. The near-wall fluid behaviour influences the inflammatory response of the artery walls due to stenting [55, 60]. However, the effects of stent struts can change notably within hours of the implantation. In particular, stent struts are covered with a layer of thrombus within a few hours to days following implantation [54]. Furthermore, the effect of different stent meshes is negligible when modelling covered stents, as often the mesh is on the outside of the stent. The bulk fluid behaviour was the focus of this thesis. The bulk fluid behaviour between stent meshes within arteries is unlikely to vary significantly across differing mesh geometries. However, differences in flow may be present based on rigidity/compliance of stents and their ability to conform to the geometry of the natural artery.

One of the major factors that alter fluid flow behaviour within a stented artery is stent oversizing. Abrupt changes in the cross-sectional area between stent and artery at both proximal and distal ends can lead to deleterious flow disturbance [54]. Stent graft oversizing guidelines vary significantly. Typically stents tend to be oversized by 10% [61]. However, Liu, et al. [62] reported stent oversizing ranges from 0 to 32% within a dissected aorta. Stent oversizing plays a pivotal role in preventing stent migration, particularly within elastic arteries as they can expand naturally with pulse pressure. However, too much oversizing can damage the endothelial cells and has been linked to deleterious wall stresses [63, 64]. As noted in Section 1.3.1., damage to endothelial cells and altered WSS increases risk cell growth dysfunction which can lead to in-stent restenosis.

Compliance matching may also influence the patency of stents. Arteries have a low and non-linear elastic modulus. They have a low stress response at low pressure but show a steep increase in elasticity at higher pressures [28]. Stent wires and grafts are comparatively rigid. Whilst PTFE and Dacron are suitable biocompatible polymers to prevent blood seepage between the stent lumen and artery wall, they have a much higher elastic modulus. Dacron is 24 times stiffer than the aorta [6]. The stent wires are also significantly more rigid than an artery [28]. The rigidity induces a compliance mismatch between the graft and the parent artery [65, 66]. As such the lumen of a grafted stent is unable to swell and accommodate the systolic pressure in a natural Windkessel motion (Figure 1.5). Stents can inhibit the natural pulse pressure damping and smoothing functions of the *in-vivo* artery. This can produce jet like flow exiting the grafted stent. Furthermore, the compliance mismatch can alter the WSS experienced by distal arteries and may exacerbate CVD progression. A decrease in upstream compliance can result in significant unsteady flow through the distal arteries [67]. As stated in Section 1.3.2., lower compliance within the aorta leads to significantly higher pulse pressure. The high systolic pressure may damage capillaries. Furthermore, diastolic flow relies on Windkessel effects to produce near continuous flow between heart beats [67]. Interest in stent graft compliance is growing with emerging research investigating the effect poorly matched compliance can have on the patency of a stent [54, 65, 66, 68]. Current research into the haemodynamic effects of stenting using *in-silico* and *in-vitro* modelling methods is reviewed in Chapter 3.

## 1.6. Summary and Thesis questions

This chapter provided a physiological background of the cardiovascular system and subsystems with a focus on systemic circulation. This thesis focuses on the human aorta and the major arteries that branch off the aorta. Haemodynamically induced WSS was identified as the primary stimulus for function and dysfunction of the endothelial cells. Changes to the WSS experienced by the endothelial cells can lead to remodelling of the arterial walls and alter arterial mechanical properties. Changes in WSS are commonly identified on the inner radius of curved arteries and branching junctions as the blood flow is not as streamlined in these locations. Endothelial cell dysfunction can cause changes in the compliance of arteries. Altered compliance can also alter the blood flow patterns within arteries and initiate CVD, such as atherosclerosis.

Stents may be used to repair arteries and mitigate CVD, including their use in bypassing blocked arteries. However, stenting can introduce other risks such as stent migration, restenosis, or damaged endothelial cells. Unmatched compliance between arteries and stents may also result in deleterious flow behaviour known to result in long-term complications. The full effects of stents on haemodynamics and the potential link to loss of stent patency is not well understood. *In-vitro* experimentation using phantom arteries and surrogate stents may potentially provide insight into some of the causes for unsatisfactory stent patency.

This thesis used *in-vitro* analysis to develop modelling methods used for investigation of the haemodynamics of specific stents orientations used for repairing complex CVD within the aorta and its immediate branches. The specific stents investigated are reviewed in their relevant chapters but include the Frozen Elephant Trunk (FET) stent-graft, the Kissing Stent (KS) geometry, and extra-anatomic bypasses within the supra-aortic arteries. The purpose of this thesis was to improve the current *in-vitro* methods and provide insight into the haemodynamic responses of the stent methods.

The thesis research questions focused on modelling the efficacy of stents. These include:

1. Can compliance mismatch be modelled *in-vitro*?
2. How does the change in compliance between an artery and a stent affect the flow of blood?
3. Can PIV be used to assess stent effects on the overall haemodynamics in an artery?

# 2. Particle Image Velocimetry

This chapter provides an overview of particle image velocimetry (PIV) and the specific PIV methods used in latter chapters of this thesis. The components that form the experimental flow circuit and scaling parameters used to model arterial waveforms are provided. A description of how phantoms were designed and manufactured is also given.

## 2.1. Background

Particle image velocimetry (PIV) is an optical measurement technique that is used to obtain instantaneous velocity vector fields [69]. PIV uses optical image capture to identify the fluid displacement between two instances in time, measured using trace particles seeded within the flow. PIV captures the motion of particles seeded in a fluid. PIV typically uses laser or diode based optical measurements to illuminate particles within a certain of the flow stream and paired image captures allow identification of fluid motion (Figure 2.1). PIV uses measurement sensors that do not influence flow within the fluid domain. External sensors allow data to be captured from the full region of interest without disrupting the fluid, such that a true velocity field can be measured.

Typically, a high-intensity monochrome light source, such as a laser, illuminates the region of interest with a beam that passes through a series of lenses that transforms the light into a thin sheet (typically <2 mm) [69]. Hence, PIV is commonly limited to pseudo two-dimensional analysis. The illuminated domain allows image capture of small trace particles (Stokes Number $\ll 1$) that follow the streamlines of the flow within the light sheet. Both planar and stereo-PIV capture flow behaviour on a single thin plane. However, stereo-PIV can also identify out-of-plane velocity components on the plane [69].

Three-dimensional modelling with PIV is possible with tomographic PIV. Tomographic PIV requires a minimum of three cameras in the setup [69]. Tomographic PIV captures a fluid volume rather than the two-dimensional sheet of planar/stereo PIV, providing a global view of the volumetric velocities. However, it is complex and time consuming to process the data. PIV is similar to particle tracking velocimetry (PTV), except that PTV focuses on single trace particles to identify a single vector, meanwhile PIV uses clusters of particles to identify a single vector of fluid motion [69]. An in-depth description of different PIV techniques and their configurations can be found in Raffel, et al. [69]. This thesis used planar PIV and typically captured two planes for each experiment to ensure out-of-plane flow of interest was not missed.

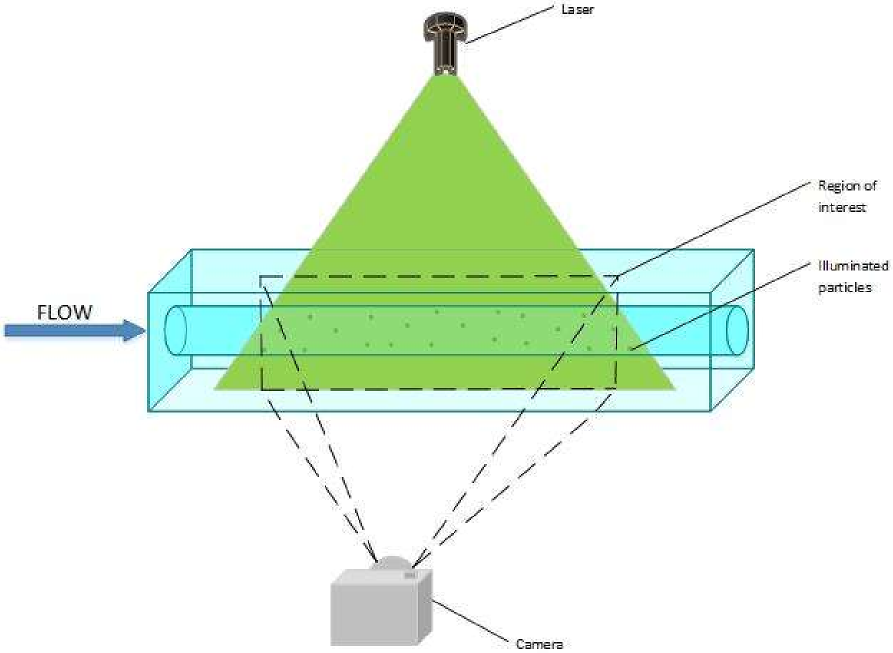

*Figure 2.1: Optical PIV set up*

PIV captures image pairs at discrete time intervals between laser pulses. PIV typically uses a cross-correlation technique to process the images and calculate the displacement field [70]. A known time delay between image captures is set and the resultant displacement of particles is used to determine the velocity [71]. Post-processing software such as TSI INSIGHT 4G, LasVision, PIVLab, etc. enable the capturing, pre- and post-processing of PIV images. Post-processing produces velocity profiles from which flow behaviour can be determined.

PIV is reliant on several subsystems to produce an accurate vector field:

- Appropriate particle selection: PIV tracks fluid motion through the illumination of tracer particles. The appropriate particle type and size is critical to PIV measurement.
- Laser or diode selection: The source of illumination must both be powerful enough to be able to visualise the particles and be able to be triggered at least twice within a short time frame.
- Image capture: Appropriate cameras will be able to capture at least two separate image frames synchronised with the laser illumination pulses.
- Calibration: A reference dimension is typically used to calibrate the captured particle displacements.
- Evaluation: PIV evaluation picks up the displacement of the particles between the light pulses.
- Post-processing: Post-processing is used to validate vectors and replace invalid vectors within complex flows.

For the modelling of pulsatile fluid flow behaviour, ensemble PIV is commonly the most accepted method due to the high repeatability required to create a spatially phase averaged vector field for a particular phase of the pule motion [72-75].

## 2.2. PIV Equipment

### 2.2.1. Trace particles

Particle selection is crucial to the accuracy of PIV measurement. PIV is an indirect measurement method that tracks the motion of particles suspended in a fluid flow, rather than direct measurement of the motion of fluid itself [76]. As such, the mechanical properties of the particles are critical to ensure accurate flow characteristics are obtained. PIV benefits from an even distribution of particles throughout the flow domain. These particles, referred to as trace particles or seeding particles, must be neutrally buoyant within the fluid and small enough to be carried by the motion of the fluid [69]. The motion of larger particles may, in part, be influenced too much by their buoyancy and their own momentum. However, the particles must be large enough to sufficiently scatter light for data capture [69].

#### *2.2.1.1. Buoyancy*

Neutral buoyancy is achieved when the density of the particles within the fluid matches the density of the fluid. If buoyancy values do not match, the particles may deviate from the direction of the fluid flow due to gravitational and inertial velocities. As PIV measured the motion of the particles, rather than the fluid, this can lead to erroneous velocity measurements and flow patterns [69].

The formula for the gravitational velocity of a particle $(U_g)$ can be derived from Stokes Drag Law (Equation 2.1) [69]. The formula is used to understand whether particles will be inclined to settle or rise within a fluid.

$$U_g = \frac{d_p^2(\rho_p - \rho_f)}{18\mu_f} g \qquad \text{(Eq. 2.1)}$$

In which $d_p$ is the particle diameter [m], $\rho_p$ is the particle density [kg·m$^{-3}$], $\rho_f$ is the fluid density [kg·m$^{-3}$], $\mu_f$ is the dynamic viscosity [Pa·s] and $g$ is gravitational acceleration [9.81 N·kg$^{-1}$]. When the particles have the same density as the fluid the top term in the equations goes to zero. This implies there is no risk of particle sedimentation.

Another important metric is the inertial effects due to accelerating and decelerating fluid. The velocity lag of a particle under constant acceleration can be estimated using Equation 2.2.

$$U_s = U_p - U_f = \frac{d_p^2(\rho_p - \rho_f)}{18\mu_f} a \qquad \text{(Eq. 2.2)}$$

This formula is similar to Equation 2.1. However, it replaces the gravitational term for fluid acceleration $(a)$. It is a measure of the particle velocity compared to the velocity of the working fluid. However, as all the experiments were conducted under pulsatile condition the fluid was continuously accelerating and deceleration. Therefore, to measure the tendency of particles to attain velocity equilibrium with a fluid the particle response time $(\tau_p)$ was calculated (Equation 2.3).

$$\tau_p = \frac{d_p^2 \rho_p}{18\mu_f} \qquad \text{(Eq. 2.3)}$$

The trace particles used for all experiments were silver coated hollow glass spheres (Dantec Dynamics Inc., Denmark). Silver coated hollow glass spheres have a density of 1100 kg·m$^{-3}$ and mean diameter of 10 µm. Two different working solutions were used in the experiments described in this thesis: 1) 40/60 water and glycerine, 2) 45.6/28.8/25.6 water, glycerine and urea. The solution ratios were measured by mass. The first working solution had a dynamic viscosity of 9.3x10$^{-3}$ Pa·s and density of 1156 kg·m$^{-3}$. The second working solution had a dynamic viscosity of 3.56x10$^{-3}$ Pa·s and density of 1130 kg·m$^{-3}$. The calculated gravitational velocity and response times of the particles are tabulated in Table 2.1.

*Table 2.1: Working solutions buoyancy properties*

| | **40/60 water-glycerine** | **45.6/28.8/25.6 water-glycerine-urea** |
|---|---|---|
| **Gravitational Velocity** | 0.283 x 10$^{-6}$ m·s$^{-1}$ | 0.459 x 10$^{-6}$ m·s$^{-1}$ |
| **Response Time** | 0.566 x 10$^{-6}$ s | 1.72 x 10$^{-6}$ s |

Experiments tended to reach a peak flow rate of 21 L·min$^{-1}$, which for a nominal bore of 25 mm leads to an average peak velocity of 0.72 m·s$^{-1}$. Despite the particles density not exactly matching the fluids, the gravitational velocities and response times in both working fluids are low enough to be negligible in comparison.

#### *2.2.1.2. Light*

PIV software identifies particles within an image, based on their light intensity [70, 77]. The intensity of the particle image is directly proportional to the light scatter power. Increasing laser power increases the image intensity. However, it is more economical to appropriately select light scattering particles. Light scattering is a function of many geometrical properties of the particle and the refractive indices of both particle and the fluid medium. However, for spherical particles with diameters larger than the wavelength of the laser light ($\lambda$), Mie's light scattering theory is applicable [69]. Mie's light scattering theory dictates that the scattering of light can be easily predicted if $q$ in Equation 2.4 is larger than 1.

$$q = \frac{\pi d_p}{\lambda} \qquad \text{(Eq. 2.4)}$$

When this condition is met, the light does not get blocked by the small particles, but spreads in all directions (Figure 2.2). However, as Figure 2.2 shows, the light intensity at 90° (the nominal optical capture angle for planar PIV), is lower than at 0 or 180°. As planar PIV involves setting up a camera perpendicular to the laser plane, this indicates that a significantly lower light intensity will be captured [69, 78]. The lower intensity can be compensated for by increasing the density of particles within the regions of interest. The light recorded by the camera is not only as a result of illumination of particles, but also the portions of scattered light from many particles [69]. The scattering increases the intensity of the particle images without necessitating larger particles or high intensity lasers. The silver coated hollow glass spheres had a mean diameter of 10 µm, and the laser output a wavelength of 532 nm. Using Equation 2.4, the seeding particles q-value was 59 and thus provided confidence that an acceptable intensity of light could be received by the camera.

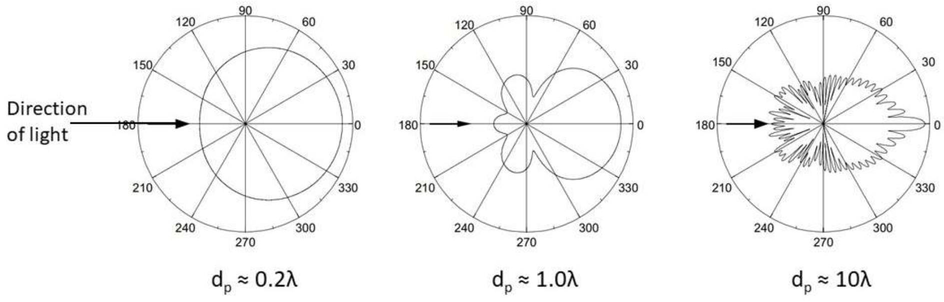

$d_p \approx 0.2\lambda$ $d_p \approx 1.0\lambda$ $d_p \approx 10\lambda$

*Figure 2.2: Mie's light scattering theory on 3 particle sizes. Reproduced with permission from [78]*

### 2.2.2. Laser and Optics Configuration

Lasers and high-power light emitting diodes (LEDs) are common sources of illumination for PIV experimentation. An EverGreen[2] dual-cavity Nd:YAG (neodymium-doped yttrium aluminium garnet crystal) laser was used for all experiments within this thesis. An Nd:YAG laser is one of the most commonly used illumination sources for PIV [79]. The laser beam is generated by $Nd^{3+}$ ions. The Nd:YAG crystal is excited by optical pumping using flash lamps [69].

Pulses were generated using active quality switching (Q-switching). Q-switches allow a high population of ions to build up within the laser cavity before opening, creating a single large pulse. Multiple large pulses can be generated using a double oscillatory system (one within each cavity) [69]. A double oscillatory system enables the user to adjust the separation times between illuminations independently of pulse strength.

The Nd:YAG laser produces a 1064 nm wavelength beam (infrared) which passes through a potassium dihydrogen phosphate doubling crystal which halves the wavelength (532 nm) to a visible green. Despite the wavelength being visible, the high power of the lasers can blind operators if they fail to wear appropriate personal protection equipment (PPE). Laser specifications for the $EverGreen^2$ double-pulse laser are provided in Table 2.2. Appropriate PPE is red-pass googles which filter the wavelengths.

*Table 2.2: Specifications for $EverGreen^2$ double-pulse laser*

| **Specifications** | |
|---|---|
| **Repetition rate per cavity (Hz)** | 1 – 15 |
| **Pulse width (ns)** | <= 10 |
| **Lasing medium** | Nd:YAG |
| **Wavelength (nm)** | 532 |
| **Maximum pulse energy (mJ)** | 200 |
| **Output beam diameter (mm)** | 6.35 |

The $EverGreen^2$ laser produces a single 6.35 mm beam that must be reconfigured to produce a thin sheet of light. The experiments used a commercial laser guide arm and optic set up purchased from Dantec Dynamics. The optic configuration enabled a laser sheet to be transformed to a variable thickness between 1 mm and 4 mm for use in either planar or stereoscopic PIV (Figure 2.3a). The optics setup was connected to the laser head via a guide arm (Dantec Dynamics Inc., Denmark). The guide arm allowed the laser sheet to be aligned with the plane of interest with greater flexibility. The laser was primarily aligned along an axis of symmetry of the models and vertical or horizontally aligned. Due to the high power of the laser, a trace laser was attached to the setup for alignment purposes. The laser was affixed to a rotary stage allowing fully ± 90° rotation to enable perpendicular alignment with the compliance chamber. The rotary stage was mounted on a sheet of acrylic and held in place using t-slot aluminium extrusion (Figure 2.3b).

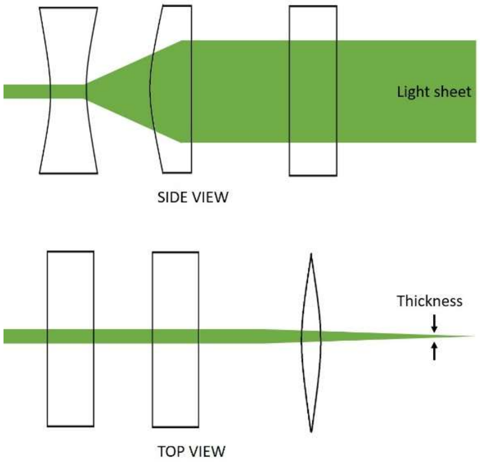

*(a)*

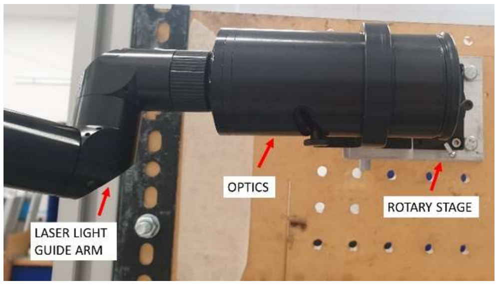

*(b)*

*Figure 2.3: (a) Example of optics to generate the laser sheet (b) Dantec Dynamics optics set up*

## 2.3. Refractive Index

The RI of a material is a measure of the speed of light through a medium relative to the speed through a vacuum. Differences in the RI can result in light appearing to bend as it passes through different mediums. This is particularly important when modelling materials with curved surfaces, in which a PIV laser light sheet cannot be aligned perpendicular to every wall. A material with a higher refractive index will slow light down and refract off the angle of incidence. RI matching is pivotal to accurate PIV measurement. PIV is an optical measurement method and therefore relies on undistorted light paths from the laser through the model and from the model to the sensor (the camera) to measure true displacements. RI matching with internal flow setups requires a solid (phantom) and liquid (working solution) medium with the same RI values, such that they become optically transparent. Figure 2.4 shows the mismatched RI and matched RI. Snell's law explains the relationship between the RI and the angle of light incidence (Equation 2.5).

$$\frac{\sin\theta_2}{\sin\theta_1} = \frac{n_1}{n_2} \qquad \text{(Eq. 2.5)}$$

In which, $n$ is the RI, $\theta$ is the angle of the incident light, and the subscripts represent the two different mediums.

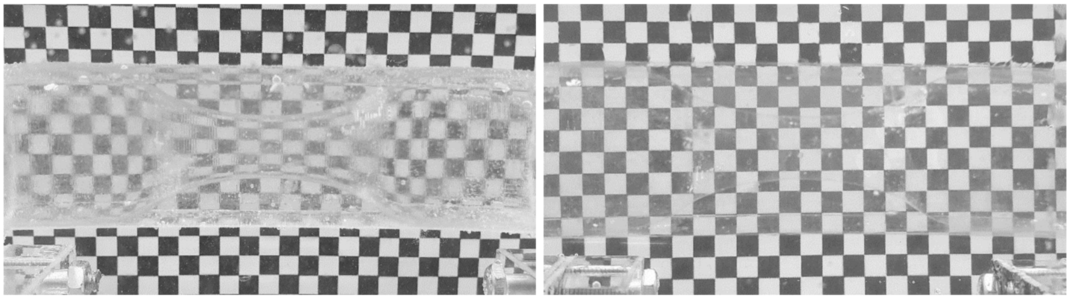

*Figure 2.4: Unmatched and matched refractive index models*

The solid medium used within this thesis was Sylgard 184 with a 10:1 mixing ratio. Sylgard 184 is an elastomer with a RI value of 1.41 [80]. It was selected as it allowed both flexible and effectively rigid models to be manufactured, dependent on the wall thickness used. Yazdi, et al. [80] carried out a review on other common elastomers. The distensibility of the models could also be matched through normalised compliance matching to the *in-vivo* values of physical arteries. Normalised compliance matching will be introduced in Section 2.8.

A 60/40 water-glycerine was a common mixture used in *in-vitro* experiments, due to its similar density (1100 kg·m$^{-3}$) and dynamic viscosity (3.63x10$^{-3}$ Pa·s) to blood [81]. However, this mixture only had a RI of 1.39 resulting in unacceptable levels of distortion of the laser light path though the phantom. The RI of Sylgard 184 could be matched by increasing the ratio of glycerine in the solution [82]. A RI of 1.41 was achieved using a 40/60 water-glycerine mixture [82]. However, this led to the dynamic viscosity of the solution (9.3x10$^{-3}$ Pa·s) to be 2-3 times higher than the viscosity of blood [81]. Dynamic scaling was thus used in Chapters 5 and 6 to match the Reynolds and Womersley numbers to *in-vivo* values despite the increased viscosity. A detailed description of dynamic matching will be provided in Section 2.7. However, Chapter 7 used a different solution that raised the RI with urea, rather than glycerine. A 45.6/28.8/25.6 water-glycerine and urea solution was used in Chapter 7. The solution had a RI of 1.41, density of 1130 kg·m$^{-3}$ and a dynamic viscosity of 3.56x10$^{-3}$ Pa·s which is comparable to blood and allowed much higher flow rates to be achieved within the phantom models for a lower pump demand.

### 2.3.1. Air bubbles

Air bubbles can create significant problems for PIV measurement. Air bubbles have a different refractive index to the silicone or working solutions and their spherical or semi-spherical form can result in significant light scattering. Air bubbles in the phantoms can be avoided by ensuring the silicone used is degassed prior to casting the phantom. Air bubbles in the working fluid can be more difficult to manage. Air bubbles are not neutrally buoyant in solution and can thus get trapped in the flow domain geometry. Furthermore, air bubbles are often significantly larger than the seed particles and tend to have a higher reflection intensity. Higher intensity particles contribute more to the measured motion of flow. Therefore, air bubbles can dominate the measured particle motion and produce erroneous vectors. Air bubbles must be purged from the working solution prior to experimentation. Careful circuit design and effective air release valve positioning can help to purge air and significantly reduce the risk of air bubbles within the fluid domain. Sometimes small bubbles may still be trapped within the circuit and pass through the model during data capture. Spatial ensemble averaging (discussed later in Section 2.5.2.3.) can mitigate some of the effects of errant air bubbles.

## 2.4. PIV Capture

This thesis captured image sequences using multi-frame/single-exposure PIV recording. Multi-frame/single-exposure PIV recording captures a single image of illuminated particles for each exposure period [69]. This allows particles to be tracked through time and, hence, produce velocity vector fields. Camera selection is pivotal in enabling PIV recording. TSI 4MP-LS Charge-coupled device (CCD) digital cameras were used in this thesis (Table 2.3). CCD cameras are commonly used for capturing PIV images due to the high image quality [83, 84]. CCD cameras have a high spatial resolution and are able to capture two images separated by a microsecond time delay. In addition, the CCD cameras frame rate was compatible with pulse repetition rates of Nd:YAG lasers.

*Table 2.3: Specifications of TSI 4MP-LS CCD digital cameras*

| **Camera specifications** | **TSI 4MP-LS** |
|---|---|
| **Imaging device** | Progressive scan interline CCD w/microlens |
| **Light sensitive pixels** | 4.19 million pixels, 2360 × 1776 |
| **Pixel size** | 5.5×5.5 µm |
| **Frame rate** | 16 frames/second |
| **Minimum frame straddling time for PIV capture** | 195 ns |
| **Dynamic range** | Selectable between 12 and 16 bit |

Nikon AF Micro-Nikkor lenses with specification shown in Table 2.4 were fitted to the cameras. The maximum frame rate of the cameras was 16 Hz. This rate is restricted by the time required to transfer the charge received by CCD array (pixels) to CCD chip for readout. This transfer time is called the 'frame straddling'. Frame straddling allows for two light exposures to be captured on separate frames. Frame straddling relies on the end of one camera exposure and the start of the second to be situated in time between the two pulses of laser.

*Table 2.4: PIV lens specifications*

| Specification | Nikon AF Micro-Nikkor lens |
|---|---|
| **Focal length (mm)** | 50 |
| **Aperture size (f-number)** | 1.8 – 22 |

A TSI 610036 synchroniser (TSI Incorporated, Minnesota, USA) was used to coordinate the firing times of the camera captures and laser pulses. The initial laser pulse delay was 180 µs which is a fixed characteristic. The time delay ($\Delta t$) between laser pulses used varied between 200 – 2500 µs dependent of the flow rate magnitude during the cardiac cycle. Figure 2.5 shows the sequencing that is required to capture two images. Traditionally, the straddling point is equidistance between the two laser pulses. However, data capture was found to be more reliable when this point was slightly closer to the second laser pulse, as per Figure 2.5.

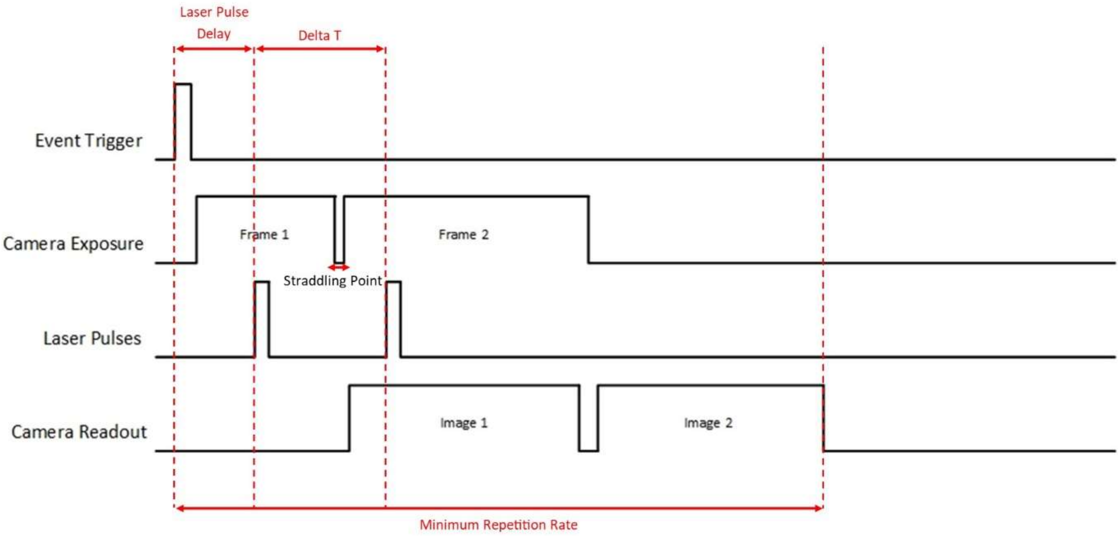

*Figure 2.5: PIV timing diagram for synchronization of the cameras and laser pulses*

## 2.5. Evaluation

Evaluation of PIV vector field images were carried out in both TSI Insight 4G [70] and PIVLab [77]. The two software packages produced identical results.

### 2.5.1. Pre-Processing

#### *2.5.1.1. Calibration*

Raw particle images had to be calibrated to convert pixels to lengths. Calibration was necessary to determine meaningful particle displacements and velocities. Without calibration the vectors would be returned in pixels per second. Typically, calibration was carried out using a known distance on the captured raw image. Commercial calibration targets can be purchased with known distances between surface markings (Figure 2.6). Calibration targets are often used to ensure suitable focusing of the camera for PIV data capture. They are highly convenient for calibrating external fluid flows. However, calibration target efficacy is reliant on the precise location of the equipment with respect to the region of interest being measured. For internal flows, using a calibration target is not always possible due to spatial constraints. In such cases, a known dimension, such as a diameter of the phantom or flange within the region of interest was selected as the reference geometry to calibrate pixels to distance.

*Figure 2.6: Calibration target, commercially available from TSI Incorporated (Minnesota, USA)*

#### *2.5.1.2. Masking*

Compliant phantoms were installed within a sealed pressure box for experimentation. The same fluid flowing within the phantom was used to fill the pressure box surrounding the phantom. This ensured the refractive index match was maintained. As such, there were many particles external to the phantom that had to be excluded from analysis. Masking is a pre-processing technique used in compliant modelling to exclude fluid external to the phantom from analysis and to focus on a particular region of interest. Masking creates a zero-flow condition within the external flow.

Static masks were manually drawn to reduce the analysis zone to only the region of interest. However, due to the pulsatile flow used for experimentation, internal pressure often changed the phantom domain geometry. As such, individual masks had to be drawn for each time step measured across a full waveform cycle. However, each image pair at a specific phase of the cycle is likely to have very similar lumen expansion for the and could thus use the same coarse mask. However, this assumption is highly dependent on the accuracy and reproducibility of the wave generated.

### 2.5.2. Processing

#### *2.5.2.1. Cross-correlation*

Cross-correlation is a method used to identify the displacement of two singularly exposed patterns of randomly distributed particle images [85]. Particles are converted to a signal intensity which help identify each particle or cluster of particles. Cross-correlation tracks the motion of two sets of data relative to one another at a single time step. It is used to determine how well a series of signals between the two sets match up to each other and identify the direction and motion of particles within the fluid flow.

Cross-correlation is carried out in five stages: 1) Grid generation, 2) Spot mask, 3) Correlate the first pattern in reference to the second pattern, 4) Locate the peaks, 5) Validate the results.

Image pairs are discretised into a uniform grid of rectangular 'interrogation windows' of $N \times M$ pixels. The image intensity of the first pattern at time step, $t$, is then compared to the second pattern at time step, $t + \Delta t$, using the correlation function for each interrogation window (Equation 2.6)

$$R_{II'}(x, y) = \sum_{i=1}^{N} \sum_{j=1}^{M} I\,(i, j) I'(i + x, j + y) \qquad \text{(Eq. 2.6)}$$

Where *I* and *I'* are the intensity value map of the first and second exposure, with $N \times M$ pixel$^2$ interrogation window size, and *x* and *y* are the pixel position in the interrogation window. The first image intensity pattern in an interrogation window is unique, like a fingerprint, referred to as a spot mask. The same spot mask is then searched for in the second image. The correlation function moves the interrogation window in the second image until it finds the best match to the cluster of particles in the first frame [85]. This produces a correlation matrix (Figure 2.7). The particle displacement is the distance between the peaks of the correlation found in the second frame to the centre of the interrogation window in the first frame. The process is repeated for all interrogation windows within the image and results in a displacement vector field. To reduce computational time, a Fast Fourier Transform (FFT) was applied.

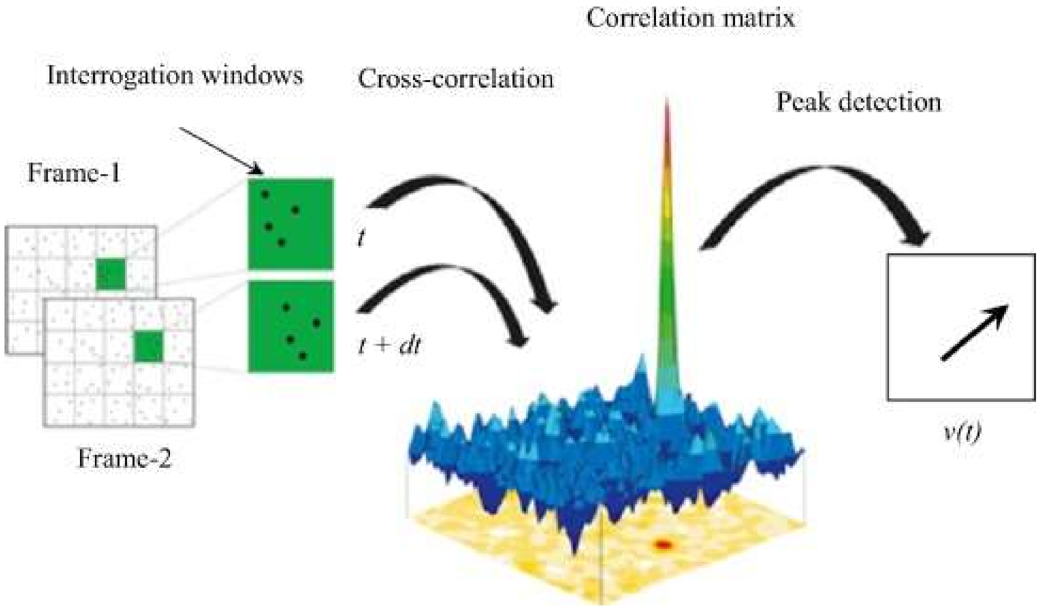

*Figure 2.7: Cross correlation technique. Reproduced with permission from A.B and Ovinis [86]*

### *2.5.2.2. Recursive Nyquist Grid*

An iterative grid refinement was proposed by Scarano and Riethmuller [87] to increase the particle signals, correlation accuracy and spatial resolution. Multi-pass grid refinement is useful in PIV with a high image density and large dynamic range in displacements. It allows large particle displacements to still be captured that may otherwise be lost with a smaller interrogation, meanwhile increasing the resolution of smaller particle motions. Typical refinement algorithms begin with large interrogation windows with a 50% overlap with neighbouring windows that are known to capture the full dynamic range of displacements following the ¼ rule. The ¼ rule states that the displacement of a particle should be no more than ¼ of an interrogation window or thickness of the laser sheet [88]. In the first pass, a standard cross-correlation is carried out using the largest selected interrogation window and any outlying vectors are replaced by interpolation. The results are then used to estimate the displacement for the second pass of refinements with windows half the height and width of the previous pass. Therefore, the interrogation window is reduced by a factor of two and the number of vector rows and columns increased by a factor of two, increasing the number of vectors four times with each pass. This method reduces the risk of particles being lost due to three-dimensional movement in and out of the capture.

A two-pass grid refinement was used in this thesis. The grid resolution began with 64 x 64 pixels$^2$ per window and reduced on a second pass to 32 x 32 pixels$^2$.

Planar PIV requires a few typical rules [88]:

1. Interrogation window size should be small enough that one vector can describe the flow within that spot
2. There should be more than 10 particles visible per interrogation window
3. The maximum in-plane displacements between image pairs should be less than ¼ of the interrogation window size

4. The maximum out-of-plane displacement between image pairs should be less than ¼ of the light sheet thickness
5. The minimum in-plane displacement between image pairs should be two particle image diameters
6. Exposure of the particles must be large enough to clearly show the particles

PIV data capturing was carried out using Insight 4G by TSI Incorporated (USA). Initial image processing was also carried out in Insight 4G, however, later experiments used PIVLab for improved plotting.

#### *2.5.2.3. Ensemble averaging*

The cross-correlation technique is affected by the image intensity with larger and brighter particles having a much higher influence on the identified flow than less intense particles. This can result in uncertainty in the results. The main causes for poor image intensity are low seeding density, out-of-plane unfocused particles, CCD noise, dark regions, or incidental low local particle density. To improve the spatial resolution of results, ensemble PIV was used for processing PIV images. This technique uses velocity vector averaging across a sequence of images pairs captured at the same specific time step across a waveform cycle [89]. Velocity vector averaging calculates the velocity vector for each interrogation window of an image pair and then averages them along the sequence of images (Figure 2.8).

For example, 18 image pairs were captured at each time step in the first experiment (Chapter 5) of this thesis. However, later experiments improved the rate of valid vectors by increasing the image pairs to 50-100 (Chapter 6 and 7).

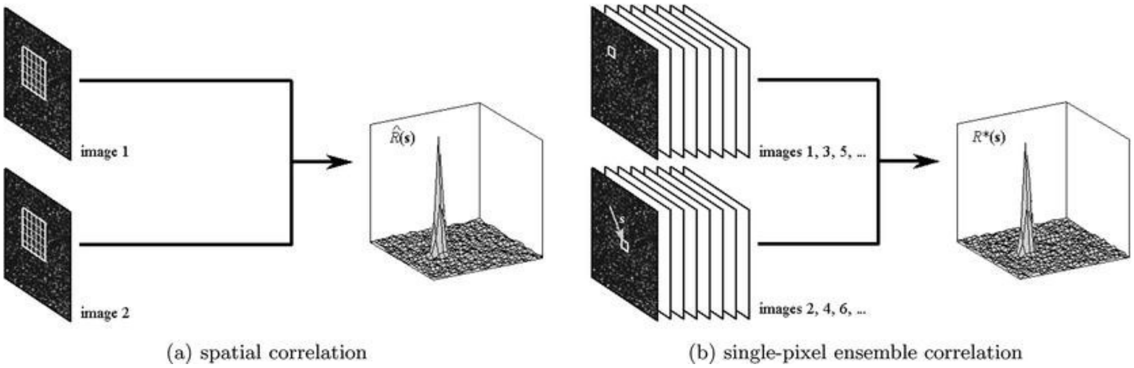

(a) spatial correlation (b) single-pixel ensemble correlation

*Figure 2.8: Single image pair PIV v Ensemble PIV. Reproduced with permission from [89]*

## 2.5.3. Post-Processing

A valid displacement vector is obtained when cross-correlation results in a distinct correlation peak [90]. PIV processing can lead to over 95% valid vectors, if the imaging and processing setup is performed following the PIV guidelines [85]. However, low density seeding, and high recirculation can result in particle loss due to movements in and out of the light plane, leading to bad vectors or holes in the vector array. Vector validation can be used to identify spurious vectors by comparing them to the median of the surrounding vectors. Rejected vectors can be interpolated using the surrounding vectors. Local and global vector validation methods can improve the quality and feasibility of results.

### *2.5.3.1. Local Vector Validation*

A vector difference validation test evaluates the feasibility of local vectors. It investigates the magnitude of the difference between a particular vector and each of its neighbouring vectors (Equation 2.7).

$$\left|U_{diff}(i,j),n,m\right| = \frac{1}{n*m}\sum_{i^*=-0.5n}^{0.5n}\sum_{j^*=-0.5m}^{0.5m}\left|U_{2D}(i^*,j^*) - U_{2D}(i,j)\right| < \epsilon_{thres} \quad where \;\; \epsilon > 0$$

(Eq. 2.7)

In which *U* is the velocity vector [m·s$^{-1}$], $\epsilon_{thres}$ is the designated threshold velocity difference [m·s$^{-1}$] and *n*m* defines the domain of evaluation [pixels]. The number of instances for which the validation criterion is not met are summated. Typically, a particular vector is rejected when it conflicts with at least half of the neighbouring vectors. The thresholds varied between experiments based on the peak velocities and working fluid used. Typically, a 0.05 – 0.1 m·s$^{-1}$ threshold was applied. In this thesis, local validation was undertaken by both TSI Insight 4G and PIVLab (versions 2.34 to 2.54), and rejected vectors were replaced via interpolation. Bad vectors can also be manually rejected [77]. Manual rejection was not commonly used as typically local vector validation would remove any spurious vectors.

### 2.5.3.2. *Global Vector Validation*

The Z-Score validation test operates globally and under the assumption that the data is normally distributed [91]. The number of standard deviations from the mean of each vector is compared to the overall mean following Equation 2.8.

$$Z_i = \frac{U_i - \mu_U}{\sigma_U} \qquad \text{(Eq. 2.8)}$$

In which the condition is met if $|Z_i| < Z_{thresh}$ for a predetermined threshold. Global z-score validation was not commonly used due to no-slip conditions at the phantom walls and the Poiseuille or plug-shaped velocity profile resulting in a large range of feasible vectors.

### 2.5.3.3. *Vector conditioning*

Vector condition is typically carried out following vector validation. Both TSI Insight 4G and PIVLab use vector conditioning to fill in holes in the vector array and to smooth the vector field [70, 77].

Gaps in the vector field can be filled by either the local mean or the local median. Typically, this thesis used the local median. Gaps were filled using a recursive filling validation method. Recursive gap filling was undertaken in an order determined by the number of valid neighbouring vectors. Gaps with a high number of local valid vectors have the highest chance of valid filling. The filled gaps then allowed evaluation of neighbouring gaps in the next pass. The process was repeated until all gaps in the vector field were filled. An alternative approach is to fill gaps systematically from a specific location on the vector field (such as the top left) irrespective of the number of valid neighbouring vectors. However, this approach may induce risk of artificial patterns being produced [70]. While recursive filling mitigates this issue, it is more time consuming.

The number of neighbouring vectors can be altered depending on the selected neighbourhood size. This thesis used a 3x3 interrogation window neighbourhood size (resulting in up to 8 neighbouring vectors).

Smoothing acts as a low-pass filter that replaces each vector with its Gaussian-weighted mean. The Gaussian-weighted mean was calculated based on the surrounding 5x5 interrogation windows. Smoothing reduces minor vector quiver within the array (Figure 2.9).

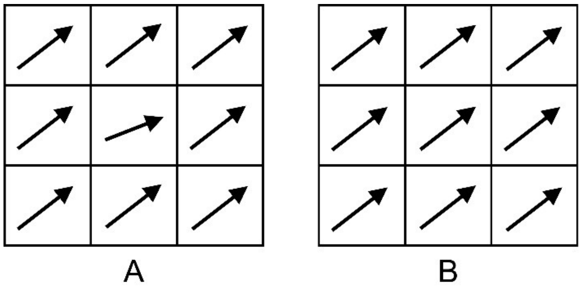

*Figure 2.9: 3x3 example of (a) before and (b) after smoothing vectors*

## 2.6. Flow Circuit Construction

PIV was used in this thesis to model the internal fluid flows through model arteries. Internal flow modelling requires a suitable flow circuit to produce the desired waveforms at the correct flow rate and timing. Two flow circuits were used in this thesis. The original flow circuit (used in Chapter 5) was upgraded to improve experiment efficiency and replace worn-out parts. The revised flow circuit was used for the remainder of experiments. Both flow circuits had similar components.

## 2.6.1. Flow Circuit Components

### *2.6.1.1. Reservoir*

The reservoir was a large tank of fluid that was used to supply the entire flow circuit during experiments and as a drainage point for the overflow weir that was used to maintain the outlet head pressure.

### *2.6.1.2. Piston pump*

A reciprocating piston pump was used to produce physiological waveforms (Figure 2.10). The pump was driven by a stepper motor connected to a ball screw that converted rotational motion into linear movement. The pump was designed using an acrylic cylinder with an internal diameter of 140 mm. The cylinder was connected to the circuit via a reducing conical adaptor which stepped down the diameter to 25 mm over a 200 mm length. Two lip seals on the piston prevented flow leakage despite the forward and backward movement. The piston rod was supported by a rail and T-slider. The T-slider was connected to the ball screw via a ball-nut sliding mechanism. The ball screw had a 5 mm pitch and was supported by bearings at the free and motorized end (Figure 2.10). The mechanism converted the rotational motion of the motor to linear motion of the piston.

The NEMA 34 stepper motor (Astrosyn International Technology, UK) had 200 steps per revolution (1.8° step angle) and therefore produces high resolution waveforms. The stepper motor was controlled using a LabView program via a National Instruments 9401 digital module and 9172 CompactDAQ chassis. The original flow circuit (Section 2.6.2) produced physiological waveforms by monotonic movement of the piston forward. However, as the piston only moved in one direction, the number of captures were limited to between 15 to 20 waves for a single run (based the total volume of fluid moved per waveform) due to the length of the piston bore. This issue was negated using the dual pumping system developed in the revised flow circuit (Section 2.6.3). In the revised flow circuit, a mean flow was provided to the system using a steady state pump. The pulsatile waveforms were produced by modulating the flow rates from the mean flow using oscillating piston motion. Up to 100 image pairs were captured during a single run using the revised flow circuit.

The frictional resistance to piston movement was lower when moving forwards compared to backwards. To ensure the pump produced the intended physiological waveform, a feedback loop was connected from an electromagnetic flowmeter to the stepper motor and output from the electromagnetic flowmeter installed at the phantom inlet were recorded within the LabView program.

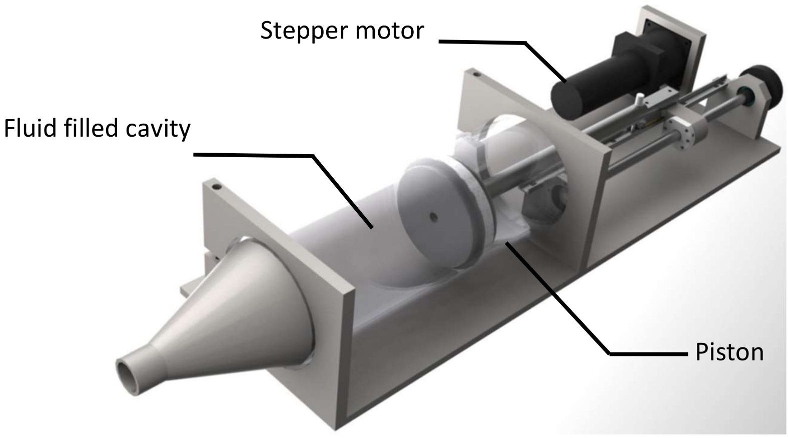

*Figure 2.10: Custom design piston pump used for physiologically flow waveform*

The desired waveform was introduced to the stepper motor. The motor steps were calculated using a MATLAB script, which converted the waveform flow rates into steps. The steps were directly introduced to the LabView program. The motor angular displacement (AD) was calculated by dividing the piston displacement (Equation 2.9) to the ball screw pitch (5 mm).

$$AD = \frac{x(t)}{pitc} 2\pi \qquad \text{(Eq. 2.9)}$$

Knowing the number of steps per revolution (SPR), the step size and motor steps input can be calculated as:

$$Step\ size = \frac{2\pi}{SPR} \qquad \text{(Eq. 2.10)}$$

$$Input\ step = \frac{AD}{Step\ size} \qquad \text{(Eq. 2.11)}$$

To capture the PIV images at a specific point of the wave, the same LabView code sent a trigger signal to the synchronizer at the corresponding point on each cycle. Once the signal was received, the synchronizer triggered the laser and camera based on the timing diagram (Figure 2.5, Section 2.4.).

#### *2.6.1.3. Steady State Pump*

A North Star 15152Q DC diaphragm pump provided the mean flow to the revised dual pumping system (Figure 2.13B). The mean flow was controlled using variable voltage, and self-maintained by drawing more amperes when required. An in-built check valve at the pump outlet prevented flow being reversed through the pump if pressures got too high

#### *2.6.1.4. Flow Straightener*

A custom flow straightener was used to reduce lateral velocity components. The straightener was designed as a honeycomb structure with passage ducts aligned with the axis of the main flow. It was particularly important in the revised flow circuit due to the 90$^o$ elbow from the piston flow potentially producing Dean vortices that needed to be eliminated prior to flow though the phantom. The flow straightener assisted in creating fully developed flow. Fully developed flow was confirmed under steady state conditions with a flow rate of 5 L·min$^{-1}$, at the inlet of the phantom of the aorto-iliac bifurcation (used in Chapter 6) (Figure 2.11).

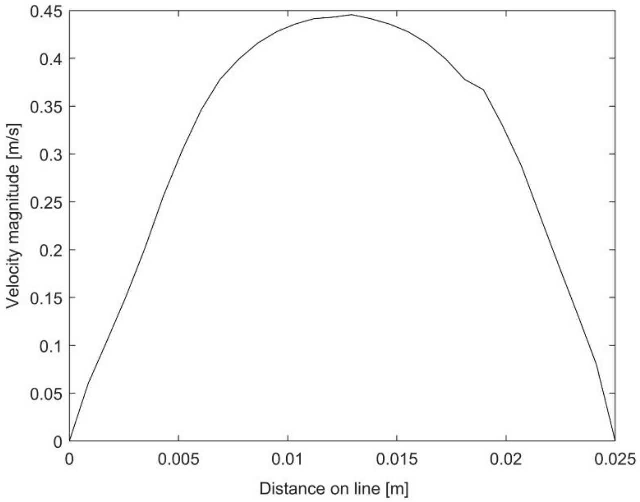

*Figure 2.11: Developed Poiseuille flow observed in-vitro*

#### *2.6.1.5. Straight Section of Pipe*

A straight section of pipe was located between the flow straightener and flowmeter. In the original flow circuit this section of pipe was 2 m long and has a diameter of 20 mm. However, steady state PIV measurement proved that only 1.5 m of pipe with a 25 mm diameter was required following a flow straightener. Therefore, to conserve vertical height, the revised flow circuit straight pipe section was only 1.5 m in length. This ensured there was ample length for flow to become fully developed prior to entering the arterial phantom.

*In-vivo, a*rteries would do not receive fully developed flow. However, in the absence of precise input velocity profiles, ensuring simple, repeatable flow conditions (such as fully developed flow) was important to ensure experimental repeatability and reduce the potential of flow abnormalities implying strange haemodynamics. The straight section of pipe in the revised circuit was changed from the original to have a 25 mm internal diameter. This was to reduce flow abnormalities being introduced due to changing diameters between the pipe and the flowmeter.

#### *2.6.1.6. Flowmeter*

Volumetric flow rate was measured using a Khrones IFC300 electromagnetic flowmeter. The flowmeter had a nominal bore diameter of 25 mm. Electromagnetic flowmeters measure flow rate using Faraday's law of induction. These flowmeters are particularly good for PIV as they do not have any moving parts and are non-intrusive. Hence, they do not produce pressure losses and are unaffected by pressure, temperature, viscosity, or density. Flowmeter readings were validated using multiple steady state flow conditions and calculating the volume of fluid output over a minute.

#### *2.6.1.7. Head Tank*

A head tank was used to provide back pressure that acted as internal static pressure within the phantom. An overflow weir ensured that the head pressure was maintained throughout the each run of the experiments. The head tank position varied with each experiment from 150 – 280 mm.

### 2.6.2. Original Flow Circuit

All the components in the original circuit were positioned at same height except for the head tank which was raised and lowered to control static internal pressure within the phantom. A steady state pump was only used for filling the system before each data capture sequence and therefore, is not included in Figure 2.12. The pumping system used a single piston pump to drive fluid forward through the circuit. The benefit of a horizontal set up was experiments could be setup at bench height meaning bolts and were easily accessible and there was minimal safety risk. Compliance chamber designs were often simpler also, as inlets and outlets tended to follow the horizontal line, meaning a simple lid could be designed for the enclosures.

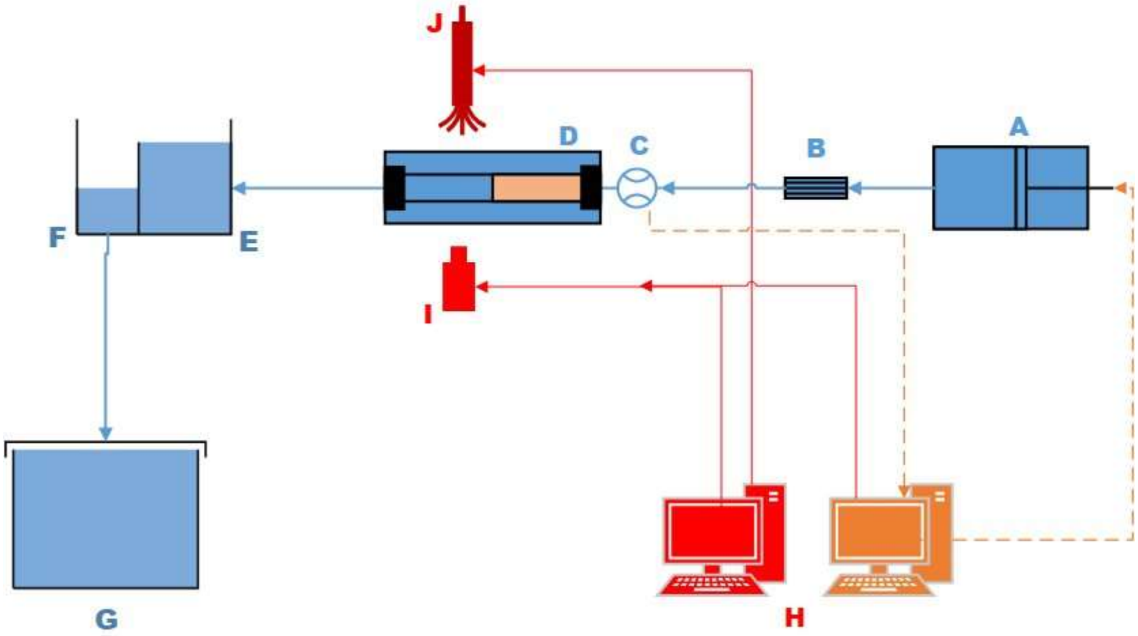

*Figure 2.12: Original flow circuit. Blue lines: fluid circuit. Red lines: laser trigger and camera data cable. Orange circuit: flow rate feedback loop. Components: A Piston pump; B Flow straightener; C Electromagnetic Flowmeter; D Phantom Model; E Head Tank; F Overflow Weir; G Reservoir; H Data Acquisition System; I Camera; J Nd:YAG Laser;*

A key limitation of the single pumping system was the time required during the set up for data captures. The initial setup each day before running the experiments could take up to 3 hours. As all the components were on the same height, air bubbles would often get trapped in even simple geometries. The system, thus, required multiple air release valves to remove air. As noted in Section 2.3.1, air bubbles can significantly affect the accuracy and validity of results and therefore must be removed from the system.

The number of consecutive runs was also limited by the volume of the piston. As the motion was monotonic, only 15-20 waveforms could be produced in a row before the system needed to be reset, depending on the stroke volume for the experiment. Resetting could result in more air bubbles getting into the system.  Hence, between runs there was also a significant amount of time was required for resetting the piston position. This made running the experiments inefficient and tedious.

### 2.6.3. Revised Flow Circuit

A revised version of the flow circuit was used for the majority of experiments within this thesis (Figure 2.13). The flow circuit was designed to pump against gravity, climbing in vertical distance. The revised flow circuit has the same components as the original circuit, but also included an inline steady state diaphragm pump. A steady-state counter-torque was applied to the stepper motor driving the piston to produce a net zero force on the piston when the system was filled. The additional height of fluid in the system led to an approximate force of 24 kPa on the piston. A largely vertical system was beneficial in reducing time during the initial experiment setup as air bubbles naturally moved towards the head tank. There was still a risk of air bubbles being trapped at junctions particularly at the outlets, however, these were easier to remove than with a horizontal set up.

The steady state pump was used to produce the mean flow rate for the waveforms. The dual pumping system was adapted from Tsai and Savaş [92] and allowed the piston pump to move back and forth on the same spot resulting in theoretically unlimited cycle capture.

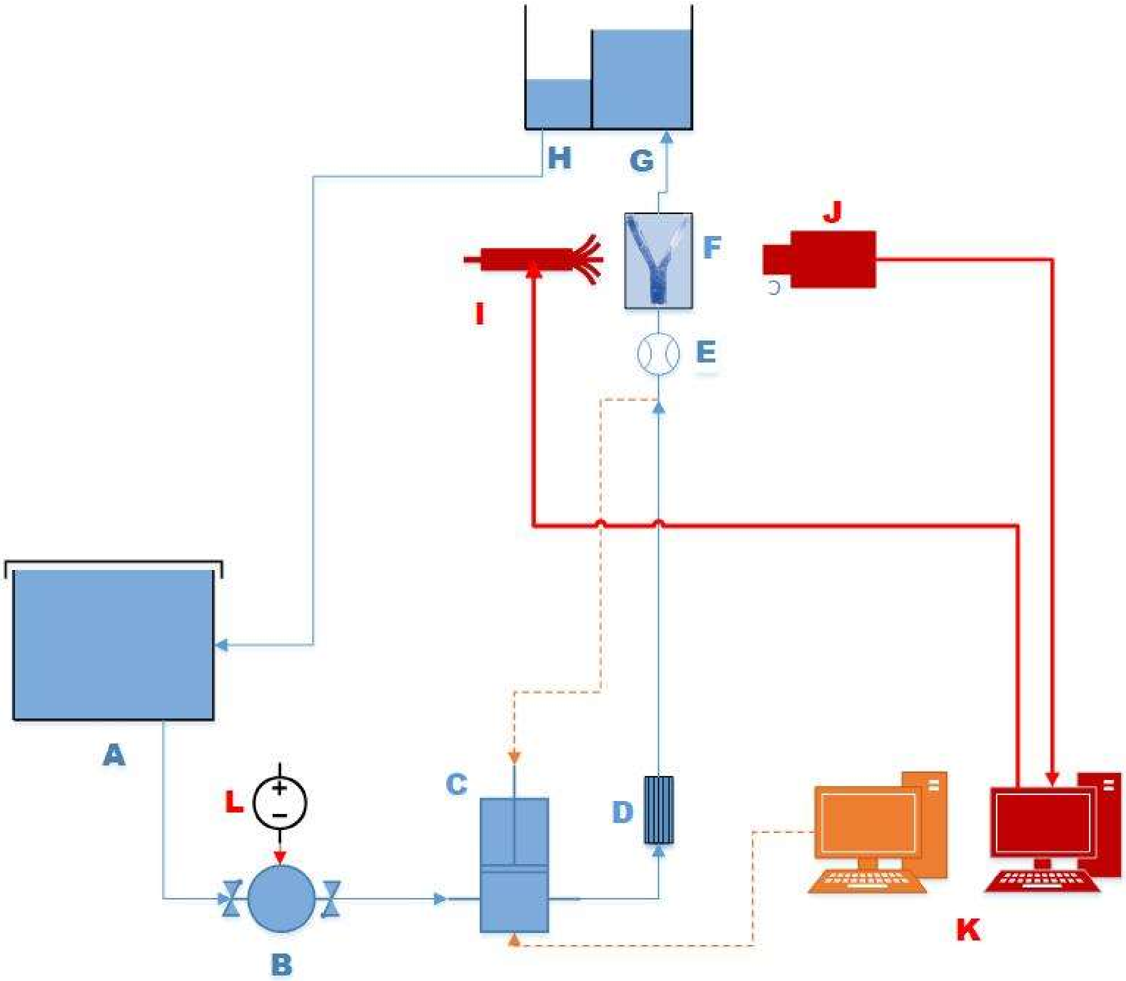

*Figure 2.13: Revised flow circuit with components. Blue lines: fluid circuit. Red lines: laser trigger and camera data cable. Orange circuit: flow rate feedback loop. Components: A Reservoir; B In-line Diaphragm pump; C Piston pump; D Flow Straightener; E Electromagnetic Flowmeter; F Phantom Model; G Head Tank; H Overflow Weir; I Nd:YAG Laser; J Camera; K Data Acquisition System; L DC Power Supply*

To ensure fully developed flow, the compliance chambers and phantoms were located approximately 2 m above ground level and often required a ladder to safely access. Hence, there were more safety considerations with the vertical flow circuit set up. The experimental design also required more careful planning to be suitable for use in the vertical flow circuit. For example, most arterial phantom inlets and outlets were aligned with the vertical axis. Hence, the outlets were often located on the top surface of the compliance chambers. As such, the top panel could not be removed to fill and drain the compliance chamber surrounding the phantom.

## 2.7. Dynamic similarity

Clinical significance of PIV results relies on the precise *in-vitro* mimicry of *in-vivo* conditions. Dynamic similarity scaling ensures meaningful replication of blood flow through the phantom. Dynamic similarity was achieved by scaling the *in-vitro* fluid properties with respect to the *in-vivo* Reynolds and Womersley Numbers (Equations 2.12 and 2.13). The Reynolds and Womersley numbers are both dimensionless numbers that define the state of the fluid. The Reynolds number defines whether a fluid is laminar or turbulent. The Womersley number is used in biofluids and describes the pulsatile flow frequency in relation to viscous effects. It is similar to the Strouhal number which is used to describe oscillating fluid mechanics. However, in haemodynamics the Womersley number is more common. As the viscosities of the working fluids were fixed by limitations in RI matching (Section 2.3.), the required flow rates and time periods were calculated to ensure similarity between blood flow and the working fluid were preserved. Flow rate and time periods were defined via Reynolds number (*Re*) and Womersley number (*Wo*) matching, respectively:

$$Re = \left(\frac{4Q}{\pi D \nu}\right)_{in-vivo} = \left(\frac{4Q}{\pi D \nu}\right)_{in-vitr} \qquad \text{(Eq. 2.12)}$$

$$Wo = \left(\frac{D}{2}\sqrt{\frac{2\pi}{T\nu}}\right)_{in-vivo} = \left(\frac{D}{2}\sqrt{\frac{2\pi}{T\nu}}\right)_{in-vitro} \qquad \text{(Eq. 2.13)}$$

Where $Q$ is flow rate [m$^3$·s$^{-1}$], $D$ is diameter [m], $\nu$ is kinematic viscosity [m$^2$·s], and $T$ is waveform period [s]. (Note: kinematic viscosity is the ratio of the fluid dynamic viscosity ($\mu$, not to be confused with the mean) and fluid density ($\nu = \frac{\mu}{\rho}$). For all experiments, 60 heartbeats per minute were considered for the *in-vivo* condition to calculate waveform period and matching the Womersley number. Equations 2.14 and 2.15 shows how Reynolds and Womersley matching lead to scaled *in-*

*vitro* flow rate and period are factors of the *in-vivo* and *in-vitro* parameters. Thus, the Reynolds and Womersley numbers were preserved.

$$Q_{in-vitro} = \left(\frac{D_{in-vitro}}{D_{in-vivo}}\right)\left(\frac{\nu_{in-vitro}}{\nu_{in-vivo}}\right)Q_{in-vivo} \qquad \text{(Eq. 2.14)}$$

$$T_{in-vitro} = \left(\frac{D_{in-vitro}}{D_{in-vi}}\right)^2\left(\frac{\nu_{in-vi}}{\nu_{in-vitro}}\right)T_{in-vivo} \qquad \text{(Eq. 2.15)}$$

Using the above equations and the properties of the working fluid (Section 2.3.), the required waveforms were scaled. Different waveforms were used for each of the experiments in this thesis based on the artery segment being measured and the phantom scaling factor. To prevent ambiguity, the waveform of each individual experiment will be presented in the associated chapter.

Two other dimensionless numbers are mentioned within this thesis. The Euler number and the Dean number. The Euler number is referred to in Chapter 4, as it is a dimensionless number that relates the pressure of a fluid to the inertial forces [93]. However, the Euler number is typically only used to model cavitation in a liquid and a literature search found it difficult to identify the Euler number for arteries in the human arteries. As such, it was not considered a useful parameter for dynamic similarity. The Dean Number is used to describe the potential for secondary flow structures in a curved pipe [94]. At high Dean numbers, counter-rotating vortices form in a flow as it moves around a bend, forming as a result of high central velocity flow being deflected to the outer radius due to centripetal forces [94].

## 2.8. Phantom fabrication

In Chapter 1 the compliant nature of large arteries was introduced. To accurately measure fluid-structure interactions under pulsatile flow conditions, the phantom artery would also need to be compliant. Many computational models of the fluid mechanics through arteries are limited by the difficulty of modelling complex fluid-structure interactions. This difficulty can be overcome in PIV analysis. However, PIV measurements do rely on the accuracy of the phantom fabrication method for the phantoms being investigated. Lost-core casting is a common method for removing the internal mould of a geometry post-casting [95]. The method requires manufacturing a sacrificial core that will be melted, dissolved or burnt out of the remaining mould. This method is relatively simple for rigid phantom castings. However, manufacture of compliant phantoms requires a higher level of skill to precisely locate the central core, and maintain accurate and precise wall thickness. Compliant phantoms were consistently used throughout this thesis.

Compliant silicone phantoms were created in the following key stages:

1. The model was designed
2. A mould was 3D printed
3. Silicone was cast
4. The phantom was installed within a compliance chamber

### 2.8.1. Model design

To design an artery phantom, general dimensions from *in-vivo* arteries were obtained through literature. These dimensions were used to design the internal core for the phantom mould. For a rigid phantom, the internal core was be constrained within an external casting and the silicone poured around the mould. However, a compliant phantom required manufacturing moulds with a minimum of three parts (1 male, internal mould part and 2 female, external mould parts). Large moulds sometimes required more external mould parts due to the build volume limitations of the 3D printers available. The manufacture method for a compliant phantom was adapted from Yazdi, et al. [95].

#### *2.8.1.1. Radial Scaling*

The first step to designing a mould was to determine what scale of phantom would be required to achieve a compliance matched model. The lower limit of model scale tends to be defined by the minimum viable wall thickness fabrication. To date, a wall thickness of 1 mm is the thinnest reliably manufacturable wall using Sylgard 184 silicone [95]. The dimensions of an *in-vivo* artery were compliance matched using Equation 2.16 and scaled to at least achieve the minimum manufacturable wall thickness [3]. Equation 2.16 ensured the circumferential changes due to pressure between an *in-vivo* artery and scaled *in-vitro* model would be clinically significant. Since Sylgard 184 has a modulus of 1.32 MPa (the thoracic aorta is 0.526 MPa [96]), scaling is ubiquitous with compliance matching.

$$C = \frac{1}{\mathrm{A}}\frac{\partial \mathrm{V}}{\partial \mathrm{P}} = \frac{D}{Eh} \qquad \text{(Eq. 2.16)}$$

In which $C$ is the cross-section normalised compliance (simply referred to as compliance in this thesis) [MPa$^{-1}$], $A$ is the cross-sectional area at rest [mm$^2$], $V$ is the volume [mm$^3$], $P$ is the pressure [MPa], $h$ is the wall thickness [mm], $E$ is the elastic modulus [MPa], and $D$ is the diameter at rest [mm].

In arteries, compliance is a measure of arterial distensibility and defines the artery wall deformation induced volume change in response to pulse pressure [15]. Cross-sectional normalised compliance defines the proportional change in diameter as a response to pulse pressure. Hence, unlike compliance, normalised compliance is scalable. Normalised compliance also has an inherent assumption of negligible axial movement of the arterial vessel due to pulse pressure. Hence, the main change in volume occurs due to the changes in the vessel diameter rather than length [97].

#### *2.8.1.2. Longitudinal Response Scaling*

Straight vessel lengths ($L$) were scaled differently to minimise the effects of the rigid fixings at inlets and outlets to the models. Vessel lengths were dependent on the Longitudinal Response formula (Equation 2.17) compiled by Geoghegan [71] to ensure similar wave propagation through the vessel limbs.

$$\frac{L_{in-vitro}}{\lambda_{flow_{in-vitro}}} = \frac{L_{in-vivo}}{\lambda_{flow_{in-vivo}}} \qquad \text{(Eq. 2.17)}$$

In which $\lambda_{flow}$ is the wave speed of the flow [m·s$^{-1}$]. Wave speed can be calculated using Equation 2.18.

$$\lambda_{flow} = Bc_0T \qquad \text{(Eq. 2.18)}$$

Where $B$ is the dispersion coefficient [unitless]. $B$ tends to 1 for pulsatile flows with a Womersley Number greater than 3.5 [98], $c_0$ is the propagation wave speed coefficient defined in Equation 2.19 based off the Moens-Korteweg formula [98], and $T$ is the waveform period [s].

$$c_0 = \sqrt{\frac{Eh}{D\rho}} \qquad \text{(Eq. 2.19)}$$

For which $\rho$ was the density of the fluid [kg·m$^{-3}$].

A male mould would be designed with reference to the scaled vessel diameters and lengths. Following design of the male mould, the two-part female mould was designed by offsetting the male core surface by the required wall thickness. To enable location within a compliance chamber additional flange connection points (shown in Figure 2.14) were included in the mould design. To prevent core motion during casting, concentric location flanges were included at every phantom inlet and outlet. The female mould design included locations for silicone injection at the base of the mould and venting holes at the top. The venting holes enable air to escape during casting. Locating bolt holes were included in the female mould and concentric flanges enabled the mould to be assembled and tightly sealed.

### 2.8.2. Mould 3D printing

In this thesis the model was ABS (acrylonitrile butadiene styrene) 3D printed. ABS was selected as the 3D print material due to its poor compatibility with acetone, making it easy to dissolve [95]. Typically, the moulds were printed using an UPBOX+ (Tiertime, Beijing, China) with a 0.2 mm layer height and 20% infill. The low infill allowed the ABS to dissolve faster without compromising the strength of the mould. The UPBOX+ had a 0.01 mm tolerance and therefore, reliably produced the moulds. The surfaces of the prints were sanded using 400 grit sandpaper and then vapour smoothed using acetone. The high grit sandpaper only removed very small amount of material whilst also removing imperfections and ridges from the print layer lines. The acetone vapour produces a glossy finish (seen in Figure 2.14).

*Figure 2.14: Example of a 3D printed moulds*

### 2.8.3. Silicone injection

All parts of the moulds were washed and dried before assembling to remove any dust particulates. The male core was located within the two-part female mould and held together using M4 nuts and bolts. A layer of PVA (polyvinyl alcohol) glue was applied between the interfacing surfaces to prevent any leakage of silicone during casting. A layer of hot glue was also applied along the join of the two female parts. Sylgard 184 silicone and a cross linking agent were mixed at a 10:1 ratio (in accordance with manufacturer recommendations by Dow Corning (USA)). The silicone was degassed in a vacuum chamber prior to casting to remove air bubbles that were introduced during mixing. After degassing, the Sylgard 184 silicone mixture was injected into the base of the mould and air vented out the top. The silicone was left to cure in the mould at room temperature (23$^{o}$C) for 48 hours.

Following curing, the hot glue, nuts and bolts were removed. The mould and casting were then submerged in water for 20 minutes to soften the PVA glue. The female mould was mechanically levered off the casting using blunt tipped tools to protect the fidelity of the casting. Removing the female mould, significantly reduced the time to dissolve the ABS. However, for complex external geometries the female mould can also be dissolved if needed. The male mould and silicone phantom was then placed in a bath of acetone. The acetone was intermittently agitated to assist ABS dissolving. A final cleaning of the phantom was carried out using acetone and cotton swabs to remove remnants of ABS. The acetone did not alter the transparency of the phantom [95].

### 2.8.4. Compliance chamber

Compliant phantoms required suspension within a compliance chamber to maintain neutral buoyancy and protect the fidelity of the model and accurately capture particle motion during experiments. Compliance chambers were laser cut from 8 mm thick PMMA (polymethyl methacrylate) sheets and silicone sealed to prevent leakages. The phantom was situated within the compliance chamber and fixed in place by hose clamps over the flange socks. During experimentation, the compliance chamber was filled with the same working fluid as was pumped through the phantom. This ensured there would be no optical distortions due to the laser passing through different mediums. Specific descriptions for each experimental set up are provided in the respective chapters.

## 2.9. Summary

A detailed description of the experimental set up was provided in this chapter. It can be summarised as follows:

- Planar PIV was used throughout this thesis.
- The particles used to seed the fluid were silver-coated hollow glass spheres with a nominal diameter of 10 µm.
- The particles had sufficient neutral buoyancy and light scattering to be effective.
- An Nd:YAG laser was used with appropriate optics to produce a 1 mm thick laser sheet to track particle patterns.
- Image capturing was carried out using TSI Insight 4G.

- Image processing was carried out using both TSI Insight 4G and PIVLab.
- The working fluid used initially was 40/60 water and glycerine. However, later experiments used 45.6/28.8/25.6 water, glycerine and urea. The working solution is specified in each chapter.
- A horizontal flow circuit was used for early experiments. However, to reduce setup and resetting time between experiments a vertical flow circuit was designed with a dual pumping system.
- Waveform were produced using a piston driven by a 400-step stepper motor attached to a ball and screw linear rail.
- Waveforms used for *in-vitro* experimentation were dynamically matched to *in-vivo* waveforms via Womersley and Reynolds number matching.
- Compliant phantoms were manufactured using a lost-core casting method, in which silicone was injected into the cavity produced by the 3D printed male and female moulds, cured and then the moulds removed.

# 3. Review of the Development of Haemodynamic Modelling Techniques to Capture Flow Behaviour in Arteries Affected by Aneurysm, Atherosclerosis and Stenting

This chapter provides a review of previous modelling methods used to assess haemodynamics within healthy, diseased and stented arteries. The specific focus will be placed on studies that investigated or simulated the effects of CVD on haemodynamics. Both CFD and PIV haemodynamic modelling techniques in stented and non-stented arteries will then be reviewed. The benefits and limitations of each experimental modelling method for determining clinically relevant conclusions will be discussed. The chapter is an adaptation of a review article that has been published in the AMSE Journal of Biomechanics [99].

## 3.1. Introduction

Chapter 1 introduced three of the main forms of CVDs considered in this thesis. As stated in Section 1.5. Treatment of CVD, vascular implants, particularly stents, are often implanted to restore normal haemodynamics. However, the haemodynamic effects of stents are still being investigated. *In-silico* modelling, such as Computational Fluid Dynamics (CFD), and *in-vitro* modelling, such as Particle Image Velocimetry (PIV) and, less commonly, Magnetic Resonance Velocimetry (MRV) have been utilised to assess the potential benefit of novel implant designs and mitigate risks in animal or preliminary human trials. However, designing or considering the efficacy of haemodynamic experiments for candidate clinical interventions requires an understanding of the physiological interaction between haemodynamics and the arterial wall.

The haemodynamic changes due to stenting have been researched extensively [100-102]. Previous studies have been carried out using *in-silico,* usually via CFD [59, 102, 103] or *in-vitro,* often via PIV [80, 104-106] though increasingly by MRV [107, 108]. *In-vivo* measurement methods have also been used such as Doppler Ultrasound [109], and Computer Tomography (CT) scans [110, 111], to investigate the physiological behaviour of healthy, diseased, and stented arteries. However, most of these studies have focused on the stents' effects on intra-aneurysmal flow to reduce risk of rupture and near wall peri-stent modelling for neo-intimal hyperplasia [39, 112-114]. The effects of radially rigid stents on the distal arterial wall and consequent haemodynamics have not been investigated as extensively [71, 115].

## 3.2. Physiology and Mechanics of Arteries and Stents

Healthy arterial walls are vital to maintain good blood perfusion throughout the body. The inner most intimal layer is made up of elastic lamina supporting a mono-layer of endothelial cells that interact directly with the blood flow [116]. As noted in Section 1.3.1. Endothelial cells, endothelial cells respond to haemodynamic factors, such as wall shear stress (WSS) by releasing vasodilator and vasoconstrictor molecules that modulate the vascular tone. Abnormal haemodynamic factors such as recirculation, reversed, or reciprocating flow proximal to the wall, may change the stimuli and therefore alter the growth patterns of endothelial cells [64, 117-122]. Altered growth of endothelial cells can result in CVD formations such as atherosclerosis, arterial delamination, or acute dissection, and affect aneurysm growth and rupture [113, 123-125].

WSS is the tangential frictional force that is produced as a result of the blood flow across the endothelial cell surface [125]. WSS has been linked to many CVD forms such as stenosis and arterial dissection. WSS is dependent on the rate of change in velocity from the centre of lumen toward the wall (shear rate) and viscosity. WSS varies throughout the cardiovascular system. Typically, WSS is higher in the carotid artery than brachial or femoral arteries. However, even within the aorta there is significant variation in WSS at different locations, such as the aortic arch and the descending aorta

[126], and at different times across the cardiac cycle. Endothelial cells respond to stimuli, such as WSS, to determine growth behaviour. Altered WSS has been linked to aneurysm growth and rupture [117, 127-129] and atherosclerotic lesion formation [130, 131] in arteries. A change in WSS can potentially lead to a change in the growth patterns of endothelial cells, which may result in deleterious effects such as intimal thickening or thinning, and occlusion within the arterial wall [123].

The time-averaged WSS (TAWSS) during a single cardiac cycle [114] has been used to provide a benchmark value for measuring patient-specific flow abnormalities. A rigid body assumption is generally sufficient for measuring TAWSS [132] as it is not generally strongly affected by Fluid-Structure Interaction (FSI). However, time varying WSS (TVWSS) is often strongly affected by FSI that rigid wall models cannot capture [120]. TVWSS magnitude and location change throughout the cardiac cycle and with the motion of the walls [133]. For measuring important haemodynamic characteristics, TAWSS has underestimated peak TVWSS by 60% [73] and may miss clinically important haemodynamic characteristics such as retrograde or recirculating flow [134]. The oscillatory shear index (OSI) is a dimensionless parameter that determines the degree of reversed flow according to the congruence of the TAWSS vector and the WSS vector throughout the pulse cycle [135]. In certain regions of main arteries such as the aorta, OSI can vary between full agreement (OSI=0) and oscillating flow (OSI≈0.5) [135].

The three forms of CVD investigated in this thesis are atherosclerosis, aneurysm and aortic dissection. Section 1.4. Cardiovascular Diseases provides a detailed description of each of these. In summary: atherosclerosis can narrow or block arteries, inhibiting blood flow and inducing flow stagnation and separation zones prone to recirculation [76, 136, 137]; aneurysms can affect flow behaviour, potentially inducing recirculation, reversed flow and other deleterious haemodynamics [138-140]; and dissections form a false lumen for flow to pass through completely altering the shear stresses experienced within the true lumen. The dissection also weakens the arterial wall potentially causing irreversible dilatation of the artery otherwise known as a pseudo-aneurysm which can lead to rupture and high risk of mortality (Figure 3.1) [141].

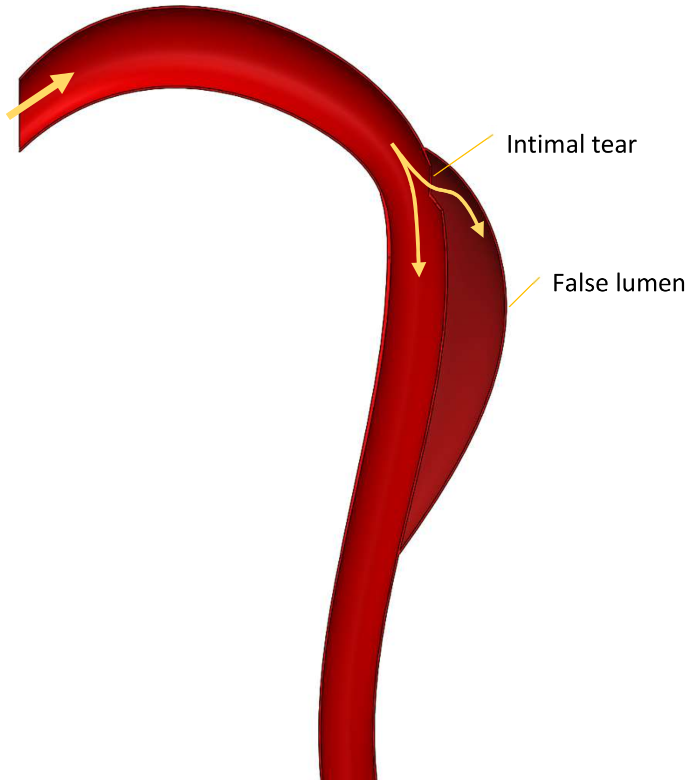

*Figure 3.1: Dissection of the arterial wall through a curved artery model. Direction of flow shown by yellow arrows*

Stent implementation is a common treatment for many forms of CVD. The function of stents was introduced in Section 1.5. Treatment of CVD. Stents grafts (i.e. covered stents) are currently popular for treating arterial disease such atherosclerosis, aneurysm or arterial dissection. Stent grafts are designed to exclude blood flow from the diseased artery and prevent neo-intimal hyperplasia and maintain healthy haemodynamics within the lumen. Stent grafts are relatively rigid compared to arterial walls and cannot expand beyond the covering fabric. Stent rigidity induces a compliance mismatch between the graft and the parent artery [65]. The significance of this mismatch has been noted as a key research question [65, 66, 100].

All arteries except for the pulmonary artery branch from the aorta and perfuse oxygenated blood to the organs [142]. CVD of the aorta are associated with high morbidity and mortality rates [35, 143]. Nearly the entire stroke volume of blood will flow through the aorta. The aortic arch supplies the head an upper limbs of the body with blood [12]. The abdominal aorta supplies blood to five major arteries that lead to the abdominal organs [12]. Hence, implanting stent grafts in the aorta must not obstruct the origins of these arteries otherwise it could result in organ necrosis [42]. The two methods clinicians use to prevent occlusion of the aortic branches are fenestration or branched stent grafts (Figure 3.2) [144]. Fenestration is the creation of a window in the stent graft at the peripheral artery location [144]. Fenestration allows blood to flow to peripheral arteries, however, relies more heavily on precise parent stent location and the condition of the peripheral artery. Branched stent grafts are stent grafts of smaller diameter stitched to the side of the main stent graft that distends into the peripheral artery [144]. Branching can help maintain the parent stent in position and is commonly used when the disease artery distends into a peripheral artery also. These methods are applicable to other branched arteries also.

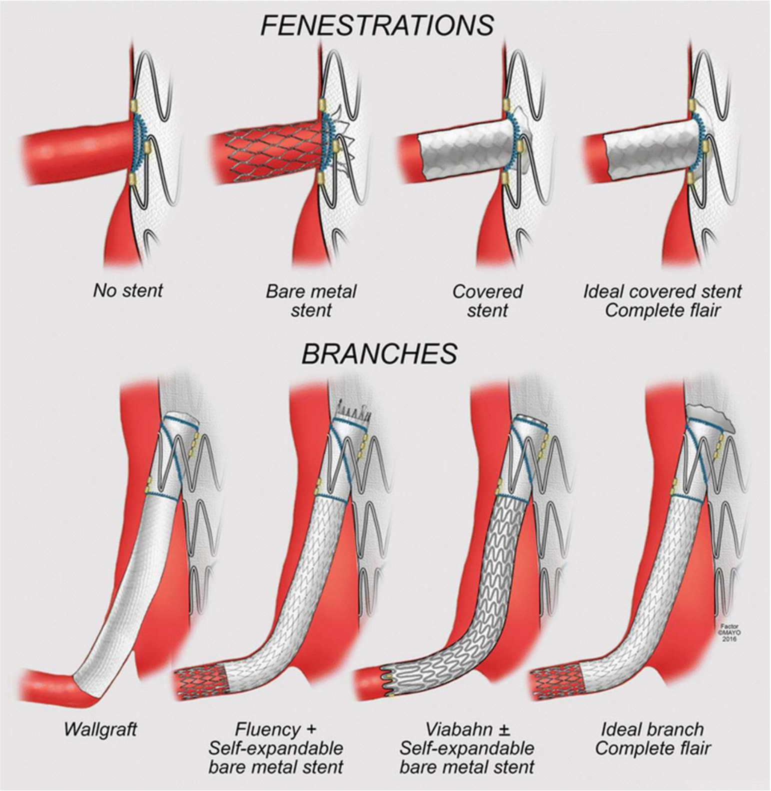

*Figure 3.2: Fenestration and branch stenting of parent stent for peripheral arteries. Reproduced with permission from [145]*

## 3.3. Computational Fluid Dynamics Modelling in Cardiovascular Disease

*In-silico* haemodynamic modelling is predominantly carried out using CFD, or CFD coupled with Finite Element Analysis (FEA), particularly when looking at the FSI. CFD typically uses finite volume, numerical analysis to determine the behaviours of a fluid within a specific domain [60]. The fluid domain is discretised into a mesh of individual elements allowing for evaluation of localised flow parameters in governing fluid dynamics models [146]. Mesh density and resolution can have a significant effect on the quality of CFD results. Typically, mesh independence is declared when increases in mesh resolution no longer produce a discernible change in the simulation results [147].

CFD simulations have been used to model haemodynamics in arteries and cardiovascular stents [55, 59, 103, 120, 143, 148]. CFD models can be generated using patient specific or idealised geometries of arteries and stents obtained by medical imaging. Patient specific results are often more physiologically representative of *in-vivo* measurements than results obtained from generalised results [149]. Healthy haemodynamic flow waveforms and cross-sectional velocity profiles have less inter-patient variability than the variability observed in diseased geometry. However, intra-patient variability can be quite high in healthy individuals. In particular, physical exertion can cause significant changes in pulse pressure, arterial diameter and flow rate [139, 150-153]. Therefore, patient specific models have limited applicability to wider populations [96, 131, 154, 155]. Idealised geometries for arteries and stents are generated by averaging measured parameters across a range of patients and producing a range of applicable parameter values [156]. Idealised geometries have a wider applicability, however, will not precisely match the haemodynamics of any particular individuals and will not necessarily be representative of diseased arteries.

Some CFD approaches for haemodynamic analysis have been reviewed previously [102, 109]. CFD can identify flow effects, such as WSS and displacement forces. Introduced in Section 1.3.1., abnormal WSS can negatively affect endothelial cell responses [118, 157, 158]. Displacement forces can be key to determining stent patency or mode of failure within patients [157, 159, 160]. However, CFD studies can be limited by the boundary conditions and the assumptions selected which may reduce the value of the results for clinical applications [161]. CFD studies commonly optimise existing stent mesh designs by varying spacing and thickness parameters to minimise undesirable haemodynamic disturbances caused by stent design [57, 156].

CFD can yield quick and low-cost indications of haemodynamic dysfunction in vascular anomalies such as atherosclerosis, stenosis, acute dissection or aneurysms [162]. CFD has also been used to predict potential failure in candidate stents for certain arterial geometries [114, 148, 156, 163]. CFD simulation allows quick, *in-silico* iterations of stent design, which is generally more time efficient and inexpensive than *in-vitro, ex-vivo* or *in-vivo* animal studies. Cerebral aneurysms are frequently researched via CFD [102, 104, 164, 165]. Aneurysms in certain arteries such as the ascending aorta, abdominal aorta, and carotid artery are also frequently simulated [73, 144, 162, 166, 167]. CFD modelling of stenosis is also conducted on cerebral arteries, the aortic arch and peripheral arteries to the aorta [109, 131, 168]. Stenosis does not commonly occur in the ascending or descending aorta. There are fewer CFD studies on the thoracic aorta [160, 169, 170]. This may be due to the significant FSI that occurs in the aorta. The aorta is highly compliant compared to other arteries in the human body, due to its high proportion of elastin fibres [1]. A high level of expertise, computational power and time are required to carry out compliant FSI modelling. Such compliant modelling is uncommon, and a rigid wall is often assumed.

### 3.3.1. CFD Studies of Artery Haemodynamics

Early identification of aneurysms is critical for successful interventions that reduce morbidity and mortality [171]. Numerous CFD studies have modelled the altered haemodynamics in arteries with CVD and improved understanding of the deleterious flow behaviours in diseased arteries [117, 127, 172]. Numata, et al. [172] used CFD to investigate the effects of thoracic aortic aneurysms in four locations in the aortic arch. In each location, haemodynamic disturbances were observed within, proximal and distal to the aneurysm. Among other outcomes, Numata, et al. [172] determined a causal link between aneurysm in the ascending aorta and the initiation site for dissection. These haemodynamic disturbances can cause changes in the spatial and temporal distribution of WSS [71]. Deviations from the characteristic WSS may be the most critical factor contributing to the evolution and rupture of aneurysms [102].

CFD studies identified that changes in WSS may exacerbate existing CVD such as aneurysms and stenosis [117, 127-129]. However, studies have opposing views regarding whether high or low WSS is the main contributor to CVD exacerbation. Low wall stress was identified at the location of ruptured aneurysms in studies conducted with seven samples by Boyd, et al. [117] and seventy-four by Xiang, et al. [127]. Conversely, high WSS was identified at the location of aneurysm ruptures in studies with nineteen and six samples by Zhang, et al. [128] and Chien, et al. [129], respectively. Perhaps both WSS states contribute to rupture via differing mechanisms. However, the contradiction leads to a degree of ambiguity in the scientific understanding of the aetiology of aneurysms. However, whilst the causes of aneurysm growth were not consistent across CFD studies, all determined that abnormal WSS was a contributing factor. Lauric, et al. [113] suggested results may be biased by size and location of aneurysms. CFD simulation showed confirmed larger aneurysms had a greater effect on the overall arterial flow, reducing the peak cross-sectional velocity at the aneurysm location. The reduced velocity may result in lower WSS within larger aneurysms further weakening arterial walls. Atherosclerotic lesion formation is more often linked to low WSS [25, 130, 131]. Frydrychowicz, et al. [131] investigated the WSS and OSI distribution at the supra-aortic branches, where atherosclerotic lesions have been known to form. Low WSS and high OSI was identified at the typical lesion locations, indicating a potential cause. A CFD model of the left carotid artery also found that regions with consistent low WSS produced irregular stenoses [130]. CFD can assist in identifying potentially deleterious flow characteristics and estimate the changes that candidate stents may provide [173]. Understanding dysfunctional haemodynamics within aneurysms *in-silico* will help to determine the potential benefits of stents on restoring normal haemodynamics *in-vivo* prior to human trials.

### 3.3.2. CFD of Stented Haemodynamics

Stent implant causes local haemodynamic disturbances in the parent artery [174]. In particular, while stents can improve haemodynamics, the outcome haemodynamics do not exactly mimic healthy haemodynamics. Abnormal WSS can cause inflammatory responses resulting in deleterious effects such as neo-intimal hyperplasia [125, 175]. Despite the risk of inflammation and abnormal growth, stents reduce the negative effects of CVD and reduce the likelihood of aneurysm rupture or atherosclerotic lesions, thereby benefiting haemodynamics and reducing mortality [45]. CFD can provide an estimate of the flow behaviour within stents that can be challenging to obtain using available *in-vitro* methods such as PIV [114]. CFD studies on stents commonly consider the geometry and design of the stent mesh. Strut design can have a significant effect on the inflammatory response of the artery [55]. CFD studies have shown that stent strut sizing is important to consider as they protrude into the arterial lumen, introducing the potential to form recirculation zones and stagnation zones [55]. Thinner struts generally lead to higher WSS than thicker struts. However, Karanasiou, et al. [55] found that the thicker struts reduced the overall percentage area of the arterial wall with low WSS values. Lower strut density results in larger areas of low WSS and more elevated WSS gradient (WSSG) [57]. In contrast, Beier, et al. [156] identified that narrow strut spacing has been linked to adverse WSSG and low WSS in the intra-stent region. LaDisa, et al. [57] suggested that the artery walls may straighten between adjacent struts, which can result in a non-circular arterial cross-section. The straightening between adjacent struts may overestimate the effect of the stent on WSS and WSSG. High WSSG has been linked to negative inflammatory responses such as intimal hyperplasia, atherosclerotic lesions and increases vessel wall permeability [156]. Below expected WSS is often found at the peri-stent location [57]. Some CFD studies have hypothesised there is an optimal strut size and spacing ratio for each artery [105, 156]. However, there is no published and generally accepted guidelines for determining these optimal parameters. Flow recirculation and stagnation occur both upstream and downstream of the struts and are strongly influenced by the size and shape of the strut [55].

There is a paucity of CFD studies that investigate haemodynamics of arteries peripheral to the stented artery. This is despite the clinical importance of such geometries [176, 177]. Sun and Chaichana [177] found that fenestration of the suprarenal arteries had little effect on the velocities measured in the renal artery, meanwhile Avrahami, et al. [176] found fenestration of the suprarenal artery introduced a risk of occlusion of the renal artery. Kandail, et al. [178] investigated volumetric flow through the renal arteries due to fenestration stenting and determined that sufficient flow was provided to the renal arteries, but the percentage of flow was highly reduced when exercising. The effects fenestration has on flow properties through the renal arteries is significantly affected by the take-off angle of the fenestrated cuff, with $90^{o}$ the optimum angle [40].

CFD can be coupled with FEA to achieve simulations that contain FSI elements. FSI coupled with CFD has been carried out to investigate the forces that may result in stent displacement or failure [159, 160]. However, FSI is often overlooked due to its complexity and high computational cost. Hence, the time variant deflection of the arterial walls due to the pulse pressure of the blood is often ignored. Furthermore, another limitations of the CFD studies is the choice of turbulence model. Previously studies mainly used Reynolds-averaged Navier–Stokes (RANS) equations which models all eddies and limited studies simulated the eddies (LES). LES simulations are more accurate than RANS modelling however, it costs high in memory and computational time. The application of LES simulations with dynamic mesh and FSI makes CFD less favourable than PIV. CFD typically considers both the stented geometry and surrounding arterial tissue effectively rigid [39, 57, 156]. This approach seems appropriate for measuring clinically relevant near wall haemodynamics. However, FSI should be included if the potential factors that may result in stent failure near the inlet or outlet of stents are to be measured [169, 170].

## 3.4. Particle Image Velocimetry Modelling in Cardiovascular Disease

*In-vitro* modelling methods of haemodynamics commonly focus on optical measurements such as PIV. PIV developed from alternate experimental laser modelling techniques, such as Laser Doppler Velocimetry. PIV has been used as a validation technique for CFD studies and novel *in-vitro* experiments carried out on arteries such as the carotid, cerebral and aorta [104, 130, 165, 179]. However, PIV measurement is limited by the requirement for transparency of the test section [71] thereby limiting the modelling of grafted stents. The need for optical transparency can be negated via Magnetic Resonance Velocimetry (MRV) [107, 108]. However, MRV is costly, limiting increased use in haemodynamic modelling. MRV is a developing measurement method that could still use PIV for validation [180]. A detailed description of PIV was provided in Chapter 2.

PIV measurement of haemodynamics requires the manufacture of a physical model, generally termed a phantom. Model transparency is required to provide the camera optical access to the region of interest and identify velocity fields and flow patterns, such as recirculation formation and reversed flow [181]. Suitable materials for manufacture of phantoms are limited by the requirement for transparency. Early modelling practices used cast glass to produce rigid phantoms [182, 183]. Currently, transparent elastomers are often used as they allow compliance matching phantoms [73, 80, 96, 184-186].

Arterial phantoms can be manufactured such that they are compliant or rigid. Compliant models are capable of dilating and changing geometry under changes in transmural pressure. Conversely, rigid models are not deformed under pressure changes in the working fluid. Computer assisted design (CAD) software is often used to design moulds for the manufacture of rigid and compliant phantoms [80, 185]. Rigid phantom manufacture generally uses a male mould and a casting box. The male mould will be chemically dissolved or broken out of the phantom via the lost core casting technique. Material selection of rigid models are broader than for compliant models. Early PIV models used glass castings of artery geometries [187]. Thick-walled transparent elastomers can also be used to produce effectively rigid models [95, 185, 188]. Compliant phantoms are produced using female and male moulds, designed with a clearance of the intended wall thickness. A transparent elastomer, such as silicone, is injected into the moulds and cured to form a phantom [95]. Section 2.8. provides a more detailed methodology for manufacturing the phantoms used for PIV analysis.

Refractive index matched fluids eliminate the optical distortion between the working fluid and the phantom [185] (Figure 3.3). A ratio of 40:60 water to glycerine solution is refractive index matched to Sylgard 184 ($n = 1.41$) [185, 189]. While silicone and the aqueous-glycerine solution are a common combination for experimentation, other combinations have also been used. For example, Friedman, et al. [190] used transparent bioplastic with eugenol as the working fluid. Sylgard 184 and sodium thiocyanate have also been paired for experimentation [191]. Sodium thiocyanate has a refractive index of $n = 1.41$, like Sylgard 184 [191]. However, sodium solutions are corrosive and may damage pumps and other equipment used for experimentation.

Two flow circuit designs are shown in Section 2.6. (Figures 2.11 and 2.12). Typical components include a piston and/or pump, flow meter, phantom, head tank and reservoir. Some studies use a flow straightener to ensure Poiseuille flow profiles at the inlet the experimental domain [119]. Compliant PIV requires a compliance chamber filled with the working fluid. An air-liquid compliance chamber is sometimes used to mimic Windkessel effects of the arterial system [192].

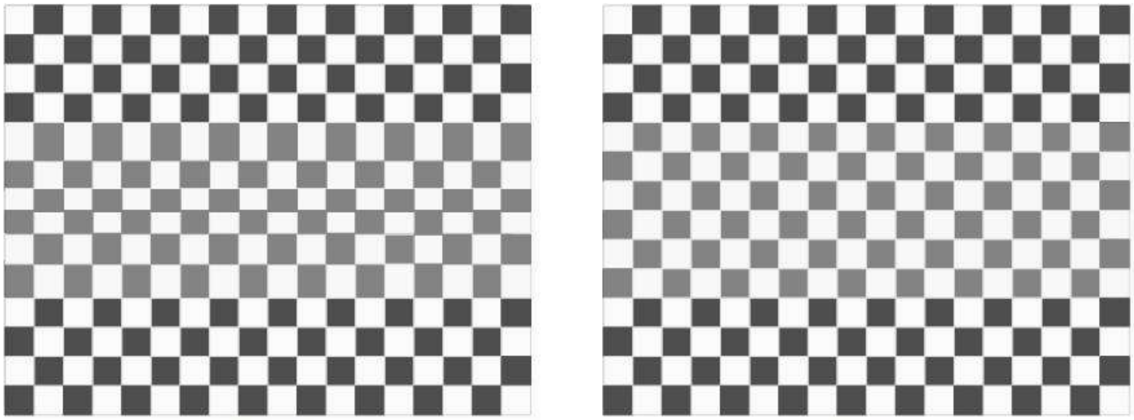
Unmatched

Matched

*Figure 3.3: Before refractive index matching (left) and after refractive index matching (right)*

### 3.4.1. PIV Studies of Artery Haemodynamics

PIV studies have yielded many clinically important findings. A 1981 study identified a negative relationship between increasing intimal layer thickness and the wall shear rate carried out on a cast of an aortic bifurcation at 15 chosen sites [193]. PIV has also been used to identify the flow patterns that may result from or be potential causes for vascular diseases such as aneurysms [186, 192] and stenosis [137, 194]. Deplano, et al. [195] investigated vortex formation in abdominal aortic aneurysms (AAA) by modelling the shear thinning process. The results implied that the AAA is linked to peak wall stresses, strength within the aneurysm and the mechanical properties of the wall. These finding were confirmed and repeated by LaDisa, et al. [57] and Beier, et al. [156]. Another study on cerebral aneurysms investigated the flow through an aneurysm [112]. The aim was to identify recirculation zones at the apex of the aneurysm which may contribute to aneurysm growth if untreated [112]. However, these recirculation results were not conclusive so an investigation into the WSS was completed. The WSS tended to be low at the regions of aneurysm growth concurring with CFD studies carried out by Boyd, et al. [117] and Xiang, et al. [127]. The effect of stenosis has been conducted in many arteries and been shown to alter the flow patterns both proximal and distal to the constricted artery [130, 137]. Doutel, et al. [130] used PIV to validate the numerical model for a stenotic carotid artery. PIV has allowed for the identification of abnormal WSS and can visualise recirculation within a model of an affected artery.

Comparison of results from compliant and rigid phantoms have been repeatedly examined [73, 186, 192, 196]. Compliance typically yields more variance in velocity profiles and the WSS experienced within certain regions of the artery [197]. Büsen, et al. [192] investigated the effect of compliance in the aorta. A reduction in compliance of 63% resulted in a 122% increase in the aortic pressures and higher mean velocities during systole [192]. Recirculation formation is also highly dependent on arterial compliance [186, 192]. Yazdi, et al. [186] compared results of a rigid model and a compliant model of an idealised ascending aorta and aortic arch. Recirculation zones were identified in the compliant artery in regions of the aorta that are at high risk for the atherosclerotic formations and therefore arterial stenosis. The recirculation zones were not present in the rigid model. Rigid phantoms have yielded overestimations of the WSS by approximately 60% compared to the compliant phantoms [73].

### 3.4.2. PIV Studies of Stented Haemodynamics

PIV allows for *in-vitro* investigations of potential stent effectiveness to aid development [198]. PIV investigations into stents are commonly focused on modelling intra-aneurysm flow or proximal and distal effects of stenting. PIV studies also commonly use specific stent brands rather than a generalised shape to model flow characteristics [105, 199, 200]. However, it may be expected the general flow behaviour will be similar across similar stents, and for only near wall effects to vary depending on strut design [105].

The effects of different stent mesh porosities have often been investigated using PIV analysis of stents in extra-cranial or cerebral aneurysms [184, 200, 201]. Rhee et al. [184] determined the effects of stent porosity on intra-aneurysmal flow and linked the porosity and flexibility of stents. Reducing porosity from 0.86 to 0.79 resulted in reduced intra-aneurysmal flow, thus potentially improving patient outcomes [184]. However, reducing porosity increases the rigidity of the stent, making it harder to manoeuvre into the appropriate position and flex with the artery. The reduction in flow was not deemed sufficiently valuable to justify the increased rigidity of the stent [184]. Dennis, et al. [201] later confirmed the study using stent meshes of differing porosity. Reducing strut spacing by 1 mm for the same length stent resulted in an 8% reduction in flow through the stented aneurysm [201]. The reduced porosity did not significantly reduce the intra-aneurysmal flow in this study. Stiffness of the stent mesh designs were not evaluated in the investigation [201]. Bouillot, et al. [198] attempted to find an optimal stent porosity using PIV. They determined that an 88% porous stent mesh significantly reduced the volumetric flow rate of intra-aneurysmal compared to higher porosity stents. They noted that further reducing stent mesh porosity did not have a significant effect on the intra-aneurysmal flow but did reduce mesh flexibility [198]. Changing porosity of stents can be modelled using CFD, however flexibility and rigidity measurements require coupling with FEA.

There are fewer intra-stent PIV investigations of haemodynamics indicating a gap in the understanding of stents and the effects they may have in arteries, particularly those afflicted by stenosis or occlusion. intra-stent PIV investigations are limited by optics resulting from mesh density and graft design. Dense mesh wires can result in high saturation of light due to reflections from the laser sheet and hence, particles cannot be identified and tracked within the flow stream. Stent grafts also typically are not transparent and hence are difficult to investigate without fabrication of surrogate grafts. Transparent surrogate stents are a newly developing modelling technique for use in optical imaging. In particular, dip-coating with transparent polyether polyurethane are an increasingly popular technique for producing optically transparent stent grafts [202, 203]. Groot Jebbink, et al. [204] used PIV to investigate the flow behaviour proximal to a reconstructed aorto-iliac bifurcation using the kissing stent, covered kissing stent and Covered Endovascular Reconstruction of Aortic Bifurcation (CERAB) configurations as a method of restoring blood flow to patients suffering from aorto-iliac occlusive disease. The stent grafts for the covered configurations were replaced with a transparent polyurethane alternative. No significant deleterious flow was identified in the experiment. Hence, the investigation determined the methods to each be safe for restoring flow, however, compliance was not investigated and may also affect the flow.

It is uncommon to investigate the effects of compliance on stented haemodynamics using PIV or other *in-vitro* modelling techniques. Charonko, et al. [105] investigated bare metal stent design effects *in-vitro* using compliant phantom vessels and found strong correlation between strut designs and WSS and OSI, which may affect endothelia cell growth and hence, the long-term patency of stents. However, much like in CFD investigations, few compliant models have investigated deleterious effects of stents proximal or distal to the stent implantation. Studies of grafted stents often overlook key haemodynamic risk factors such as endoleak and atherosclerotic formation as a result of stenting. This is a key area for development.

## 3.5. Boundary Conditions

All haemodynamic modelling methods need appropriate boundary conditions to yield clinically informative results. Results will significantly vary based on the boundary conditions applied and assumptions made. Inlet and outlet boundary conditions do not vary significantly across stented and non-stented segments of the arterial structure. However, no single set of generalisable rules for defining boundary conditions for arterial modelling have been accepted and results can thus vary for similar investigations. The lack of comparability introduces ambiguity into the results [109]. Wall boundary conditions are more consistent with a common assumption being rigid walls in both CFD and PIV [39, 154, 200, 205]. However, Geoghegan, et al. [73] demonstrated that rigid wall assumptions can overestimate WSS by up to 60%.

Precise haemodynamic flow properties in specific regions of the arterial structure can be clinically obtained and used as inlet boundary conditions in CFD and PIV. Phase contrast-MRI (PC-MRI) is a method for determining patient specific inlet and outlet boundary conditions [148, 206, 207]. However, not all research groups have easy access to patients, expertise and equipment needed for *in-vivo* flow properties to be measured. In such cases, generalised inlet and outlet conditions are obtained and modelled based on a generic cardiac cycle can be used [161, 164, 208].

### 3.5.1. CFD Boundary Conditions

In CFD, the definition of the input flows, fluid properties, the domain boundary conditions, and computational methods can have a strong effect on simulations. Appropriate boundary conditions, working fluid properties, and stable numerical methods are required for accurate CFD modelling. The specific parameters of blood can be implemented in simulation [209, 210]. In most CFD analyses, the inlet condition is a set velocity profile, and the outlet is defined as a pressure condition [109, 161, 164, 172, 207, 210]. However, there can still be significant variance in the set-up methodology and variables defining inlet and outlet conditions. The bounding walls are commonly rigid [154, 155, 210]. Thus, the fluid-solid interactions that underlie the Windkessel effects (Section 1.3.2.) are not realized. Inlet, outlet and wall conditions can have a significant effect on the estimated WSS values, peak pressures, recirculation zones and velocities during systole and diastole [161].

#### *3.5.1.1. CFD Inlet*

When modelling the stent strut effects, steady state flow is often defined at the inlet. This choice enables indicative results rather than physiological waveforms [57]. Few studies have used pulsatile flow [156]. For pulsatile modelling the inlet conditions are most set as a user-defined velocity waveform. The waveforms are typically set up using measured physiological parameters, such as flow rates and pulse frequency [161, 207, 210]. The model is initialised by running the simulation for a set number of cardiac cycles and uses the data collected during the final cardiac cycle for analysis [156, 161, 207]. The appropriate number of cardiac cycles for initialisation is not consistent between papers with as few as 3 cycles to as many as 6 cycles being reported. Results from the initialising simulation were not reported. An alternate inlet boundary condition used a uniform mass flow rate with a pulsatile wave initiated at five diameters upstream of the geometry of interest to allow flow to develop [172].

Xu, et al. [109] compared two inlet conditions, one derived from the volume flow rate and the other from Womersley derived analytical solutions, to determine the variation in results for the same stenosed arteries. The volumetric flow rate was derived using digital subtraction angiography by dividing through by the transparent time of the angiography [109, 172]. The Womersley analytical solutions were based on the assumptions that arterial expansion is neglected, and the pressure gradient varies with time only. The two different inlet boundary conditions resulted in different WSS distributions but did not result in a significant pressure gradient variation [109]. However, the variance increased with the degree of stenosis. WSS is one of the most important parameters affecting CVD [64, 112, 125, 211]. The poor comparability between WSS for two separate inlet conditions presents an area of uncertainty and potential for further investigation.

PC-MRI has been utilised by some researchers to obtain data specific to the patient they are modelling [148, 207]. PC-MRI uses four-dimensional mapping to identify patient-specific velocity and WSS parameters [148]. Patient-specific inlet data may model vascular anomalies more accurately than generalised waveforms at the cost of wider applicability. PC-MRI produced inlet velocity waveforms that were specific to particular CVD forms in specific patients. Inputting the profiles obtained at the inlet and outlet into a CFD solver provided promising functional analysis of the thoracic aorta [148]. Romarowski, et al. [207] compared two different inlet boundary conditions for the thoracic aorta; an inflow profile produced by Morbiducci, et al. [212] and by using patient specific inlet data obtained from PC-MRI. PC-MRI flow acquisitions for the full region of interest were used as the gold standard to quantify the errors of CFD simulation [207]. Despite the inflow profile from Morbiducci, et al. [212] performing reasonably well, there was a notably higher error than in the patient specific inlet conditions data compared to the PC-MRI flow acquisitions. However, simulations using patient specific data input are difficult to undertake and interpret in a timeframe that could be clinically beneficial.

#### *3.5.1.2. CFD Outlet*

Patient specific outlet data is also expensive and time consuming to obtain. Hence, non-specific data is often used. Nicoud and Schönfeld [213] modelled the outlet conditions as a suction condition, rather than a positive pressure condition at the inlet. The sucking condition was easier to model, however ultimately led to inconclusive results with poor repeatability in some CFD applications [213].

A common approach to modelling the outlet boundary conditions in CFD is to create downstream resistance by applying a pressure outlet condition [109, 161, 164, 172, 207, 210]. The pressure condition is included in the formulation of the Navier-Stokes equations used for solving finite element problems [207]. The Windkessel model has been used at the outlet to develop a relationship between the blood pressure ($P$) and flow rate ($Q$) [109, 206]. The Windkessel motion was introduced in Section 1.3.2. The Windkessel model describes the Windkessel motion of the arterial system with analogous electrical components such as resistance, capacitance and impedance to represent arterial resistance to flow, compliance of the arterial wall and local inertial effects, respectively [214]. A 3-element Windkessel model can be implemented to mimic the proximal and distal resistance of the flow as well as the compliance of the artery (Figure 3.4a). The 3-element Windkessel assumes a linear relationship between the blood pressure and flow rate. However, this model is only applicable when the radius of the distal vascular network is sufficiently small [109]. Romarowski, et al. [207] observed improved accuracy in a 4-element Windkessel model (Figure 3.4b) but acknowledged that the improved accuracy was not significant enough to justify the increased complexity. The 4-element Windkessel model incorporated less variability in the development of the outlet boundary conditions. The Windkessel model tends to be the most common outlet condition, with a general tendency to use the 3-element model over the 2- or 4-element alternatives. Alishahi, et al. [215] and Abraham, et al. [216] used open outlet boundary conditions along with static outlet pressure profiles. In a cardiac cycle there is both forward and reversed flow [216]. An open boundary condition was applied to allow for flow reversal at the outlet. An open outflow boundary condition also allows outlet pressure to be modulated which the standard outflow boundary condition typically does not allow [215].

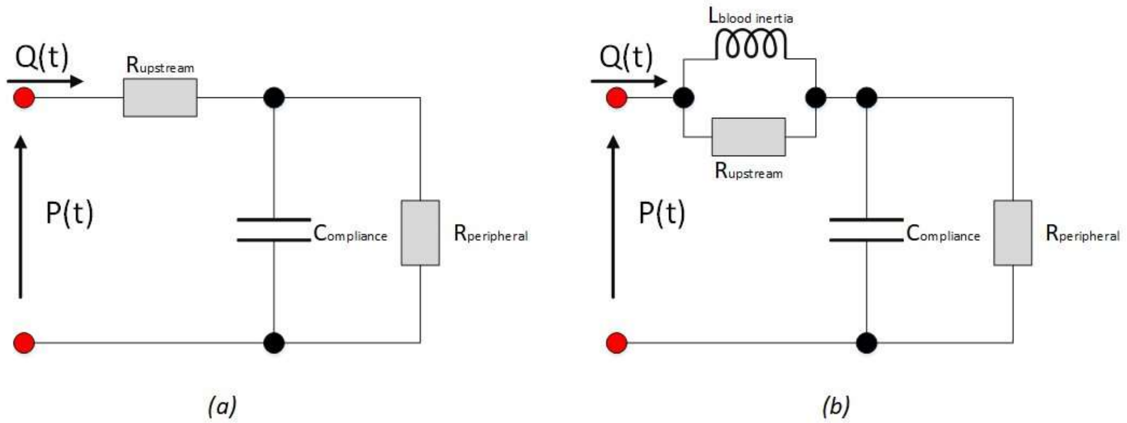

*Figure 3.4: Electrical circuit representation of the (a) 3-Element Windkessel model (b) 4-Element Windkessel model adapted from Stergiopulos, et al. [217]*

### 3.5.1.3. *CFD Boundary Wall Conditions*

CFD is capable of providing indicative results to the behaviour of blood flow in arteries and stents. Due to the difficulties and high computational time involved in modelling of moving meshes, the walls of the artery model are often assumed rigid [109, 161, 164, 172, 207, 210]. The rigid wall assumption results in non-physiological haemodynamics through non-stented regions of the arteries. However, for stented arteries, the rigid wall assumption may lead to clinically relevant results of the internal flow behaviour and effects of stent mesh and strut design. A limitation of the rigid wall assumption is the flow interaction between the artery and the stent. The effect of radial compliance mismatch between the model arterial walls and rigid medical implants cannot be modelled. Cebral, et al. [158] combined geometry data from a myriad of sources to develop an understanding of the degradation of arterial walls, primarily focused on aneurysm evolution in patients and gain an understanding of the FSI. However, CFD requires a moving mesh for compliant analysis which are also highly dependent on the accuracy of the measured arterial elastic behaviour. Midulla, et al. [148] produced a moving mesh using MRI images and a process using cardiac-gated cine sequences which covered the entirety of the thoracic aorta. However, the moving mesh can be complicated to implement and significantly increases computational cost [148]. Figueroa, et al. [218] presented a novel method of modelling blood flow through a deformable domain referred to as the coupled momentum method for fluid–solid interaction (CMM-FSI) problems. The CMM-FSI model allowed wall motion to be determined using pure fluids parameters, without the requirement for additional solving post-simulation. The FSI simulation research provided a promising method to model compliant arteries, however, current methods have not been validated and still rely on validation from *in-vivo* data or *in-vitro* experimentation to confirm findings.

Many studies carried out using CFD use a limited pool of data. Often CFD is carried out on patient specific models where the patient population ranges from 1 to 10 patients [161, 164, 172]. However, intra and inter-patient haemodynamics are highly variable. Hence, the results from a particular patient specific investigation cannot necessarily be assumed for another patient. For the development of CFD models, patient specific approaches can be useful as they provide comparison and validation [207]. However, Beier, et al. [156] and Xiang, et al. [127] both successfully collected data from a population pool of over 100 patients to produce more generalised results. Xu, et al. [219] also investigated an idealised aneurysm with different parent vessel curvatures resulting in non-specific results that are widely applicable.

### 3.5.2. PIV Boundary Conditions

PIV can potentially provide greater control of the model boundary conditions compared to CFD, though the boundary conditions are more difficult to alter. For example, determination of mechanical properties of certain arteries [96] have enabled fabrication of dynamic compliance matching PIV phantoms [80]. The control of boundary conditions allows physiologically relevant results via non-invasive *in-vitro* investigation [185]. However, even when a compliant phantom is successfully produced, it is often attached to a rigid flow circuit [220]. Zamir [98] suggested that a relationship between the length of the compliant phantom and propagation wavelength would minimise the effects of the rigid fixations.

#### *3.5.2.1. PIV Inlet/Outlet*

PIV haemodynamics can be set up based on flow rates and pressures [195]. Typically, studies were conducted using scaled data from *in-vivo* investigations [137, 195, 221]. Inlet and outlet pressures and flow rates can be monitored at certain locations using transducers and flowmeters, respectively [195]. However, peri-model pressures cannot be measured as simply. Typical PIV analysis does not provide global pressures throughout the model. However, the static pressures may be reconstructed from PIV velocity profiles [222].

Inlet flow rates are generally set up using a pump to propel the fluid and a flowmeter to measure it [73, 104, 192, 205]. For pulsatile flow, a closed loop feedback control system can be necessary to correct the flow profile between cycles. The pressure of flow waveforms implemented in or across the phantom can vary depending on the pump system used. Yazdi, et al. [80] reviewed multiple flow circuit designs, and determined most investigations were carried out using a reciprocating piston pump driven by stepper motors to achieve a high-resolution control. However, pulsatile pumps can better mimic the full flow characteristics at specific regions of the arterial system. Haemodynamic mimicry can be achieved by dynamic similarity matching the *in-vitro* values to the measured *in-vivo* Reynolds and Womersley number [185]. While CFD studies can define complex inlet velocity profiles, the limitations of a physical setup mean that there is generally less flexibility in PIV inlet possibilities.

Appropriate pulsatile waveforms can be difficult to produce accurately without access to feedback control mechanisms and the appropriate expertise. As such, some PIV studies are carried out under steady flow conditions [57, 140, 200]. Steady state flow has been useful to determine the changing porosity effects on intra-aneurysmal flows [200]. However, steady flow conditions can also limit clinical applicability of results as acceleration and deceleration during the cardiac cycles potentially affect the momentum forces and haemodynamic states. For WSS evolution, OSI, and some vortices formation, steady flow simulations yield inaccurate characteristic behaviours [98].

Outlet pressures are commonly controlled by a head tank producing back pressure, indicative of the downstream resistance to flow [80, 137]. Deplano, et al. [195] produced a downstream Windkessel effect using compliance chambers and resistance valves. However, outlet flow is not commonly controlled, rather measured. Outlet flow behaviour is a key area for development in PIV.

#### *3.5.2.2. PIV Boundary Wall Conditions*

Compliant phantom fabrication techniques have been utilised since 1990 [197]. However, due to difficulty of fabrication, researchers will commonly opt to use an effectively rigid model that can limit the clinical relevance of results. Rigid PIV will commonly compare well with CFD investigations that equally use rigid assumptions [104, 165]. While artery-stent dynamics are difficult to measure with rigid phantoms, the effects of the stent struts on the peri-stent region can be observed. Hence, rigid PIV can be suitable, depending on the parameters that are being measured. In contrast to the anisotropic mechanical properties of arteries [223], the properties of Sylgard 184 and many other elastomers are isotropic [224]. However, Weizsacker and Pinto [223] investigated the properties of rat carotid arteries and determined the elasticity of arteries can be assumed as incrementally isotropic considering the range of deformations that occur *in-vivo*. To date, no known studies have successfully modelled the anisotropy of arteries in silicone.

PIV can be carried out using generalised or patient-specific geometries [112, 165]. Patient specific geometry can be expensive to obtain and the resulting phantom difficult to manufacture. Consequentially PIV results can require more time to obtain than rigid CFD studies of equivalent geometry. PIV often uses idealised geometries to simplify the modelling and experimental analysis [119, 186, 200]. Hütter, et al. [96] compiled data from MRI scan images and CT scans of the human thoracic aorta and provided an idealised geometry for PIV experimentation [186, 196]. Bouillot, et al. [198] used an idealised geometry of a saccular intracranial aneurysm to investigate the effects stenting had on intra-aneurysmal flow and determined that even highly porous stent meshes would help to direct flow. However, the directed flow was highly sensitive to porosity changes. Studies have also been carried out on an idealised carotid artery [73] and aorta geometries [114, 220, 225].

### 3.5.3. Working Fluid

Newtonian fluids such as water or the aqueous-glycerine mixtures often used in PIV have a constant viscosity across all shear rates [93, 95]. In contrast, non-Newtonian fluids have a viscosity that is dependent on shear rate [93]. As noted in Section 1.2.**,** blood becomes noticeably non-Newtonian in smaller arteries when the concentration of red blood cells is greater than 10% [22]. This occurs at low shear rates when a rouleaux forms with the aggregation of the red blood cells. However, in arteries with a large internal diameter, blood behaves similar to Newtonian fluids [22]. The viscosity of blood decreases as the shear rate increases [226], a phenomenon referred to as shear thinning. CFD is capable of modelling non-Newtonian fluids such as blood [168, 227]. Meanwhile, Newtonian fluids are typically used for PIV modelling despite blood being a non-Newtonian fluid for shear rates below 100 $s^{-1}$ [73, 80, 228].

In CFD, different models have been used in studies to model the Newtonian and non-Newtonian fluid behaviour. Navier-Stokes equation solvers are used for modelling Newtonian fluids [229]. The power law is commonly used to model non-Newtonian fluid in straight geometries [230]. ‘Casson’, ‘Ballyk’ and ‘Carreau-Yasuda’ are typical non-Newtonian models that have been used to model blood shear thinning behaviour in CFD studies [130, 229-231]. These models exhibit a yield stress followed by a non-linear relationship between the shear stress and shear rate [93]. Arzani [229] investigated the comparison between non-Newtonian and Newtonian modelling of blood within two aneurysms, an intracranial aneurysm and an abdominal aorta aneurysm. Results between the Newtonian model and the non-Newtonian model were similar except in regions of low shear rate where rouleaux formed within an aneurysm [229]. Arzani [229] suggested that the Newtonian model is likely to be appropriate for haemodynamic simulations in aneurysm except in the specific case of rouleaux formation within the aneurysm.

In PIV, non-Newtonian studies are not common, however a few have been carried out. Friedman, et al. [232] carried out a study on an aortic bifurcation investigating the intimal thickness response to increasing shear rates. The study used sodium thiocyanate as a Newtonian solution and sodium thiocyanate with additional 0.13 percent (by weight) Separan AP-30 to achieve a non-Newtonian solution. Both fluids produced similar results that intimal thickness increased with the shear rate. The lack of significant differences across the Newtonian and non-Newtonian fluid may be the result of using a normalised shear rate [232]. The lack of difference may also be due to the size of an aorta. Being a large artery, the ratio of artery diameter to red blood cell diameter is sufficiently large that the fluid effectively becomes Newtonian [4]. Typically, an aqueous-glycerine solution will be used in PIV modelling [80, 106, 137, 232]. A ratio of 60/40 water to glycerine has a similar viscosity to blood but poor refractive index matching with many transparent elastic polymers [81]. Meanwhile, a ratio of 40/60 water to glycerine has a viscosity almost three times that of blood but matches the refractive index of typical polymers [185]. A high viscosity can affect the allowable scaling of a model. Scaling a compliant *in-vitro* model up by 1.5× can increase the flow rate by a factor of nearly five, using Reynolds scaling (Equation 2.12). Though the velocity field similarity is preserved, using Reynolds matching, the 5× increase in fluid flow will not preserve pressure similarity between *in-vitro* and *in-vivo* models. The increased viscosity also affects the Womersley number, (Equation 2.13), used to accurately scale for an appropriate time period, potentially requiring wave periods that cannot be produced by typical pump systems. On occasion, salts such as sodium thiocyanate and potassium iodide, or urea may be used in conjunction with aqueous glycerine to increase the fluid refractive index without significantly increasing viscosity [81].

CFD is advantageous for modelling blood flow as it does not require an analogous fluid to be used. However, it still is highly dependent on the appropriate fluid parameters and fluid models being used.

PIV cannot use blood as a working fluid due to the need for optical transparency, and therefore is reliant on analogous transparent fluids. However, there has been sufficient work on determining appropriate fluid analogues, and dynamic matching to allow reasonable physiological relevance.

## 3.6. Summary

*In-silico* modelling through CFD provides investigators with the ability to view the internal haemodynamics of a stented artery. However, CFD is often limited by the complexity of moving meshes. As such, CFD studies typically fail to identify the FSI occurring at inlets and outlets of stented arteries and walls of both non-stented and bare metal stented arteries. *In*-vitro modelling by PIV surpasses CFD when investigating FSI for non-stented arteries and when examining interactions at inlets and outlets for stented arteries. PIV has also been successful in modelling the effects of stenting on intra-aneurysmal flow. However, optical requirements have hindered PIV investigations into the internal haemodynamics of a stented artery. The manufacture of optically transparent stent grafts is highly uncommon and a very recent development. PIV investigations between rigid and compliant non-stented phantom models have highlighted the importance of compliance matching on identifying pivotal haemodynamic changes such as estimation of WSS and vortices formation. However, CFD has highlighted the importance of stent strut design on near wall flow which can significantly affect the inflammatory response of endothelial cells. CFD does not rely on the use of a transparent blood analogue, therefore, is not limited by fluid mechanic scaling parameters, unlike PIV.

CFD and PIV have been used with varying degrees of success to determine haemodynamics in arteries and how implementing stents can improve flow. CFD and PIV platforms are able to examine the effects of stenting without risk to human life, allowing for safer design investigation before deployment. However, factors such as the effect of compliance mismatch between stent and artery and the effects that stents have on arteries outside of the stented region has not been adequately researched. Continued improvement in CFD, PIV, and other velocimetry modalities will provide improved prediction of the efficacy of candidate stents.

# *4. Literature survey for in-vivo Reynolds and Womersley Numbers of various arteries and implications for compliant in-vitro modelling*

A pivotal limitation of compliant *in-vitro* modelling is due to difficulty finding the appropriate information to use to model major arteries. The purpose of this chapter was to compile Reynolds and Womersley Numbers for 14 of the major arteries within the human body for ease of access and to highlight key paucities in information. Case studies of a large and a small artery, respectively, determined the optimal experimental design for optical measurement with respect to applying the Reynolds and Womersley Numbers. An adaptation of this chapter is currently under review at Annals of Biomedical Engineering.

## 4.1. Introduction

### 4.1.1. Background

Research on the long-term effects of surgical repair for many forms of cardiovascular disease has led to ambiguous outcomes [233]. Optical *in-vitro* experimentation is a growing research domain for cardiovascular disease modelling [80, 234]. Optical measurement methods such as Particle Image Velocimetry (PIV) or injection dye tracing allow for the *in-vitro* investigation of haemodynamic behaviour in analogous arteries and stenting [80]. PIV and injection dye tracing methods allow representative haemodynamic effects to be captured in life-like models of human arteries. The methods can also be used to predict how repair methods such as stenting or valve replacements affect arteries. Optical *in-vitro* experimentation does not typically use biological materials and therefore does not have the ethical obstacles that *in-vivo* animal or human studies have.

The outcomes of optical analysis are limited by the suitability of the experimental conditions utilised. This is particularly important in haemodynamic modelling as the fluid structure interaction is a key element of the fluid dynamics. In particular Geoghegan et al. found that the rigid-wall assumption led to a 61% over-estimate of maximum relative wall shear stress estimation at peak systole [73]. Improving *in-vitro* modelling methods to better represent *in-vivo* conditions can provide a safer platform for haemodynamic investigation and cardiovascular implant testing prior to human trials and present a validation method to further develop computational or numerical models and simulations [80].

### 4.1.2. Reynolds and Womersley Number *in-vivo*

*In-vitro* modelling often uses dimensionless scaling of fluid parameters to ensure dynamic similarity between the experiment and the physiology represented. Section 2.7 provides detailed description on how dynamic similarity is achieved. In summary, the Reynolds Number ($Re$ – Equation 2.12) can be used to model the viscous and momentum effects in haemodynamics, whereas the Womersley Number ($Wo$ – Equation 2.13) can match the time-dependent (pulsatile) behaviour in order to provide clinical significance to the experiment.

The Reynolds number is used to quantify the ratio of inertial fluid forces to viscous fluid forces. Therefore, the Reynolds Number determines the velocity ($V$ [$\mathrm{m \cdot s^{-1}}$]) or flow rate ($Q$ [$\mathrm{m^3 \cdot s^{-1}}$]), that the experimental working fluid (blood substitute) must achieve to allow dimensional similarity, given the differences in kinematic viscosity ($\nu$ [$\mathrm{m^2 \cdot s^{-1}}$]) between the experimental working fluid and blood. Similarly, Womersley number matching ensures the oscillatory behaviours (at frequency $f$ [Hz]) are also kinematically and dynamically matched. Other dimensionless parameters exist such as the Strouhal Number and Euler Number, however these metrics are not commonly used to determine experimental conditions. The Strouhal number is a function of Reynolds and Womersley Numbers, so will be matched if Reynolds and Womersley are matched. The Euler number represents the pressures, which are less important than wall shear stress in disease development, and wall shear stress is determined by Reynolds and Womersley.

The haemodynamic pressure and flow rate waveforms change throughout the body [22]. *In-vitro* analysis of arteries is typically segmental, meaning the cardiac waveform for the specific artery being analysed must be isolated. In haemodynamic modelling, it is important to determine the Reynolds and Womersley Numbers for each specific artery to enable dimensional similarity between the *in-vivo* artery and *in-vitro* model. However, there is no large, current, and publicly available data bank with the Reynolds Number and Womersley Number ranges for the main arteries in the human body. As such, finding these parameters for arteries is not always possible. Canine data has been compiled [4]. However, canine Reynolds and Womersley Numbers are not necessarily indicative of human numbers [235] and using canine waveforms in human geometry may not preserve the clinical significance of *in-vitro* experimentation. Some studies also have also used parameters for porcine arteries due to their physiological similarities to human arteries [236].

### 4.1.3. Compliant Phantoms *in-vitro*

Optical *in-vitro* modelling methods are continually improving with new flow circuits designs and production of more complex and representative arterial geometries. Compliant modelling is increasingly being used as studies have shown the importance of compliance in arteries such as the carotid, brachiocephalic and the aorta [74, 95, 137, 191, 205, 209]. Rigid modelling has a tendency to over-predict wall shear stresses and under-predict recirculation [73, 95]. Both flow characteristics can have a significant effect on the growth patterns of the endothelial cells that line the artery and therefore on the regeneration of the artery [64, 113, 175]. Thus, compliant artery models may provide a method of safe investigation into the potential for deleterious flow behaviours caused by candidate stents.

However, optical modelling techniques require optically transparent materials for phantom artery manufacture to capture fluid flow. Hence, *in-vitro* phantom materials are typically optically transparent [80]. The most common elastomer used in *in-vitro* arterial modelling is Sylgard 184 (Dow Corning, Midland, MI., USA) [74, 80, 237]. Sylgard 184 has a Young's Modulus of 1.32 MPa when cured at 23°C. However, the Young's modulus of Sylgard 184 does not match the Young's modulus of thoracic arteries (typically 0.526 to 0.700 MPa [96]). Hence, the *in-vitro* phantoms must be normalised compliance matched to the *in-vivo* arteries (Equation 2.16).

Compliant model construction is limited by manufacturability of phantom arteries with suitable wall thickness. To date, a phantom artery with a 1 mm (±10%) wall thickness represents the smallest consistent wall thickness reported [95]. Thinner walls tend to have higher proportional wall variability and are prone to uneven expansion or rupture [95]. To achieve appropriate wall thicknesses within fabrication limitations, models typically have to be scaled up to greater than life-scale. Scaling up the phantom requires scaling up the flow rate of the working fluid (commonly aqueous). Increasing flow may also increase pressure demands which may not be a cost-effective solution for experimental models of large arteries, such as the aorta. Rigid-wall models are not dependent on the lower limit of wall thickness manufacturability and therefore can readily be manufactured at life-scale or smaller for more cost-effective experimentation.

### 4.1.4. Working Fluid Analogues

The working fluid presents another design limitation of experimental modelling using a compliant phantom. The working fluid must be transparent and refractive index matched to the elastomer used in the phantom. Refractive matching removes light distortion through a model, thereby making the model almost invisible when filled with the working fluid (Figure 2.4). The most common mixture used is a water-glycerine solution [30, 173]. The mixture is easily maintained and reasonably inexpensive (glycerine costing \$21.08 USD per kilogram). However, the kinematic viscosity of the popular 40/60 water-glycerine ratio is nearly three times that of blood (Table 4.1). Occasionally, sodium iodide is included in an aqueous glycerine mixture to raise the refractive index without significantly raising the viscosity. However, sodium iodide has a high cost of around \$320 USD per kilogram and some associated health risks [81]. Another alternative uses urea to raise the refractive index of a water and glycerine mixture while maintaining a similar viscosity to blood. Urea is significantly cheaper, costing $19.80 USD per kilogram and has a lower health risk rating [81].

*Table 4.1: Properties of transparent blood analogues (W = water, Gly = glycerine, NaI = sodium iodide, U = urea)*

| **Fluid** | **Density $\rho$ [kg.m$^{-3}$]** | **Dynamic Viscosity $\mu$ [$\times 10^{-3}$ Pa·s]** | **Kinematic Viscosity $\nu$ [$\times 10^{-6}$ m$^2$·s$^{-1}$]** | **Refractive index** | **Cost per KG (US $) +** |
|---|---|---|---|---|---|
| **Blood** | 1060 | 3.80 | 3.58 | Opaque | N/A |
| **40/60 W-Gly [80]** | 1156 | 10.8 | 9.34 | 1.41 | 12.83 |
| **46/29/25 W-Gly-U [81]** | 1130 | 3.56 | 3.15 | 1.41 | 11.00 |
| **46/29/25 W-Gly-NaI [81]** | 1229 | 3.12 | 2.53 | 1.41 | 86.10 |

+ Prices obtained from Carolina Biological Supply Company (NC, USA), laboratory grade

## 4.2. Methodology

### 4.2.1. Part 1: Literature Search

A literature search was conducted on the peak Reynolds and Womersley numbers of 14 key arteries in the human body: ascending aorta, aortic arch, descending aorta, suprarenal aorta, infrarenal aorta, common iliac, femoral, brachiocephalic, subclavian, carotid, renal, superior mesenteric, basilar and internal carotid arteries (ICA). The peak Reynolds Number was selected for investigation, as it indicated the maximum flow rate that must be achieved to maintain physiological accuracy. Multiple search engines were used including Google Scholar, ResearchGate and PubMed. “Reynolds Number”, “Womersley Number”, “In-vivo” and each of the 14 arteries were used as keywords for each search. Of these only 10 articles provided novel *in-vivo* information specific to the human body. Ranges for the peak Reynolds and Womersley numbers were collected from *in-vitro* or *in-silico* sources when an *in-vivo* source could not be found. In the absence of *in vivo* data, the *in-vitro* and *in-silico* sources were accepted provided that the outputted data values were obtained using *in-vivo* inputs. *In-vitro* and *in-silico* data was also compared against the *in-vivo* ranges of peak Reynolds and Womersley number values for sections of the aorta. The overall number of sources found with information on the peak Reynolds number and Womersley number was 21. Data was compiled by type and the range of peak Reynolds and Womersley Numbers were averaged (Table 4.4). The standard deviation calculation for the Reynolds number was weighted according to the overall population of each source and provided as a range in Table 4.4. Symmetry was assumed between left and right variants of the common iliac, femoral and subclavian arteries. In reality, there are geometric, flow and, therefore Reynolds and Womersley number differences across the left and right variants of these arteries. However, the intra-artery differences were assumed negligible compared to the inter-artery differences.

### 4.2.2. Part 2: Case Studies

Two case studies were carried out comparing three working solutions against different scale models manufactured from Sylgard 184. The first case study investigated *in-vitro* modelling an ascending aorta geometry. The ascending aorta is the largest, most compliant artery in the human body and is subject to the highest Reynolds and Womersley numbers in the arterial system (Table 4.4). These factors make it difficult to mimic *in-vitro*.

The second case study focuses on the left common carotid artery. This artery was selected as it is much smaller and less compliant than the ascending aorta, but also had a good basis of *in-vivo* information available to inform the model. Though it is not smallest artery considered, it represents the other end of the spectrum for modelling compared to the ascending aorta. The *in-vivo* geometry parameters and compliance ranges used for the case studies of each artery are provided in Table 4.2.

*Table 4.2: Structural parameters for the in-vivo ascending aorta and left common carotid artery*

| | **Young's Modulus [MPa]** | **Average Diameter at rest [mm]** | **Normalised Compliance Range [MPa$^{-1}$]** |
|---|---|---|---|
| **Ascending aorta** | 0.526 | 32.0 [154] | 29.0 – 37.7 |
| **Left Common Carotid** | 0.700 | 8.00 [96] | 16.8 – 19.3 |

Normalised compliance as a function of wall thickness was calculated for Sylgard 184 silicone using the diameter provided in Table 4.2 at 1x, 1.5x and 2x life scale for the ascending aorta and 1x, 3x and 5x life scale for the common carotid artery (Equation 2.16). The curves were then plotted against known compliance ranges of the two arteries [3]. The curves were analysed to determine which scales were or were not capable of being manufactured using Sylgard 184. 1 mm was assumed to be the minimum manufacturable wall thickness as this is the smallest consistently manufactured wall thickness using lost-core casting seen in the literature to date [95].

The optimal *in-vitro* model configuration was selected as the model with the lowest required pump power. The power was inferred based on flow rate and time requirements for physiological matching. The Reynolds and Womersley numbers were linked using diameter (*D*) and kinematic viscosity (*v*). Four equations were produced, as shown in Table 4.3.

*Table 4.3: Equations 4a-d formation*

| | **Eliminating diameter** | **Eliminating viscosity** |
|---|---|---|
| **Rearrange $Re$ (Eq. 2.12)** | $\rightarrow D = \frac{4Q}{\pi Re \nu}$ | $\rightarrow \nu = \frac{4Q}{\pi Re D}$ |
| **Substitute into $Wo$ (Eq. 2.13)** | $Wo = \frac{2Q}{\pi Re \nu}\sqrt{\frac{2\pi f}{\nu}}$ | $Wo = \frac{D}{2}\sqrt{\frac{2\pi^2 f Re}{4Q}}$ |
| **Rearrange for $Q$** | $Q = \sqrt{\frac{Wo^2 Re^2 \pi \nu^3}{8f}}$ | $Q = \frac{\pi^2 f Re D^3}{8Wo^2}$ |
| **Optimise for the largest range produced Equation 4.1a-d** | (a) $Q = \sqrt{\frac{Wo_{max}^2 Re_{max}^2 \pi \nu^3}{8f}}$ | (c) $Q = \frac{\pi^2 f Re_{max} D^3}{8Wo_{min}^2}$ |
| | (b) $Q = \sqrt{\frac{Wo_{min}^2 Re_{min}^2 \pi \nu^3}{8f}}$ | (d) $Q = \frac{\pi^2 f Re_{min} D^3}{8Wo_{max}^2}$ |

The four equations were plotted in Figures 4.3 and 4.5 for each working solution viscosity (Eq. 4.1a-b) and scale diameter (Eq. 4.1c-d).

Blood was assumed Newtonian in the ascending aorta as the concentration of red blood cells in the bloodstream was less than 10% [22]. Non-Newtonian blood analogues were ignored in this study as the primary focus was on determining a method to model the largest and most compliant artery in the human body, and the effects of shear thinning are significant predominantly in smaller arteries where the concentration of red blood cells exceeds 10% of the overall fluid [22].

## 4.3. Results

### 4.3.1. Part 1: Literature Search

The ranges for the minimum and maximum peak Reynolds and Womersley numbers for each of the 14 arteries were combined and reported in Table 4.4 along with their data type and source. There was a larger pool of primary sources to collect information from for the segments of the aorta. However, there was very limited information on the smaller arteries such as the femoral, renal and superior mesenteric. The *in-vivo* Reynolds numbers for the sections of the aorta were typically reported higher than those used in *in-vitro* or *in-silico* studies, meanwhile the Womersley Numbers were typically lower.

*Table 4.4: Reynolds and Womersley Numbers for 14 key arteries. Light grey = inferred values based on surrounding data.*

| **Artery** | **Min Re$_{peak}$** | **Min Re$_{peak}$ Range (1 S.D.)** | **Max Re$_{peak}$** | **Max Re$_{peak}$ Range (1 S.D.)** | **Min Wo** | **Max Wo** | **Data type** | **Sources** |
|---|---|---|---|---|---|---|---|---|
| **Ascending Aorta** | 3144 | 1357 | 6836 | 1570 | 15.0 | 20.6 | *In-vivo* | [167, 238-241] |
| | 2970 | | 3302 | | 19.3 | 22.7 | *In-vitro* and *In-silico* | [15, 154, 242-244] |
| **Aortic Arch** | 3318 | 176 | 5733 | 1102 | 13.3 | 17.2 | *In-vivo* | [239, 245] |
| | 2431 | | 2666 | | 14.5 | 15.9 | *In-vitro* and *In-silico* | [154, 246, 247] |
| **Descending Aorta** | 2728 | 867 | 4805 | 289 | 11.2 | 14.2 | *In-vivo* | [238-240] |
| | 1169 | | 2196 | | 11.1 | 15.9 | *In-silico* | [154, 242] |
| **Suprarenal Aorta** | 2000 | N/A | 6000 | N/A | 12 | 12 | *In-vivo* | [238] |
| **Infrarenal Aorta** | 1324 | 403 | 3536 | 1063 | 12 | 12 | *In-vivo* | [238, 248] |

| | | | | | | | | |
|---|---|---|---|---|---|---|---|---|
| **Common Iliac** | 390 | N/A | 620 | N/A | 7.7 | 12 | *In-vivo* | [248] |
| **Femoral** | 980 | | 980 | | 7.74 | 7.74 | *In-vitro* | [249] |
| **Brachiocephalic** | 720 | N/A | 1080 | N/A | 8.2 | 9.8 | *In-vivo* | [240] |
| **Subclavian** | 720 | N/A | 880 | N/A | 6.8 | 8.1 | *In-vivo* | [240] |
| **Common Carotid** | 556 | 129 | 716 | 72 | 5.66 | 6.46 | *In-vivo* | [240, 250] |
| | 750 | | 766 | | 4.51 | 4.51 | *In-vitro* and *In-silico* | [15, 251, 252] |
| **Renal** | 277 | N/A | 900 | N/A | 6.6 | 6.6 | *In-vitro* | [253] |
| **Superior Mesenteric** | 12 | N/A | 200 | N/A | 5.27 | 5.27 | *In-silico* | [242, 254] |
| **Basilar** | 150 | N/A | 500 | N/A | 2.73 | 2.73 | *In-vivo* | [255] |
| **ICA** | 150 | N/A | 300 | N/A | 5.33 | 5.33 | *In-vivo* | [255] |

Figure 4.1 presents the tabulated *in-vivo* data. Where *in-vivo* data was not available *in-vitro* or *in-silico* measurements were plotted (as accepted in Table 4.4). The proximal arteries such as sections of the aorta had significantly higher Reynolds and Womersley numbers. The reported *in-vivo* ranges were also much larger than distal arteries showing that inter-patient variability must be higher in the larger, more compliant, arteries. However, the variability may also be a function of the higher number of studies reporting on larger arteries.

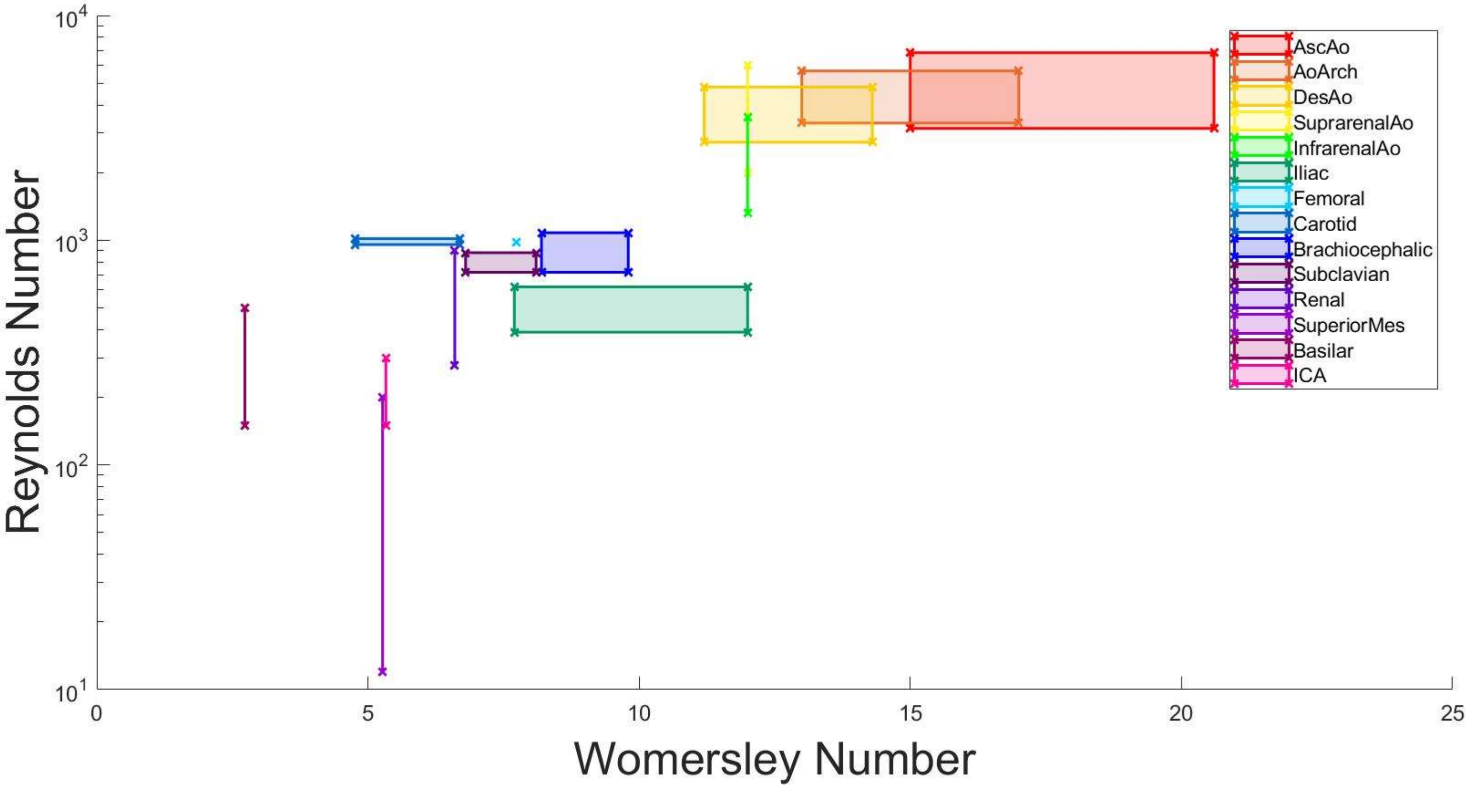

*Figure 4.1: Reynolds and Womersley for 14 main arteries*

### 4.3.2. Case Study: 1 – Ascending Aorta

The compliance for each scale model manufactured from Sylgard 184 was calculated based on the wall thickness and the diameter scale. Figure 4.2 shows that a life scale model cannot be reliably manufactured to match the compliance of the human ascending aorta, as it falls below the minimum wall thickness requirement of 1 mm. However, both 1.5x and 2x life scale models can be reliably manufactured.

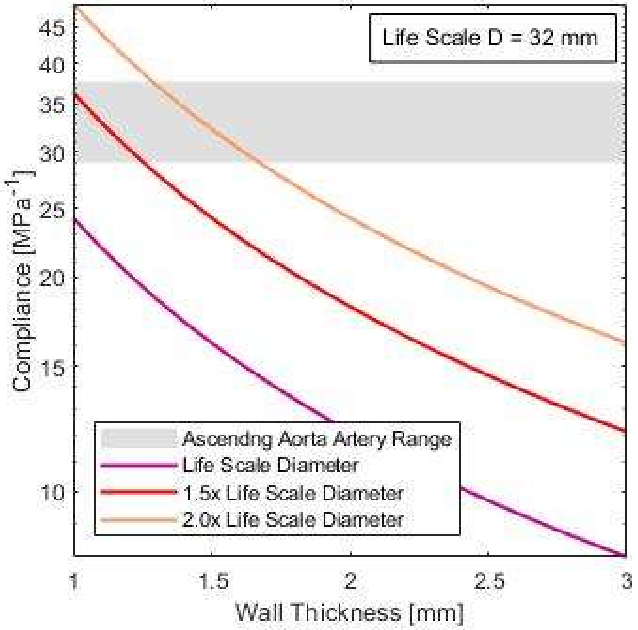

*Figure 4.2: Model compliance for variable wall thickness of Sylgard 184 for different scales of the ascending aorta diameter*

Three potential working solutions were investigated to determine the flow rate and frequency requirements to achieve known ranges of peak Reynolds and Womersley Numbers for each of the feasible model scales identified in Figure 4.2. The lines of the Figure 4.3 denote fixed diameter curves and fixed viscosity curves for the maximum (solid lines) and minimum (dashed lines) Reynolds and Womersley numbers. The domain between the intersections of these curves can generate a range within which the Reynolds and Womersley numbers are representative of the ascending aorta (Figure 4.3). Six allowable ranges were identified, represented by the shaded boxes. Figure 4.2 indicates that a 1.5x life scale model would require a peak flow rate of between 27 and 91 L·min$^{-1}$ using a water, glycerine and sodium iodide solution. However, significant overlap can be seen between the sodium iodide solution (green) and the urea solution (purple). To fit within the Womersley and Reynolds range of the ascending aorta, a 40/60 water-glycerine working fluid (blue) has a minimum flow rate of 53.5 L·min$^{-1}$ maximum flow rate of 178 L·min$^{-1}$ for the smallest manufacturable model (1.5x).

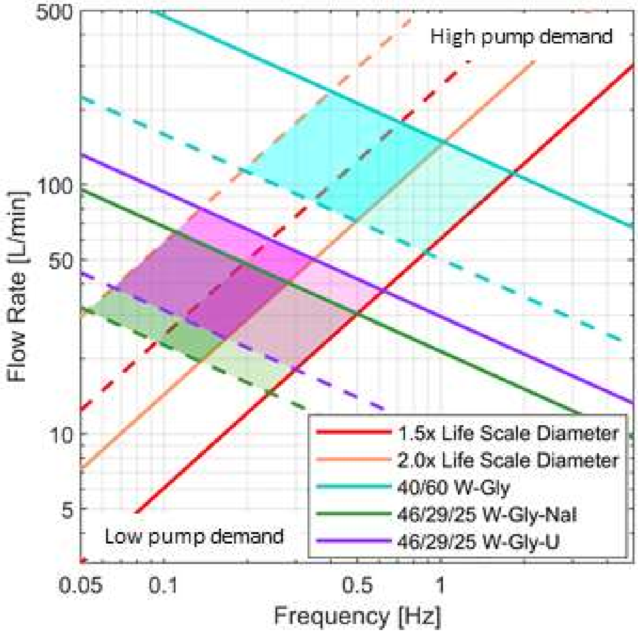

*Figure 4.3: Maximum (solid lines) and minimum (dashed lines) allowable flow rates and frequencies for comparison of ascending aorta model scales and working solutions for in-vitro experimental set-up (W = water, Gly = glycerine, NaI = sodium iodide, U = urea)*

### 4.3.3. Case Study: 2 – Left Common Carotid Artery

The compliance for each scale of the left common carotid artery is presented in Figure 4.4. A life scale model cannot be reliably manufactured to match the compliance of the common carotid artery. However, both 3x and 5x life scale models can achieve the common carotid artery compliance. The range of allowable wall thicknesses are presented in Table 4.5.

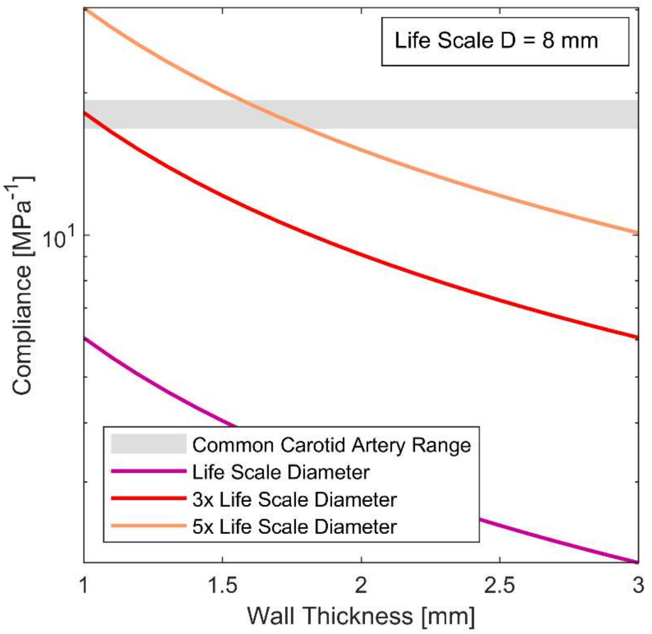

*Figure 4.4: Model compliance for variable wall thickness of Sylgard 184 for different scales of the common carotid artery diameter*

The three potential working solutions were reviewed for manufacturability to determine the potential setups for modelling a carotid artery *in-vitro,* highlighted by the shaded regions. Figure 4.5 indicates that increasing the life scale above 3x leads to a low flow pulse frequency and thus long cycle period. The peak flow rate of the water-glycerine solution (blue) was 13.7 L·min$^{-1}$ which was smaller than the lowest required flow rate for the ascending aorta model. The overlap between solutions is significantly less than for the ascending aorta model.

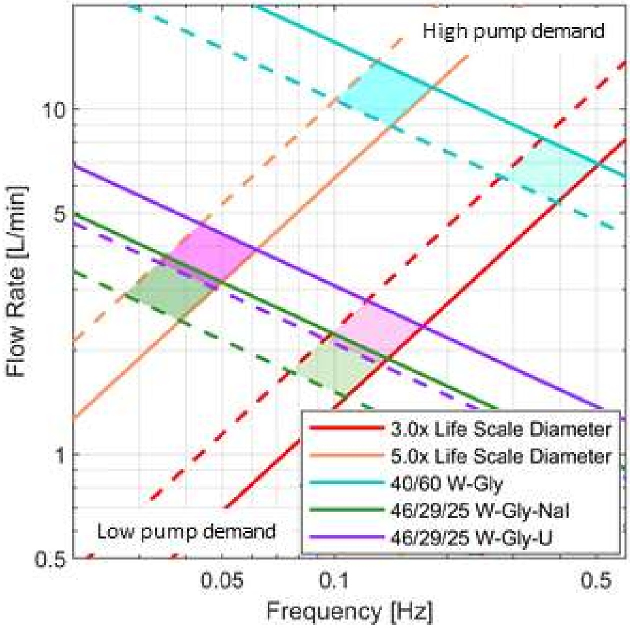

*Figure 4.5: Maximum (solid lines) and minimum (dashed lines) allowable flow rates and frequencies for comparison of common carotid artery model scales and working solutions for in-vitro experimental set-up (W = water, Gly = glycerine, NaI = sodium iodide, U = urea)*

### 4.3.4. Summary

The limits of wall thickness, and bounds of volumetric flow rate and pulse frequency, as determined in case study 1 and 2 for the ascending aorta and common carotid artery as summarised in Table 4.5. Where the criteria for manufacturability was not met, the entire column was greyed out and the remaining potential solutions discussed. Note that the wall thickness range captures the range of acceptable compliance values, and the flow rate and frequency ranges are representative of the reported Reynolds and Womersley ranges.

*Table 4.5: Summary of ascending aorta and common carotid artery case study outcomes. Greyed out boxes indicate non-achievable models.*

| | **Ascending Aorta** | | | **Left Common Carotid Artery** | | |
|---|---|---|---|---|---|---|
| | **1.0 x life scale** | **1.5 x life scale** | **2.0 x life scale** | **1.0 x life scale** | **3.0 x life scale** | **5.0 x life scale** |
| **Phantom Material** | | **Wall Thickness** | | | **Wall Thickness** | |
| **Sylgard 184** | < 1 mm | 1.0 – 1.3 mm | 1.3 – 1.7 mm | < 1 mm | 1.0 – 1.1 mm | 1.6 – 1.8 mm |
| **Working fluid** | | **Flow rate [L·min$^{-1}$]** | | | **Flow rate [L·min$^{-1}$]** | |
| **40/60 W-Gly** | | 53.5 – 178 | 71.4 – 237 | | 5.35 – 8.22 | 8.92 – 13.7 |
| **46/29/24 W-Gly-U** | | 18.1 – 60.2 | 24.2 – 80.2 | | 1.81 – 2.79 | 3.02 – 4.64 |
| **46/29/24 W-Gly-NaI** | | 14.6 – 48.5 | 19.5 – 64.7 | | 1.46 – 2.25 | 2.44 – 3.74 |
| **Working fluid** | | **Frequency [Hz]** | | | **Frequency [Hz]** | |
| **40/60 W-Gly** | | 0.345 – 1.830 | 0.194 – 1.029 | | 0.278 – 0.508 | 0.100 – 0.183 |
| **46/29/24 W-Gly-U** | | 0.117 – 0.620 | 0.066 – 0.349 | | 0.0942 – 0.172 | 0.0339 – 0.0619 |
| **46/29/24 W-Gly-NaI** | | 0.094 – 0.500 | 0.053 – 0.281 | | 0.0760 – 0.139 | 0.0274 – 0.0499 |

## 4.4. Discussion

### 4.4.1. Part 1: Literature Search

Precise and relevant experimental modelling of haemodynamic flow in human arteries is reliant on precise mimicry of *in-vivo* dynamic fluid properties and realistic fluid-structure interactions. A literature search for Reynolds and Womersley Numbers of 14 specific arteries in the human body showed a paucity of information for some arteries, despite their clinical interest. The Reynolds and Womersley numbers for various arteries have been complied for canines [4]. The values for smaller arteries have also been provided for other animals such as pigs, rabbits and horses [4]. However, precise clinical relevance relies on knowledge of human haemodynamic parameters. Table 4.4 shows that there was rich information on haemodynamics in each section of the aorta. The common carotid artery was also well researched. However, there was a lack of data regarding the arteries that branch from the aorta.

Many important arteries, such as the femoral, renal and superior mesenteric arteries did not yield any *in-vivo* Reynolds or Womersley number values. The lack of *in-vivo* information can make modelling impossible without assumptions that may not have been validated and therefore reduce the clinical applicability of the results obtained. The input data from *in-silico* and *in-vitro* studies were included when *in-vivo* data could not be located [133, 242, 248, 253]. Since the domains of these arteries shown in Figure 4.1 seem like sensible extrapolations from the Reynolds and Womersley numbers of proximal arteries, it was assumed these values should not necessarily be rejected. However, this may be expected as the *in-vitro*/*in-silico* numbers were derived as functions of *in-vivo* numbers. The Reynolds and Womersley numbers of the femoral, and superior mesenteric arteries are similar to similar sized arteries. However, the range of *in-vivo* values of the renal artery is comparably large. While these studies may provide a good indication of the likely Reynolds and Womersley, direct *in-vivo* validation would be preferable.

Search results for *in-vivo* Reynolds and Womersley numbers will commonly present canine data collated by Caro [4]. However, canines typically have lower Reynolds and Womersley numbers than human subjects. For example, searching "Abdominal Aorta Womersley number" on scholar.google.com will currently return *Wo*=8 as the result, linked to the 'Womersley number' Wikipedia page [256]. Following the citation path indicates that this Womersley number was determined for a canine abdominal aorta at 2 Hz, meanwhile the human abdominal aorta Womersley number is typically 12 (Table 4.4). Failing to note this discrepancy will lead to inappropriate dynamic matching and therefore unrepresentative results and recommendations from simulation and experimentation.

There were notable discrepancies between the measured *in-vivo* and selected *in-vitro* Reynolds and Womersley numbers. Table 4.4 shows that *in-vitro* and *in-silico* Reynolds numbers were typically lower than *in-vivo*. This discrepancy suggests that experiments tended to use lower flow rates than may be expected in reality. Achieving the appropriate flow rate may be difficult in large arteries such as the ascending aorta, particularly when using blood analogues that have a higher kinematic viscosity than blood. However, the Womersley number tended to be reported higher *in-vitro* and *in-silico* than *in-vivo*. The higher Womersley was most notable in the ascending aorta which may be accounted for by model scaling in *in-vitro* studies [74, 95]. The Womersley number is proportional to diameter (Equation 2.13), and therefore scaling models larger, without compensating for time period, leads to a higher Womersley number and lower Reynolds number. Typically, lower Reynolds numbers are accepted *in-vitro* due to the large range of potential peak Reynolds numbers presented across papers and the large standard deviations. In particular, Figure 4.1 indicates there is large variability in Reynolds numbers in the human aorta. However, the large range, may also be representative of the number of sources identified.

In some *in-vitro* and *in-silico* investigations, a time-averaged or mean Reynolds number was presented despite modelling pulsatile flow [119, 251]. The diameter of an artery or compliant model increases at peak systole and makes determining an accurate peak Reynolds number more difficult, and therefore providing the mean Reynolds may be more accepted. However, since the mean Reynolds number is 25-33% of the peak Reynolds, there may be a risk of characterising laminar flow when using the mean value, rather than the turbulent flow that is likely to occur at high Reynolds values [239]. However, some investigations purposely utilise steady-state conditions to determine the basic haemodynamic effects of cardiovascular implants [140, 200]. For example, Liepsch, et al. [253] showed that steady flows may identify some haemodynamic anomalies which are caused by features of the arterial geometry.

### 4.4.2. Part 2: Case Studies

The trend across Figures 4.2-4.5 is that increasing the scale of the model increases the wall thickness, flow rate and pulse frequency required to achieve a physiological model. The aorta is one of the more well studied arteries, as evident by the much high incidence of *in-vivo* information obtained (Table 4.3). However, as the case study of the ascending aorta indicates, sections of the aorta can be some of the hardest arteries to experimentally model when trying to achieve a compliance matched, physiological model. For an ascending aorta model, a life scale model cannot be manufactured from Sylgard 184 silicone. Sylgard 184 could be used to make a 1.5x – 2x life scale model of the ascending aorta or a 3x – 5x life scale model of the common carotid artery.

When modelling the ascending aorta, a water and glycerine working solution consistently required a volumetric flow rate 3x greater for than the urea or sodium iodide solutions for the same Reynolds number. The lowest allowable flow rate for the water and glycerine mixture had a 4.3% overlap with the highest flow rates allowable using the urea mixture. This means that a much higher pump power is needed for to achieve physiologically matched waveforms. Furthermore, frequencies of more than approximately 1 Hz is required for the water and glycerine mixture. The higher pulse frequency requires higher pump resolution to precisely match the input waveform. The working solution with sodium iodide has the lowest flow rate and lowest pulse frequency, irrespective of diameter. As a three-part working solution, it may be harder to maintain the solution long-term due to disproportionate evaporation rates. However, careful storage and maintenance of the solution could ameliorate this issue. Sodium iodide has associated health risks to consider and costs more than glycerine and urea (Table 4.1). There is a 66-67% overlap in the flow rates and a 73% overlap in frequency of the waveform between the sodium iodide and urea solutions to achieve the same Reynolds and Womersley numbers. This implies similar pump demands across the working fluids. The urea solution is a three-part solution with the same water, glycerine and salt ratio (by mass) as the sodium iodide solution. Urea also has a lower health risk than sodium iodide. As such it may be a suitable solution for modelling large arteries such as the aorta.

There was less overlap in the flow rates and frequencies for the different working solutions of the common carotid artery model. The urea and sodium iodide solutions only overlapped by 33% in flow rate and 47% in frequency. The peak flow rate for the sodium iodide solution was 3.74 $L \cdot min^{-1}$ for a model that is 5x life size and would require a time period of at least 20 seconds per waveform. A waveform with such a long time period would not be efficient for ensemble PIV measurement where multiple image pairs are required for temporal or spatial averaging [69]. For injection dye tracing, the slow flow, long waveform could be beneficial to capture high-resolution fluid motion. The urea solution could achieve the same Reynolds and Womersley numbers with a slightly higher flow and shorter period so may allow a more efficient experimental setup. The water and glycerine two-part mixture required a maximum flow of 13.7 $L \cdot min^{-1}$ for the 5x life scale model. Despite being over four times higher than the flow required for the sodium iodide solution, the flow rate is still lower than the smallest needed flow rate for the ascending aorta model. Thus, achieving flow rates required to model the common carotid artery is easier than the aorta. The waveform for the 5x life scale model required a time period of at least 5.46 seconds for Womersley matching. A 5.46 seconds waveform duration may be more suitable for experimental set ups that require high repeatability such as ensemble PIV analysis [69].

A water and glycerine working solution is an inexpensive, easily mixed and easily maintained two-part working solution that is refractive matched at a mass ratio of 40:60. However, for modelling the largest artery in the human body, the pump demands are high, and it is potentially difficult to achieve Reynolds and Womersley number matching (Figure 4.3). A trade-off between achieving Reynolds or Womersley number matching is often necessary when using water and glycerine solutions in models of large arteries. Whilst there are many pumping systems capable of achieving flows over 237 $L \cdot min^{-1}$, they rarely have the response time to change direction, accelerate and decelerate within the time period required to also meet acceptable Womersley number ranges. It may be possible to design and manufacture a piston pump with powerful enough actuators to provide the appropriate flow within required time period, however, changing the working solution would provide a more cost-effective solution.

### 4.4.3. Limitations

This chapter focused on three Newtonian transparent blood analogues. The water and glycerine two-part mixture is the most commonly used working fluid in *in-vitro* experimentation [74, 81, 95, 192] and sodium iodide is a common additive [81]. The three-part solution with urea is not as common. However, urea solutions are becoming more popular after Brindise et al. determined its behaviour is very similar to sodium iodide [81]. Non-Newtonian transparent blood analogues were not considered in this investigation as the focus was on experimental modelling of larger arteries. Non-Newtonian behaviour becomes more important when modelling smaller arteries or capillaries as the red blood cells are a greater portion of the fluid flow [22]. Transparent blood analogues that could not achieve a refractive index of 1.41 were also ignored as this is the common refractive index range for elastomers, and refractive index matching is required to avoid optical distortion in PIV experimentation and dye tracing.

## 4.5. Conclusions

A key limitation of *in-vitro* modelling of non-aortic arterial mechanics is the paucity of available literature on the *in-vivo* fluid parameters of many arteries. In this chapter, a literature search was carried out to identify and compile currently available haemodynamic properties for 14 arteries within the human body. The search determined the aorta and carotid arteries as have the largest amount of available data. Meanwhile smaller arteries rarely had more than one source for *in-vivo* information. This chapter highlighted the lack of information on smaller arteries while simultaneously compiling the currently available information in one accessible location.

Case studies of *in-vitro* investigations of a compliance matched ascending aorta (large artery) and common carotid (comparatively small artery) were used to identify some physical limitations when using optical modelling. These limitations include wall thickness fabrication and blood analogue transparency, refractive index and viscosity. Both the aorta and the carotid models required scaled models to enable precise phantom fabrication. Reynolds matching in the large aorta led to high experimental flow rates. The aorta, in particular, would require a significant pump demand. A cost-effective solution for modelling the aorta was using a three-part water, glycerine and urea solution in a 1.5x life-scale model. Meanwhile, for modelling the common carotid, a two-part, water and glycerine mixture could be used in a 3x life-scale model.

# 5. *PIV Analysis of Haemodynamics Distal to the Frozen Elephant Trunk Stent Surrogate*

This chapter describes the capture of the development of a Type 1B endoleak due to the implementation of the Frozen Elephant Trunk (FET) stent. PIV measurement has not previously been utilised to capture a Type 1B endoleak develop. The methods focus on the manufacture of a compliant phantom artery and surrogate stent used for experimentation and on the experimental set up. The results identified some potential deleterious flow behaviour caused by the surrogate stent implantation. Recirculation occurred at the distal edge of the stent and may indicate the potential for long term intimal layer inflammatory issues such as atherosclerosis. The identification of the Type 1B endoleak proved that *in-vitro* modelling can be used to investigate complex compliance changes and wall motions. The content of this chapter has been published in the Journal of Cardiovascular Engineering and Technology [74].

## 5.1. Background

In Sections 1.4.2 and 1.4.3., two key forms of CVD were introduced, aortic aneurysm and aortic dissection. Aortic aneurysm and dissection are particularly dangerous forms of CVD as all oxygenated blood passes through the aorta while being transported to various tissues and organs. Abnormal aortic haemodynamics can lead to devastating consequences.

The Frozen Elephant Trunk (FET) stent is a hybrid-prosthesis combining the features of a conventional vascular prosthesis and a stent graft (Figure 5.1) [6]. The FET stent may be implemented in the event of an aneurysm or dissection of the aortic arch or superior region of the descending aorta. The FET stent has been specifically designed to accommodate the brachiocephalic trunk, left common carotid artery, and left subclavian artery which branch from the aortic arch. The mean age of recipients of the FET stent is 56.5 ± 13.6 years of age which is reasonably young for this class of implant [5].

Stent implantation via a median sternotomy has a high success rate [257, 258]. A median sternotomy is a surgical procedure in which a vertical inline incision is made along the sternum following which the sternum itself is opened [259]. Peri-operative mortality during FET implant is 7% [6] which is lower than the 8.9% (1st stage) and 7.7% (2nd stage) for conventional aortic aneurysm reconstruction procedure [260]. Hence, given the lower mortality rates, less invasive FET stent placement is becoming an attractive method for aortic aneurysm and dissection repair.

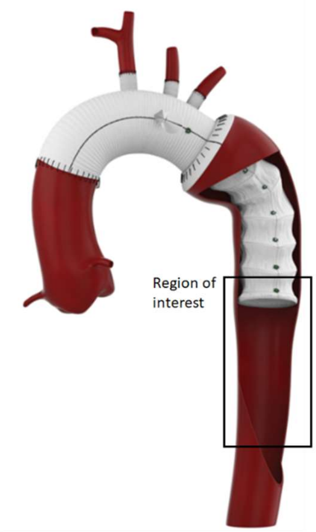

*Figure 5.1: Frozen Elephant Trunk stent in the descending aorta (from Di Bartolomeo, et al. [261]). Region of interest indicated*

FET stents are generally sutured to the proximal aorta close to the efferent arteries and have a friction grip at the distal end [6]. Due to variance in arterial diameter, the friction grip can fail and cause flow between the arterial wall and stent graft interface. Such flow is called a Type 1B endoleak [6]. The type 1B endoleak leads to deleterious outcomes caused by the rubbing of the stent graft on the artery wall and the increased arterial pressure in a region that has previously had an aneurysm [262]. Ultimately, the failure of the distal friction grip can cause recurrence of the aneurysm which may be fatal without surgical remediation.

In this chapter, PIV was utilised to identify and observe the haemodynamics that occur around a rigid FET surrogate. The modelling will focus on the effect of the flow behaviour on the arterial geometry distal to the FET stent. The FET stent can be 24 times more radially stiff than the human aorta [6]. The increased rigidity reduces the ability of the aorta to dampen peak pulsatile pressures. In particular, systolic pressure in the FET stent are high as the aortic arch cannot expand to accommodate a portion of the stroke volume. Hence, the normal haemodynamics of the descending aorta can be significantly altered and are worth investigating.

As identified in Chapter 3, the mismatch between a radially compliant artery and a radially rigid stent have not been extensively analysed *in-vitro* or *in-silico,* despite an understanding that it will affect fluid flow behaviour. Compliant PIV was used to capture fluid/solid interaction (FSI). Small changes in the compliance of a model can have notable changes in fluid and lumen wall pressure distributions, pulse wave velocity and blood velocity [73, 192]. Unjustified rigid assumptions may also result un-representative vortex formation [192]. Hence, when modelling the transition from the radially rigid FET stent to the compliant descending aorta, compliant PIV is necessary. In this study, haemodynamics distal to the stented lumen were analysed using an optically transparent, compliant phantom and PIV modelling techniques.

## 5.2. Method

### 5.2.1. Geometry of Stented Model

An idealised compliant geometry of the descending aorta was designed using dimensions obtained by a meta-analysis of reported descending aorta geometric parameters [96]. The geometry was compliance matched as per the normalised compliance formula (Equation 2.16) in Section 2.8.1. Compliance matching required the geometry to be scaled up 50% to achieve a 1 mm wall thickness

(Figure 5.2). The phantom was manufactured using PDMS silicone elastomer (Sylgard 184, Dow Corning) with a 10:1 cross-linking agent.

Using Equation 2.16, the mechanical properties of Sylgard 184 and the *in-vitro* artery led to the calculation of scaled phantom wall thickness shown in Table 5.1.

*Table 5.1: Healthy descending aorta geometry*

| **Descending Aorta** | ***In-vivo 1.0 x life*** | ***In-vitro 1.5 x life*** |
|---|---|---|
| ***E* [MPa]** | 0.40 – 1.07 | 1.32 (silicone) |
| ***h* [mm]** | 1.16 – 1.20 | 1.0 |
| ***D* [mm]** | 18.3 – 25.0 | 27.5 |
| ***C* [$MPa^{-1}$]** | $14.8 \times 10^{-6}$ – $53.9 \times 10^{-6}$ | $20.8 \times 10^{-6}$ |

There is a large range for the arterial wall compliance shown in Table 5.1 [96]. A conservative approach was taken in selecting a compliance of $20.8 \times 10^{-6}$ $MPa^{-1}$. Arterial walls typically stiffen with aging and older patients have a higher incidence of stent implementation [263]. Selecting a phantom wall compliance from the lower end of the range would ultimately lead to a smaller potential for observation of the Type 1B endoleak. This ensured the conditions utilised could not be considered cynically motivated such that an observation of the endoleak occurred.

The physical FET stent has a constant internal diameter from inlet to outlet. The stent is manufactured with diameters ranging between 20 – 40 mm. The total length of the graft Is 180 – 230 mm (JOTEC GmbH, Hechinger, Germany). The bending geometry of the FET stent in the region of the aortic arch would likely result in Dean vortices which may have a significant effect on distal flow behaviour. Dean vortices are a secondary flow pattern wherein a pair of counter-rotating cells across the cross section normal to the direction of flow. However, the manufactured compliant phantom focused on the simplified descending aorta (Figure 5.2). A rigid 90-degree arc was incorporated into the inlet flange to mimic Dean vortices that are likely to be generated in the prosthetic aortic arch. The peak Dean

Number (*De*) was calculated using Equation 5.1 where, *Re* is the Reynolds number, *D* is the internal diameter of the graft, and $R_C$ is the radius of curvature measured at the centreline of the lumen (50 mm, Figure 5.2). The peak Dean Number of the model was 1111. As the Dean number was greater than 956, it may be assumed the peak flow would be fully developed with stable counter-circulating vortices [264, 265]. Therefore, the secondary flow was not investigated further.

$$De_{peak} = Re_{peak}\sqrt{\frac{D}{2R_C}} \quad \text{(Eq. 5.1)}$$

The rigid 90-degree inlet flange had a radius of curvature of 50 mm, resulting in an arc length of 78.5 mm and a 20 mm straight section before the surrogate. The surrogate stent graft was designed to be 105 mm in length (red outline in Figure 5.2). Producing a 223.5 mm length FET stent surrogate. The internal diameter of the FET stent surrogate was 28 mm with a 0.4 mm wall thickness, 5% oversized of the phantom diameter. A thin PVC ring at the distal friction grip of the FET increased the oversizing to 7%. The woven Dacron grafts are 3.9 times more rigid than an artery [28]. Hence, similar to *in-vivo*, the surrogate graft could move in a transverse direction, but resisted axial motion and radial expansion.

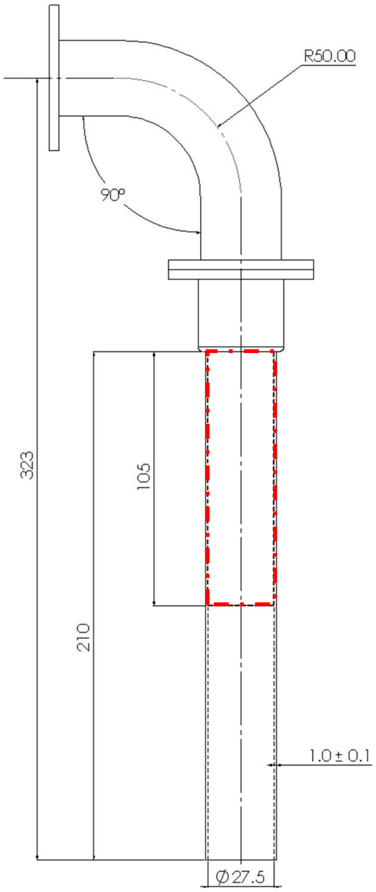

*Figure 5.2: Descending aorta idealised geometry. Stent graft location indicated in red. All measurements are in mm.*

### 5.2.2. Phantom Manufacture

A mould was manufactured following the methodology outlined in Section 2.8 (Figure 5.3). The moulds were rapid prototyped using fused deposition modelling (FDM) 3D printing. Sylgard 184 silicone was injected into the cavity between moulds and left to cure at room temperature for 48 hours. After curing, the female mould was mechanically removed, and the male mould dissolved in acetone.

The surrogate stent graft was manufactured from ABS using FDM 3D printing with a 0.2 mm wall thickness and 105 mm length. The ABS surrogate was printed with a layer height of 0.1 mm. the surface roughness of ABS printed at 0.1 mm layer height is 64.1 ± 12.2 µm [266]. A 0.5 mm thick acrylic ring at the distal end provided oversizing for stent graft anchoring similar to the physiological range of stents (Figure 5.4). Since only the flow distal and around the stent graft is clinically interesting, the stent graft surrogate was opaque, and only the distal flow was analysable.

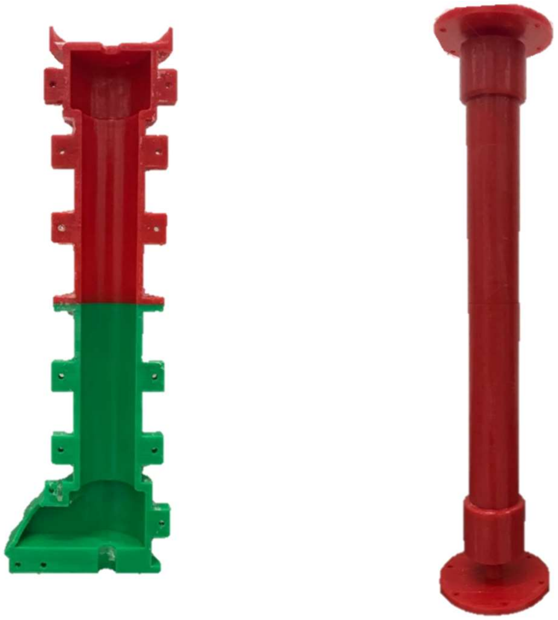

*Figure 5.3: Female (left) and male (right) mould for phantom artery casting; due to the limitation of the 3D printer height, the moulds were printed in two pieces.*

*(a)*

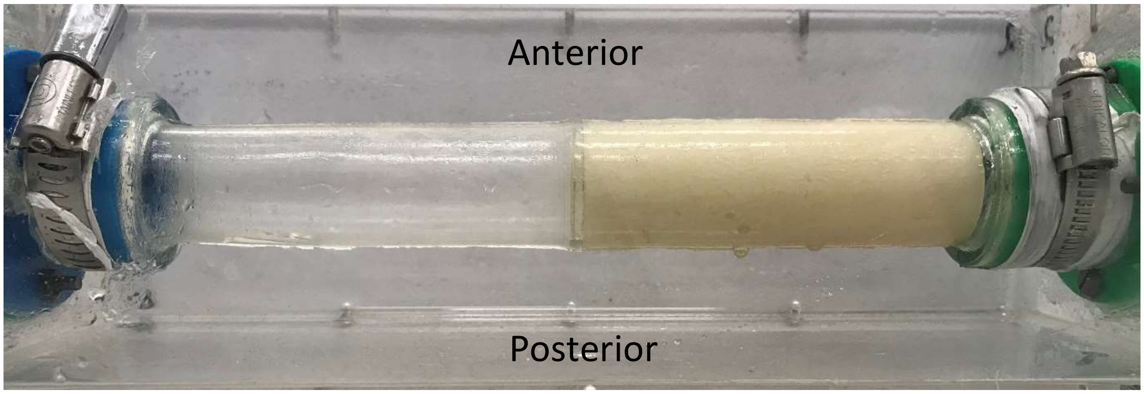

*(b)*

*Figure 5.4: (a) Assembly of phantom stented descending aorta (b) capture plane for PIV experimentation*

### 5.2.3. Flow Circuit Construction and PIV measurements

The silicone phantom had a refractive index of 1.41 at room temperature [80]. A 40/60 water-glycerine working fluid matched the refractive index of the phantom eliminated the optical distortion for PIV analysis. The working fluid was seeded with buoyant micro silver-coated hollow glass spheres. The mixture had a density of 1156 kg·m$^{-3}$ and a dynamic viscosity of 9.30 x 10$^{-3}$ Pa·s at 20°C [96]. By comparison blood has a density of 1060 kg·m$^{-3}$ and dynamic viscosity of 3.5 x 10$^{-3}$ Pa·s at the normal human body temperature. Dynamic scaling was carried out to account for the different properties using the Reynolds Number (Equation 2.12) and Womersley Number (Equation 2.13), as introduced in Section 2.7.

Flow waveforms change throughout the arterial system due to arterial geometry and compliance [267]. However, since the FET stent heavily reduces the apparent compliance of the aortic arch and initial segment of the descending aorta, an ascending aorta waveform was used. The ascending and descending aorta shapes are similar though not exactly equivalent. This lack of equivalence in wave shape was assumed to be predominantly due the compliance of the aortic arch rather than the effects of the efferent arteries. The waveform driven through the flow system, introduced in Chapter 2, Section 2.6.2, (Figure 5.5a) via a LabView controlled piston pump. The waveform for the ascending aorta was obtained from Stalder, et al. [267]. However, the flow rate reduced by 45% to account for flow to the branches of the aortic arch [268-270] and to represent a conservative low flow case. The scaled waveform to match a 1.5x diameter model is displayed in Figure 5.5b.

Typical Womersley numbers within the descending aorta have been reported between the range 6.1 [271] to 13.1 [4, 242]. In this study, a conservative *in-vitro* Womersley number of 6.6 was used. The peak Reynolds number induced by the flow circuit was 2100. A Reynolds number of 2100 is within the range of values for the descending aorta provided by [238] (2000 – 5000) and therefore was deemed acceptable for conservative experimentation.

PIV was used to capture the fluid dynamics distal of the stent graft. 18 image pairs were captured at each time step using a TSI PowerView 4MP LS PIV camera (TSI Inc., USA) with 2360 × 1776 pixels resolution captured the pairs of images used to determine the seeded particles displacement in the working fluid. A 1 mm laser light sheet was produced using a Nd:YAG double pulse laser which illuminated the region of interest. The laser was triggered by the flow waveform using a TSI LaserPulse synchroniser. The analysis was phased-locked, and eighteen image pairs were captured at each discrete time step. The images were processed using the cross-correlation method in TSI INSIGHT 4G software to map the particles displacement and therefore the velocity (Yazdi et al., 2018). Masks were applied to exclude fluid external to the model and account for wall movement across all time-steps. An iterative grid generation engine was used with 64 × 64 pixels interrogation window refined to 32 × 32 pixels.

There was a concern that the manufacturing processes may lead to inconsistent wall thickness in the phantoms [95]. Hence, to determine if the flow profiles observed in the phantom were a function of imprecise phantom fabrication, the phantom was rotated by $90^{o}$ and the experiment was repeated.

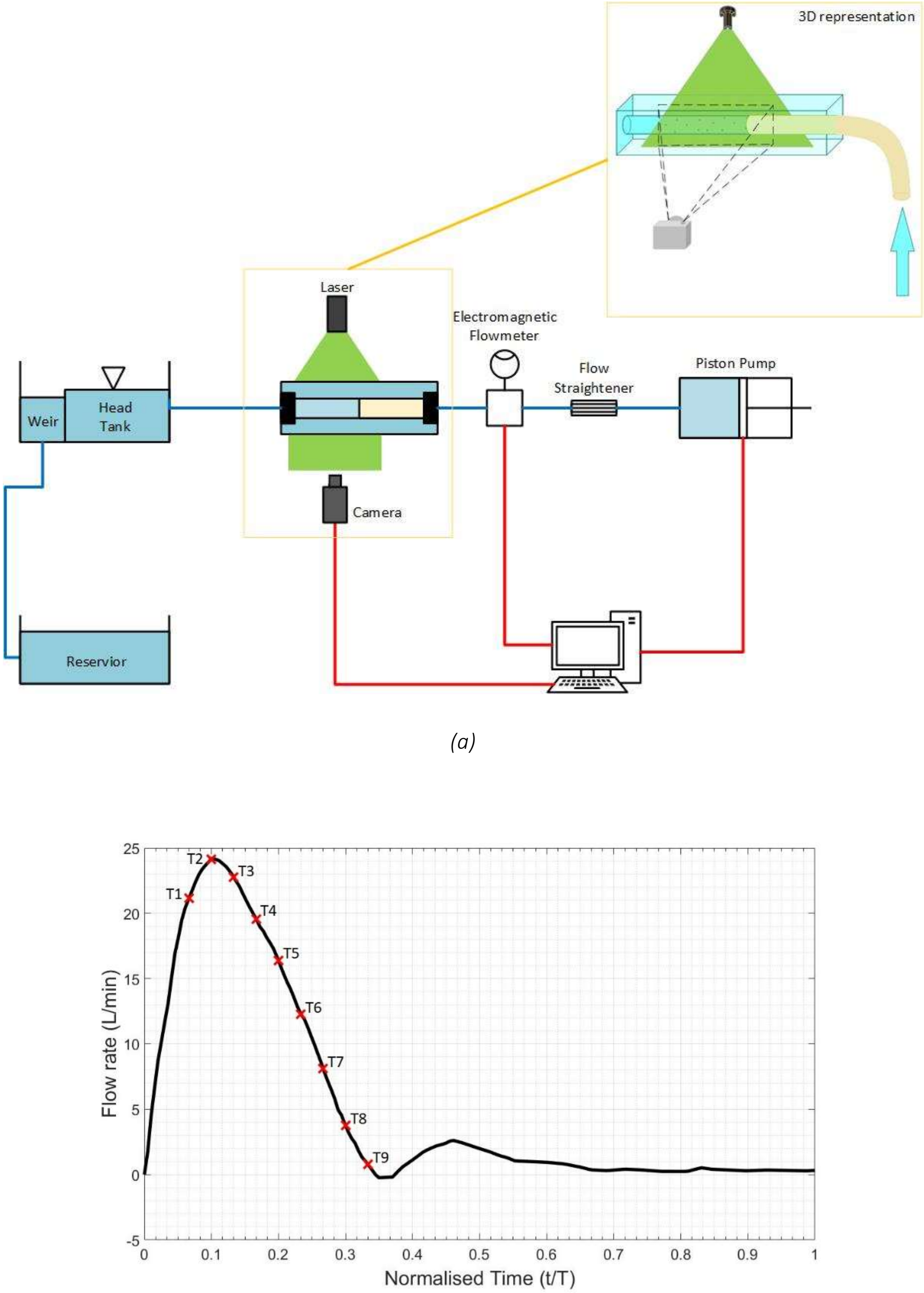

*(a)*

*(b)*

*Figure 5.5: (a) Working experimental fluid circuit setup: (red) electrical network, (blue) fluid network (network to fill system excluded) (b) Scaled experimental in-vitro inlet physiological flow waveform with measured time steps marked; Dimensionless scaling using Reynolds and Womersley matching*

## 5.3. Results

Investigations were carried out on the distal FET stent flow behaviour. Raw PIV images exhibited a Type 1B endoleak occurring during systole occurring on the anterior surrogate stent graft and phantom aorta interface (top right in each image) (Figure 5.6).

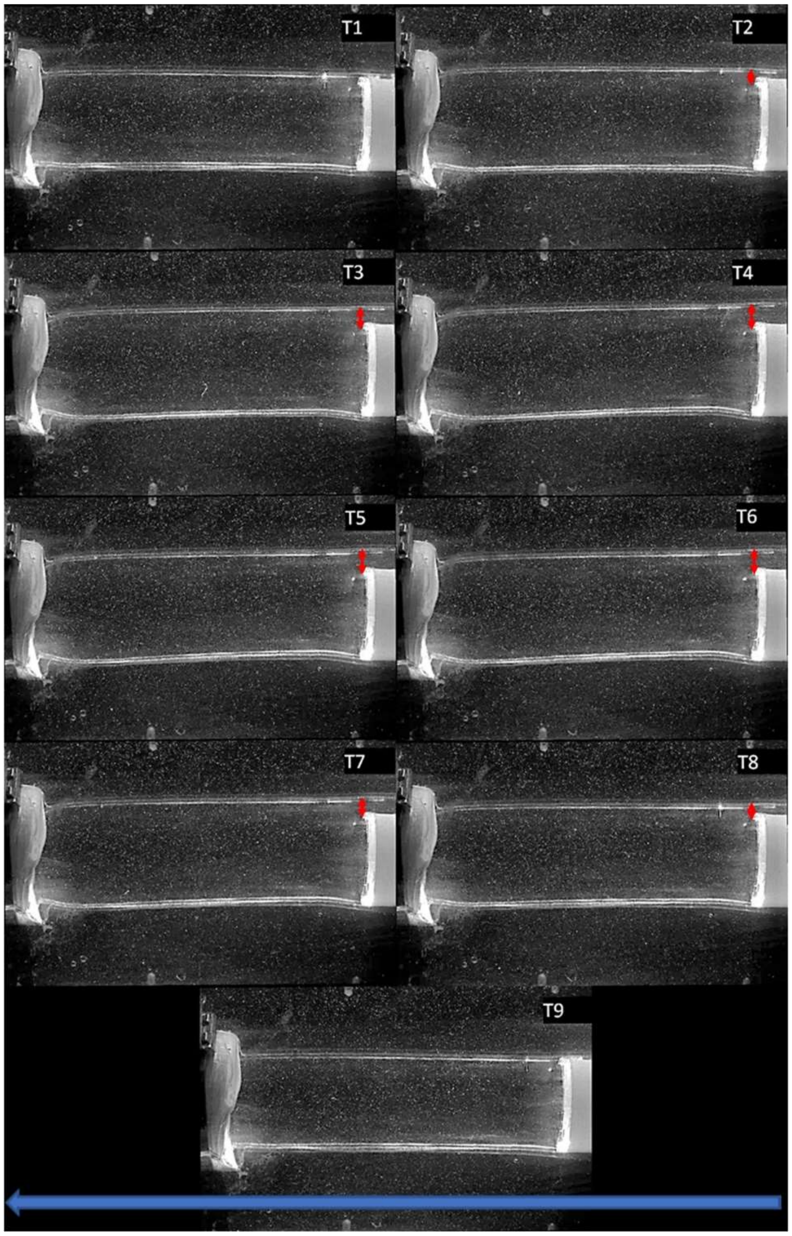

*Figure 5.6: Evolution of a Type 1B endoleak throughout systole identified at the right anterior surface for T2-T8. Primary flow direction is right to left (blue arrow). Red arrows show the endoleak evolving on the anterior surface*

During accelerating systole, flow accelerated temporally in the proximal region, but decelerated in the distal region as it exited the stented regions (Figure 5.7). This created a flow that appears to be a diffusing submerged jet, **identified by the high velocity immediately distal of the stent outlet and vectors angling towards the walls of the lumen.** Some vectors were almost perpendicular to the phantom artery wall, **exiting the FET stent**, and denote expansion.

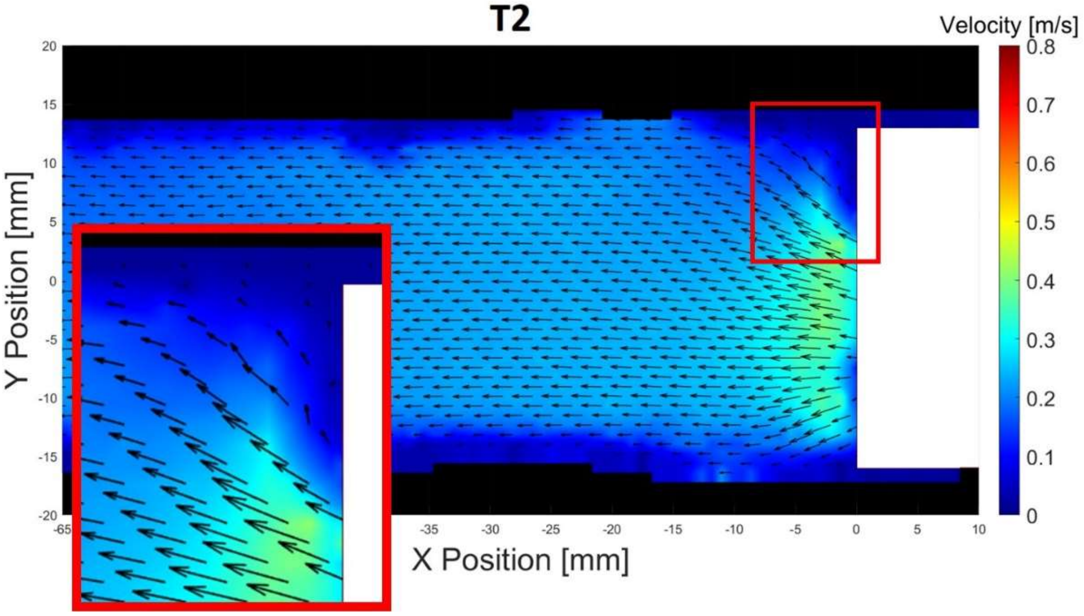

*Figure 5.7: Velocity vector profile for T2, peak systolic flow. The red box shows an example of vectors that are misaligned with bulk flow*

Figure 5.8 shows that the endoleak was not symmetric causing the lower wall to distort up towards the upper wall. The dimensions of the endoleak were the greatest at T4, where flow can still be identified separating the surrogate stent graft and phantom artery interface. Reversed flow can be identified flowing between the surrogate stent graft and phantom artery interface. Reversed flow into the endoleak has a low velocity, peaking around 0.2 $m \cdot s^{-1}$ at T4. Recirculation was identified downstream along the posterior dorsal wall (Figure 5.8a). Rotating the phantom artery and surrogate stent graft, $90^{o}$ clockwise, within the compliance chamber also captured disturbed flow on the lower wall with a recirculation zone identified at a similar location (Figure 5.8b). A potential flow stagnation zone can also be seen in Figure 5.8b. The endoleak could be identified at both the anterior and posterior surrogate stent graft and phantom interfaces. However, the anterior endoleak was larger (Figure 5.9).

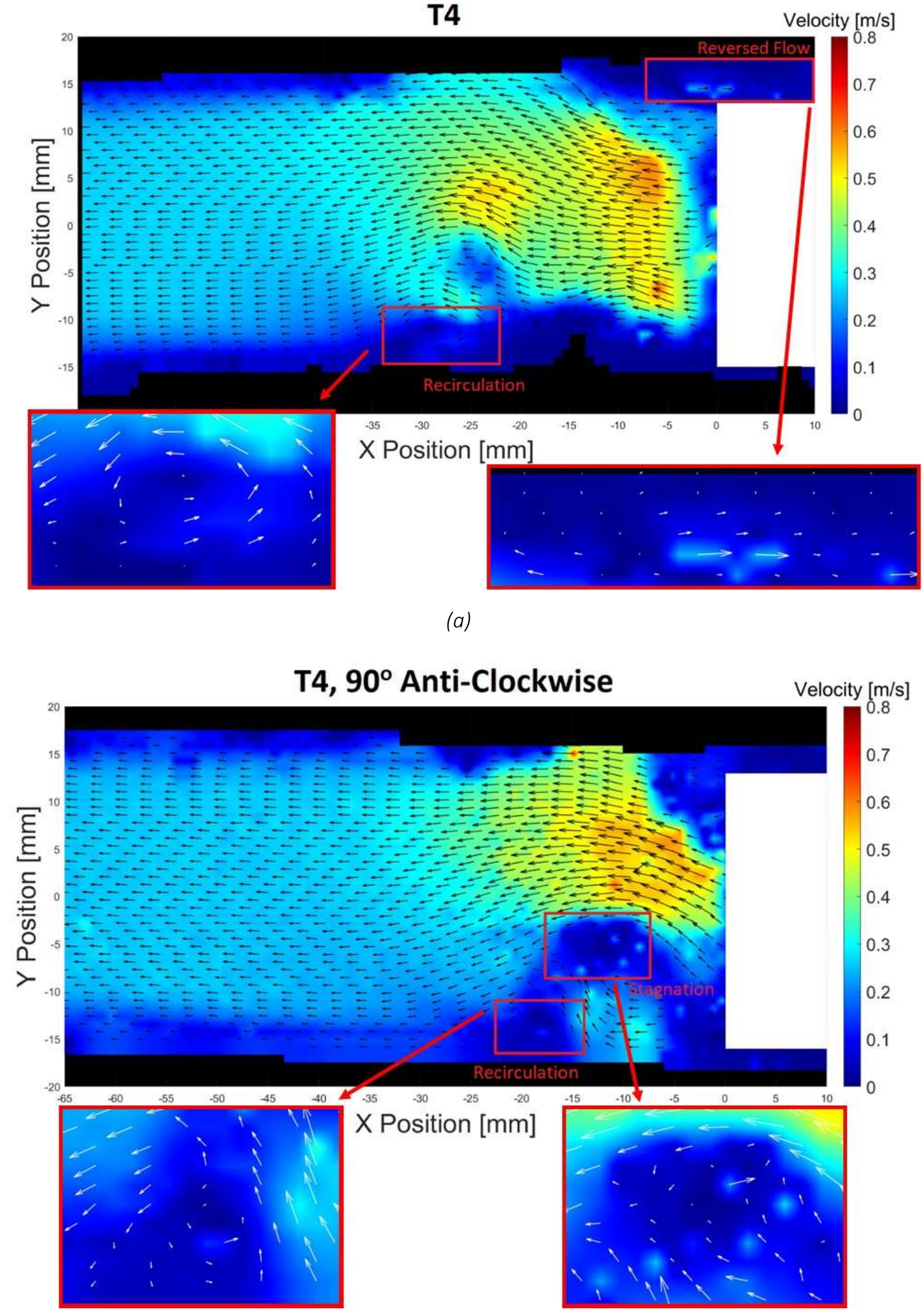

(a)

(b)

*Figure 5.8: (a) Velocity vector profile for T4, with evident recirculation and reversed flow into Type 1B endoleak*

*(b) Velocity vector profile for rotated phantom at T4, with recirculation and stagnant flow has been identified.*

*Note: zoomed images showed white vectors for clarity*

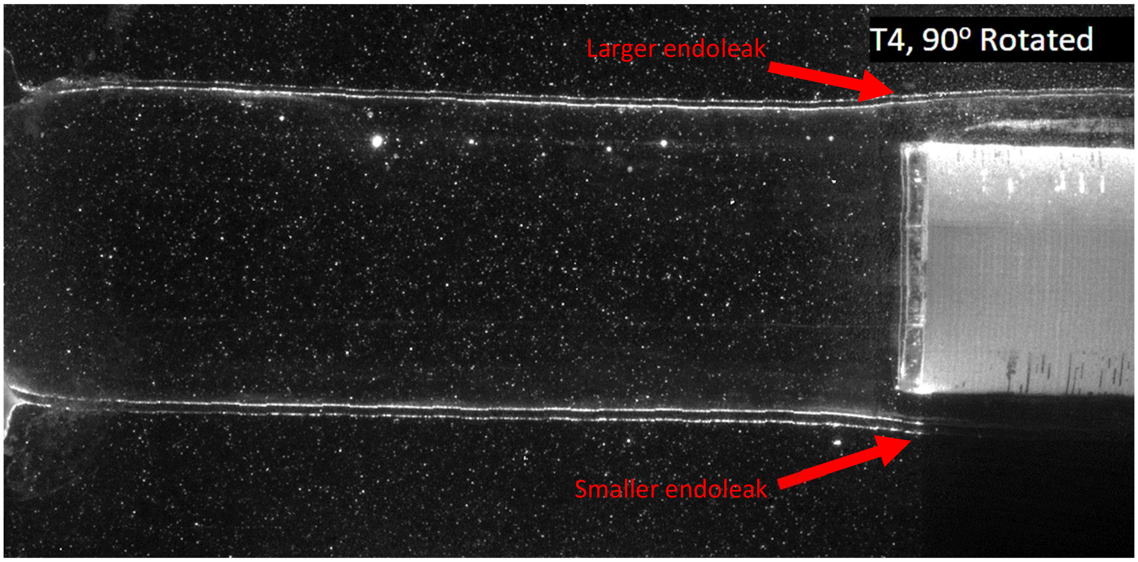

*Figure 5.9: Raw image for T4s time step, endoleak larger at anterior interface than posterior interface*

The multiple potential recirculation zones in Figure 5.8 can be identified downstream at the following time step, T5, mid-decelerating systole (Figure 5.10).

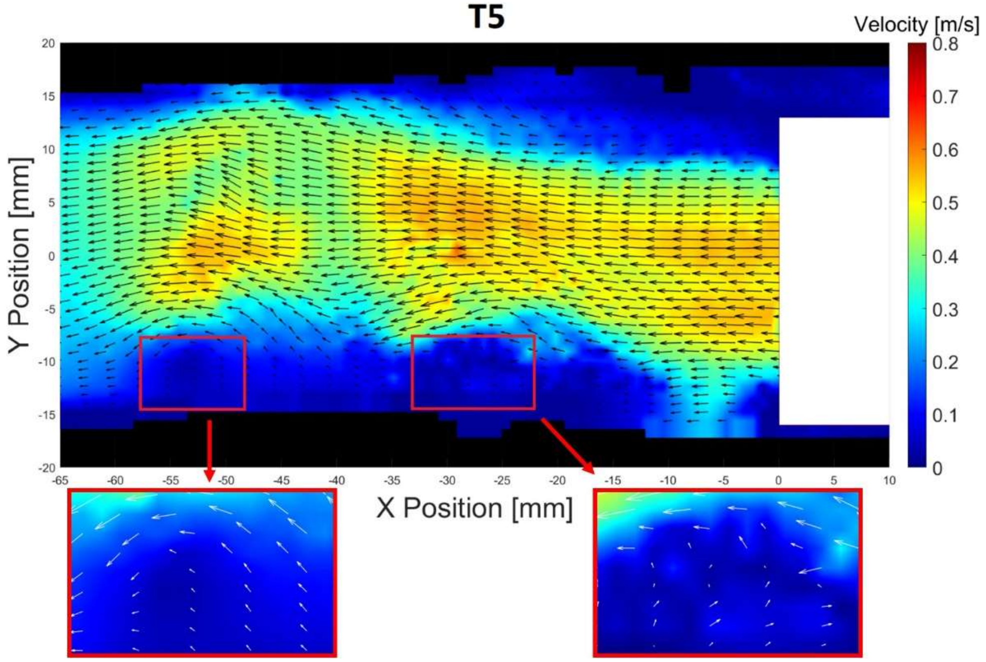

*Figure 5.10: Velocity vector profile for T5 with recirculation zones identified 20-35 mm and 48-58 mm downstream of the FET stent outlet. Note: zoomed images show white vectors for clarity*

Following T4 the Type 1B endoleak reduces, returning the arterial phantom lumen to its original size. The decrease in size is not obvious in the raw data images capturing the Type 1B endoleak. However, in Figure 5.11 a strong stream of flow can be seen ejecting from the site of the Type 1B endoleak disturbing the main flow. The flow from the endoleak has comparably high velocities. Figure 5.11 has a peak ejecting endoleak flow around 0.3 m·s$^{-1}$, meanwhile the main flow from the FET stent surrogate reaches 0.5 m·s$^{-1}$.

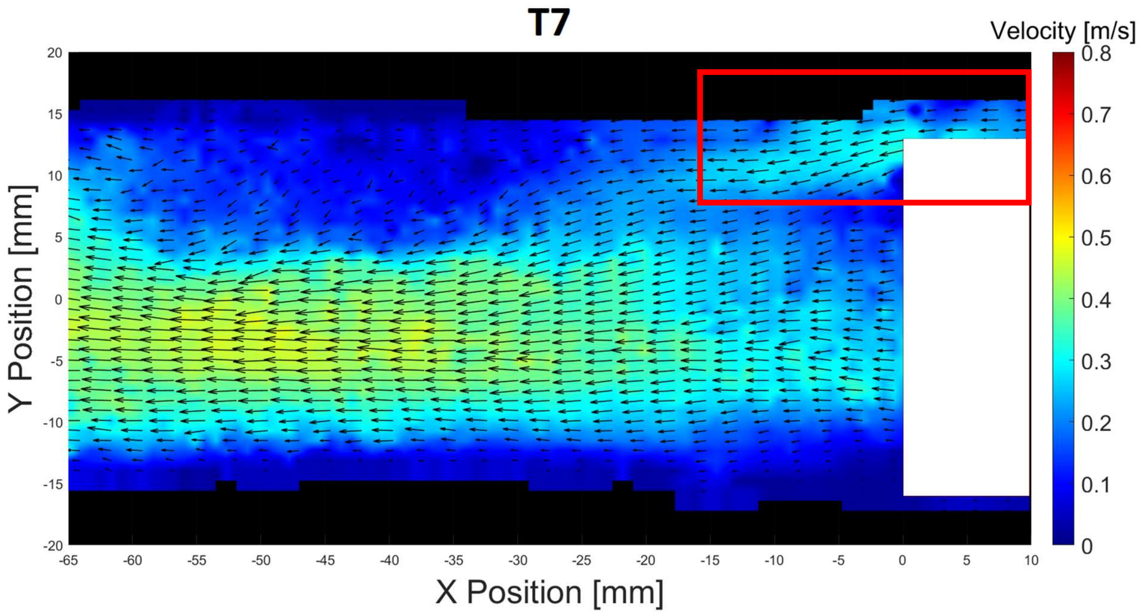

*Figure 5.11: Velocity vector profile for T7, comparably high flow rate ejecting from endoleak site indicated by the red box*

## 5.4. Discussion

The Type 1B endoleak is a known failure method of the FET stent *in-vivo*, however this failure mode has not been identified *in-vitro* previously. This chapter presents the first *in-vitro* flow analysis carried out using a surrogate FET stent in an idealised phantom artery. A Type 1B endoleak was identified and potential flow behaviours that may contribute to the endoleak were identified (Figure 5.6). Analysis of distal stent graft haemodynamics also identified a potential recirculation zone downstream of the FET stent which may affect the long-term efficacy of the stent.

Flow exiting the FET stent surrogate had a higher velocity than the downstream flow. Unscaled velocity at the outlet of the FET stent peaked at 0.60 $m \cdot s^{-1}$ compared to a peak downstream velocity of 0.45 $m \cdot s^{-1}$. Similar velocity differences between rigid and compliant phantoms have been noted previously [73, 95]. The difference in compliance between the stent graft and arterial surrogates caused a diverging flow at peak systole at the distal friction grip of the surrogate stent (Figure 5.7). Figure 5.7 also shows diverging vectors pressing out on the walls of the phantom artery, likely resulting in the Type 1B endoleak forming. The submerged jet behaviour can result in ring vortices forming at the jet boundary as the higher velocity flow mixes with the surrounding lower velocity flow [272]. The ring vortices can cause disrupted and recirculating flow distal to the stent outlet which may have caused the recirculation identified in Figures 5.8 and 5.10. The Type 1B endoleak occurred despite the consistent selection of conservative experimental parameters such as reduced flow rates and a more rigid wall. The peak pressure in systole led to expansion of the arterial phantom and divergence of the flow. At peak systole, velocity vectors immediately distal to the surrogate FET stent were misaligned with the bulk of the fluid flow, tending to point radially towards the phantom wall, rather than approximately tangential as expected in healthy arteries. The positive transmural pressure expanded the arterial phantom diameter to greater than the oversized surrogate FET stent, resulting in the formation of the Type 1B endoleak (Figure 5.6) [6].

The Type 1B endoleak observed in this study was not symmetric. A variety of factors may contribute to the asymmetry. One potential cause is unintentional variation in the circumferential wall thickness of the phantom artery caused by inaccuracy inherent in the moulding process. Yazdi, et al. [95] measured the wall thickness variation for the casting method used in this study and found a variation of ± 10%. Variation of wall thickness is physiological. Arterial wall thickness varies throughout the body, both longitudinally and circumferentially, as it is affected by the remodelling and regeneration of endothelial cells. Across multiple studies, the mean wall thickness has shown to vary from 2% [196] to 14% [273] for human aortas. Therefore, circumferential wall thickness variation is common. The variance however may be due to the casting method resulting in the anterior dorsal wall being thinner than the posterior dorsal wall. Wall variation may also account for the formation of a recirculation zone forming on the posterior sagittal plane. Intrasaccular flow occurs when the anterior dorsal wall and surrogate stent graft interface separates, reducing the pressure on the posterior wall, which may result in the deformation at the surrogate stent graft outlet (Figure 5.6) [274, 275]. The asymmetry may also have been influenced by the secondary flow patterns due to the high Dean Number. The counter-circling vortices skews the velocity profile to the outer edge of the $90^o$ bend. However, rotating the phantom and surrogate stent caused posterior and anterior endoleak, rather than anterior endoleak observed in the initial implementation of the experiment. This change in observation indicates that secondary flow behaviour was not the sole cause for the Type 1B endoleak asymmetry, and small regional differences in phantom wall compliance are suspected to also contribute to the geometry of the endoleak. This compliance variability is not unexpected *in-vivo* [96].

A low velocity flow entered the Type 1B endoleak along the anterior surface (Figure 5.8a). The low flow may indicate there were abnormal shear stresses on the wall Changes to wall shear stress may lead to abnormal cell growth and the potential for thrombosis. The stagnation zone identified in Figure 5.8b may also indicate a risk of thrombus formation. Stagnation and low velocity flow zones can result in multi-directional shear stresses that change the growth patterns of the endothelial cells lining artery walls [276]. The stagnation zone may indicate a risk to the FET stent patency.

Rotating the surrogate stent graft and phantom artery $90^o$ showed a similar disturbance to the flow. The consistent disruption on the posterior surface may be increased by the weight of the surrogate stent graft. As the walls dilate the stent graft may settle downwards, directing flow into lower wall and producing a separation zone downstream and creating the symmetry of the endoleak. However, in contrast to the initial experimental orientation, the Type 1B endoleak occurred at both anterior and posterior edges of the dorsal line. This suggests that either the phantom fabrication led to slightly thinner lateral walls of the phantom, or that FET stent misalignment is a potential cause for the non-symmetric endoleak. However, Type 1B endoleak occurred in both cases.

The identification of the recirculation at T4 in both Figures 5.8a and 5.8b and T5 in Figure 5.10 indicate that the recirculation is not the result of wall thickness variation or geometry distortion caused by the Type 1B endoleak. The recirculation is likely caused due to the discontinuous compliance at the transition from the stent graft to arterial phantoms. The change in compliance produced a jet like flow. As high velocity flow entered the distal phantom artery, momentum is transferred to the surrounding lower velocity flow, as in Figure 5.7. The momentum transfer can result in ring vortices [272]. The potential recirculation zones may also suggest the presence Dean vortices. Pulsatile flow through curved geometries can introduce more complicated secondary flows that lead to flow reversals [277]. Ku [277] does not consider the effects of compliance on Dean vortex formations, however another study has shown compliance has negligible effect on secondary flow generation [265]. Dean vortices formation were not investigated as previous studies have already identified their presence in rigid pulsatile flow [265, 278, 279].

A Type 1B endoleak introduces a second stream of flow exiting the surrogate stent graft and phantom artery interface. The second stream sustains high velocities into late systole (Figure 5.11). The introduced stream may have affected flow at the phantom wall reducing velocities and skewing the overall flow profile to the posterior dorsal wall and producing the low velocity flow seen on the arterial dorsal wall in Figure 5.11. Disturbed flow affects wall shear stress, which has been linked to inflammatory responses of arterial linings [100]. Furthermore, arterial linings can respond to directional stimuli of the local flow [64]. Reversed flow may lead to altered arterial linings with time which can have further health complications and potentially require stent revision.

The experimental approach in this study employed conservative assumptions. The flow rate was reduced by 45% of the original physiological waveform and thus reduced the propensity for the Type

1B endoleak to occur. The phantom artery wall compliance was conservatively selected to account for the stiffening that occurs during degeneration with age [263]. Selecting a lower compliance resulted in the 1 mm wall thickness and requires a higher pressure to deform. Resultantly, it was less likely to result in the formation of a Type 1B endoleak. Despite conservative assumptions a Type 1B endoleak was still identified.

It is known that a healthy aorta can swell to 10 – 15% of its original diameter [280]. The phantom descending aorta model expanded to nearly 20% greater than its original diameter, which is higher than expected for healthy arterial walls. However, recipients of the FET stent generally have diseased arterial walls which can expand significantly over the 10 – 15% reported [281, 282]. A key limitation of this investigation was the pressure profile induced in the geometry. In particular, matching Reynolds and Womersley numbers in a certain geometry requires a specific pressure profile. Therefore, the pressure profile may have been higher than intended, resulting in an over-exaggerated Type 1B endoleak. However, a Type 1B endoleak pressure field for the FET stent has not been captured *in-vivo*, and pressure scaling between *in-vivo* and *in-vitro* models is not common. Pressure may potentially be scaled using Euler number. However, this information was not found. This is an area for further research for compliant *in-vitro* modelling.

The surrogate FET stent was a generalised design that was not specific to any FET stent manufacturers. The stent graft was based off a reported geometry [6, 283] and ignored strut design. Insufficient stent graft oversizing may have contributed to the Type 1B endoleak occurrence. Generally, the FET stent is oversized by around 10% of the healthy distal aorta diameter when deployed [61]. Oversizing by 10% produces a chronic outward force on the healthy distal aorta that enables a distal seal between the stent and when arterial expansion is below 10%. The surrogate stent graft was only oversized by 5%. The ring that aided the friction grip was oversized 7%. Oversizing was reduced to enable situation of the manufactured stent graft within the delicate silicone phantom. This may have reduced the pressure required to produce a Type 1B endoleak. However, this was considered an acceptable risk due to the 45% reduced flow rates utilised in the experiment. The surrogate stent manufactured for experimentation did not produce a chronic outward force that a true stent graft may produce. A healthy artery can swell radially to accommodate high flow and slowly release fluid through diastole [214]. After deployment in an artery, a true stent graft dilation is tiny compared to the dilation of a healthy artery. If the distal artery continues to dilate beyond the maximum stent graft diameter, the outward force of the stent graft becomes zero. Therefore, it was assumed that the lack of chronic outward force of the stent on the artery during diastole would not have a significant effect on the overall flow behaviour and therefore the FDM manufactured surrogate stent would be adequate. Another limitation introduced in the modelling of the FET stent was the assumption that 3D tortuosity could be ignored. *In-vivo,* the aorta curves through the body around more than one plane. The phantom model produced models the 2D curvature of the aortic arch but then assumes in-plane flow through the thoracic aorta, ignoring the 3D tortuosity. The main effect of this simplification is the inhibition of possible helical flow production, which is known to occur in natural physiology. However, due to the limitations of planar PIV, helical flow cannot be captured, and the flow fields captured were assumed to provide quality indicative results.

## 5.5. Conclusions

The FET stent is a life-saving hybrid-prosthesis, designed to improve the quality-of-life for the recipients. The analysis of the FET stent surrogate provided insight into the fluid dynamics that may contribute to the formation of a Type 1B endoleak. The failure is linked to the compliance disparity of the stent graft surrogate to the phantom model which indicates the compliance disparity may also cause the FET stent failure *in-vivo*. Further research into more compliant biocompatible materials may assist in restoring healthy flow in patients, therefore improving the quality-of-life years. Longevity of the FET stent is particularly important as the mean age of recipients is 56.5 years old. Compliance mismatch has been identified as problematic previously and is a growing area of research [65, 101]. Other deleterious flow behaviours were identified downstream *in-vitro* such as a recirculation and flow pattern disturbances that may lead to irregular endothelial cell growth and have long term negative effects on patient quality of life.

Compliance mismatch is a key problem for the FET stent as identified within this chapter. Further research into compliance transitioning and compliance matching stents may aid the long-term patency of stents such as the FET stent. Research into compliance transitioning and matching stents is relatively new and increasing in importance. However, the development of these stents is still slow, potentially due to the high-risk nature of testing the devices *in-vivo*. However, this chapter shows that initial testing could be carried out using *in-vitro* modelling methods, and candidate strategies to mitigate the 1B endoleak could thus be safely tested and optimised.

# 6. *PIV evaluation of haemodynamics proximal to the kissing stent configuration in the aorto-iliac bifurcation*

This chapter presents an investigation of how the kissing stent (KS) reconstruction of the aorto-iliac bifurcation affects both proximal and distal flow. Deployment of the KS geometry has a high technical success rate. However, stent patency reduces in the first five years potentially due to deleterious flow behaviour. Previous modelling methods of the KS have not investigated the effect of compliance and area change on the abdominal aorta and iliac arteries. The research presented in this chapter has been compiled and submitted to the Journal of Biomechanics (UK) for publication.

## 6.1. Introduction

Atherosclerosis was introduced in Chapter 1 as the most common form of CVD. Aorto-iliac occlusive disease (AIOD) is a form of atherosclerosis affecting the abdominal aorta and common iliac limbs. AIOD can be treated using parallel stenting methods such as the 'kissing stents' (KS) [284]. AIOD is a narrowing (stenosis) or blockage (occlusion) of the iliac arteries and/or abdominal aorta, depending on the classification and severity of lesions, leading to hypo-perfusion of blood (Figure 6.1) [285]. The specific AIOD is classified based on TASC II guidelines. Type A and B AIOD are less severe with short regions of stenotic artery. However, Type C and D are more severe and can present as total occlusion of the iliac limbs and/or abdominal aorta, or stenotic lesions that extend typically over 100 mm in length within the arteries (Figure 6.1). Estimates of AIOD prevalence have ranged from 3.5-14% with occurrence increasing with age [285]. However, the actual prevalence is difficult to determine as many people with AIOD may be asymptomatic [285].

The KS configuration implants two stents into the common iliac arteries and are located adjacent to one another in the distal aorta [286] (Figure 6.1). The KS may use bare metal or covered stents, though, covered stents have demonstrated higher long-term patency [7, 49]. The improved performance may potentially be due to their ability to inhibit neo-intimal growth, preventing the stent from stenosis and occlusion [7, 49]. Protrusion of the stents into the abdominal aorta is also suggested to have a negative impact on the stent patency [287]. Preferred protrusion is up to 10 mm of the stent, however for Type C and D atherosclerotic lesions may require further protrusion [204, 287].

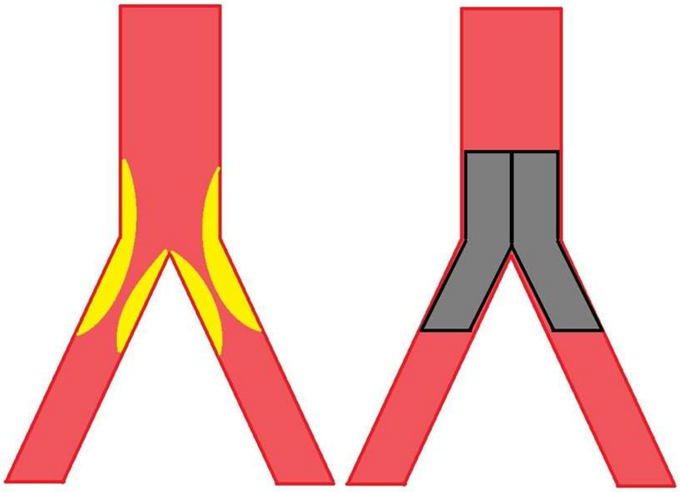

*Figure 6.1: (left) Simplified geometry of severe limb occlusion in the aorto-iliac bifurcation. Yellow = occlusion and (right) the Kissing stent geometry. Grey = stented region*

KS insertion is a minimally invasive, but difficult to perform surgery, with a high peri-operative success rate of 99.1% [288]. However, primary patency rates drop to 76.9% at five-year follow up [288]. The KS sometimes requires revision due to stent failure or complications including atherosclerotic lesions and thrombosis. However, no surveys that identify the location of these complications have been published. Stent thrombosis and distal embolism are known outcomes of changes in haemodynamics affecting the endothelial growth patterns of the arterial lining.

The KS has previously been investigated via CFD [289-291]. However, few of these studies were carried out on the aorto-iliac bifurcation. Rigatelli, et al. [290] investigated the effects of stent take-off angle and protrusion of the stents in the aorta on the regeneration of atherosclerotic lesions. A higher protrusion and take off angle of $45^o$ was most optimal. Morris, et al. [289] and Chiastra, et al. [291] both carried out studies on the KS within coronary arteries. CFD studies typically used rigid simulations and simulated haemodynamic effects of tortuous geometry to estimate short- and long-term patency. *In-vivo* investigation has also been conducted into the area mismatch in patients [284]. Groot Jebbink, et al. [284] investigated methods of reducing the area mismatch in the KS such as including using covered endovascular reconstruction of the aortic bifurcation (CERAB) which channels flow into the KS inlets and using crush stenting methods which used tapered stents that are purposely oversized within the aorta to form D-shaped stent inlets. Potentially deleterious flow patterns caused by stent protrusion into the aorta have not extensively been investigated [286]. Some *in-vitro* studies have considered the KS in the aorto-iliac bifurcation [204, 292, 293]. These *in-vitro* investigations were carried out using a rigid model. Injection dye modelling has been used, however, it is limited to displaying a single or cluster of streamlines at a time, thus limiting the temporal and spatial information obtained [292]. Particle Image velocimetry (PIV) was used to investigate the flow behaviour of a rigid aorto-iliac bifurcation treated with the KS [204]. The study measured instantaneous flow behaviour at three points in the flow cycle and did not investigate actively driven backflow. Backflow at the infra-renal aorta was identified by Les, et al. [221].

The KS configuration is commonly used within the coronary arteries [289, 294] and the basilar artery [295]. However, the haemodynamics of the coronary and basilar arteries differs significantly from that of the abdominal aorta. The abdominal aorta is typically 10x larger by diameter and has a 5x higher flow rate [221, 296] than the coronary and intracranial arteries [297, 298]. However, unlike the coronary and basilar arteries [289, 294, 295] there has been a paucity of experimental research carried out within the aorto-iliac bifurcation. This chapter presents PIV captured peripheral flow phenomena within a compliant phantom that has been stented using a KS configuration. PIV is an indirect measurement method that traces the motion of small particles between two images within a transparent fluid using a pulse laser sheet [80]. The particle displacement and known time delay between image captures produce an array of velocity vectors and enable the identification of abnormal flow [299]. This chapter used planar PIV to capture two image planes along the central coronal and sagittal planes.

Despite previous studies, the cause for in-stent restenosis remains uncertain for covered KS. The aim of This chapter aim was to evaluate fluid behaviour both proximal and distal of the KS across the full cardiac cycle and identify potential haemodynamics that may result in stent occlusion. A compliant model was selected to represent a healthy artery outside of the diseased portion of artery.

## 6.2. Methods

### 6.2.1. Aorto-Iliac Bifurcation Phantom

Design and manufacture of the aorto-iliac bifurcation phantom followed the methodology outlined in Section 2.8. An idealised geometry of the aorto-iliac bifurcation was designed for this experiment (Figure 6.2) based on the geometries defined in Table 6.1 [18, 296]. The geometry was scaled up to 1.25x life size to comply with wall thickness limitations in fabrication. In contrast to *in-vivo*, the phantom bifurcation was assumed symmetrical along the sagittal plane. The wall thickness was scaled using normalised compliance matching (Equation 2.16) to produce an *in-vitro* wall thickness of 1.2 mm that was physiologically matched to the elastic properties of an *in-vivo* artery.

AIOD can make an artery more rigid. However, proximal and distal landing zones of stents are situated within healthy compliant artery. Limb lengths were calculated based on the longitudinal response formula (Equation 2.17-2.19) which resulted in a 1.83x scale factor from the *in-vivo* limbs to the *in-vitro* limbs to ensure similar wave propagation.

*Table 6.1: Dimensions obtained and selected for aorto-iliac bifurcation geometry*

| **Property** | **In-vivo values used (reported range*)** | **In-vitro values 1.25x nominal size** |
|---|---|---|
| ***E* [MPa]** | 0.74 (0.74) | 1.32 (silicone) |
| **Proximal *D* [mm]** | 20.0 (19.4 – 26.2) | 25.0 |
| **Abdominal aorta (below inferior mesenteric artery) *L* [mm]** | 40.0 (30.0 – 40.0) | 75.0 |
| **Bifurcation *D* [mm]** | 17.6 (14.3 – 19.5) | 22.0 |
| **Iliac *d* [mm]** | 8.8 (6.8 – 11.8) | 11.0 |
| **Take-off angle** | 25.0$^0$ (25.8±4.3$^0$) | 25.0$^0$ |
| **Iliac *L* [mm]** | 54.0 (53.8±18.3) | 99.0 |
| ***h* [mm]** | 1.7 (1.4 – 2.0) | 1.2 |
| ***C* [MPa$^{-1}$]** | 15.7 (15.7) | 15.7 |

* in-vivo geometry and compliance obtained from Deswal et al., (2014) [18] and Lang et al., (1994) [296].

*Figure 6.2: Idealised geometry of the aorto-iliac bifurcation and 3D printed male and female mould*

A Sylgard 184 silicone elastomer (Dow Corning, MI, USA) phantom was cast using the lost-core method described in Section 2.8.3. A male mould and two-part female mould were designed using SolidWorks (SolidWorks, MA, USA) (Figure 6.2). A 1.2 mm clearance between male and female mould produced the desired wall thickness. These moulds were 3D printed in ABS using a fuse deposition modelling (FDM) UPBOX printer (Tiertime, Beijing, China). The mould surfaces were sanded and smoothed with acetone vapour. Silicone was injected into the mould at the base, venting air out the top. The cast was cured for 48 hours at 23°C. The female mould was then mechanically removed from the cast and the male mould was dissolved in acetone.

### 6.2.2. Surrogate Covered Stent

A braided monofilament mesh was designed with a 40 mm pitch to represent a low-density stent (Figure 6.3), similar to many commercial stents such as the Wallstent (Boston Scientific, MA, USA). The stent protruded 40 mm distally into the iliac limbs and proximal of the bifurcation [284]. A lower protrusion is often preferred, however, for patients presenting with Type D lesions, a larger protrusion may be required. Furthermore, a larger protrusion presented a worst-case scenario for analysis [287]. The stent pattern was embedded within the graft with little to no protrusion into the fluid flow. Thus, the stent phantom's contribution to the model was predominantly to yield similar rigidity to *in-vivo* stents. The stent surrogate was designed to be flexible such that it may conform to the geometry of the native phantom limb. The braided wire geometry was manufactured from blacked Nitinol wire with a 30°C transformation temperature. Nitinol wire is a shape memory alloy that can recover from deformation when heated above the transformation temperature. To set the Nitinol wire shape, it was then annealed at 550°C (red hot) for 10 minutes and air quenched back to room temperature. Two braided mesh stents were manufactured. Typically, balloon expended stents are more used in the iliac limbs for AIOD [290]. However, this investigation focuses on the fluid flow behaviour following deployment, rather than the deployment method used.

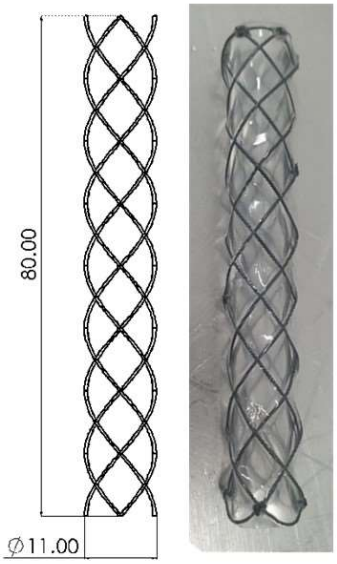

*Figure 6.3: (left) Monofilament braided stent geometry and (right) manufactured surrogate stent*

The stent grafts were manufactured from Sylgard 184 silicone. The wire mesh was fixed onto a 10.5 mm stainless steel shaft. The grafts were applied to the wire mesh by painting the silicone onto the shaft within the wire mesh region up to 1 mm thick. This resulted in an external diameter of 11.5 mm (5% larger than the phantom iliac limb). It was assumed that wire mesh and the wall thickness of the graft would lead to an effectively stiff stent, and thus variance in the graft thickness would not be critical. The silicone was cured at 100°C for approximately 40 minutes, rotating constantly, followed by baking at 80°C for 30 minutes. Heat treating at 100°C increases the elastic modulus of Sylgard 184 to 2.05±0.12 MPa [300]. The complete surrogate stent was mechanically removed from the stainless steel shaft. Experimentation focused on the upstream flow behaviour and downstream left limb. A total graft was applied to the left surrogate stent (Figure 6.3) and the right stent graft was applied up to the bifurcation. The partial graft of the right stent was unlikely to have had a significant effect on the flow. The oversizing resulted in an interference fit with the phantom at the right proximal iliac preventing flow entering the iliac limbs from the aorta around the covered stents, even with a partial graft on the right stent.

### 6.2.3. Assembly of Model

Each surrogate stent was stretched longitudinally, thereby reducing the stent diameter to allow for deployment within the silicone phantom model. 50°C water was used to shape set the surrogate in position. This process provided sufficient radial force and prevented stent migration. The phantom artery and surrogate stents were located within a compliance chamber (Figure 6.4).

*Figure 6.4: Full assembly of KS stented aorto-iliac bifurcation (left) coronal plane, (right) sagittal plane*

### 6.2.4. Flow Circuit Setup

This experiment used the revised flow circuit introduced in Section 2.6.3. The flow circuit and data acquisition setups are shown in Figure 6.5a. The working solution was 40/60 water-glycerine which matches the refractive index of Sylgard 184 silicone (n=1.41) thus eliminating risk of optical distortion.

The overall mixture has a kinematic viscosity of $9.3\text{x}10^{-6}$ $m^2 \cdot s^{-1}$ at 23°C [96], almost 3x higher than blood ($3.3\text{x}10^{-6}$ $m^2 \cdot s^{-1}$). An *in-vivo* flow profile for the abdominal aorta was adapted from Les, et al. [221]. *In-vivo* Reynolds (Equation 2.12) and Womersley (Equation 2.13) numbers were scaled so *in-vitro* model size and fluid viscosity dynamically matched, as per Section 2.7. The resulting waveform used for this *in-vitro* experiment is shown in Figure 6.5b. Dimensionless scaling ensured physiological relevance and clinical significance. The scaled waveform had a peak Reynolds number of 1750 and a Womersley number of 7.25. Literature provides a range of Womersley numbers for the abdominal aorta from 7.38–14 [242, 301]. Low Womersley numbers may reduce the oscillatory shear index [302], and theoretically lead to a lower disturbance within the flow [242]. The low value was used in this study for two reasons: The value implies a resting state *in-vivo* [150], which is a more common state, and this value also approached the limits of precision and magnitude of flow available with the pump system.

Neutrally buoyant, silver-coated hollow glass spheres (density = 1100 $kg \cdot m^{-3}$ and nominal diameter = 10 μm) seeded the fluid as tracer particles (Dantec Dynamics, DK). The fluid through the model (Figure 6.5a.F) was pumped against gravity requiring the model to be orientated upside down. Pumping against gravity allowed the internal static pressure in the model to be modulated by the head tank and weir height set to 280 mm above the model outlet. The head tank estimates the unknown arterial back pressure (Figure 6.5a.G). A dual-pumping system was adapted from Tsai and Savaş [92] was used to drive fluid through the circuit. A diaphragm pump with built-in check valves provided the mean flow through the circuit (Figure 6.5a.B). A stepper motor driven piston pump then modulated the mean flow to achieve the desired flow rate waveform (Figure 6.5a.C). Flow rate was monitored using an electromagnetic flowmeter (immediately proximal of the phantom) and maintained through a feedback loop (Figure 6.5a.E). A 1.5 m length pipe connected the flow straightener to the flowmeter to ensure fully developed, undisturbed flow. Effects of gravity were assumed negligible due to the feedback from the flowmeter.

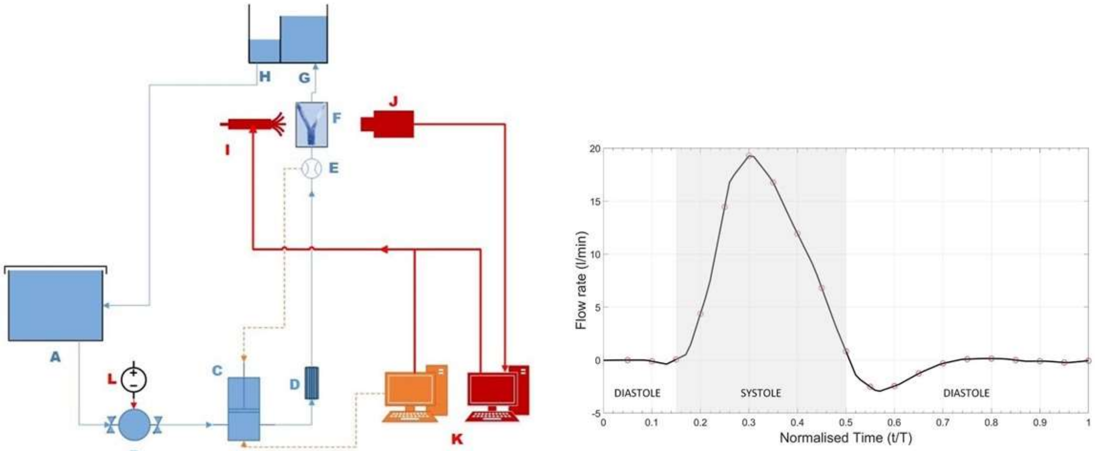

*(a)* *(b)*

*Figure 6.5: (a) Blue lines: fluid circuit. Red lines: laser trigger and camera data cable. Orange circuit: flow rate feedback loop. Components: A Reservoir; B In-line Diaphragm pump; C Piston pump; D Flow Straightener; E Electromagnetic Flowmeter; F Phantom Model; G Head Tank; H Overflow Weir; I Nd:YAG Laser; J Camera; K Data Acquisition System; L DC Power Supply (b) In-vitro waveform for healthy aorto-iliac at rest. The noughts (o) indicate the capture times*

### 6.2.5. Data Capture and Processing

Planar PIV was used to capture images and identify the flow behaviour. An EverGreen$^2$ Nd:YAG double pulse laser (Quantel Laser Systems, USA) was used to generate a 1 mm light sheet for illuminating the coronal and sagittal planes in successive experiments. Data was captured at regular intervals, marked in Figure 6.5b. A TSI PowerView 4MP LS PIV camera (TSI Inc., USA) with 2360×1776 pixels resolution was used to capture 50 image pairs at each interval for the coronal and sagittal plane. Time delays between image captures varied between 230 µs and 2500 µs dependent on the flow rate at each interval. These image pairs were spatially ensemble averaged using cross-correlation on an iterative grid refinement to track particle movement through the model and produce a displacement vector field. The grid interrogation windows reduced from 64x64 to 32x32 pixels. Processing was carried out using TSI INSIGHT 4G (TSI Inc., USA). Mean testing of the neighbouring grid was used to validate vectors and reject outliers. Outlier vectors were replaced using interpolation of the local median. The data sets had an average of 93% good vectors. Masking excluded particles in the fluid surrounding the phantom from being measured.

## 6.3. Results

The investigation captured flow behaviour across the coronal and sagittal plane of the aorto-iliac bifurcation. Flow within the stented regions was neglected in this study as the rigid stent behaviour inhibited the capture of particle motion within the stents. The stent regions were outlined with a white border. Peak velocity did not occur at peak systolic flow ($t/T$=0.3). The vector profile at peak systolic flow is shown in Figure 6.6a, in which the velocity reached 0.69 $m \cdot s^{-1}$ proximal to the stented region. Velocity continued to increase to the next time step, shown in Figure 6.6b. At $t/T$=0.35 the proximal velocity reached 0.71 $m \cdot s^{-1}$, similar to Figure 6.6a. Distal of the stents the flow ejects at a peak velocity of 1.4 $m \cdot s^{-1}$ into the downstream iliac limbs. In Figure 6.6a-b some flow can be identified leaking into the right limb stent at the bifurcation. WSS at the stent inlet on the coronal plane was 1.1 Pa *in-vitro* and reduced to 0.8 Pa moving further proximal. WSS on the sagittal walls was nearly half the coronal plane value (0.62 Pa reducing to 0.42 Pa when moving further proximal of the stents) despite the planes having similar velocity plug-shaped profiles.

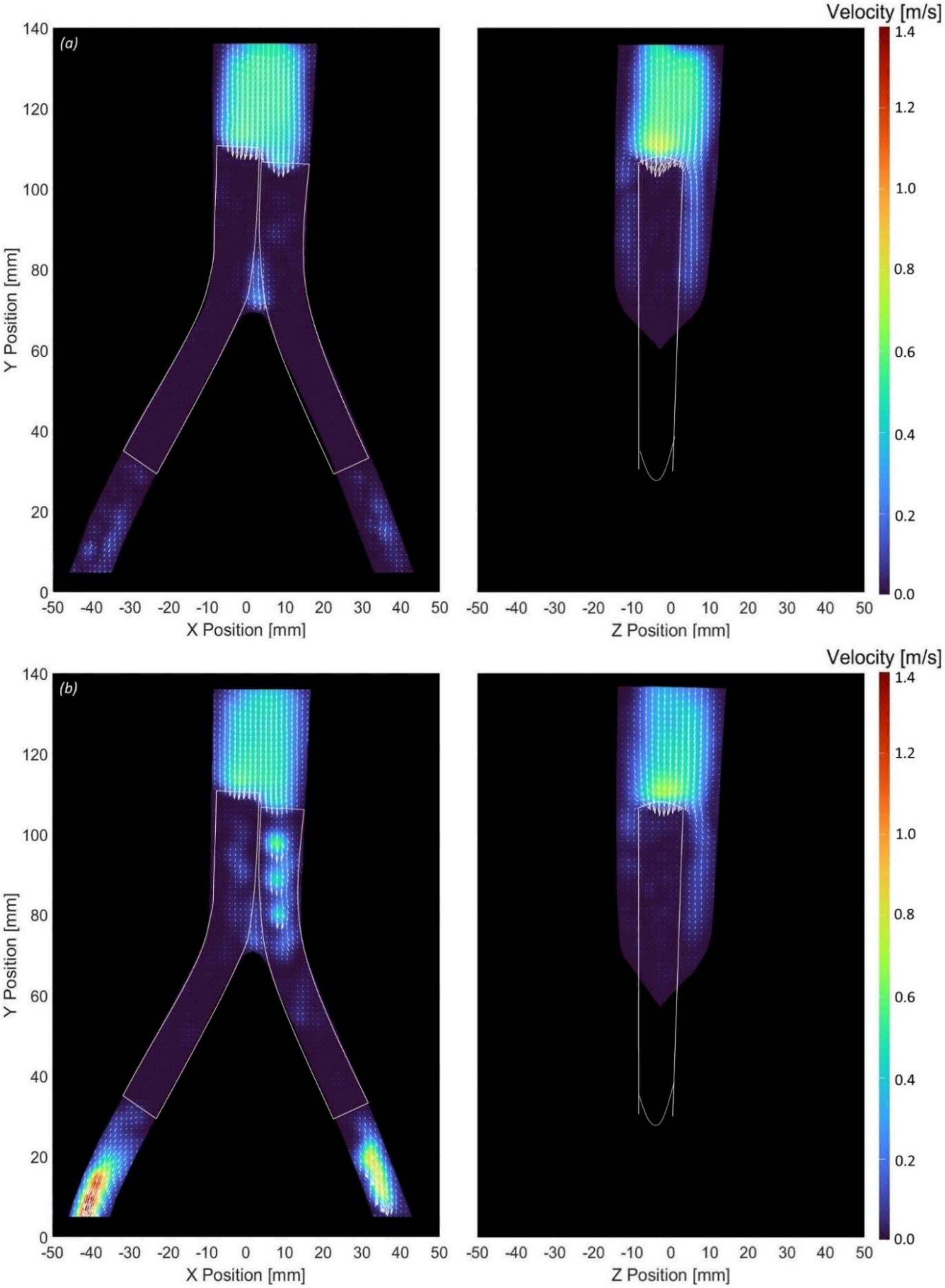

*Figure 6.6: (a) t/T=0.3 peak systolic flow (b) t/T=0.35 peak velocity flow in iliac limbs (white = stent location)*

Flow reversal was first identified at *t/T*=0.45 in both coronal and sagittal planes. Figure 6.7 shows that the boundary layer separated at walls proximal to the KS leading to reverse flow in both the coronal and sagittal planes during decelerating systole. The flow at the arterial walls has the least momentum and, hence, reverses direction ahead of the rest of the flow [22].

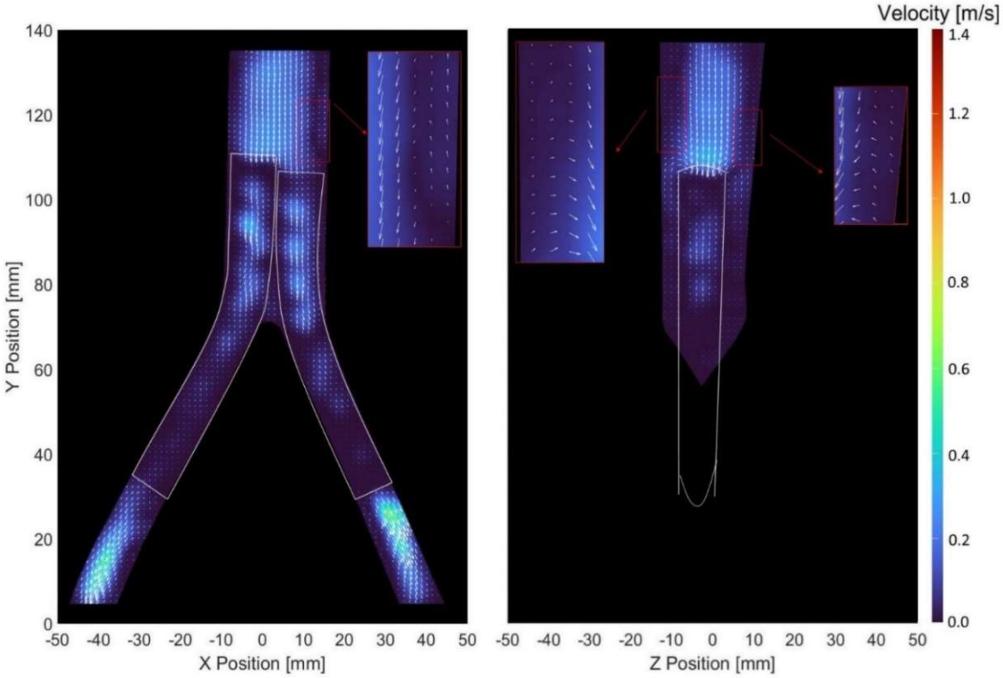

*Figure 6.7: Flow reversal at proximal arterial walls at t/T=0.45 (white = stent location)*

The peak backflow velocity was 0.70 m·s$^{-1}$ occurring at *t/T*=0.55 (Figure 6.8a). The flow magnitude was identified in both common iliac branches of the phantom. Fluid accumulated in the extra-stent region during systole and was ejected back into the phantom abdominal aorta during diastole causing disruption to the flow uniformity. On the sagittal plane, the flow from the surrogate stents appears to be reversing direction, with vectors pointing normal to the walls, indicating expected distortion of the compliant phantom. Disturbed flow continued to be identified proximal to the surrogate stent through to *t/T*=0.65 (Figure 6.8b). The most notable disturbance occurred at *t/T*=0.6 (Figure 6.8b). A recirculation can be identified in the central coronal inlet flow (Figure 6.8b), along with forward flow at the walls in both the coronal and sagittal planes (Figure 6.8b-c).

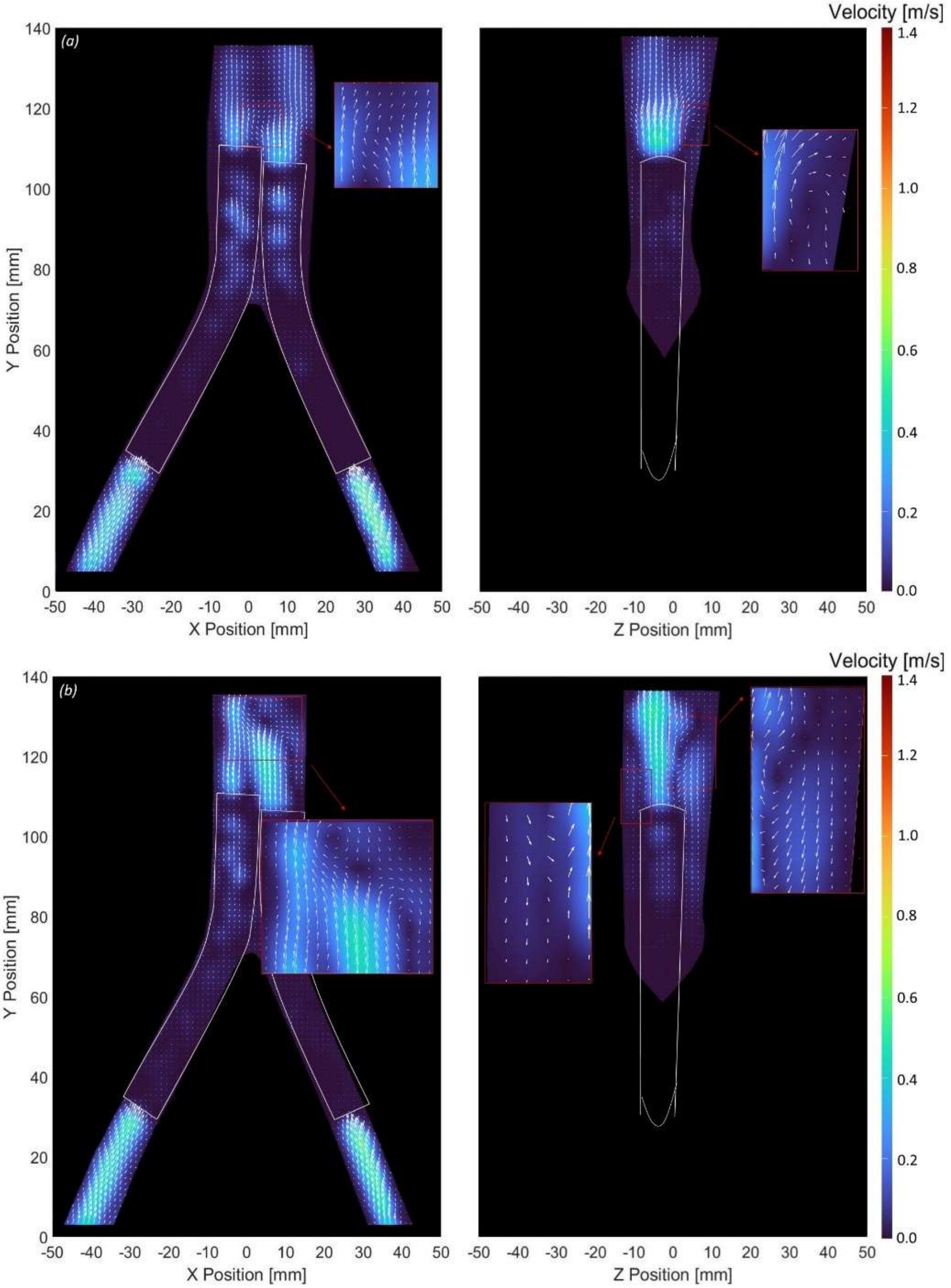

*Figure 6.8: (a) t/T=0.55 Peak reversed identified in both iliac limbs (b) t/T=0.6 disturbed flow proximal to surrogate stents (c) t/T=0.65 further disturbed flow (white = stent location) (continued on next page)*

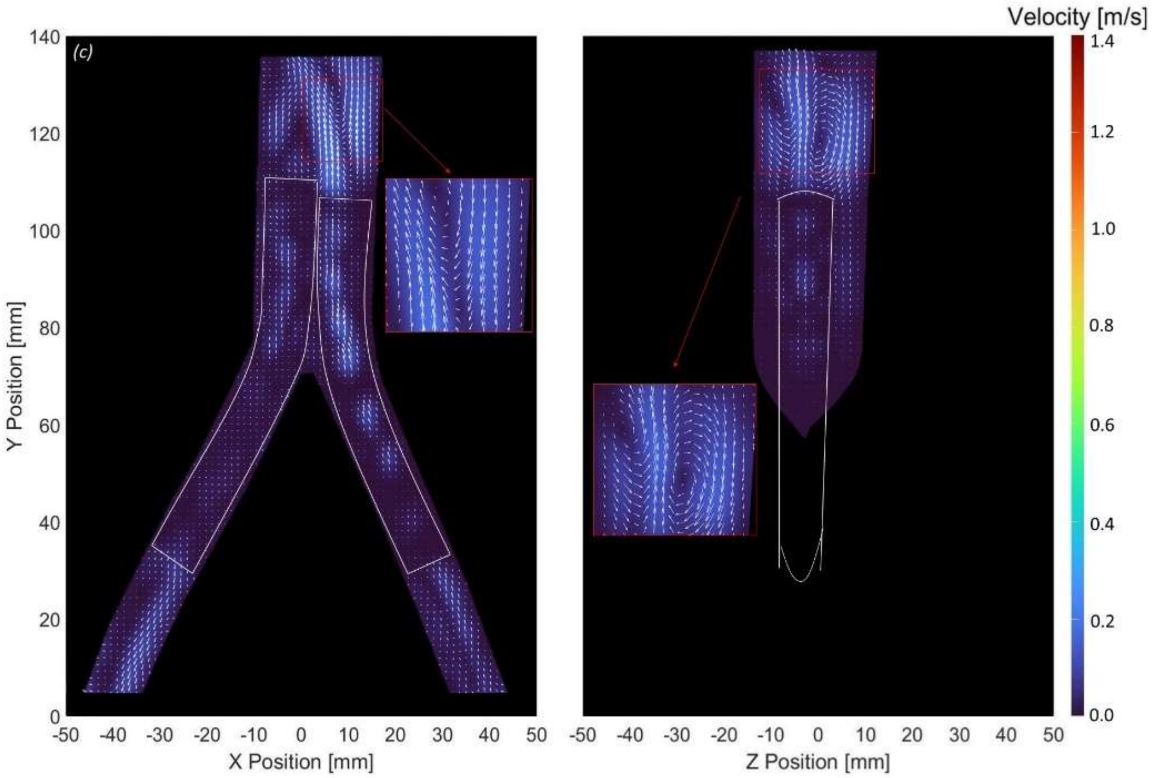

*Figure 6.8: (a) t/T=0.55 Peak reversed identified in both iliac limbs (b) t/T=0.6 disturbed flow proximal to surrogate stents (c) t/T=0.65 further disturbed flow (white = stent location)*

The change in diameter for the phantom’s coronal and sagittal axes across one cycle is shown in Figure 6.9. Note that pixilation of the images led to relatively low-resolution estimations. Nonetheless, the reduction on the sagittal cross-section between *t/T*=0.55 and 0.65 was significant.

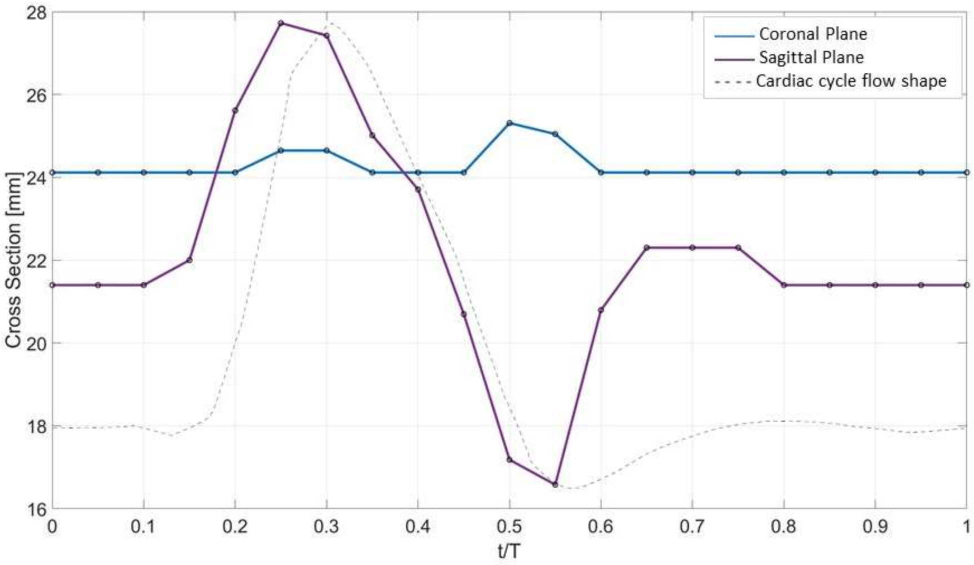

*Figure 6.9: Cross-section diameters measured 20 mm proximal to the aorto-iliac bifurcation with cardiac waveform shape overlaid (18 mm line indicates 0 L.min$^{-1}$ flow)*

## 6.4. Discussion

The flow behaviour caused by a surrogate KS within the aorto-iliac bifurcation was investigated using PIV analysis in an idealised phantom geometry. Proximal and distal stent flow behaviour was identified at regular intervals throughout the duration of the waveform. Compliant modelling of the potential stenting haemodynamics due to the KS has not previously been investigated and yielded important effects, particularly proximal to the stents. While AIOD is ubiquitous with rigid arteries, stents are generally deployed such that their inlets and outlets and situated within healthy compliant artery. Hence, arterial compliance is an important factor in the haemodynamics caused by the KS. Precise analysis of the intra-stent flow was not conducted due to the light reflections making the data collected unreliable in this region.

The vector profiles during late systole were uniform and aligned with the direction of flow, as expected, due to the high momentum forces overcoming the adverse pressure gradient which may contribute to boundary layer separation. Flow reversal was first identified proximal to the stents at the phantom walls in Figure 6.7 at *t/T*=0.45 despite the input flow rate still being positive until after *t/T*=0.5. The flow rate in the centre of the lumen was positive until *t/T*=0.5. The profile is typical of decelerating systolic flow prior to backflow [22]. The profile indicates there was a low wall pressure during late systole.

At the peak systolic flow, the proximal velocity in the phantom was identified as 0.69 $m \cdot s^{-1}$ in Figure 6.6a corresponding to an *in-vivo* flow rate of 0.31 $m \cdot s^{-1}$. A flow rate of 0.31 $m \cdot s^{-1}$ is within the reported range for infra-renal abdominal aorta velocities at rest (0.23 $m \cdot s^{-1}$–0.45 $m \cdot s^{-1}$) [303, 304]. The velocity is similar to the experimental velocity identified by Groot Jebbink, et al. [204] (0.3–0.4 $m \cdot s^{-1}$). The peak flow was uniform and appeared plug-shaped with no-slip at the phantom artery walls. The sagittal wall had a lower WSS value compared to the coronal plane walls. Low WSS has been linked to thrombosis [305] which may aid the reduction of dead space between the proximal KS inlets and the native aorto-iliac bifurcation. However, this has not been confirmed and the low WSS may also exacerbate the progression of atherosclerotic lesions resulting in edge-of-stent and in-stent restenosis. The peak velocity through the iliac arteries distal of the surrogate stents was identified as 1.4 $m \cdot s^{-1}$ at *t/T*=0.35 *in-vitro* (Figure 6.6b). Reynolds number scaling implies this velocity corresponds to an *in-vivo* peak velocity of 0.62 $m \cdot s^{-1}$. The flow velocity within the iliac arteries is poorly documented and there are a range of values identified. Luo, et al. [306] modelled the velocity in the common iliac arteries and determined peak velocity was about 0.60–0.75 $m \cdot s^{-1}$ across both pseudo-compliant and rigid models. The peak velocity modelled was well within this range. Meanwhile, peak velocity *in-vivo* was 1.1-2.9 $m \cdot s^{-1}$, according to Langsfeld, et al. [307]. The large variance between studies makes defining healthy flow difficult. However, the flow through the iliac limbs appeared plug-shaped and undisturbed. Conservation of mass principles indicate the *in-vitro* outlet velocity should be approximately 1.83 $m \cdot s^{-1}$, assuming a rigid model. An experimental study on endovascular grafts similarly showed a jet flow at the graft trailing edge [308]. Disrupted or abnormal flow was not identified in the iliac limb. The flow was plug-shaped and velocity magnitudes within reported ranges.

The haemodynamics imply the KS does not cause significant deleterious downstream effects on the flow or endothelial growth patterns of the iliac limbs. *In-vivo* studies of healthy haemodynamics in the iliac limbs are difficult to find. However, similar result in the iliac limbs were found by Groot Jebbink, et al. [204].

Disrupted flow was identified at *t/T*=0.55 to 0.65 in the coronal and sagittal planes (Figure 6.8). Anterograde flow was identified at the phantom walls in Figure 6.8b-c, despite input flow rate being negative (Figure 6.6). The disturbed flow occurs immediately after the minimum sagittal diameter was measured (Figure 6.8b). The coronal diameter was larger than the sagittal diameter during this period, indicating an elliptical contraction. As the phantom artery geometry was restored, it created a low-pressure pocket in the region of the form collapse. A negative pressure gradient pulled fluid from the bulk of the flow into the pocket, creating a region of forward flow despite the negative input flow. Mallory, et al. [7] identified that grafted stents inhibit but do not preclude neo-intimal growth, thereby reducing the risk of in-stent thrombosis. The collapse observed in Figure 6.9 and deleterious flow behaviour may be linked to stent thrombosis or distal embolism. However, the sagittal collapse has not previously been identified *in-vivo.* Specific *in-vivo* studies may elucidate the relative contribution of the haemodynamics observed in this study to stented arterial patency.

This study was limited to proximal and distal stent flow behaviour. Intra-stent particles had poor trackability as a result of light reflections. The obstruction led to unfeasibly low intra-stent velocity despite the high outlet velocity (Figure 6.6b). Despite this, the data sets still have a high percentage of valid velocity vectors. Future research may use fluorescent particles and colour filters to reduce reflections and try improving particle visibility through the stented region.

The use of a partial graft on one stent enabled precise co-location of both stent phantoms within the arterial phantom and allow air to be released within the model during experimental set up. The partial graft allowed transverse flow from the bifurcation to the right limb stent at peak systole, *t/T*=0.3-0.35 (Figure 6.6), but effectively sealed at all other times, precluding additional flow to the right limb stent.

Both stents received axial flow from upstream of the bifurcation. The effects of the transverse flow on the peak velocities of the stent outlets were ambiguous. The omission of the graft on the right limb increased the effective compliance, allowing for greater phantom expansion, and thereby smoothing the flow. The smoothing was likely to result in reduced the peak velocity in the right stent outlet. However, the increased potential flow into the right stent via the bifurcation leak may have increased the peak flow. Ultimately, velocity magnitudes were consistent across limbs (Figures 6.7 and 6.8).

Non-crossing KS in the abdominal aorta are currently preferred as they have higher primary patency rates than KS that cross or helix [309]. The modelled configuration in this investigation had a 5% diameter cross-over. This degree of crossover is sufficiently small for the experiment to be considered non-crossing orientation. The contact between the stents and the aorta wall on the coronal plane may have aided the sagittal collapse. The stents protruded into a circular cross-section, deforming the walls at rest. This contact caused the 3.6% discrepancy in the resting diameter across the coronal and sagittal planes (Figure 6.9) and may cause the lower WSS on the sagittal walls. The space between the stents and descending aorta created a dead space region on the sagittal walls. The low pressure induced in this area during reversed flow caused collapse of this cavity. The collapse does not seem to have been explicitly noted in the relevant literature. Furthermore, the lack of published data noting an unacceptable rate of revision due to dysfunction in this dead space or case study reports implies that if such collapse occurs *in-vivo*, it presents a low risk to patients. The dead space may thrombose and eliminate the mismatch area, post-operation, before a potential collapse can create a notable dysfunction. However, there is no study supporting this conjecture.

The KS is a commonly used stenting method for patients with atherosclerosis of the left and/or right iliac limbs. Flow proximal and distal to the KS appears to maintain reasonably normal haemodynamics, throughout systole and from mid to late diastole. Disturbed flow was identified during early diastole within the phantom. The clinical impact of this observation may be exacerbated by stent orientation and requires further investigation. The KS configuration has high long-term patency despite potential disturbed flow proximal to the stents. The covered endovascular reconstruction of the aortic bifurcation (CERAB) configuration is a modification of the KS configuration. CERAB treatment includes a third stent component proximal to the KS that better directs flow from the aorta into the stented iliac limbs by reducing the area mismatch [293]. The CERAB may counteract the potential disturbed flow that some patients may be susceptible to. However, the CERAB treatment requires a more precise implementation than the KS.

Haemodynamics identified in this chapter support the use of the KS configuration to improve haemodynamics through the iliac limbs. A paucity of deleterious flow behaviour was identified proximal or distal the stent geometry. The disturbed flow in Figure 6.8 occurred due to the minor collapse in the abdominal aorta phantom at *t/T*=0.45 to *t/T*=0.55 which may have been the result of manufactured wall thickness discrepancy or stent placement.

## 6.5. Conclusions

This comprehensive *in-vitro* study of the KS was the first PIV study of a compliant phantom of the aorto-iliac bifurcation. Previous studies of the KS effect in both the aorta-iliac and coronary arteries used rigid models [204, 310]. Compliant models have been shown to reduce the risk of overestimated WSS [185] and enable phantom deformation with pulse pressure. Peak velocities at the inlet and outlet were within reported physiological ranges. Disturbed flow was identified during early diastole, immediately following a collapse in the sagittal plane which may be linked to early stent failure in some patients. The study aids the prediction of local flow behaviour proximal and distal to a stented aorto-iliac bifurcation across a full heartbeat cycle. The results provide confidence in the safety for implementation of a KS configuration as a first step repair for AIOD despite the area mismatch and rigidity of the stents.

# *7. Analysis of flow through extra-anatomic bypasses between supra-aortic branches using PIV*

This chapter investigates the haemodynamic behaviour within supra-aortic extra-anatomic bypasses. Bypasses are stent grafts used to revascularize arteries that would otherwise be unable receive sufficient blood. However, bypassing arteries that are not totally occluded introduces a potential for competitive flow which may cause the bypasses to failure. Competitive flow within the supra-aortic arteries has not previously been identified. This chapter aimed to identify deleterious haemodynamics due to prophylactic inclusion of bypasses from the brachiocephalic artery and left common carotid artery, and from the left common carotid artery and left subclavian artery. Four model setups investigated the necessity of intentionally blocking the proximal left subclavian and/or left common carotid artery.

## 7.1. Introduction

As introduced in Chapter 1, cardiovascular diseases of the aortic arch can be difficult to treat due to the complexity of the arterial geometry [6]. Thoracic endovascular aortic repair (TEVAR) is a popular repair method for stenosis, dissection and/or aneurysm of the aorta. The comparative simplicity of TEVAR to open arch repair methods leads to lower intra-operative mortality and shorter recovery times [8]. TEVAR is a minimally invasive stenting method that feeds a stent through a small incision in the groin up to the location of the arterial disease. TEVAR stent implants require a minimum 20 mm of healthy aorta proximal and distal of the disease region to effectively prevent endoleak. Depending on the location of the arterial dysfunction, the TEVAR graft may need to cover the supra-aortic arteries [311]. To maintain blood perfusion to the upper extremities, rerouting flow to the supra-aortic arteries is necessary.

The aortic arch was introduced in Section 1.1.1.2. There are typically three arteries that branch from the aorta. The brachiocephalic artery (BCA) is the first and largest branch. The BCA bifurcates into the right common carotid artery (RCCA) and right subclavian artery (RSA). The left common carotid artery

(LCCA) is the second branch off the aortic arch, and the left subclavian artery (LSA) is the third branch. The BCA, LCCA and LSA provide blood to the upper limbs, thorax and brain [4]. Revascularisation of the affected arteries prevents cerebral malperfusion and upper limb ischemia [8, 312]. Sufficient blood perfusion is pivotal to prevent brain damage, organ necrosis and mortality.

Thoracic extra-anatomic bypasses (EAB) are grafted stents used to revascularise supra-aortic arteries that blocked by the TEVAR graft. EAB create alternate pathways for blood to flow (Figure 7.1). EAB can be used to circumvent occlusion of proximal supra-aortic arteries [313], or when surgical intervention, such as TEVAR, leads to blockage of blood flow [314]. Bypasses between the BCA and LCCA (BC bypass) and between the LCCA and LSA (SC bypass) may be used for occlusive disease of the proximal LCCA and/or LSA, and for TEVAR that is situated over the LCCA and LSA inlets [314].

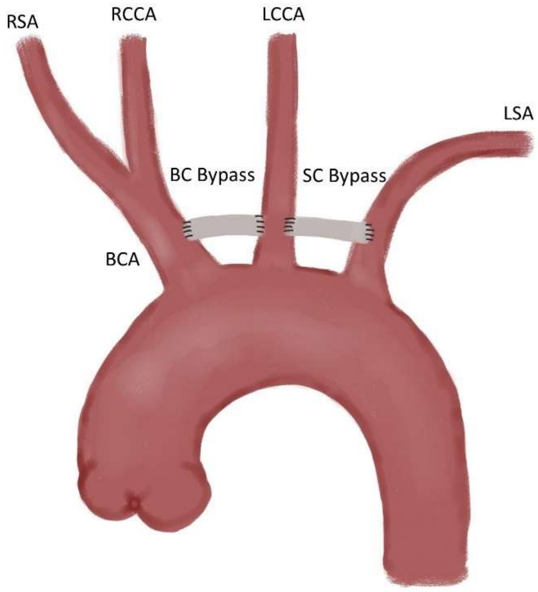

*Figure 7.1: Extra-anatomic bypass example*

Clinical studies have been conducted on the efficacy of revascularisation of the LSA via EAB [8, 51, 311, 312, 315]. Failing to revascularise the limb has a higher incidence of upper extremity ischemia [311]. The effects of revascularisation of the LCCA via EAB has not been studied as frequently as revascularisation of the LSA. However, revascularising the LCCA is always necessary to prevent neurovascular compromise [9, 316, 317]. EAB may be implemented prior to TEVAR surgery [314, 315]. Prophylactic revascularisation is encouraged in non-emergency cases [314]. Bypass grafts implemented prior to TEVAR surgery have been associated with lower incidence of neurologic complications and limb ischemia [8, 312]. However, it is not clear whether proximal limbs such as the LSA and LCCA should be embolized/ligated following prophylactic revascularisation. In particular, coil embolization or vascular plugs are sometimes located between the revascularisation and the aortic arch to intentionally prevent flow entering at the proximal LSA or LCCA prior to TEVAR placement [8, 315]. Feezor and Lee [311] suggest failing to embolize the proximal limbs may result in bypass graft occlusion due to low intra-graft flow rates and high recirculation zones. This low flow rate can be caused by a phenomena termed ‘competitive flow’. Competitive flow can occur when the affected artery is not totally occluded, thereby enabling some flow through the anastomosed artery rather than the bypass [52]. Thus, competitive flow can lead to low rates of perfusion through the graft, and may lead to intra-graft stenosis.

The aim of this study was to identify the risk of competitive flow and evaluate the necessity for proximal limb ligation/embolization of the LCCA and LSA following the implementation of various BC and CS bypass. Competitive flow is defined as persistently low/stagnating flow in the BC or CS bypasses. Highly disrupted flow within the bypasses was also considered to result in an increased risk of stenosis. While competitive flow may cause stenosis formation in the bypasses, competitive flow within the BC and CS bypasses has not previously been investigated, *in-vivo, in-vitro* or *in-silico*. This study uses particle image velocimetry (PIV) to capture haemodynamic behaviour across the lateral plane in a silicone model of the aortic arch with prophylactic revascularisation of supra-aortic arteries.

## 7.2. Methods

### 7.2.1. Model Design

An idealised model of the aortic arch with three supra-aortic arteries was designed using geometric dimensions of the aortic arch, brachiocephalic, left common carotid and left subclavian artery from Hütter, et al. [96] (1.5x scale in Figure 7.2). Supra-aortic arteries were designed perpendicular to the aortic wall. Distal branching beyond the brachiocephalic bifurcation was omitted from the model and the branch lengths were increased to reduce the effects of rigid fixings on the fluid flow behaviour. Tortuosity of the aortic arch and branched arteries was also omitted to ensure planar illumination of the PIV system yielded meaningful full field results. A simplified model was used as there are some common mutations that alter the morphology, leading to high inter-patient variability [14, 318, 319]. Thus, the simplified model ensures generalisability.

The phantom was manufactured with Sylgard 184 silicone (Dow Corning, MI, USA). Sylgard 184 has a Young's modulus of 1.32 MPa. The model geometry was scaled to be 1.5x life scale to produce a consistently achievable wall thickness of 1.0 mm, using normalised compliance matching (Equation 2.16).

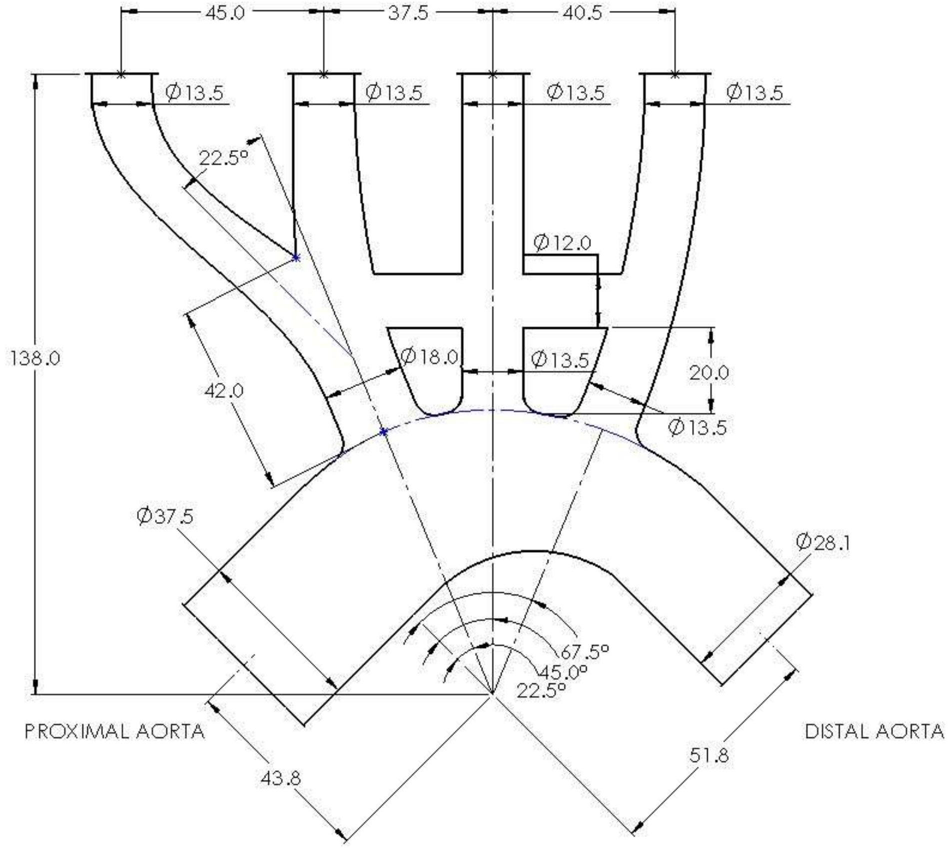

*Figure 7.2: Scaled in-vitro idealised geometry. All dimensions in mm except when specified*

An EAB from the BCA to LCCA and the LCCA to LSA artery was included 20 mm distal of the aorta-LCCA intersection. The bypass location was determined via clinical expertise of a cardiovascular surgeon collaborator. The EAB had a scaled diameter of 12 mm. This diameter is 1.5x of a typical diameter for carotid-subclavian bypass grafts (8 mm) [51]. The bypass was designed with a 2 mm wall thickness to achieve a compliance mismatch mimicking the mismatch between grafts and arterial tissue. The dimensions used and the potential *in-vivo* rangers are provided in Table 7.1.

*Table 7.1: In-vivo and in-vitro arterial parameters for aortic arch and supra-aortic branches*

| | ***In-vivo (range)*** | ***In-vitro 1.5x scale*** |
|---|---|---|
| **Young's modulus [MPa]** | 0.561 (0.4 – 1.071) | 1.32 |
| **Arterial wall thickness [mm]** | 1.2 (1.16 – 1.63) | 1.0 |
| **Bypass grafts wall thickness [mm]** | N/A | 2.0 |
| **Ascending aorta Diameter [mm]** | 25.0 (25.0 – 29.0) | 37.5 |
| **Descending aorta Diameter [mm]** | 18.7 (18.3 – 25.0) | 28.1 |
| **BCA Diameter [mm]** | 12.0 (8.5 – 12.4) | 18 |
| **BCA length [mm]** | 28.0 (28 – 34) | 42 |
| **Right Subclavian Artery (RSA) Diameter [mm]** | 9.0 (8.4 – 9.9) | 13.5 |
| **Right Common Carotid (RCCA) Diameter [mm]** | 9.0 (7.4 – 9.5) | 13.5 |
| **LCCA Diameter [mm]** | 9.0 (7.4 – 9.5) | 13.5 |
| **LSA Diameter [mm]** | 9.0 (8.4 – 9.9) | 13.5 |
| **Bypass grafts Diameter [mm]** | 8.0 | 12 |

### 7.2.2. Phantom Manufacture

The phantom was manufactured using a lost-core casting method, introduced in Section 2.8.2. A two-part female mould and one-part male mould, with three concentric locating flanges, were designed using SolidWorks (DS SolidWorks, VIY, France). A cavity between the moulds created the negative phantom geometry (Figure 7.3). The moulds were fuse deposition moulded (FDM) using the Stratasys F370 3D printer (Stratasys, REH, Israel). The moulds were assembled, and the cavity filled by injecting Sylgard 184 silicone (Dow Corning, MI, USA) from the base, allowing air to vent from the top. The silicone was cured at room temperature for 48 hours. Following curing, the female mould was mechanically removed, and the male mould was dissolved in acetone.

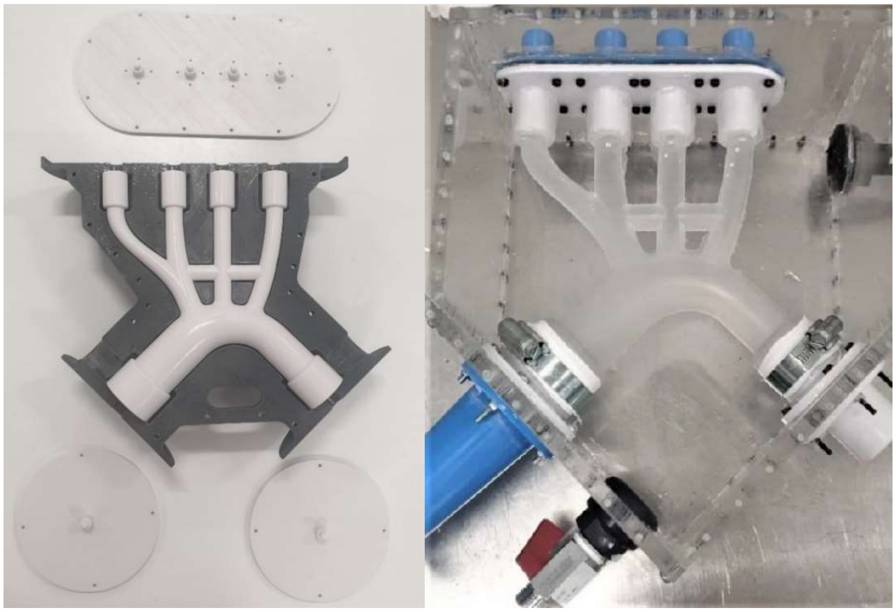

Figure 7.3: 3D printed mould and resultant thin-walled silicone phantom

The effects of ligation/embolization or atherosclerotic occlusion of proximal arteries was mimicked using a small silicone plug (Figure 7.4). The geometry of the silicone plug produced sufficient radial hoop stresses to remain located within the proximal supra-aortic LSA and LCCA during and between experiments. The plug protruded 1 mm into the aortic arch flow to create an effective seal. However, the protrusion into the aorta had a negligible effect on the flow within the supra-aortic arteries and bypasses. To model the potential presence of competitive flow, four model configurations were investigated: A) no blockages of any artery, B) blocked flow to the LCCA, C) blocked flow to the LSA, D) blocked flow to both the LCCA and LSA (Figure 7.5). Configuration 1 was used as the benchmark to compare the other configurations to.

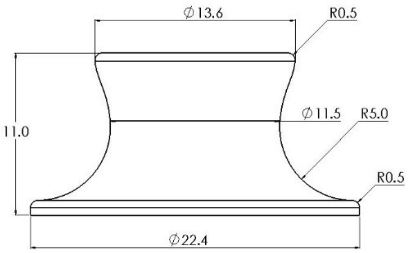

Figure 7.4: Silicone plug geometry

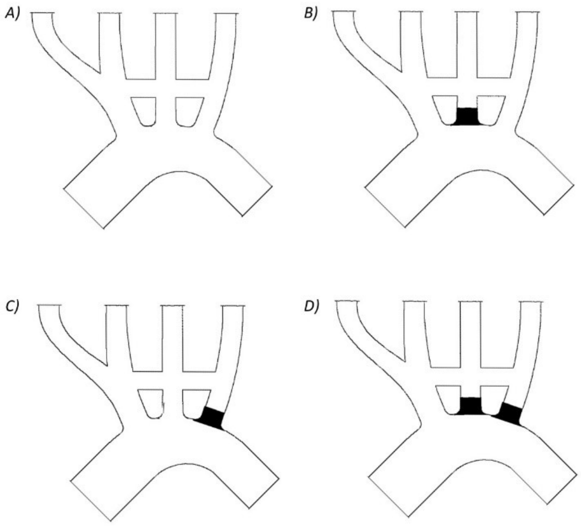

Figure 7.5: Model configurations A) no blockages of any artery, B) blocked flow to the LCCA, C) blocked flow to the LSA, D) blocked flow to both the LCCA and LSA

### 7.2.3. Experimental Configuration:

A three-part transparent working solution containing 45.6% (by mass) water, 28.8% glycerine and 25.6% urea was used. The working solution had a refractive index of 1.41, matching that of Sylgard 184 silicone, and a kinematic viscosity $(\nu)$ of 3.15x10$^{-6}$ m$^{2}\cdot$s$^{-1}$ [81]. The scale and fluid viscosity were matched to *in-vivo* geometry and blood viscosity (3.51x10$^{-6}$ m$^{2}\cdot$s$^{-1}$) via dynamic matching of the Reynolds $(Re)$ and Womersley $(Wo)$ Numbers (Equations 2.12 and 2.13, respectively). Silver coated, hollow glass spheres, of nominal diameter 10 µm, were used to seed the flow.

A pulsatile waveform was scaled from Stalder, et al. [239] for the proximal aortic arch averaged across 30 young volunteers (23.8±3.3 years old), taken at rest (Figure 7.6). The waveform was achieved with a dual-pump system described in Section 2.6.3. The experiment had peak Reynolds and Womersley numbers of 3880 and 17.4, respectively. Figure 7.7 shows the flow circuit. A diaphragm pump with in-built check valves (Figure 7.7.B) provided the mean flow to the system, whilst a piston pump driven by a stepper motor (Figure 7.7.C) modulated flow to form the pulsatile waveform. The piston was controlled by a DAQ acquisition system developed in LabVIEW (Figure 7.7.K). A Krohne IFC300 electromagnetic flowmeter monitored the flow immediately proximal to the phantom inlet (Figure

7.7.E). A 1.5 m pipe connected the flow straightener and flowmeter to allow flow to fully develop prior to entering the phantom. Repeatable waves were maintained using a closed feedback loop from the electromagnetic flowmeter to the DAQ acquisition system. The outlet pressure was controlled by a head tank 150 mm above the model LSA outlet (Figure 7.7.G). A single head tank controlled the head pressure of all the model outlets.

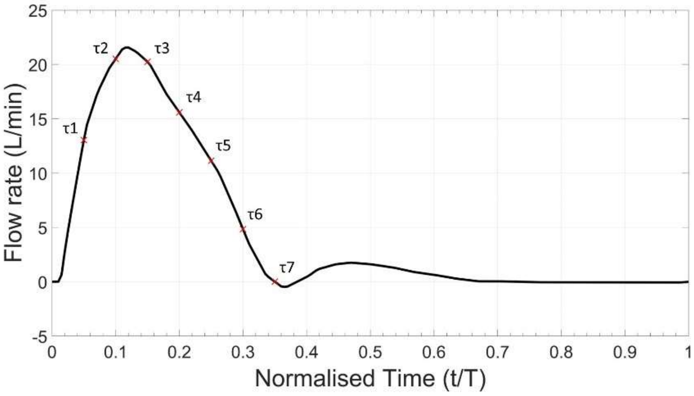

*Figure 7.6: In-vitro waveform for proximal aortic arch*

Planar PIV was used to capture the fluid behaviour through the phantom. A Double Pulse EverGreen[2] Nd:YAG laser illuminated the particles within a 1 mm thick slice of the fluid flow along the centre lateral plane. Fifty image pairs were captured at seven discrete timesteps (τ) across the waveform (noted in Figure 7.6). To maintain accurate tracking of particles within the flow, the time delays between image pair captures varied depending on the flow rate of the fluid, from 200 µs to 1200 µs. A single TSI PowerView 4MP LS PIV camera (TSI Inc., USA) with 2360 × 1776 pixels resolution captured image pairs. TSI Insight 4G (TSI Inc., USA) was used for the initial processing of the image pairs and confirmed a minimum good vector validity of 92% across all image pairs. Full processing was carried out using PIVLab in MATLAB (MathWorks, MA, USA). Image pairs were spatially ensemble averaged using a two-pass recursive nyquist grid beginning with a 64x64 interrogation window resolution and reducing to 32x32 on the second pass. A local median threshold rejected vectors if they were more than 0.05 m·s$^{-1}$ different from over half of the surrounding vectors. Rejected vectors were replaced with interpolated estimates. 1.3% of vectors were rejected based on the local median threshold.

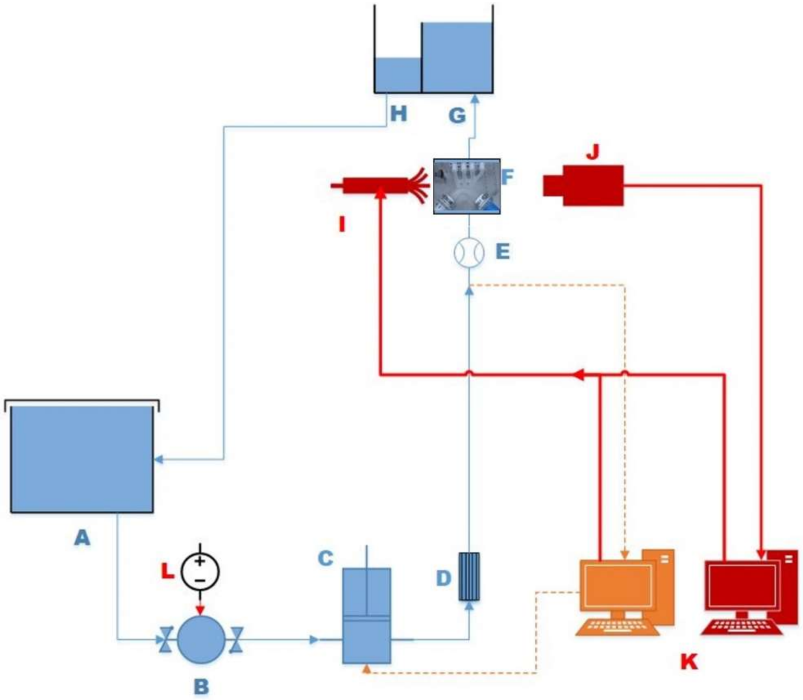

*Figure* 7.7*: The blue lines represent the fluid circuit. The red lines are the laser trigger and camera data cable. The orange circuit is the flow rate feedback loop. The components are: A Reservoir; B In-line Diaphragm pump; C Piston pump; D Flow Straightener; E Electromagnetic Flowmeter; F Phantom Model; G Head Tank; H Overflow Weir; I Nd:YAG Laser; J Camera; K Data Acquisition System; L DC Power Supply.*

Flow perfusion through the proximal supra-aortic arteries was evaluated for risk of ischemia to the head and upper limbs. Volumetric flow rate was determined at 6 locations in the aortic arch phantom: 1) the proximal arch, 2) the BCA, 3) the proximal LCCA, 4) the proximal LSA, 5) the BC bypass and 6) the CS bypass (Figure 7.8). Five segments were extracted from each location and averaged to improve accuracy. Volumetric flow rate was calculated with Equation 7.1.

$$Q = \sum_1^n \frac{1}{n} \int_{-r}^{r} \pi \mathbf{v}(\rho) \cdot \mathbf{b} d\rho \qquad \text{(Eq. 7.1)}$$

Where: *n* is the number of segments used, **b** is a vector defining the distal axial direction, $\mathbf{v}(\rho)$ is the velocity vector at some variable radius from the centre of the lumen $(\rho)$, the limits of $\rho$ are –*r*, and *r*.

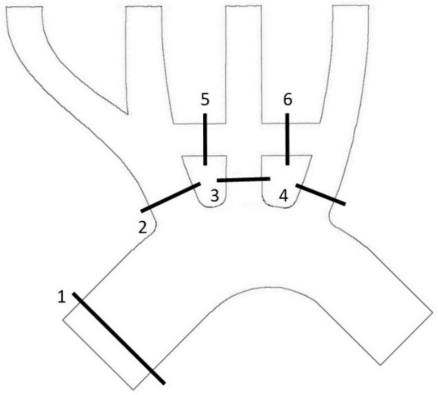

*Figure 7.8: Flow rate extraction locations: 1) the proximal arch, 2) the BCA, 3) the proximal LCCA, 4) the proximal LSA, 5) the BC bypass and 6) the CS bypass*

## 7.3. Results

The vector profile for each of the configurations at τ2 showed normal flow through the aortic arch (Figure 7.9). The velocity profiles show the velocity profile through the BC bypass and CS bypass (labelled 5 and 6 in Figure 7.8) across the full waveform (τ1-τ7), for each of the configurations. The vector profiles show that flow velocity through the BCA was comparatively higher than the velocity through the proximal LCCA or LSA, regardless of the different configurations. Though, the velocities in the BCA did increase in configurations B-D, as to be expected. Configuration A had a low flow velocity through both the BC and CS bypasses. The low flow is confirmed in the velocity profiles, which, even at peak systole, did not exceed 0.1 m·s-1. The velocity vectors for configuration B had a much-improved flow through the BC bypass at peak systole. However, there is very little flow through the CS bypass. The velocity profiles indicate that during late systole indicate there was retrograde flow through late systole. Blocking the proximal LSA for configuration C showed good flow through both the BC and CS bypasses at τ2. However, there does appear to be some disruption to the flow path in the CS bypass. The CS bypass velocity profiles throughout systole have an s-shaped curve that presents negative velocities on the lower edge and positive velocities on the upper edge. Configuration D had a high velocity flow through the BC bypass at τ2. The velocity, though lower, sustained the flow through the CS bypass as well. The velocity profile through both bypasses peaked at a higher velocity that any other configuration. There were some s-shaped curves through the BC bypass during late systole.

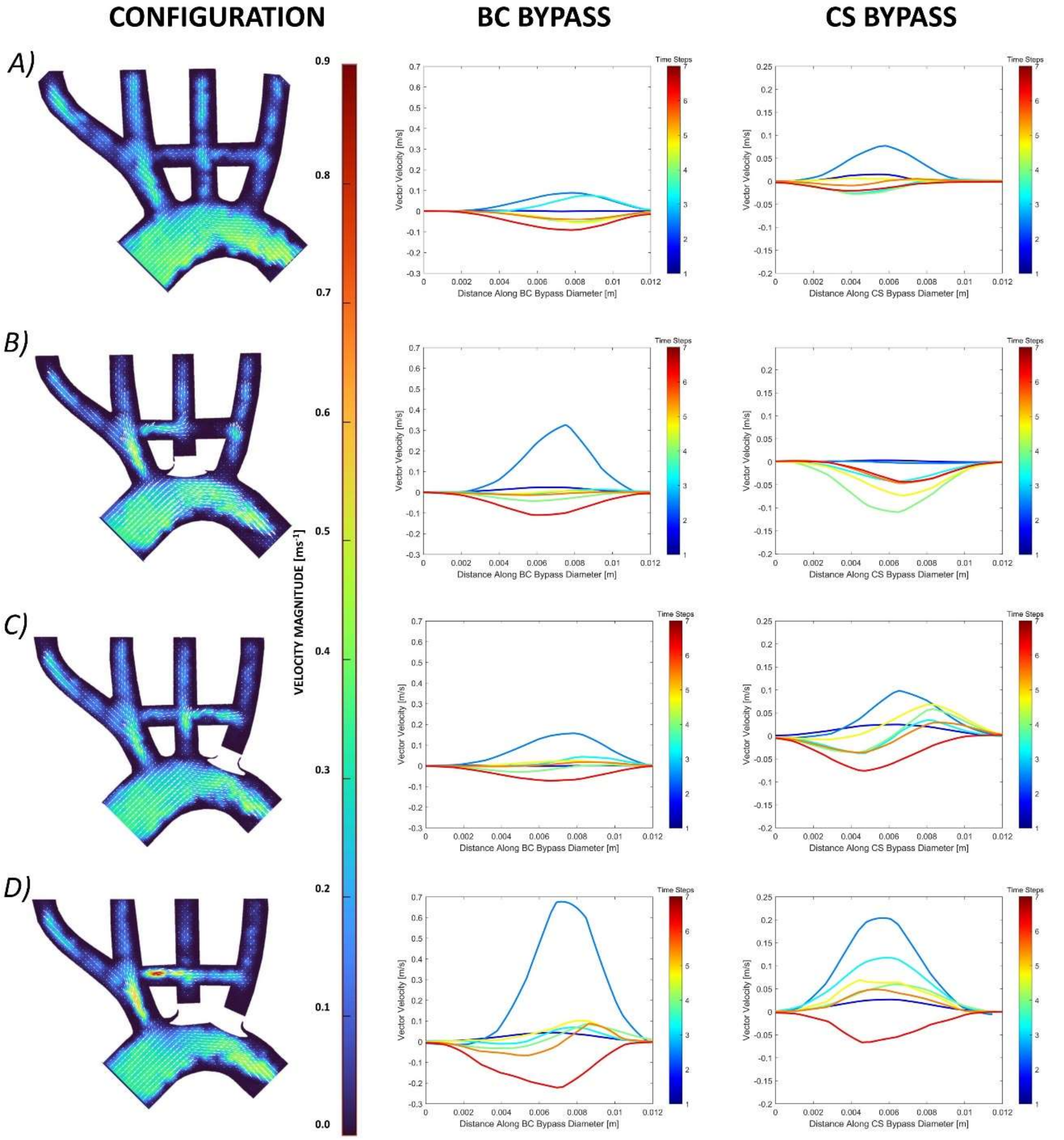

*Figure 7.9: Velocity vector map at peak systole and respective systolic velocity profiles through the BC and CS bypasses for each configuration*

The low velocities identified through the BC bypass in configurations A (Figure 7.10a) and C (Figure 7.10b) were inspected for stagnation and recirculation. At τ1 there was a clear stagnation of flow in both configurations A and C. Reciprocating flow was identified through the bypass of configuration A at τ2-τ4. Configuration C also had clear disruption to the flow at τ3 and τ4. The flow disruptions and sudden flow direction changes were not present in configurations B and D.

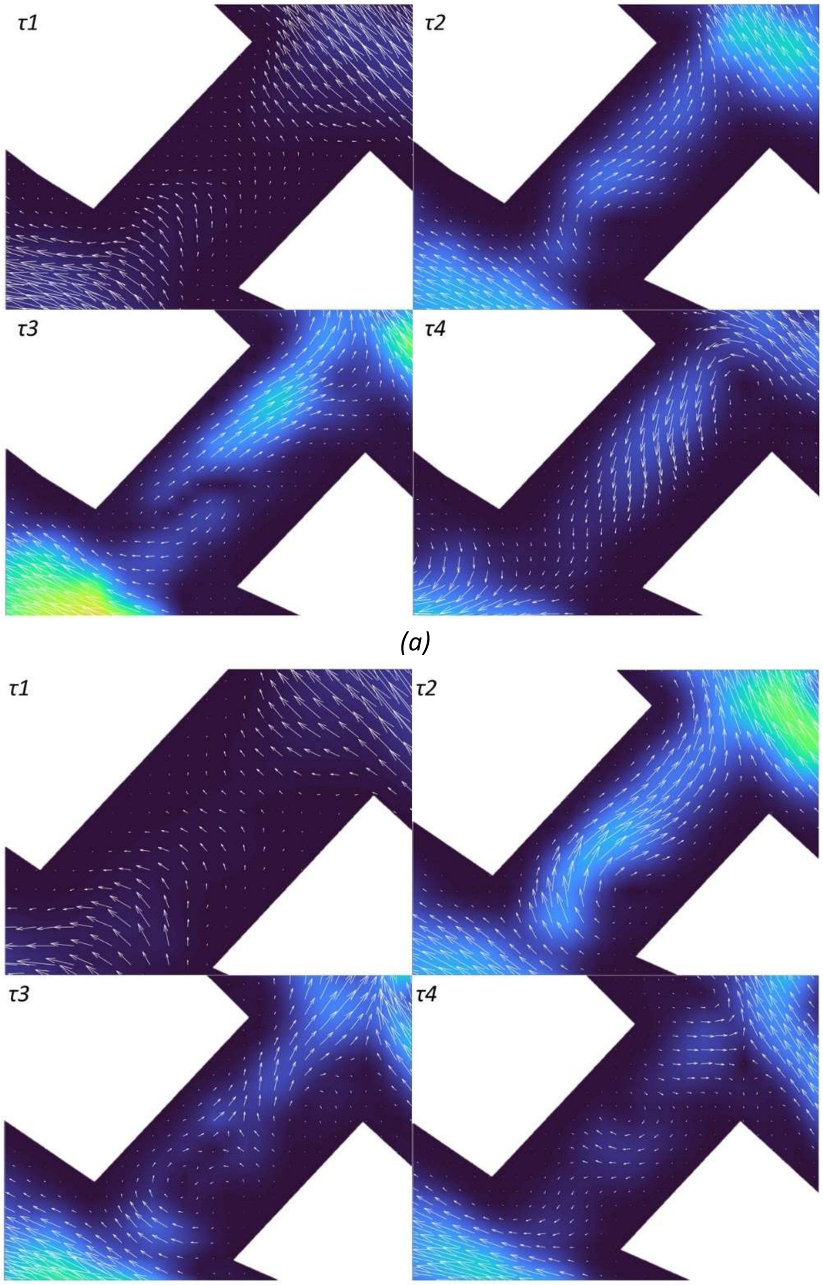

(a)

(b)

*Figure* 7.10*: Flow through BC bypass during peak systole (τ1-τ4) for (a) configuration A and (b) configuration C*

Velocities within the CS bypass in configuration B had significant stagnations at τ1 and τ2 before establishing retrograde flow from the proximal LSA to distal LCCA (Figure 7.11a). The stagnation in the

SC likely occurred due to the distal LCCA being fed by both bypasses, but the flow from the BC bypass had a shorter distance to travel. There was no stagnation within the CS bypass for configuration C (Figure 7.11b). However, recirculating flow was observed within the CS bypass resulting in the s-curve identified in Figure 9.

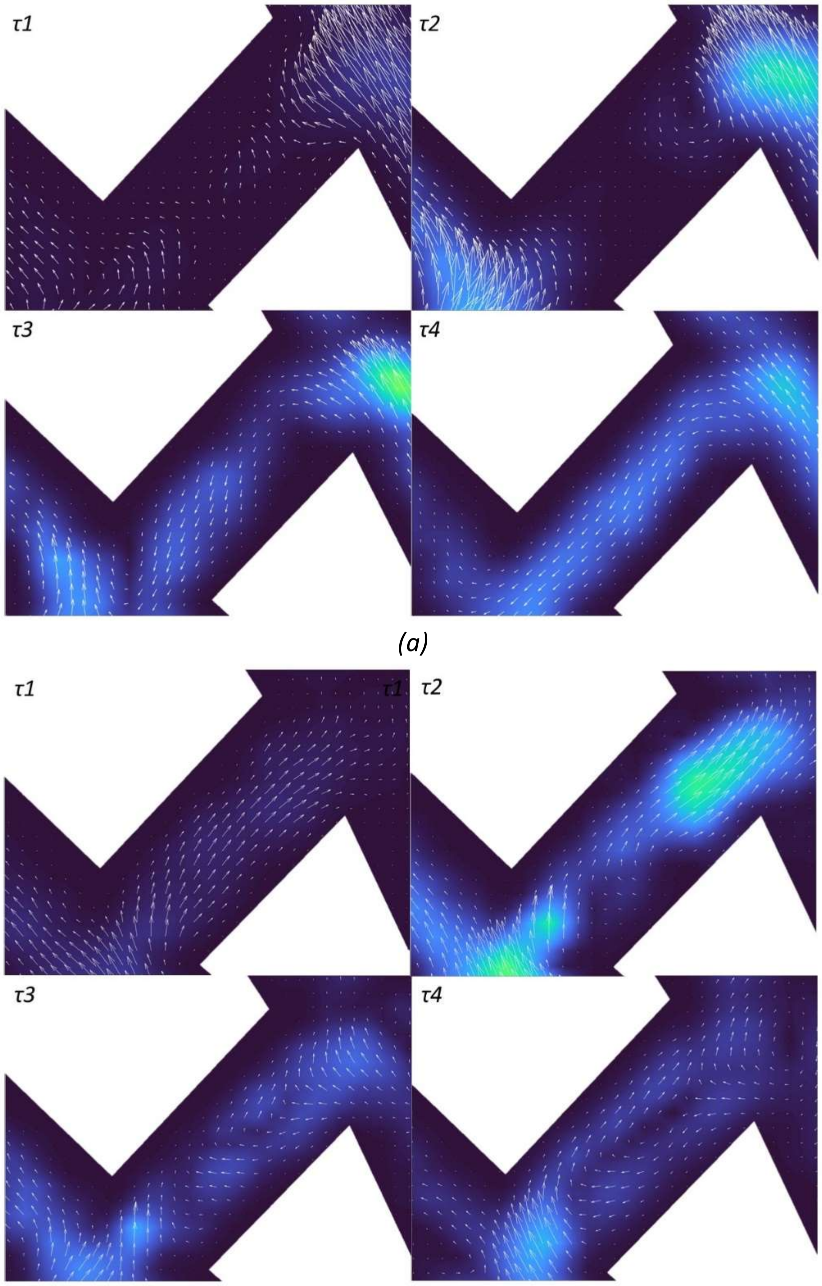

*(a)*

*(b)*

*Figure 7.11: Flow through CS bypass during peak systole (τ1-τ4) for (a) configuration B and (b) configuration C*

The net volume of flow through each of the six locations (identified in Figure 7.8) throughout systole is presented in Table 7.2. Configuration D had the lowest total volume of flow from proximal aorta to the supra-aortic arteries (6.0%). Perfusion through configuration A was similar to configuration D. Configuration B had the highest perfusion through the supra-aortic arteries of 8.0%. The net flow through both bypasses for all configurations is highest in configuration D. Configuration D had more than 4x the volume of flow through the BC bypass than any other configuration. The volume of flow through the bypasses of configuration A was far lower than any other configuration.

*Table 7.2: Volume of flow throughout systole*

| **Systolic Volume (τ1-τ7) [L]** | **Proximal Aorta** | **BCA** | **LCCA** | **LSA** | **Flow through supra-aortic arteries (% of inlet flow)** | **BC bypass** | **CS bypass** |
|---|---|---|---|---|---|---|---|
| **Configuration A** | 0.1301 | 0.0050 | 0.0016 | 0.0016 | 0.0082<br>(6.3%) | -0.0003 | -0.0001 |
| **Configuration B** | 0.1403 | 0.0078 | N/A | 0.0034 | 0.0112<br>(8.0%) | 0.0005 | -0.0015 |
| **Configuration C** | 0.1356 | 0.0069 | 0.0026 | N/A | 0.0095<br>(7.0%) | 0.0006 | 0.0007 |
| **Configuration D** | 0.1408 | 0.0084 | N/A | N/A | 0.0084<br>(6.0%) | 0.0026 | 0.0020 |

## 7.4. Discussion

This experiment modelled the haemodynamics within extra-anatomic BC and CS. In-vitro analysis was carried out using a phantom aortic arch and bypasses to identify flow behaviour that may affect bypass patency. The potential for flow competition was investigated within the bypasses. The presence of stagnating flow and recirculation zones within the bypasses may indicate a high risk of graft occlusion therefore requiring further intervention to remedy [311]. The analysis focused on the supra-aortic arteries, despite imaging the total aortic arch. The proximal aortic arch was measured to confirm inlet volumetric flow only. Artefacts within the arch flow and distal of the bypasses were not investigated.

Figure 7.9 presented the velocity profiles and vector maps for each of the configuration at τ2. The *in-vitro* peak velocities within the aortic arch were 0.48 $m \cdot s^{-1}$ Reynolds number scaling leads to *in-vivo* velocity of 0.75 $m \cdot s^{-1}$, which is within the expected physiological range of peak systolic velocities *in-vivo* through the aortic arch for a patient at rest [320]. Configurations B-D showed higher flow velocities through the BCA as a result of blocking the other proximal arteries despite the geometry of the BCA and the outlet head pressure remaining the same across all configurations (Figure 7.9). Endothelial cells have strong regenerative properties enabling them to grow through some synthetic materials used in the manufacture of stents and bypasses. A newly deployed stent will typically be covered in a layer of cells within a few hours to days [54]. However, endothelial cell growth is highly dependent on the direction of fluid stimuli [4]. Stagnating and recirculating flow can result in multi-directional shear stresses that change the growth patterns of endothelial cells through the bypasses [276]. This may lead to the abnormal aggregation of cells, which can result in narrowing the lumen of the bypass and potentially leading to total occlusion prior to TEVAR deployment. The low flow through the bypasses of configuration A indicate there is likely a risk of bypass failure due to low shear stresses. However, the stagnant flow was much more notable through the CS bypass of configuration B. The vector map in Figure 7.9 shows an almost total lack of flow through the bypass indicating a notable stagnation. The velocity profile through the CS bypass indicates that there was little flow until late systole. Figure 7.11a confirms the notable stagnation at τ1 and τ2 due to competing flow through the BC bypass and proximal LSA. Configuration C had improved flow through each of the bypasses, however, throughout mid to late systole the velocity across the CS bypass had an s-shaped profile. To have both positive and negative flow within the bypass there must be a recirculation occurring as was identified at τ4 in Figure 7.11b. Configuration D had the highest absolute velocities through each of the bypasses (Table 2). Typically, the flow was also parabolic indicating a much lower risk of flow competition compared to other configurations (Figure 7.9). High velocity flow indicates higher wall shear stresses. Typically, it is low wall shear stress that leads to aggregation of fatty lipids and cell growth, prone to causing occlusion. As such, it can be assumed that the higher velocity flow correlates to a lower risk of bypass failure in configuration D.

Table 7.2 showed the net volume of fluid passing through both bypasses of configuration D was higher than any other configuration. Comparatively the flow through configuration A bypasses was almost zero. Low flow rates result in a low shear stress which has been linked to atherosclerotic lesion formation [25]. Flow through the CS bypass was similar between configurations B and D, though it flowed in inverse directions. The low flow through the CS bypass in configuration A and C implies a higher risk of bypass failure. However, Figure 7.11a shows that flow stagnated in the CS bypass of configuration B for two of the measured time steps. The comparatively low flow through the BC bypass of configurations A-C also indicates a risk of occlusion. Figure 7.10 identified flow stagnating within the BC bypass when none of the arteries were blocked (configuration A) and when the when the proximal LSA was occluded (configuration C). Stagnant flow indicates that the BC bypass of configuration A and C and the CS bypass of configuration B have a high risk of graft occlusion due to abnormal cell growth.

This experiment used an idealised model that ignored the tortuosity of the aortic arch and positioned the bypasses based on the expertise of a cardiovascular surgeon collaborator. However, the positioning of the bypasses is often at the discretion of the surgeon and may not be aligned as they were in this experiment. Altering the alignments of the bypasses may change the momentum of flow. Any branching and bifurcations downstream of the BCA bifurcation was also ignored. The distal limbs were elongated beyond physiological lengths to reduce effect of wave reflection or fluid disturbances due to the rigid outlet fixings. However, the distal fluid flow behaviour was not evaluated in this experiment. Any downstream behaviour was assumed to have negligible effect on the flow through the proximal arteries or bypasses.

Understanding the behaviour of flow through SAB between the supra-aortic arteries is vital for determining the risks of flow competition for different configurations. Configurations A-C each presented with a stagnation zones and disrupted flow throughout systole. The disruptions may indicate the prophylactic use of the BC and CS bypasses prior to TEVAR deployment requires ligation of both the proximal LSA and LCCA to reduce the risk of bypass failure. Configuration A also had low flow throughout diastole which indicated that it had the highest risk of bypass occlusion. The results of this paper will aid cardiovascular surgeons in their decision to intentionally block the proximal LCCA and/or LSA.

## 7.5. Conclusions

Clinically relevant results were obtained in this experiment, despite flow through the supra-aortic arteries being lower than expected. The goal was to understand the flow behaviour and interactions across the arteries and bypasses within the four configurations. The use of the BC and CS bypasses allowed fluid to flow to the distal LCCA and LSA even when the proximal arteries were blocked. There was a risk of flow competition within the bypasses for model configurations A-C. Configuration A appeared to have the highest risk. Throughout systole, the flow rates in configuration A remained very low and stagnation and recirculation zones could be identified, particularly through the BC bypass (Figure 7.9). Flow stagnated for the longest period of time however in the CS bypass of configuration B (Figure 7.11a). The presence of competitive flow within the EAB has been suggested but has not previously been captured experimentally within the supra-aortic branches. The confirmation of stagnating and recirculating flow in the BC or CS bypasses of the configurations A-C (Figures 7.10 and 7.11), indicated that ligating or embolization of proximal arteries after being revascularised may be necessary to reduce the loss of bypass patency or further progression of arterial disease. The identification of competitive flow through the BC bypass and CS bypass in configurations A-C but not in configuration D indicated that prophylactic use of the bypasses for TEVAR may require the ligation or coil embolization of the proximal LCCA and LSA.

# 8. Conclusions / Future Work

This chapter summarises the main conclusions of this research as well as some potential future work that could use the content of this thesis as a foundation.

## 8.1. Conclusions

This thesis contributed to *in-vitro* research into some aorta stenting methods that are known to have associated risks. The research was carried out using PIV modelling methods. Experimental measurement of fluid dynamics within compliant phantom arteries with surrogate stents were investigated.

Chapter 4 identified and compiled *in-vivo* Reynolds and Womersley Numbers for 14 of the major arteries. However, the chapter also identified a paucity of information for some of the smaller arteries. This represents a major limitation for *in-vitro* and *in-silico* modelling while modelling many important arteries within the human body. The *in-vitro* case studies presented in this chapter show that there are indications of potentially valid model inputs that enable small arteries to be modelled using surrogate models and transparent blood analogues. However, the lack of direct information for these arteries requires potentially incorrect estimates of Reynolds or Womersley numbers. These assumptions may lead to results that are not physiologically representative.

Chapter 4 also identified a simple method for designing experimental setups required to model haemodynamics in certain arteries. For example, it was shown that effectively mimicking arterial compliance and the high flow and frequency demands of the large arteries is most attainable with a three-part working fluid. The case studies determined that the common carotid arteries required a higher level of scaling compared to the ascending aorta, despite the common carotid being a smaller and less compliant artery. Three working solutions commonly used in optical modelling methods for Newtonian modelling were compared on flow rate and time period for each of the case studies conducted to physiologically match *in-vivo* flow to *in-vitro* waveforms. A 40/60 water and glycerine solution is a reasonably inexpensive solution that can be easily sourced. However, for modelling large arteries such as the aorta, there is a high pump demand to achieve physiological relevance due to the high viscosity of the working fluid. Both three-part solutions required a much lower pump demand, however, the 46/29/24 water, glycerine and urea solution was more cost effective. A smaller artery, such as the common carotid could easily use the 40/60 water and glycerine solution without requiring excessive pump demand.

The FET stent is a hybrid endovascular device that may be implemented in the event of an aneurysm or aortic dissection of the aortic arch or superior descending aorta. A Type 1B endoleak can lead to intrasaccular flow during systole and has been identified as a known failure of the FET stent graft. The purpose of Chapter 5 was to develop an *in-vitro* modelling technique that enabled the investigation of the known failure mode. A silicone aortic phantom and 3D printed surrogate stent graft were manufactured to investigate the haemodynamics of a Type 1B endoleak. Physiological pulsatile flow dynamics distal to the surrogate stent graft were investigated *in-vitro* using Particle Image Velocimetry (PIV). PIV captured recirculation zones and an endoleak distal to the surrogate stent graft. The endoleak was developed at the peak of systole and sustained until the onset of diastole. The endoleak was asymmetric, indicating a potential variation in the phantom artery wall thickness, stent alignment, or secondary flow characteristic. Recirculation was identified on the posterior dorsal line during late systole. The identification of the Type 1B endoleak proved that *in-vitro* modelling can be used to investigate complex compliance changes and wall motions. The recirculation may indicate the potential for long term intimal layer inflammatory issues such as atherosclerosis. These results may aid future remediation techniques or stent design. Further development of the methods used in this experiment may assist with the future testing of stents prior to animal or human trial.

The haemodynamics of the KS method for use in the aorto-iliac bifurcation were investigated using *in-vitro* experimentation within Chapter 6. A compliant phantom of the aorto-iliac bifurcation was manufactured for investigation. Two surrogate stent-grafts were manufactured and deployed into the phantom in the KS configuration to investigate effects of the compliance mismatch and position of the stents on the haemodynamics proximal and distal to the KS. The investigation used pulsatile flow through a flow circuit to simulate abdominal aortic flow. PIV identified peak proximal and distal velocity *in-vitro* was 0.71 $m \cdot s^{-1}$ and 1.40 $m \cdot s^{-1}$, respectively. These velocity values were within physiological ranges. Throughout systole, flow appeared normal and undisturbed. A lumen wall collapse in the sagittal plane formed during late systole and continued to early diastole proximal to the aorto-iliac bifurcation, distal to the inlet stent position. The wall collapse led to disturbed flow proximal to the stented region in early diastole producing potential recirculation zones and abnormal flow patterns. The normal systolic flow behaviour indicates the KS configuration is safe to use for repairing AIOD. The collapse has not been previously identified and requires further investigation. It may be possible this collapse could be linked to long-term patency reduction.

Thoracic extra-anatomic bypasses (EAB) are grafted stents that may be used to prophylactically revascularize supra-aortic arteries that risk being blocked by thoracic endovascular aortic repair (TEVAR) methods. EAB enable flow to pass through the supra-aortic arteries via an alternate route. However, prophylactic use of EAB may potentially introduce a risk of failure due to competitive flow within the bypasses. Competitive flow is defined as abnormally low or disturbed flow within the EAB. The abnormal flow behaviour may result in the bypass becoming blocked. However, the presence of competitive flow within the bypasses between supra-aortic arteries has never been confirmed. In Chapter 7, the potential for competitive flow was modelled using an idealised compliant phantom aorta with three supra-aortic branches and two bypasses was produced out of Sylgard 184 silicone. A silicone plug was used to mimic four scenarios of ligation/occlusion of the proximal supra-aortic arteries. Particle image velocimetry (PIV) was used to assess each model configuration for flow abnormalities and potential for flow competition. This investigation found potential for competitive flow in the BC bypass when just the LSA was blocked and when no supra-aortic arteries were blocked.

Competitive flow was observed in the CS bypass when the LCCA was blocked. Flow stagnated at the initiation of systole within the BC bypass when just the LSA was blocked and when no supra-aortic arteries were blocked, along with notable recirculation zones and reciprocating flow occurring throughout the rest of systolic flow. Flow stagnated in the CS bypass at in early diastole when the LCCA was blocked. Blocking both the LSA and LCCA only suffered from mildly disrupted flow at the onset of diastole, potentially caused by the experimental setup rather than the model configuration. The presence of competitive flow in the other configurations indicated that it may be necessary to intentionally ligate or block flow entering the proximal supra-aortic artery, following prophylactic implementation prior to TEVAR. The results of Chapter 7 will assist cardiovascular surgeons in their decision in whether or not to intentionally block the supra-aortic arteries following prophylactic placement of EAB.

## 8.2. Future Work

Within this thesis the results are limited to instantaneous results. These results can be used to predict high risk areas of the arteries. However, they cannot be used to estimate the long-term effects of stent use as they cannot remodel in the ways that *in-vivo* arteries do. As such, the results from this research do require clinical validation.

Chapter 4 identified that most research on the arteries of humans focuses on the aorta, common carotid and intra-cranial arteries due to a paucity of *in-vivo* research into the other human arteries. Meaningful PIV research of arteries requires the ability to match *in-vitro* model compliance and fluid parameters to the *in-vivo* parameters. As such, an area that requires future research is a survey of the human arterial compliance and fluid parameters for peripheral arteries. Currently, such a survey specifically lacks values for the distal extremities. A greater pool of *in-vivo* information will enable clinically relevant PIV research into arteries and improve future experimentations and results. Increased distal arterial modelling will also help to improve the downstream pressure modelling. One of the major limitations identified within this thesis related to the downstream pressure modelling. The current flow circuit does not have a pressure gauge or downstream valves capable of dynamically controlling pressure. As such, the internal pressures within the model were not actively controlled or monitored, despite using a head tank to provide a static back pressure for each experiment. The introduction of pressure gauges and electronically controlled valves into the flow circuit downstream of the phantom outlets would enable better monitoring and control of the distal flow. However, a better understanding of the peripheral artery resistance is necessary for clinically relevant results.

Furthermore, compliant *in-vitro* phantoms of arteries typically require scaling to reliably manufacture. Hence, the internal pressures may be changed. Another area for future research may be identifying a method to ensure that the pressure waveform for arterial models scales in concert with flow rate and frequency. Pressure can be very difficult to scale as there is no key dimensionless parameter that factors in the pressure other than the Euler number which has not been reported in many arteries. Potential research may include investigating the ratio of the change in diameter to the original diameter for multiple model scales each having dynamic similarity matching. Confirmation that the $\frac{\Delta D}{D}$ ratio is consistent between the different scales will provide reasonable confidence that dynamically matching the flow rate waveform for experiments will also preserve the pressure waveform. However, if the ratio changes at different scales, further research will need to be carried out into scaling the pressure waveform to ensure clinical relevance.

Another alternative is to look at altering the mixture ratio of Sylgard 184. A study by Glover, et al. [321] indicates that changing the ratio of silicone to cross-linking agent from 10:1 to 20:1 resulted in the elastic modulus from 1.72 MPa decreasing to 0.62 MPa (much closer to the modulus of arterial walls). Changing the cross-link ratio presents the potential to carry out similar experiments as presented in this thesis, without having the scale to models to manufacture a normalised compliance matched phantom. This may simplify compliant *in-vitro* modelling and dynamic similarity matching in future experiments.

Chapters 5-7 each conducted experiments using surrogates in place of physical stents. Future research may carry out similar experiments to those in Chapter 5-7 using real stent grafts. A comparison of results between the surrogate and real stents would improve the clinical reliability of the results and aid future *in-vitro* research. Real stents may be difficult to access for some research groups, and hence, the comparison between the real and surrogate may allow vascular implant modelling to be more accessible to a wider research group. Furthermore, the attachment methods for real stents may not be suitable for location in silicone phantoms. Often stents and stent grafts have small external hooks which are used to fix the stent on to the artery wall. However, these hooks may puncture the silicone, causing the phantom to tear.

Chapter 6 identified that it was difficult to track particles within a grafted stent, even when using a transparent graft. This led to unrealistic flow within the stented regions for the experiment that did not agree with conservation of mass principles. Future research may use fluorescent particles and filters to reduce reflections and try improving particle visibility through the stented region. However, the density of stent wires may still result in particle loss. Lost particles may result in the identification of bad vectors that are not representative of the true flow.

Planar and stereo-PIV are limited to capturing a 2-dimensional plane of flow, though, stereo-PIV can also identify if particles are moving transverse across the captured plane. However, blood flow in the aorta is often helical, resulting in significant 3-dimensional flow behaviour which cannot be captured using planar-PIV or stereo-PIV. Both Chapter 5 and 7 ignored the tortuosity of the aorta, and hence helical flow was not captured and may thus have miscalculated the appearance of abnormal flow. Future work may include looking at the potential to use tomographic PIV which would enable full 3-dimensional flow capture of the entire domain. Tomographic PIV will eliminate the necessity to ignore tortuosity. However, tomographic PIV requires significant set up time and calibration to carry out accurately. Another potential would be to look at conducting PIV using multiple wave lengths of light to illuminate the flow across a much wider plane. Captured images could then the processed using light filters to obtain the third dimension of particle motion. Careful alignment and calibration of the wavelength would allow multi-colour PIV to capture multiple planes could be obtained with one setup, thereby reducing capture time.

# 9. References

[1] R. E. Klabunde, *Cardiovascular physiology concepts*. Second edition. Philadelphia, PA : Lippincott Williams &amp; Wilkins/Wolters Kluwer, [2012] ©2012, 2012.

[2] F. N. v. d. Vosse and N. Stergiopulos, "Pulse Wave Propagation in the Arterial Tree," *Annual Review of Fluid Mechanics,* vol. 43, pp. 467-499, 2011.

[3] J. F. Lee Waite, "Applied Biofluid Mechanics," ed: McGraw-Hill, 2007, pp. 149 - 152.

[4] C. G. Caro, *The mechanics of the circulation*, 2nd ed. (no. Book, Whole). Cambridge;New York;: Cambridge University Press, 2012.

[5] D. H. Tian, B. Wan, M. Di Eusanio, D. Black, and T. D. Yan, "A systematic review and meta-analysis on the safety and efficacy of the frozen elephant trunk technique in aortic arch surgery," (in eng), *Annals of cardiothoracic surgery,* vol. 2, no. 5, pp. 581-591, 2013, doi: 10.3978/j.issn.2225-319X.2013.09.07.

[6] C. Singh, X. Wang, Y. Morsi, and C. Wong, "Importance of stent-graft design for aortic arch aneurysm repair," (in en), *AIMS Bioengineering,* vol. 4, no. 1, pp. 133-150, 2017 2017, doi: 10.3934/bioeng.2017.1.133.

[7] A. Mallory, S. Giannopoulos, P. Lee, D. G. Kokkinidis, and E. J. Armstrong, "Covered Stents for Endovascular Treatment of Aortoiliac Occlusive Disease: A Systematic Review and Meta-Analysis," *Vascular and Endovascular Surgery,* p. 15385744211010381, 2021, doi: 10.1177/15385744211010381.

[8] S. Xydas *et al.*, "Use of carotid–subclavian arterial bypass and thoracic endovascular aortic repair to minimize cerebral ischemia in total aortic arch reconstruction," *The Journal of Thoracic and Cardiovascular Surgery,* vol. 139, no. 3, pp. 717-722, 2010/03/01/ 2010, doi: https://doi.org/10.1016/j.jtcvs.2009.10.040.

[9] D. K. Han, C. Jokisch, and J. McKinsey, "Expanding the landing zone for TEVAR," *Endovasc Today,* vol. 15, pp. 85-90, 2016.

[10] B. Alyavi and J. Uzokov, "Peripheral artery disease in the lower extremities: indications for treatment," *E-journal of Cardiology Practice,* vol. 16, no. 9, pp. 1-10, 2018.

[11] T. Cleveland Clinic. "Aorta Anatomy." Cleveland Clinic. https://my.clevelandclinic.org/health/articles/17058-aorta-anatomy (accessed 8 November 2021, 2021).

[12] R. Drake, A. W. Vogl, and A. W. M. Mitchell, *Gray's Basic Anatomy E-Book*, 2nd ed. (no. Book, Whole). Philadelphia: Elsevier (in English), 2017.

[13] P. T. C. B. Bordoni, "Anatomy, Thorax, Aortic Valve," *StatPearls [Internet],* 2021.

[14] P. Popieluszko *et al.*, "A systematic review and meta-analysis of variations in branching patterns of the adult aortic arch," *Journal of Vascular Surgery,* vol. 68, no. 1, pp. 298-306.e10, 2018/07/01/ 2018, doi: https://doi.org/10.1016/j.jvs.2017.06.097.

[15] K. B. Chandran, S. E. Rittgers, and A. P. Yoganathan, *Biofluid mechanics: the human circulation*, 2nd ed. (no. Book, Whole). Boca Raton: CRC Press, Taylor & Francis Group, 2012.

[16] O. Rahimi and Z. Geiger, "Anatomy, Thorax, Subclavian Arteries," in *StatPearls*. Treasure Island (FL): StatPearls Publishing Copyright © 2021, StatPearls Publishing LLC., 2021.

[17] W.-S. Yun and K. Park, "Iliac anatomy and the incidence of adjunctive maneuvers during endovascular abdominal aortic aneurysm repair," (in eng), *Ann Surg Treat Res,* vol. 88, no. 6, pp. 334-340, 2015, doi: 10.4174/astr.2015.88.6.334.

[18] A. Deswal, B. K. Tamang, and A. Bala, "Study of aortic- common iliac bifurcation and its clinical significance," (in eng), *Journal of clinical and diagnostic research : JCDR,* vol. 8, no. 7, pp. AC06-AC8, 2014, doi: 10.7860/JCDR/2014/8767.4559.

[19] N. Zaunbrecher and N. S. Samra, "Anatomy, Abdomen and Pelvis, Internal Iliac Arteries," *StatPearls [Internet],* 2020.

[20] E. Hammond, A. Nassereddin, and M. Costanza, "Anatomy, Abdomen and Pelvis, External Iliac Arteries," in *StatPearls*. Treasure Island (FL): StatPearls Publishing Copyright © 2021, StatPearls Publishing LLC., 2021.

[21] G. D. O. Lowe, "Blood Viscosity and Cardiovascular Disease," (in En), *Thromb Haemost,* vol. 67, no. 05, pp. 494-498, 1992.

[22] D. A. McDonald, *Blood flow in arteries*, [2d]. ed. (no. Book, Whole). London U6 Arnold, 1974.

[23] B. c. Staff, "Medical Gallery of Blausen Medical 2014," *WikiJournal od Medicine,* no. 1, 2014, doi: DOI:10.15347/wjm/2014.010.

[24] B. Alberts, *Molecular biology of the cell*, 4th ed. (no. Book, Whole). New York: Garland Science (in English), 2002.

[25] G. Favero, C. Paganelli, B. Buffoli, L. F. Rodella, and R. Rezzani, "Endothelium and Its Alterations in Cardiovascular Diseases: Life Style Intervention," *BioMed Research International,* vol. 2014, p. 801896, 2014/02/26 2014, doi: 10.1155/2014/801896.

[26] J. S. Pober and W. C. Sessa, "Evolving functions of endothelial cells in inflammation," (in English), *Nature Reviews. Immunology,* vol. 7, no. 10, pp. 803-15, Oct 2007 2014-03-30 2007, doi: http://dx.doi.org/10.1038/nri2171.

[27] W. D. Tucker, Y. Arora, and K. Mahajan, "Anatomy, Blood Vessels," in *StatPearls*. Treasure Island (FL): StatPearls Publishing Copyright © 2021, StatPearls Publishing LLC., 2021.

[28] C. Singh, C. S. Wong, and X. Wang, "Medical Textiles as Vascular Implants and Their Success to Mimic Natural Arteries," (in eng), *Journal of functional biomaterials,* vol. 6, no. 3, pp. 500-525, 2015, doi: 10.3390/jfb6030500.

[29] M. E. Safar, "Peripheral Pulse Pressure, Large Arteries, and Microvessels," *Hypertension,* vol. 44, no. 2, pp. 121-122, 2004, doi: doi:10.1161/01.HYP.0000135448.73199.75.

[30] World Health Organization (WHO), "Cardiovascular diseases (CVDs): Fact sheet No. 317. 2012," *Geneva: World Health Organization,* 2012.

[31] R. Pahwa and I. Jialal, "Atherosclerosis," in *StatPearls*. Treasure Island (FL): StatPearls Publishing Copyright © 2021, StatPearls Publishing LLC., 2021.

[32] A. J. Lusis, "Atherosclerosis," *Nature,* vol. 407, no. 6801, pp. 233-241, 2000/09/01 2000, doi: 10.1038/35025203.

[33] N. Patchett, "Late Complications of Atherosclerosis," ed. Wikipedia, 2015, p. File Image.

[34] J.-J. Chiu and S. Chien, "Effects of disturbed flow on vascular endothelium: pathophysiological basis and clinical perspectives," (in eng), *Physiol Rev,* vol. 91, no. 1, pp. 327-387, 2011, doi: 10.1152/physrev.00047.2009.

[35] J. Z. Goldfinger, J. L. Halperin, M. L. Marin, A. S. Stewart, K. A. Eagle, and V. Fuster, "Thoracic Aortic Aneurysm and Dissection," *Journal of the American College of Cardiology,* vol. 64, no. 16, pp. 1725-1739, 2014/10/21/ 2014, doi: https://doi.org/10.1016/j.jacc.2014.08.025.

[36] G. A. Roth, C. Johnson, A. Abajobir, and e. al., "Global, Regional, and National Burden of Cardiovascular Diseases for 10 Causes, 1990 to 2015," *Journal of the American College of Cardiology,* vol. 70, no. 1, pp. 1-25, 2017, doi: 10.1016/j.jacc.2017.04.052.

[37] M. Faluk and O. De Jesus, "Saccular Aneurysm," in *StatPearls*. Treasure Island (FL): StatPearls Publishing Copyright © 2021, StatPearls Publishing LLC., 2021.

[38] B. J. Doyle, *Abdominal aortic aneurysms: new approaches to rupture risk assessment* (no. Book, Whole). Hauppauge, N.Y: Nova Science (in English), 2010.

[39] T. Suess *et al.*, "Examination of near-wall hemodynamic parameters in the renal bridging stent of various stent graft configurations for repairing visceral branched aortic aneurysms," *Journal of vascular surgery,* vol. 64, 07/22 2015, doi: 10.1016/j.jvs.2015.04.421.

[40] H. Kandail, M. Hamady, and X. Y. Xu, "Comparison of Blood Flow in Branched and Fenestrated Stent-Grafts for Endovascular Repair of Abdominal Aortic Aneurysms," *Journal of Endovascular Therapy,* vol. 22, no. 4, pp. 578-590, 2015, doi: 10.1177/1526602815587261.

[41] A. B. Lumsden, *Advanced endovascular therapy of aortic disease* (no. Book, Whole). Oxford;Malden, Mass;: Blackwell Futura, 2007.

[42] M. J. Salameh and E. V. Ratchford, "Aortic dissection," *Vascular Medicine,* vol. 21, no. 3, pp. 276-280, 2016.

[43] K. J. Macura, F. M. Corl, E. K. Fishman, and D. A. Bluemke, "Pathogenesis in Acute Aortic Syndromes: Aortic Dissection, Intramural Hematoma, and Penetrating Atherosclerotic Aortic Ulcer," *American Journal of Roentgenology,* vol. 181, no. 2, pp. 309-316, 2003/08/01 2003, doi: 10.2214/ajr.181.2.1810309.

[44] D. Chen *et al.*, "Virtual stenting with simplex mesh and mechanical contact analysis for real-time planning of thoracic endovascular aortic repair," (in eng), *Theranostics,* vol. 8, no. 20, pp. 5758-5771, 2018, doi: 10.7150/thno.28944.

[45] J. Iqbal, J. Gunn, and P. W. Serruys, "Coronary stents: historical development, current status and future directions," *British Medical Bulletin,* vol. 106, no. 1, pp. 193-211, 2013, doi: 10.1093/bmb/ldt009.

[46] P. Jamshidi, K. Mahmoody, and P. Erne, "Covered stents: A review," *International Journal of Cardiology,* vol. 130, no. 3, pp. 310-318, 2008/11/28/ 2008, doi: https://doi.org/10.1016/j.ijcard.2008.04.083.

[47] G. L. Tang and M. D. Morasch, "Role of Stents, Drug-Eluting Stents, and Stent-Grafts in Treatment of Infrainguinal Arterial Disease," *Seminars in Vascular Surgery,* vol. 20, no. 1, pp. 37-41, 2007/03/01/ 2007, doi: https://doi.org/10.1053/j.semvascsurg.2007.02.004.

[48] C. E. Ruiz, H. P. Zhang, J. T. Douglas, C. W. Zuppan, and C. J. C. Kean, "A Novel Method for Treatment of Abdominal Aortic Aneurysms Using Percutaneous Implantation of a Newly Designed Endovascular Device," *Circulation,* vol. 91, no. 9, pp. 2470-2477, 1995/05/01 1995, doi: 10.1161/01.CIR.91.9.2470.

[49] V. Kumar, "Defining the role of covered stents in aorto-iliac interventions," *Interventional Cardiology,* vol. 5, no. 1, pp. 45-52, 2013.

[50] N. D. Appleton, D. Bosanquet, G. Morris-Stiff, H. Ahmed, P. Sanjay, and M. H. Lewis, "Extra-anatomical bypass grafting--a single surgeon's experience," (in eng), *Ann R Coll Surg Engl,* vol. 92, no. 6, pp. 499-502, 2010, doi: 10.1308/003588410X12664192076890.

[51] A. F. AbuRahma, P. A. Robinson, and T. G. Jennings, "Carotid-subclavian bypass grafting with polytetrafluoroethylene grafts for symptomatic subclavian artery stenosis or occlusion: A 20-year experience," *Journal of Vascular Surgery,* vol. 32, no. 3, pp. 411-419, 2000/09/01/ 2000, doi: https://doi.org/10.1067/mva.2000.108644.

[52] H. Nakajima, J. Kobayashi, O. Tagusari, K. Bando, K. Niwaya, and S. Kitamura, "Competitive flow in arterial composite grafts and effect of graft arrangement in off-pump coronary revascularization," *The Annals of thoracic surgery,* vol. 78, no. 2, pp. 481-486, 2004.

[53] D. Glineur and C. Hanet, "Competitive flow in coronary bypass surgery: is it a problem?," (in eng), *Curr Opin Cardiol,* vol. 27, no. 6, pp. 620-8, Nov 2012, doi: 10.1097/HCO.0b013e3283583000.

[54] J. E. Moore and J. L. Berry, "Fluid and Solid Mechanical Implications of Vascular Stenting," *Annals of Biomedical Engineering,* vol. 30, no. 4, pp. 498-508, 2002/04/01 2002, doi: 10.1114/1.1458594.

[55] G. S. Karanasiou *et al.*, "Stents: Biomechanics, Biomaterials, and Insights from Computational Modelling," *Annals of biomedical engineering,* vol. 45, no. 4, pp. 853-872, 2017.

[56] S. Morlacchi *et al.*, "Patient-specific simulations of stenting procedures in coronary bifurcations: two clinical cases," (in eng), *Med Eng Phys,* vol. 35, no. 9, pp. 1272-81, Sep 2013, doi: 10.1016/j.medengphy.2013.01.007.

[57] J. F. LaDisa *et al.*, "Circumferential vascular deformation after stent implantation alters wall shear stress evaluated with time-dependent 3D computational fluid dynamics models," *Journal of Applied Physiology,* vol. 98, no. 3, pp. 947-957, 2005/03/01/ 2005, doi: 10.1152/japplphysiol.00872.2004.

[58] C. Conway, G. J. Desany, L. R. Bailey, J. H. Keating, B. L. Baker, and E. R. Edelman, "Fracture in drug-eluting stents increases focal intimal hyperplasia in the atherosclerosed rabbit iliac artery," *Catheterization and Cardiovascular Interventions,* vol. 93, no. 2, pp. 278-285, 2019, doi: https://doi.org/10.1002/ccd.27726.

[59] C. Conway, F. Sharif, P. McGarry, and P. McHugh, *A Computational Test-Bed to Assess Coronary Stent Implantation Mechanics Using a Population-Specific Approach*. 2012.

[60] C. Conway, "Coronary Stent Fracture: Clinical Evidence Vs. the Testing Paradigm," *Cardiovascular Engineering and Technology,* journal article vol. 9, no. 4, pp. 752-760, December 01 2018, doi: 10.1007/s13239-018-00384-0.

[61] A. Damberg, G. Schälte, R. Autschbach, and A. Hoffman, "Safety and pitfalls in frozen elephant trunk implantation," *Annals of Cardiothoracic Surgery,* vol. 2, no. 5, pp. 669-676, 2013/09// 2013, doi: 10.3978/j.issn.2225-319X.2013.09.16.

[62] L. Liu, S. Zhang, Q. Lu, Z. Jing, S. Zhang, and B. Xu, "Impact of Oversizing on the Risk of Retrograde Dissection After TEVAR for Acute and Chronic Type B Dissection," *Journal of Endovascular Therapy,* vol. 23, no. 4, pp. 620-625, 2016, doi: 10.1177/1526602816647939.

[63] R. J. Russo, P. D. Silva, and M. Yeager, "Coronary artery overexpansion increases neointimal hyperplasia after stent placement in a porcine model," (in eng), *Heart,* vol. 93, no. 12, pp. 1609-15, Dec 2007, doi: 10.1136/hrt.2006.105981.

[64] H. Y. Chen, J. Hermiller, A. K. Sinha, M. Sturek, L. Zhu, and G. S. Kassab, "Effects of stent sizing on endothelial and vessel wall stress: potential mechanisms for in-stent restenosis," *Journal of Applied Physiology,* vol. 106, no. 5, pp. 1686-1691, 2009, doi: 10.1152/japplphysiol.91519.2008.

[65] L. Morris, F. Stefanov, N. Hynes, E. B. Diethrich, and S. Sultan, "An Experimental Evaluation of Device/Arterial Wall Compliance Mismatch for Four Stent-Graft Devices and a Multi-layer Flow Modulator Device for the Treatment of Abdominal Aortic Aneurysms," (in en), *European Journal of Vascular and Endovascular Surgery,* vol. 51, no. 1, pp. 44-55, 2016/01// 2016, doi: 10.1016/j.ejvs.2015.07.041.

[66] N. K. C. Selvarasu, D. K. Tafti, and P. P. Vlachos, "Hydrodynamic effects of compliance mismatch in stented arteries," (in eng), *Journal of Biomechanical Engineering,* vol. 133, no. 2, p. 021008, 2011/02// 2011, doi: 10.1115/1.4003319.

[67] K. Cameron, M. El Hassan, R. Sabbagh, D. H. Freed, and D. S. Nobes, "Experimental investigation into the effect of compliance of a mock aorta on cardiac performance," *PloS one,* vol. 15, no. 10, p. e0239604, 2020.

[68] L. Morris, F. Stefanov, and T. McGloughlin, "Stent graft performance in the treatment of abdominal aortic aneurysms: the influence of compliance and geometry," *Journal of biomechanics,* vol. 46, no. 2, pp. 383-395, 2013.

[69] M. Raffel *et al.*, *Particle Image Velocimetry: A Practical Guide*, 3rd 2018.;3rd 2018; ed. (no. Book, Whole). Cham: Springer International Publishing, 2018.

[70] I. TSI, "INSIGHT 4G™ GLOBAL IMAGE, ACQUISITION, ANALYSIS, & DISPLAY SOFTWARE User Guide." USA: TSI Incorpoated, 2017, ch. Chapter 10.

[71] P. H. Geoghegan, "In Vitro Experimental Investigation Into the Effect of Compliance on Models of Arterial Hemodynamics," College of Engineering, University of Canterbury, New Zealand, 2012.

[72] H. Hong, E. Yeom, H. S. Ji, H. D. Kim, and K. C. Kim, "Characteristics of pulsatile flows in curved stenosed channels," *PLOS ONE,* vol. 12, no. 10, p. e0186300, 2017, doi: 10.1371/journal.pone.0186300.

[73] P. H. Geoghegan, M. C. Jermy, and D. S. Nobes, "A piv comparison of the flow field and wall shear stress in rigid and compliant models of healthy carotid arteries," *Journal of Mechanics in Medicine and Biology,* vol. 17, no. 03, p. 1750041, 2016/07/21/ 2016, doi: 10.1142/S0219519417500415.

[74] P. N. Williamson, P. D. Docherty, S. G. Yazdi, A. Khanafer, N. Kabaliuk, and M. Jermy, "PIV Analysis of Haemodynamics Distal to the Frozen Elephant Trunk Stent Surrogate," *Cardiovascular Engineering and Technology,* 2021/03/05 2021, doi: 10.1007/s13239-021-00521-2.

[75] S. G. Yazdi *et al.*, "In vitro pulsatile flow study in compliant and rigid ascending aorta phantoms by stereo particle image velocimetry," *Medical Engineering & Physics,* vol. 96, pp. 81-90, 2021/10/01/ 2021, doi: https://doi.org/10.1016/j.medengphy.2021.08.010.

[76] A. D. Anastasiou, A. S. Spyrogianni, K. C. Koskinas, G. D. Giannoglou, and S. V. Paras, "Experimental investigation of the flow of a blood analogue fluid in a replica of a bifurcated small artery," *Medical Engineering & Physics,* vol. 34, no. 2, pp. 211-218, 2012/03/01/ 2012, doi: https://doi.org/10.1016/j.medengphy.2011.07.012.

[77] W. S. Thielicke, E.J. , "Particle Image Velocimetry for MATLAB: Accuracy and enhanced algorithms in PIVlab," *Journal of Open Research Software,* 9: 12., 2021, doi: https://doi.org/10.5334/jors.334.

[78] K. D. Jensen, "Flow measurements," *Journal of the Brazilian Society of Mechanical Sciences and Engineering,* vol. 26, pp. 400-419, 2004.

[79] B. Thurow, N. Jiang, and W. Lempert, "Review of ultra-high repetition rate laser diagnostics for fluid dynamic measurements," *Measurement Science and Technology,* vol. 24, no. 1, p. 012002, 2012/10/29 2012, doi: 10.1088/0957-0233/24/1/012002.

[80] S. G. Yazdi, P. H. Geoghegan, P. D. Docherty, M. Jermy, and A. Khanafer, "A Review of Arterial Phantom Fabrication Methods for Flow Measurement Using PIV Techniques," (in en), *Annals of Biomedical Engineering,* vol. 46, no. 11, pp. 1697-1721, 2018/11// 2018, doi: 10.1007/s10439-018-2085-8.

[81] M. C. Brindise, M. M. Busse, and P. P. Vlachos, "Density and Viscosity Matched Newtonian and non-Newtonian Blood-Analog Solutions with PDMS Refractive Index," (in eng), *Experiments in fluids,* vol. 59, no. 11, p. 173, 2018, doi: 10.1007/s00348-018-2629-6.

[82] K. Takamura, H. Fischer, and N. R. Morrow, "Physical properties of aqueous glycerol solutions," *Journal of Petroleum Science and Engineering,* vol. 98-99, pp. 50-60, 2012/11/01/ 2012, doi: https://doi.org/10.1016/j.petrol.2012.09.003.

[83] W. T. Lai, D. C. Bjorkquist, M. P. Abbott, and A. A. Naqwi, "Video systems for PIV recording," *Measurement Science and Technology,* vol. 9, no. 3, pp. 297-308, 1998/03/01 1998, doi: 10.1088/0957-0233/9/3/002.

[84] R. Hain, C. J. Kähler, and C. Tropea, "Comparison of CCD, CMOS and intensified cameras," *Experiments in Fluids,* vol. 42, no. 3, pp. 403-411, 2007/03/01 2007, doi: 10.1007/s00348-006-0247-1.

[85] R. D. Keane and R. J. Adrian, "Theory of cross-correlation analysis of PIV images," *Applied Scientific Research,* vol. 49, no. 3, pp. 191-215, 1992/07/01 1992, doi: 10.1007/BF00384623.

[86] O. A.B and M. Ovinis, "A review of in-situ optical flow measurement techniques in the Deepwater Horizon oil spill," *Measurement,* vol. 153, p. 107396, 2020/03/01/ 2020, doi: https://doi.org/10.1016/j.measurement.2019.107396.

[87] F. Scarano and M. L. Riethmuller, "Iterative multigrid approach in PIV image processing with discrete window offset," *Experiments in Fluids,* vol. 26, no. 6, pp. 513-523, 1999/05/01 1999, doi: 10.1007/s003480050318.

[88] R. D. Keane and R. J. Adrian, "Optimization of particle image velocimeters. I. Double pulsed systems," *Measurement Science and Technology,* vol. 1, no. 11, pp. 1202-1215, 1990/11/01 1990, doi: 10.1088/0957-0233/1/11/013.

[89] J. Westerweel, P. F. Geelhoed, and R. Lindken, "Single-pixel resolution ensemble correlation for micro-PIV applications," *Experiments in Fluids,* vol. 37, no. 3, pp. 375-384, 2004/09/01 2004, doi: 10.1007/s00348-004-0826-y.

[90] R. J. Bastiaans, *Cross-correlation PIV; theory, implementation and accuracy*. Eindhoven University of Technology, Faculty of Mechanical Engineering, 2000.

[91] J. R. Taylor, *An introduction to error analysis: the study of uncertainties in physical measurements*, 2nd ed. (no. Book, Whole). Sausalito, Calif: University Science Books (in English), 1997.

[92] W. Tsai and O. Savaş, "Flow pumping system for physiological waveforms," (in eng), *Medical & biological engineering & computing,* vol. 48, no. 2, pp. 197-201, 2010, doi: 10.1007/s11517-009-0573-6.

[93] F. M. White, *Fluid mechanics*, 7th ed. (no. Book, Whole). New York, N.Y: McGraw Hill, 2011.

[94] A. Kalpakli, R. Örlü, and P. H. Alfredsson, "Dean vortices in turbulent flows: rocking or rolling?," *Journal of Visualization,* vol. 15, no. 1, pp. 37-38, 2012/02/01 2012, doi: 10.1007/s12650-011-0108-8.

[95] S. G. Yazdi *et al.*, "A Novel Fabrication Method for Compliant Silicone Phantoms of Arterial Geometry for Use in Particle Image Velocimetry of Haemodynamics," *Applied Sciences,* vol. 9, no. 18, p. 3811, 2019. [Online]. Available: https://www.mdpi.com/2076-3417/9/18/3811.

[96] L. Hütter, P. H. Geoghegan, P. D. Docherty, M. S. Lazarjan, D. Clucas, and M. Jermy, "Application of a meta-analysis of aortic geometry to the generation of a compliant phantom for use in particle image velocimetry experimentation," (in en), *IFAC-PapersOnLine,* vol. 48, no. 20, pp. 407-412, 2015 2015, doi: 10.1016/j.ifacol.2015.10.174.

[97] P. Tozzi, A. Corno, and D. Hayoz, "Definition of arterial compliance," *American Journal of Physiology-Heart and Circulatory Physiology,* vol. 278, no. 4, pp. H1407-H1407, 2000, doi: 10.1152/ajpheart.2000.278.4.H1407.

[98] M. Zamir, *The physics of pulsatile flow* (no. Book, Whole). New York: AIP Press, 2000.

[99] P. N. Williamson *et al.*, "Review of the Development of Haemodynamic Modelling Techniques to Capture Flow Behaviour in Arteries Affected by Aneurysm, Atherosclerosis and Stenting " *ASME Journal of Biomechanics,* Review 2021 2021.

[100] J. L. Berry, E. Manoach, C. Mekkaoui, P. H. Rolland, J. E. Moore, and A. Rachev, "Hemodynamics and Wall Mechanics of a Compliance Matching Stent: In Vitro and In Vivo Analysis," *Journal of Vascular and Interventional Radiology,* vol. 13, no. 1, pp. 97-105, 2002/01/01/ 2002, doi: https://doi.org/10.1016/S1051-0443(07)60015-3.

[101] W.-M. P. F. Bosman, J.-W. Hinnen, D. J. Rixen, and J. F. Hamming, "Effect of Stent-Graft Compliance on Endotension After EVAR," (in English), *Journal of Endovascular Therapy; Phoenix,* vol. 16, no. 1, pp. 105-13, 2009/02// 2009. [Online]. Available: http://search.proquest.com/docview/211142315/abstract/7BA6F53D12A444AFPQ/1.

[102] B. Chung and J. R. Cebral, "CFD for Evaluation and Treatment Planning of Aneurysms: Review of Proposed Clinical Uses and Their Challenges," (in en), *Annals of Biomedical Engineering,* vol. 43, no. 1, pp. 122-138, 2015/01/01/ 2015, doi: 10.1007/s10439-014-1093-6.

[103] E. L. Boland, J. A. Grogan, C. Conway, and P. E. McHugh, "Computer Simulation of the Mechanical Behaviour of Implanted Biodegradable Stents in a Remodelling Artery," *JOM,* journal article vol. 68, no. 4, pp. 1198-1203, April 01 2016, doi: 10.1007/s11837-015-1761-5.

[104] M. Raschi *et al.*, "CFD and PIV analysis of hemodynamics in a growing intracranial aneurysm," *International Journal for Numerical Methods in Biomedical Engineering,* vol. 28, no. 2, pp. 214-228, 2012, doi: 10.1002/cnm.1459.

[105] J. Charonko, S. Karri, J. Schmieg, S. Prabhu, and P. Vlachos, "In Vitro, Time-Resolved PIV Comparison of the Effect of Stent Design on Wall Shear Stress," (in English), *Annals of Biomedical Engineering,* vol. 37, no. 7, pp. 1310-21, 2009/07// 2009, doi: http://dx.doi.org.ezproxy.canterbury.ac.nz/10.1007/s10439-009-9697-y.

[106] C. N. Ionita, Y. Hoi, H. Meng, and S. Rudin, "Particle image velocimetry (PIV) evaluation of flow modification in aneurysm phantoms using asymmetric stents," in *Medical Imaging 2004*, 2004: International Society for Optics and Photonics, pp. 295-306.

[107] C. J. Elkins and M. T. Alley, "Magnetic resonance velocimetry: applications of magnetic resonance imaging in the measurement of fluid motion," *Experiments in Fluids,* journal article vol. 43, no. 6, pp. 823-858, December 01 2007, doi: 10.1007/s00348-007-0383-2.

[108] R. F. Neville, C. J. Elkins, M. T. Alley, and R. B. Wicker, "Hemodynamic Comparison of Differing Anastomotic Geometries Using Magnetic Resonance Velocimetry1," *Journal of Surgical Research,* vol. 169, no. 2, pp. 311-318, 2011/08/01/ 2011, doi: https://doi.org/10.1016/j.jss.2009.12.008.

[109] P. Xu *et al.*, "Assessment of boundary conditions for CFD simulation in human carotid artery," *Biomechanics Modeling in Mechanobiology,* journal article vol. 17, no. 6, pp. 1581-1597, December 01 2018, doi: 10.1007/s10237-018-1045-4.

[110] C. Figueroa, C. Taylor, A. J Chiou, V. Yeh, and C. K Zarins, "Magnitude and Direction of Pulsatile Displacement Forces Acting on Thoracic Aortic Endografts," *Journal of endovascular therapy : an official journal of the International Society of Endovascular Specialists,* vol. 16, pp. 350-8, 07/01 2009, doi: 10.1583/09-2738.1.

[111] M. Shrestha, M. Pichlmaier, A. Martens, C. Hagl, N. Khaladj, and A. Haverich, "Total aortic arch replacement with a novel four-branched frozen elephant trunk graft: first-in-man results†," (in en), *European Journal of Cardio-Thoracic Surgery,* vol. 43, no. 2, pp. 406-410, 2013/02// 2013, doi: 10.1093/ejcts/ezs296.

[112] T. Tanoue, S. Tateshima, J. P. Villablanca, F. Viñuela, and K. Tanishita, "Wall Shear Stress Distribution Inside Growing Cerebral Aneurysm," *American Journal of Neuroradiology,* vol. 32, no. 9, pp. 1732-1737, 2011, doi: 10.3174/ajnr.A2607.

[113] A. Lauric, J. Hippelheuser, A. D. Cohen, L. M. Kadasi, and A. M. Malek, "Wall shear stress association with rupture status in volume matched sidewall aneurysms," *Journal of NeuroInterventional Surgery,* vol. 6, no. 6, pp. 466-473, 2014, doi: 10.1136/neurintsurg-2013-010871.

[114] C. Ong *et al.*, "Hemodynamic analysis of a novel stent graft design with slit perforations in thoracic aortic aneurysm," *Journal of Biomechanics,* 2019/01/19/ 2019, doi: 10.1016/j.jbiomech.2019.01.019.

[115] M. Matsuura, S. Tupin, and M. Ohta, "Compliance Effect on the Flow Condition in Vascular In Vitro Experiments," no. 52026, p. V003T04A031, 2018, doi: 10.1115/IMECE2018-87362.

[116] J. D. Humphrey, "Blood Vessels, Mechanical and Physical Properties of," in *Encyclopedia of Materials: Science and Technology*, K. H. J. Buschow *et al.* Eds. Oxford: Elsevier, 2001, pp. 748-751.

[117] A. J. Boyd, D. C. S. Kuhn, R. J. Lozowy, and G. P. Kulbisky, "Low wall shear stress predominates at sites of abdominal aortic aneurysm rupture," *Journal of Vascular Surgery,* vol. 63, no. 6, pp. 1613-1619, 2016/06/01/ 2016, doi: https://doi.org/10.1016/j.jvs.2015.01.040.

[118] G. D. Giannoglou, J. V. Soulis, T. M. Farmakis, D. M. Farmakis, and G. E. Louridas, "Haemodynamic factors and the important role of local low static pressure in coronary wall thickening," *International Journal of Cardiology,* vol. 86, no. 1, pp. 27-40, 2002/11/01/ 2002, doi: https://doi.org/10.1016/S0167-5273(02)00188-2.

[119] R. F. Huang, T.-F. Yang, and Y. K. Lan, "Pulsatile flows and wall-shear stresses in models simulating normal and stenosed aortic arches," (in en), *Experiments in Fluids,* vol. 48, no. 3, pp. 497-508, 2010/03// 2010, doi: 10.1007/s00348-009-0754-y.

[120] J. Lantz, J. Renner, and M. Karlsson, "Wall shear stress in a subject specific human aorta—influence of fluid-structure interaction," *International Journal of Applied Mechanics,* vol. 3, no. 04, pp. 759-778, 2011.

[121] G. A. Truskey, K. M. Barber, T. C. Robey, L. A. Olivier, and M. P. Combs, "Characterization of a sudden expansion flow chamber to study the response of endothelium to flow recirculation," *Journal of biomechanical engineering,* vol. 117, no. 2, pp. 203-210, 1995.

[122] P. F. Davies and S. C. Tripathi, "Mechanical stress mechanisms and the cell. An endothelial paradigm," *Circulation research,* vol. 72, no. 2, pp. 239-245, 1993.

[123] K. Alkhalili *et al.*, "The effect of stents in cerebral aneurysms: A review," *Asian Journal of Neurosurgery,* vol. 13, no. 2, p. 201, 2018.

[124] J. E. Moore, C. Xu, S. Glagov, C. K. Zarins, and D. N. Ku, "Fluid wall shear stress measurements in a model of the human abdominal aorta: oscillatory behavior and relationship to atherosclerosis," *Atherosclerosis,* vol. 110, no. 2, pp. 225-240, 1994/10/01/ 1994, doi: https://doi.org/10.1016/0021-9150(94)90207-0.

[125] Y. S. Chatzizisis, A. U. Coskun, M. Jonas, E. R. Edelman, C. L. Feldman, and P. H. Stone, "Role of Endothelial Shear Stress in the Natural History of Coronary Atherosclerosis and Vascular Remodeling," *Molecular, Cellular, and Vascular Behavior,* vol. 49, no. 25, pp. 2379-2393, 2007, doi: 10.1016/j.jacc.2007.02.059.

[126] F. M. Callaghan and S. M. Grieve, "Normal patterns of thoracic aortic wall shear stress measured using four-dimensional flow MRI in a large population," *American Journal of Physiology-Heart and Circulatory Physiology,* vol. 315, no. 5, pp. H1174-H1181, 2018, doi: 10.1152/ajpheart.00017.2018.

[127] J. Xiang, J. Yu, K. V. Snyder, E. I. Levy, A. H. Siddiqui, and H. Meng, "Hemodynamic-morphological discriminant models for intracranial aneurysm rupture remain stable with increasing sample size," *Journal of neurointerventional surgery,* vol. 8, no. 1, pp. 104-110, 2016, doi: 10.1136/neurintsurg-2014-011477.

[128] Y. Zhang, H. Takao, Y. Murayama, and Y. Qian, "Propose a wall shear stress divergence to estimate the risks of intracranial aneurysm rupture," *The Scientific World Journal,* vol. 2013, 2013.

[129] A. Chien, S. Tateshima, M. Castro, J. Sayre, J. Cebral, and F. Viñuela, "Patient-specific flow analysis of brain aneurysms at a single location: comparison of hemodynamic characteristics in small aneurysms," *Medical & Biological Engineering & Computing,* journal article vol. 46, no. 11, p. 1113, October 18 2008, doi: 10.1007/s11517-008-0400-5.

[130] E. Doutel, N. Viriato, J. Carneiro, J. B. L. M. Campos, and J. M. Miranda, "Geometrical effects in the hemodynamics of stenotic and non-stenotic left coronary arteries—numerical and in vitro approaches," *International Journal for Numerical Methods in Biomedical Engineering,* vol. 35, no. 8, p. e3207, 2019, doi: 10.1002/cnm.3207.

[131] A. Frydrychowicz *et al.*, "Three-dimensional analysis of segmental wall shear stress in the aorta by flow-sensitive four-dimensional-MRI," vol. 30, no. 1, pp. 77-84, 2009, doi: doi:10.1002/jmri.21790.

[132] M. Alimohammadi, J. Sherwood, M. Karimpour, O. Agu, S. Balabani, and V. Díaz-Zuccarini, "Aortic dissection simulation models for clinical support: Fluid-structure interaction vs. rigid wall models," *Biomedical engineering online,* vol. 14, p. 34, 04/15 2015, doi: 10.1186/s12938-015-0032-6.

[133] S. Park *et al.*, "Computational modeling with fluid-structure interaction of the severe m1 stenosis before and after stenting," (in eng), *Neurointervention,* vol. 8, no. 1, pp. 23-28, 2013, doi: 10.5469/neuroint.2013.8.1.23.

[134] A. Arzani and S. C. Shadden, "Characterizations and Correlations of Wall Shear Stress in Aneurysmal Flow," (in eng), *Journal of biomechanical engineering,* vol. 138, no. 1, pp. 0145031-01450310, 2016, doi: 10.1115/1.4032056.

[135] D. Fytanidis, J. Soulis, and G. Giannoglou, "Patient-specific arterial system flow oscillation," (in eng), *Hippokratia,* vol. 18, no. 2, pp. 162-165, 2014. [Online]. Available: https://www.ncbi.nlm.nih.gov/pubmed/25336881.

[136] U. Morbiducci, A. M. Kok, B. R. Kwak, P. H. Stone, D. A. Steinman, and J. J. Wentzel, "Atherosclerosis at arterial bifurcations: evidence for the role of haemodynamics and geometry," (in eng), *Thromb Haemost,* vol. 115, no. 3, pp. 484-92, Mar 2016, doi: 10.1160/th15-07-0597.

[137] P. H. Geoghegan, N. A. Buchmann, J. Soria, and M. C. Jermy, "Time-resolved PIV measurements of the flow field in a stenosed, compliant arterial model," (in English), *Experiments in Fluids,* vol. 54, no. 5, pp. 1-19, 2013/05/03 2013, Art no. 1528, doi: 10.1007/s00348-013-1528-0.

[138] E. A. Finol and C. H. Amon, "Blood Flow in Abdominal Aortic Aneurysms: Pulsatile Flow Hemodynamics," *Journal of Biomechanical Engineering,* vol. 123, no. 5, pp. 474-484, 2001, doi: 10.1115/1.1395573.

[139] G.-Y. Suh *et al.*, "Hemodynamic Changes Quantified in Abdominal Aortic Aneurysms with Increasing Exercise Intensity Using MR Exercise Imaging and Image-Based Computational Fluid Dynamics," *Annals of Biomedical Engineering,* journal article vol. 39, no. 8, pp. 2186-2202, August 01 2011, doi: 10.1007/s10439-011-0313-6.

[140] S. C. M. Yu and J. B. Zhao, "A steady flow analysis on the stented and non-stented sidewall aneurysm models," *Medical Engineering & Physics,* vol. 21, no. 3, pp. 133-141, 1999/04/01/ 1999, doi: https://doi.org/10.1016/S1350-4533(99)00037-5.

[141] I. M. Tiessen and M. R. Roach, "Factors in the Initiation and Propagation of Aortic Dissections in Human Autopsy Aortas," *Journal of Biomechanical Engineering,* vol. 115, no. 1, pp. 123-125, 1993, doi: 10.1115/1.2895461.

[142] P. I. Aaronson, J. P. T. Ward, and M. J. Connolly, *The Cardiovascular System at a Glance*. John Wiley & Sons (in en), 2012, p. 516.

[143] C. F. Gonzalez, Y. I. Cho, H. V. Ortega, and J. Moret, "Intracranial aneurysms: flow analysis of their origin and progression," *AJNR. American journal of neuroradiology,* vol. 13, no. 1, p. 181, 1992.

[144] J. L. Anderson, D. J. Adam, M. Berce, and D. E. Hartley, "Repair of thoracoabdominal aortic aneurysms with fenestrated and branched endovascular stent grafts," *Journal of Vascular Surgery,* vol. 42, no. 4, pp. 600-607, 2005/10/01/ 2005, doi: https://doi.org/10.1016/j.jvs.2005.05.063.

[145] B. C. Mendes and G. S. Oderich, "Selection of Optimal Bridging Stents for Fenestrations and Branches," in *Endovascular Aortic Repair: Current Techniques with Fenestrated, Branched and Parallel Stent-Grafts*, G. S. Oderich Ed. Cham: Springer International Publishing, 2017, pp. 359-374.

[146] H. K. Versteeg and W. Malalasekera, *An introduction to computational fluid dynamics: the finite volume method*, 2nd ed. (no. Book, Whole). New York;Harlow, England;: Pearson Education, 2007.

[147] S. Prakash and C. R. Ethier, "Requirements for Mesh Resolution in 3D Computational Hemodynamics," *Journal of Biomechanical Engineering,* vol. 123, no. 2, pp. 134-144, 2000, doi: 10.1115/1.1351807.

[148] M. Midulla *et al.*, "Haemodynamic imaging of thoracic stent-grafts by computational fluid dynamics (CFD): presentation of a patient-specific method combining magnetic resonance imaging and numerical simulations," *European Radiology,* journal article vol. 22, no. 10, pp. 2094-2102, October 01 2012, doi: 10.1007/s00330-012-2465-7.

[149] S. Morlacchi and F. Migliavacca, "Modeling Stented Coronary Arteries: Where We are, Where to Go," *Annals of Biomedical Engineering,* journal article vol. 41, no. 7, pp. 1428-1444, July 01 2013, doi: 10.1007/s10439-012-0681-6.

[150] C. P. Cheng, R. J. Herfkens, and C. A. Taylor, "Abdominal aortic hemodynamic conditions in healthy subjects aged 50–70 at rest and during lower limb exercise: in vivo quantification using MRI," *Atherosclerosis,* vol. 168, no. 2, pp. 323-331, 2003/06/01/ 2003, doi: https://doi.org/10.1016/S0021-9150(03)00099-6.

[151] C. A. Taylor, T. J. Hughes, and C. K. Zarins, "Effect of exercise on hemodynamic conditions in the abdominal aorta," (in eng), *J Vasc Surg,* vol. 29, no. 6, pp. 1077-89, Jun 1999, doi: 10.1016/s0741-5214(99)70249-1.

[152] A. S. Les *et al.*, "Quantification of hemodynamics in abdominal aortic aneurysms during rest and exercise using magnetic resonance imaging and computational fluid dynamics," (in eng), *Ann Biomed Eng,* vol. 38, no. 4, pp. 1288-313, Apr 2010, doi: 10.1007/s10439-010-9949-x.

[153] B. T. Tang *et al.*, "Abdominal aortic hemodynamics in young healthy adults at rest and during lower limb exercise: quantification using image-based computer modeling," (in eng), *Am J*

*Physiol Heart Circ Physiol,* vol. 291, no. 2, pp. H668-76, Aug 2006, doi: 10.1152/ajpheart.01301.2005.

[154] K. M. Tse, R. Chang, H. P. Lee, S. P. Lim, S. K. Venkatesh, and P. Ho, "A computational fluid dynamics study on geometrical influence of the aorta on haemodynamics," *European Journal of Cardio-Thoracic Surgery,* vol. 43, no. 4, pp. 829-838, 2012.

[155] V. Mendez, G. Marzio Di, and S. Pasta, "Comparison of hemodynamic and structural indices of ascending thoracic aortic aneurysm as predicted by 2-way FSI, CFD rigid wall simulation and patient-specific displacement-based FEA," (in English), *Computers in Biology and Medicine,* vol. 100, pp. 221-229, 2018, doi: http://dx.doi.org/10.1016/j.compbiomed.2018.07.013.

[156] S. Beier *et al.*, "Hemodynamics in Idealized Stented Coronary Arteries: Important Stent Design Considerations," *Annals of Biomedical Engineering,* journal article vol. 44, no. 2, pp. 315-329, February 01 2016, doi: 10.1007/s10439-015-1387-3.

[157] F. P. P. TAN, R. TORII, A. BORGHI, R. H. MOHIADDIN, N. B. WOOD, and X. Y. XU, "Fluid-Structure Interaction Analysis Of Wall Stress And Flow Patterns In A Thoracic Aortic Aneurysm," *International Journal of Applied Mechanics,* vol. 01, no. 01, pp. 179-199, 2009, doi: 10.1142/s1758825109000095.

[158] J. R. Cebral *et al.*, "Combining data from multiple sources to study mechanisms of aneurysm disease: Tools and techniques," *International Journal for Numerical Methods in Biomedical Engineering,* vol. 34, no. 11, p. e3133, 2018, doi: 10.1002/cnm.3133.

[159] A. Prasad, N. Xiao, X.-Y. Gong, C. K. Zarins, and C. A. Figueroa, "A computational framework for investigating the positional stability of aortic endografts," *Biomechanics and Modeling in Mechanobiology,* vol. 12, no. 5, pp. 869-887, 2013/10/01 2013, doi: 10.1007/s10237-012-0450-3.

[160] A. Prasad, L. K. To, M. L. Gorrepati, C. K. Zarins, and C. A. Figueroa, "Computational Analysis of Stresses Acting on Intermodular Junctions in Thoracic Aortic Endografts," *Journal of Endovascular Therapy,* vol. 18, no. 4, pp. 559-568, 2011/08/01 2011, doi: 10.1583/11-3472.1.

[161] A. Marzo, P. Singh, P. Reymond, N. Stergiopulos, U. Patel, and R. Hose, "Influence of Inlet Boundary Conditions on the Local Haemodynamics of Intracranial Aneurysms," *Computer Methods in Biomechanics: Biomedical Engineering Online,* vol. 12, no. 4, pp. 431-444, 2009.

[162] B.-K. Lee, "Computational Fluid Dynamics in Cardiovascular Disease," *Korean Circ J,* vol. 41, no. 8, pp. 423-430, 8/ 2011. [Online]. Available: http://synapse.koreamed.org/DOIx.php?id=10.4070%2Fkcj.2011.41.8.423.

[163] K. V. Bulusu and M. W. Plesniak, "Experimental Investigation of Secondary Flow Structures Downstream of a Model Type IV Stent Failure in a 180° Curved Artery Test Section," *Journal of Visualized Experiments : JoVE,* no. 113, 2016/07/19/ 2016, doi: 10.3791/51288.

[164] A. Marzo *et al.*, "Computational Hemodynamics in Cerebral Aneurysms: The Effects of Modeled versus Measured Boundary Conditions," *Annals of Biomedical Engineering,* vol. 39, no. 2, pp. 884-896, 2011.

[165] M. D. Ford *et al.*, "PIV-Measured Versus CFD-Predicted Flow Dynamics in Anatomically Realistic Cerebral Aneurysm Models," *Journal of Biomechanical Engineering,* vol. 130, no. 2, pp. 021015-021015-9, 2008, doi: 10.1115/1.2900724.

[166] P. Sandiford, D. Mosquera, and D. Bramley, "Trends in incidence and mortality from abdominal aortic aneurysm in New Zealand," *BJS,* vol. 98, no. 5, pp. 645-651, 2011, doi: 10.1002/bjs.7461.

[167] P. D. Stein and H. N. Sabbah, "Turbulent blood flow in the ascending aorta of humans with normal and diseased aortic valves," (in en), *Circulation Research,* vol. 39, no. 1, pp. 58-65, 1976/07// 1976, doi: 10.1161/01.RES.39.1.58.

[168] P. Jhunjhunwala, P. M. Padole, S. B. Thombre, and A. Sane, "Prediction of blood pressure and blood flow in stenosed renal arteries using CFD," *IOP Conference Series: Materials Science and Engineering,* vol. 346, p. 012066, 2018/04 2018, doi: 10.1088/1757-899x/346/1/012066.

[169] S. K. Lam, G. S. K. Fung, S. W. K. Cheng, and K. W. Chow, "A computational study on the biomechanical factors related to stent-graft models in the thoracic aorta," *Medical & Biological Engineering & Computing,* vol. 46, no. 11, pp. 1129-1138, 2008/11/01 2008, doi: 10.1007/s11517-008-0361-8.

[170] Y.-H. Lu, K. Mani, B. Panigrahi, W.-T. Hsu, and C.-Y. Chen, "Endoleak assessment using computational fluid dynamics and image processing methods in stented abdominal aortic aneurysm models," *Computational and mathematical methods in medicine,* vol. 2016, 2016.

[171] A. N. DeMaria, W. Bommer, A. Neumann, L. Weinert, H. Bogren, and D. T. Mason, "Identification and localization of aneurysms of the ascending aorta by cross-sectional echocardiography," *Circulation,* vol. 59, no. 4, pp. 755-761, 1979, doi: doi:10.1161/01.CIR.59.4.755.

[172] S. Numata *et al.*, "Blood flow analysis of the aortic arch using computational fluid dynamics," *European Journal of Cardio-Thoracic Surgery,* vol. 49, no. 6, pp. 1578-1585, 2016.

[173] S. Seshadhri, G. Janiga, O. Beuing, M. Skalej, and D. Thévenin, "Impact of Stents and Flow Diverters on Hemodynamics in Idealized Aneurysm Models," *Journal of Biomechanical Engineering,* vol. 133, no. 7, pp. 071005-071005-9, 2011, doi: 10.1115/1.4004410.

[174] A. W. Martinez and E. L. Chaikof, "Microfabrication and nanotechnology in stent design," *Wiley interdisciplinary reviews. Nanomedicine and nanobiotechnology,* vol. 3, no. 3, pp. 256-268, May-Jun 2011, doi: 10.1002/wnan.123.

[175] R. Xing *et al.*, "Temporal and spatial changes in wall shear stress during atherosclerotic plaque progression in mice," *Royal Society Open Science,* vol. 5, no. 3, p. 171447, 2018, doi: 10.1098/rsos.171447.

[176] I. Avrahami, M. Brand, T. Meirson, Z. Ovadia-Blechman, and M. Halak, "Hemodynamic and mechanical aspects of fenestrated endografts for treatment of Abdominal Aortic Aneurysm," *European Journal of Mechanics - B/Fluids,* vol. 35, pp. 85-91, 2012/09/01/ 2012, doi: https://doi.org/10.1016/j.euromechflu.2012.03.010.

[177] Z. Sun and T. Chaichana, "Fenestrated Stent Graft Repair of Abdominal Aortic Aneurysm: Hemodynamic Analysis of the Effect of Fenestrated Stents on the Renal Arteries," *Korean J Radiol,* vol. 11, no. 1, pp. 95-106, 2/ 2010. [Online]. Available: http://synapse.koreamed.org/DOIx.php?id=10.3348%2Fkjr.2010.11.1.95.

[178] H. S. Kandail, M. Hamady, and X. Y. Xu, "Hemodynamic Functions of Fenestrated Stent Graft under Resting, Hypertension, and Exercise Conditions," (in English), *Frontiers in Surgery,* Original Research vol. 3, no. 35, 2016-June-14 2016, doi: 10.3389/fsurg.2016.00035.

[179] M. Shakeri, I. Khodarahmi, M. K. Sharp, and A. A. Amini, *Optical imaging of steady flow in a phantom model of iliac artery stenosis: comparison of CFD simulations with PIV measurements* (SPIE Medical Imaging). SPIE, 2010.

[180] G. Iaccarino and C. Elkins, "Towards Rapid Analysis of Turbulent Flows in Complex Internal Passages," *Flow, Turbulence and Combustion,* vol. 77, pp. 27-39, 11/01 2006, doi: 10.1007/s10494-006-9035-5.

[181] D. Wendt *et al.*, "Development and In Vitro Characterization of a New Artificial Flow Channel," (in en), *Artificial Organs,* vol. 35, no. 3, pp. E59-E64, 2011, doi: 10.1111/j.1525-1594.2010.01166.x.

[182] M. Minakawa *et al.*, "Hydrodynamic evaluation of axillary artery perfusion for normal and diseased aorta," *General thoracic and cardiovascular surgery,* vol. 56, no. 5, pp. 215-221, 2008.

[183] P. Van Ooij *et al.*, "Complex flow patterns in a real-size intracranial aneurysm phantom: phase contrast MRI compared with particle image velocimetry and computational fluid dynamics," *NMR in Biomedicine,* vol. 25, no. 1, pp. 14-26, 2012.

[184] K. Rhee, M. H. Han, and S. H. Cha, "Changes of flow characteristics by stenting in aneurysm models: influence of aneurysm geometry and stent porosity," *Annals of biomedical engineering,* vol. 30, no. 7, pp. 894-904, 2002.

[185] P. Geoghegan, N. Buchmann, C. Spence, S. Moore, and M. Jermy, "Fabrication of rigid and flexible refractive-index-matched flow phantoms for flow visualisation and optical flow measurements," *Experiments in fluids,* vol. 52, no. 5, pp. 1331-1347, 2012.

[186] S. G. Yazdi *et al.*, "The flow field in compliant and rigid models of the human aortic arch," presented at the 19th International Symposium on the Application of Laser and Imaging Techniques to Fluid Mechanics, Lisbon, Portugal, July 16-18, 2018, 2018, 57.

[187] W. E. Stehbens, "Flow In Glass Models Of Arterial Bifurcations And Berry Aneurysms At Low Reynolds Numbers," *Quarterly Journal of Experimental Physiology and Cognate Medical Sciences,* vol. 60, no. 3, pp. 181-192, 1975, doi: 10.1113/expphysiol.1975.sp002310.

[188] M. Friedman, B. Kuban, P. Schmalbrock, K. Smith, and T. Altan, *Fabrication of Vascular Replicas From Magnetic Resonance Images*. 1995, pp. 364-6.

[189] C. J. T. Spence, N. A. Buchmann, M. C. Jermy, and S. M. Moore, "Stereoscopic PIV measurements of flow in the nasal cavity with high flow therapy," *Experiments in Fluids,* journal article vol. 50, no. 4, pp. 1005-1017, April 01 2011, doi: 10.1007/s00348-010-0984-z.

[190] M. Friedman, C. Bargeron, G. Hutchins, F. Mark, and O. Deters, "Hemodynamic measurements in human arterial casts, and their correlation with histology and luminal area," *Journal of biomechanical engineering,* vol. 102, no. 3, pp. 247-251, 1980.

[191] O. Deters, C. Bargeron, F. Mark, and M. Friedman, "Measurement of wall motion and wall shear in a compliant arterial cast," *Journal of biomechanical engineering,* vol. 108, no. 4, pp. 355-358, 1986.

[192] M. Büsen *et al.*, "Development of an *In Vitro* PIV Setup for Preliminary Investigation of the Effects of Aortic Compliance on Flow Patterns and Hemodynamics," (in en), *Cardiovascular Engineering and Technology,* vol. 8, no. 3, pp. 368-377, 2017/09/01/ 2017, doi: 10.1007/s13239-017-0309-y.

[193] M. H. Friedman, G. M. Hutchins, C. Brent Bargeron, O. J. Deters, and F. F. Mark, "Correlation between intimal thickness and fluid shear in human arteries," *Atherosclerosis,* vol. 39, no. 3, pp. 425-436, 1981/06/01/ 1981, doi: https://doi.org/10.1016/0021-9150(81)90027-7.

[194] S. Kefayati, J. S. Milner, D. W. Holdsworth, and T. L. Poepping, "In vitro shear stress measurements using particle image velocimetry in a family of carotid artery models: effect of stenosis severity, plaque eccentricity, and ulceration," *PloS one,* vol. 9, no. 7, p. e98209, 2014.

[195] V. Deplano, C. Guivier-Curien, and E. Bertrand, "3D analysis of vortical structures in an abdominal aortic aneurysm by stereoscopic PIV," (in en), *Experiments in Fluids,* vol. 57, no. 11, p. 167, 2016/10/14/ 2016, doi: 10.1007/s00348-016-2263-0.

[196] L. Hütter, P. H. Geoghegan, P. D. Docherty, M. S. Lazarjan, D. Clucas, and M. Jermy, "Fabrication of a compliant phantom of the human aortic arch for use in Particle Image Velocimetry (PIV) experimentation," *Current Directions in Biomedical Engineering,* vol. 2, no. 1, pp. 493-497, 2016.

[197] D. Duncan *et al.*, "The effect of compliance on wall shear in casts of a human aortic bifurcation," *Journal of biomechanical engineering,* vol. 112, no. 2, pp. 183-188, 1990.

[198] P. Bouillot, O. Brina, R. Ouared, K.-O. Lovblad, M. Farhat, and V. M. Pereira, "Particle Imaging Velocimetry Evaluation of Intracranial Stents in Sidewall Aneurysm: Hemodynamic Transition Related to the Stent Design," *PLOS ONE,* vol. 9, no. 12, p. e113762, 2014, doi: 10.1371/journal.pone.0113762.

[199] E. Foucault, S. Huberson, P. Braud, and D. Coisne, "On the pulsatile flow through a coronary bifurcation with stent," *European Journal of Mechanics - B/Fluids,* vol. 61, pp. 177-186, 2017/01/01/ 2017, doi: 10.1016/j.euromechflu.2016.11.007.

[200] C.-h. Yu, K. Matsumoto, S. Shida, D. J. Kim, and M. Ohta, "A steady flow analsys on a cerebral aneurysm model with several stents for new stent design using PIV," (in English), *Journal of Mechanical Science and Technology; Heidelberg,* vol. 26, no. 5, pp. 1333-1340, 2012/05// 2012, doi: http://dx.doi.org.ezproxy.canterbury.ac.nz/10.1007/s12206-012-0322-x.

[201] K. D. Dennis, T. L. Rossman, D. F. Kallmes, and D. Dragomir-Daescu, "Intra-aneurysmal flow rates are reduced by two flow diverters: an experiment using tomographic particle image velocimetry in an aneurysm model," *Journal of neurointerventional surgery,* vol. 7, no. 12, pp. 937-942, 2015.

[202] M. Liu, A. Sun, and X. Deng, "Numerical and Experimental Investigation of the Hemodynamic Performance of Bifurcated Stent Grafts with Various Torsion Angles," *Scientific Reports,* vol. 8, no. 1, p. 12625, 2018/08/22 2018, doi: 10.1038/s41598-018-31015-2.

[203] Y. Lei *et al.*, "A new process for customized patient-specific aortic stent graft using 3D printing technique," *Medical Engineering & Physics,* vol. 77, pp. 80-87, 2020/03/01/ 2020, doi: https://doi.org/10.1016/j.medengphy.2019.12.002.

[204] E. Groot Jebbink *et al.*, "Hemodynamic comparison of stent configurations used for aortoiliac occlusive disease," *Journal of Vascular Surgery,* vol. 66, no. 1, pp. 251-260.e1, 2017/07/01/ 2017, doi: https://doi.org/10.1016/j.jvs.2016.07.128.

[205] V. Deplano, Y. Knapp, E. Bertrand, and E. Gaillard, "Flow behaviour in an asymmetric compliant experimental model for abdominal aortic aneurysm," *Journal of Biomechanics,* vol. 40, no. 11, pp. 2406-2413, 2007/01/01/ 2007, doi: https://doi.org/10.1016/j.jbiomech.2006.11.017.

[206] D. Dillon-Murphy, A. Noorani, D. Nordsletten, and C. A. Figueroa, "Multi-modality image-based computational analysis of haemodynamics in aortic dissection," *Biomechanics Modeling in Mechanobiology,* vol. 15, no. 4, pp. 857-876, 2016.

[207] R. M. Romarowski, A. Lefieux, S. Morganti, A. Veneziani, and F. Auricchio, "Patient-specific CFD modelling in the thoracic aorta with PC-MRI–based boundary conditions: A least-square three-element Windkessel approach," *International Journal for Numerical Methods in Biomedical Engineering,* vol. 34, no. 11, p. e3134, 2018.

[208] M. Guarini, J. Urzua, A. Cipriano, and W. Gonzalez, "Estimation of cardiac function from computer analysis of the arterial pressure waveform," *IEEE Transactions on Biomedical Engineering,* vol. 45, no. 12, pp. 1420-1428, 1998, doi: 10.1109/10.730436.

[209] R. Moreno, M. Chau, B. Tayllamin, H. Rousseau, and F. Nicoud, "Correct rheology simulation on compliant thoracic aorta model: comparison between CFD and MRI velocity measurements," *Computer Methods in Biomechanics and Biomedical Engineering,* vol. 12, no. sup1, pp. 195-196, 2009/08/01 2009, doi: 10.1080/10255840903091551.

[210] P. Dwidmuthe, C. S Mathpati, and J. B Joshi, *CFD Simulation of Blood Flow inside the Human Artery: Aorta*. 2018.

[211] M. Y. Pahakis, J. R. Kosky, R. O. Dull, and J. M. Tarbell, "The role of endothelial glycocalyx components in mechanotransduction of fluid shear stress," (in en), *Biochemical and Biophysical Research Communications,* vol. 355, no. 1, pp. 228-233, 2007/03// 2007, doi: 10.1016/j.bbrc.2007.01.137.

[212] U. Morbiducci *et al.*, "In Vivo Quantification of Helical Blood Flow in Human Aorta by Time-Resolved Three-Dimensional Cine Phase Contrast Magnetic Resonance Imaging," *Annals of Biomedical Engineering,* journal article vol. 37, no. 3, p. 516, December 06 2008, doi: 10.1007/s10439-008-9609-6.

[213] F. Nicoud and T. Schönfeld, "Integral boundary conditions for unsteady biomedical CFD applications," *International Journal for Numerical Methods in Fluids,* vol. 40, no. 3-4, pp. 457-465, 2002.

[214] N. Westerhof, J.-W. Lankhaar, and B. E. Westerhof, "The arterial Windkessel," *Medical Biological Engineering Computing,* journal article vol. 47, no. 2, pp. 131-141, February 01 2009, doi: 10.1007/s11517-008-0359-2.

[215] M. Alishahi, M. M. Alishahi, and H. Emdad, "Numerical simulation of blood flow in a flexible stenosed abdominal real aorta," *Scientia Iranica,* vol. 18, no. 6, pp. 1297-1305, 2011/12/01/ 2011, doi: https://doi.org/10.1016/j.scient.2011.11.021.

[216] J. P. Abraham, E. M. Sparrow, and R. D. Lovik, "Unsteady, three-dimensional fluid mechanic analysis of blood flow in plaque-narrowed and plaque-freed arteries," *International Journal of Heat and Mass Transfer,* vol. 51, no. 23, pp. 5633-5641, 2008/11/01/ 2008, doi: https://doi.org/10.1016/j.ijheatmasstransfer.2008.04.038.

[217] N. Stergiopulos, B. E. Westerhof, and N. Westerhof, "Total arterial inertance as the fourth element of the windkessel model," *American Journal of Physiology-Heart and Circulatory Physiology,* vol. 276, no. 1, pp. H81-H88, 1999, doi: 10.1152/ajpheart.1999.276.1.H81.

[218] C. A. Figueroa, I. E. Vignon-Clementel, K. E. Jansen, T. J. R. Hughes, and C. A. Taylor, "A coupled momentum method for modeling blood flow in three-dimensional deformable arteries," *Computer Methods in Applied Mechanics and Engineering,* vol. 195, no. 41, pp. 5685-5706, 2006/08/15/ 2006, doi: https://doi.org/10.1016/j.cma.2005.11.011.

[219] J. Xu *et al.*, "Combined Effects of Flow Diverting Strategies and Parent Artery Curvature on Aneurysmal Hemodynamics: A CFD Study," (in English), *PLoS One,* vol. 10, no. 9, 2015, doi: http://dx.doi.org/10.1371/journal.pone.0138648.

[220] S. G. Yazdi *et al.*, "In-vitro measurement of hemodynamics in rigid and compliant silicone replicas of aortic arch using stereoscopic particle image velocimetry " in *Fluids in New Zealand (FiNZ)*, Dunedin, New Zealand, F. Montiel, Ed., 31 Jan - 1 Feb 2019.

[221] A. S. Les, J. J. Yeung, G. M. Schultz, R. J. Herfkens, R. L. Dalman, and C. A. Taylor, "Supraceliac and Infrarenal Aortic Flow in Patients with Abdominal Aortic Aneurysms: Mean Flows, Waveforms, and Allometric Scaling Relationships," *Cardiovascular Engineering and Technology,* journal article vol. 1, no. 1, pp. 39-51, March 01 2010, doi: 10.1007/s13239-010-0004-8.

[222] P. D. Docherty *et al.*, "Integral-based reconstruction of static pressure in a compliant axisymmetric vessel using velocity field data from particle image velocimetry (PIV) analysis," in *Fluids in New Zealand (FiNZ)*, Dunedin, New Zealand, F. Montiel, Ed., 31 Jan - 1 Feb 2019.

[223] H. W. Weizsacker and J. G. Pinto, "Isotropy and anisotropy of the arterial wall," *Journal of Biomechanics,* vol. 21, no. 6, pp. 477-487, 1988/01/01/ 1988, doi: https://doi.org/10.1016/0021-9290(88)90240-0.

[224] M.-W. Han *et al.*, "Woven type smart soft composite for soft morphing car spoiler," *Composites Part B: Engineering,* vol. 86, 10/01 2015, doi: 10.1016/j.compositesb.2015.10.009.

[225] P. N. Williamson *et al.*, "PIV Analysis of Stented Haemodynamics in the Descending Aorta," presented at the 41st Annual International Conference of the IEEE Engineering in Medicine & Biology Society (EMBC), Berlin, Germany, 23-27 July, 2019.

[226] D. A. Fedosov, W. Pan, B. Caswell, G. Gompper, and G. E. Karniadakis, "Predicting human blood viscosity in silico," (in eng), *Proceedings of the National Academy of Sciences of the United States of America,* vol. 108, no. 29, pp. 11772-11777, 2011, doi: 10.1073/pnas.1101210108.

[227] K. Shimogaito, K. Ohara, A. Ichikawa, T. Kubo, and T. Fukuda, "The study of valved hybrid fractal stent for the next generation medical care—The blood flow simulation in cerebral aneurysm by CFD," in *Micro-NanoMechatronics and Human Science (MHS), 2016 International Symposium on*, 2016: IEEE, pp. 1-3.

[228] P. N. Williamson *et al.*, "Particle Image Velocimetry (PIV) Analysis of Haemodynamics Distal of a Frozen Elephant Trunk Stent Phantom," in *Fluids in New Zealand*, Dunedin, New Zealand, F. Montiel, Ed., 31 Jan - 1 Feb 2019.

[229] A. Arzani, "Accounting for residence-time in blood rheology models: do we really need non-Newtonian blood flow modelling in large arteries?," *Journal of The Royal Society Interface,* vol. 15, no. 146, p. 20180486, 2018, doi: doi:10.1098/rsif.2018.0486.

[230] S.-W. Lee and D. A. Steinman, "On the Relative Importance of Rheology for Image-Based CFD Models of the Carotid Bifurcation," *Journal of Biomechanical Engineering,* vol. 129, no. 2, pp. 273-278, 2006, doi: 10.1115/1.2540836.

[231] X. Liu, Y. Fan, X. Deng, and F. Zhan, "Effect of non-Newtonian and pulsatile blood flow on mass transport in the human aorta," *Journal of biomechanics,* vol. 44, no. 6, pp. 1123-1131, 2011.

[232] M. Friedman, C. Bargeron, D. Duncan, G. Hutchins, and F. Mark, "Effects of arterial compliance and non-Newtonian rheology on correlations between intimal thickness and wall shear," *Journal of biomechanical engineering,* vol. 114, no. 3, pp. 317-320, 1992.

[233] R. J. Lefkowitz and J. T. Willerson, "Prospects for Cardiovascular Research," *JAMA,* vol. 285, no. 5, pp. 581-587, 2001, doi: 10.1001/jama.285.5.581.

[234] A. M. Hoving, E. E. de Vries, J. Mikhal, G. J. de Borst, and C. H. Slump, "A Systematic Review for the Design of In Vitro Flow Studies of the Carotid Artery Bifurcation," *Cardiovascular Engineering and Technology,* vol. 11, no. 2, pp. 111-127, 2020/04/01 2020, doi: 10.1007/s13239-019-00448-9.

[235] B. B. Lieber, "Arterial macrocirculatory hemodynamics," *The biomedical engineering handbook,* vol. 1, 2000.

[236] H. C. Hughes, "Swine in cardiovascular research," (in eng), *Laboratory animal science,* vol. 36, no. 4, pp. 348-350, 1986/08// 1986. [Online]. Available: http://europepmc.org/abstract/MED/3534437.

[237] S. F. Wright, I. Zadrazil, and C. N. Markides, "A review of solid–fluid selection options for optical-based measurements in single-phase liquid, two-phase liquid–liquid and multiphase solid–liquid flows," *Experiments in Fluids,* vol. 58, no. 9, p. 108, 2017/08/02 2017, doi: 10.1007/s00348-017-2386-y.

[238] H. Ha *et al.*, "Age-Related Vascular Changes Affect Turbulence in Aortic Blood Flow," (in English), *Frontiers in Physiology,* Original Research vol. 9, no. 36, 2018-January-25 2018, doi: 10.3389/fphys.2018.00036.

[239] A. F. Stalder *et al.*, "Assessment of flow instabilities in the healthy aorta using flow-sensitive MRI," *Journal of Magnetic Resonance Imaging,* vol. 33, no. 4, pp. 839-846, 2011, doi: https://doi.org/10.1002/jmri.22512.

[240] M. Nakamura, S. Wada, S. Yokosawa, H. Isoda, H. Takeda, and T. Yamaguchi, "Measurement of Blood Flow in the Left Ventricle and Aorta Using Clinical 2D Cine Phase-Contrast Magnetic Resonance Imaging," *Journal of Biomechanical Science and Engineering,* vol. 2, no. 2, pp. 46-57, 2007, doi: 10.1299/jbse.2.46.

[241] C. A. Kousera, N. B. Wood, W. A. Seed, R. Torii, D. O'Regan, and X. Y. Xu, "A Numerical Study of Aortic Flow Stability and Comparison With In Vivo Flow Measurements," *Journal of Biomechanical Engineering,* vol. 135, no. 1, 2012, doi: 10.1115/1.4023132.

[242] O. San and A. Staples, "An Improved Model For Reduced-Order Physiological Fluid Flows," *Journal of Mechanics in Medicine and Biology,* vol. 12, 10/19 2012, doi: 10.1142/S0219519411004666.

[243] C. Del Gaudio, U. Morbiducci, and M. Grigioni, "Time Dependent Non-Newtonian Numerical Study of the Flow Field in a Realistic Model of Aortic Arch," *The International Journal of Artificial Organs,* vol. 29, no. 7, pp. 709-718, 2006, doi: 10.1177/039139880602900711.

[244] H. Liu *et al.*, "Influences of nonplanarity, bifurcations, dynamics, inflow and outflows on blood flow patterns in aortic arch: A multi-scale computational study," *Proc. ASME-BED2003,* 2003.

[245] S. Miyazaki *et al.*, "Validation of numerical simulation methods in aortic arch using 4D Flow MRI," *Heart and vessels,* vol. 32, no. 8, pp. 1032-1044, 2017.

[246] Z. Cheng, C. Juli, N. B. Wood, R. G. J. Gibbs, and X. Y. Xu, "Predicting flow in aortic dissection: Comparison of computational model with PC-MRI velocity measurements," *Medical*

*Engineering & Physics,* vol. 36, no. 9, pp. 1176-1184, 2014/09/01/ 2014, doi: https://doi.org/10.1016/j.medengphy.2014.07.006.

[247] N. Shahcheraghi, H. A. Dwyer, A. Y. Cheer, A. I. Barakat, and T. Rutaganira, "Unsteady and Three-Dimensional Simulation of Blood Flow in the Human Aortic Arch," *Journal of Biomechanical Engineering,* vol. 124, no. 4, pp. 378-387, 2002, doi: 10.1115/1.1487357.

[248] P. D. Stein, H. N. Sabbah, D. T. Anbe, and F. J. Walburn, "Blood velocity in the abdominal aorta and common iliac artery of man," *Biorheology,* vol. 16, pp. 249-255, 1979, doi: 10.3233/BIR-1979-16313.

[249] D. A. Steinman, B. Vinh, C. R. Ethier, M. Ojha, R. S. Cobbold, and K. W. Johnston, "A numerical simulation of flow in a two-dimensional end-to-side anastomosis model," (in eng), *J Biomech Eng,* vol. 115, no. 1, pp. 112-8, Feb 1993, doi: 10.1115/1.2895457.

[250] N. Buchmann, M. Jermy, and C. Nguyen, "Experimental investigation of carotid artery haemodynamics in an anatomically realistic model," *International Journal of Experimental and Computational Biomechanics,* vol. 1, pp. 172-192, 01/01 2009, doi: 10.1504/IJECB.2009.029192.

[251] R. Savabi, M. Nabaei, S. Farajollahi, and N. Fatouraee, "Fluid structure interaction modeling of aortic arch and carotid bifurcation as the location of baroreceptors," *International Journal of Mechanical Sciences,* vol. 165, p. 105222, 2020/01/01/ 2020, doi: https://doi.org/10.1016/j.ijmecsci.2019.105222.

[252] J. Duijndam, "Design and implementation of an in-vitro carotid artery flow circuit with pulsatile flow conditions," University of Twente, 2020.

[253] D. Liepsch, A. Poll, J. Strigberger, H. N. Sabbah, and P. D. Stein, "Flow Visualization Studies in a Mold of the Normal Human Aorta and Renal Arteries," *Journal of Biomechanical Engineering,* vol. 111, no. 3, pp. 222-227, 1989, doi: 10.1115/1.3168369.

[254] Y. J. Park, C.-W. Park, K. B. Park, Y. N. Roh, D.-I. Kim, and Y.-W. Kim, "Inference from clinical and fluid dynamic studies about underlying cause of spontaneous isolated superior mesenteric artery dissection," *Journal of Vascular Surgery,* vol. 53, no. 1, pp. 80-86, 2011/01/01/ 2011, doi: https://doi.org/10.1016/j.jvs.2010.07.055.

[255] M. C. Brindise *et al.*, "Multi-modality cerebral aneurysm haemodynamic analysis: in vivo 4D flow MRI, in vitro volumetric particle velocimetry and in silico computational fluid dynamics," (in eng), *Journal of the Royal Society, Interface,* vol. 16, no. 158, pp. 20190465-20190465, 2019, doi: 10.1098/rsif.2019.0465.

[256] Wikipedia. "Womersley Number." Wikipedia. https://en.wikipedia.org/wiki/Womersley_number (accessed 14/06/2021, 2021).

[257] Y. Guan, L. Wang, J. Lin, and M. W. King, "Compliance Study of Endovascular Stent Grafts Incorporated with Polyester and Polyurethane Graft Materials in both Stented and Unstented Zones," *Materials,* vol. 9, no. 8, 2016/08/05/ 2016, doi: 10.3390/ma9080658.

[258] M. Karck, A. Chavan, N. Khaladj, H. Friedrich, C. Hagl, and A. Haverich, "The frozen elephant trunk technique for the treatment of extensive thoracic aortic aneurysms: operative results and follow-up," (in en), *European Journal of Cardio-Thoracic Surgery,* vol. 28, no. 2, pp. 286-290, 2005/08/01/ 2005, doi: 10.1016/j.ejcts.2005.02.046.

[259] C. E. Reed, R. H. Feins, T. W. Shields, and J. L. III, *General Throacic Surgery*, 7th ed. Lippincott Williams and Wilkins, 2009.

[260] M. Karck and H. Kamiya, "Progress of the treatment for extended aortic aneurysms; is the frozen elephant trunk technique the next standard in the treatment of complex aortic disease including the arch?," (in eng), *European Journal of Cardio-Thoracic Surgery: Official Journal of the European Association for Cardio-Thoracic Surgery,* vol. 33, no. 6, pp. 1007-1013, 2008/06// 2008, doi: 10.1016/j.ejcts.2008.02.030.

[261] R. Di Bartolomeo *et al.*, "Frozen versus conventional elephant trunk technique: application in clinical practice," (in en), *European Journal of Cardio-Thoracic Surgery,* vol. 51, no. suppl_1, pp. i20-i28, 2017/01/01/ 2017, doi: 10.1093/ejcts/ezw335.

[262] N. Uchida *et al.*, "Long-term results of the frozen elephant trunk technique for extended aortic arch disease," (in en), *European Journal of Cardio-Thoracic Surgery,* vol. 37, no. 6, pp. 1338-1345, 2010/06// 2010, doi: 10.1016/j.ejcts.2010.01.007.

[263] G. F. Mitchell *et al.*, "Changes in arterial stiffness and wave reflection with advancing age in healthy men and women: the Framingham Heart Study," vol. 43, no. 6, pp. 1239-1245, 2004.

[264] S. C. R. DENNIS and M. NG, "DUAL SOLUTIONS FOR STEADY LAMINAR FLOW THROUGH A CURVED TUBE," *The Quarterly Journal of Mechanics and Applied Mathematics,* vol. 35, no. 3, pp. 305-324, 1982, doi: 10.1093/qjmam/35.3.305.

[265] M. R. Najjari and M. W. Plesniak, "Secondary flow vortical structures in a 180° elastic curved vessel with torsion under steady and pulsatile inflow conditions," *Physical Review Fluids,* vol. 3, no. 1, p. 013101, 01/22/ 2018, doi: 10.1103/PhysRevFluids.3.013101.

[266] M. S. Alsoufi and A. E. Elsayed, "Surface roughness quality and dimensional accuracy—a comprehensive analysis of 100% infill printed parts fabricated by a personal/desktop cost-effective FDM 3D printer," *Materials Sciences and Applications,* vol. 9, no. 1, pp. 11-40, 2018.

[267] A. Stalder, M. Russe, A. Frydrychowicz, J. Bock, J. Hennig, and M. Markl, "Quantitative 2D and 3D phase contrast MRI: optimized analysis of blood flow and vessel wall parameters," *Magnetic resonance in medicine,* vol. 60, no. 5, pp. 1218-1231, 2008.

[268] W. R. Milnor, *Cardiovascular physiology*. Oxford University Press, USA, 1990.

[269] C. Y. Xing *et al.*, "Distribution of cardiac output to the brain across the adult lifespan," (in eng), *J Cereb Blood Flow Metab,* vol. 37, no. 8, pp. 2848-2856, Aug 2017, doi: 10.1177/0271678x16676826.

[270] J. A. Calbet *et al.*, "Cardiac output and leg and arm blood flow during incremental exercise to exhaustion on the cycle ergometer," (in eng), *J Appl Physiol (1985),* vol. 103, no. 3, pp. 969-78, Sep 2007, doi: 10.1152/japplphysiol.01281.2006.

[271] M. Beraia, "Arterial pulse impact on blood flow," *Health,* vol. 2, pp. 532-540, 2010, doi: 10.4236/health.2010.26080.

[272] J. Chang *et al.*, "Investigation of Vortex Rings for Free Jet and Synthetic Jet at Various Reynolds Numbers and Strouhal Numbers," *Mathematical Problems in Engineering,* vol. 2020, p. 1503628, 2020/08/13 2020, doi: 10.1155/2020/1503628.

[273] B. Mensel, J.-P. Kühn, T. Schneider, A. Quadrat, and K. Hegenscheid, "Mean Thoracic Aortic Wall Thickness Determination by Cine MRI with Steady-State Free Precession: Validation with Dark Blood Imaging," *Academic Radiology,* vol. 20, no. 8, pp. 1004-1008, 2013/08/01/ 2013, doi: https://doi.org/10.1016/j.acra.2013.03.014.

[274] F. R. Arko *et al.*, "Intrasac flow velocities predict sealing of type II endoleaks after endovascular abdominal aortic aneurysm repair," *Journal of Vascular Surgery,* vol. 37, no. 1, pp. 8-15, 2003/01/01/ 2003, doi: https://doi.org/10.1067/mva.2003.55.

[275] M. Knowles *et al.*, "In Vitro Analysis of Type II Endoleaks and Aneurysm Sac Pressurization on Longitudinal Stent-Graft Displacement," (in English), *Journal of Endovascular Therapy,* vol. 18, no. 4, pp. 601-6, Aug 2011, 2015-10-24 2011.

[276] D. E. McMillan, "Blood flow and the localization of atherosclerotic plaques," *Stroke,* vol. 16, no. 4, pp. 582-587, 1985.

[277] D. N. Ku, "Blood Flow In Arteries," *Annual Review of Fluid Mechanics,* vol. 29, no. 1, pp. 399-434, 1997, doi: 10.1146/annurev.fluid.29.1.399.

[278] M. R. Najjari, "On the Formation of Vortices Under Transient and Pulsatile Inflow Conditions in a Curved Pipe," Ph.D., The George Washington University, Ann Arbor, 13419802, 2019.

[279] A. Pantokratoras, "Steady laminar flow in a 90° bend," *Advances in Mechanical Engineering,* vol. 8, no. 9, p. 1687814016669472, 2016, doi: 10.1177/1687814016669472.

[280] M. O'Rourke, "Mechanical Principles in Arterial Disease," *Hypertension,* vol. 26, no. 1, pp. 2-9, 1995, doi: doi:10.1161/01.HYP.26.1.2.

[281] Nordic Society of Medical Radiology, "Chapter VI: Deformation of the Ascending Aorta During One Heart Cycle," *Acta Radiologica,* vol. 57, no. sup213, pp. 51-55, 1962/01/01 1962, doi: 10.3109/00016926209173871.

[282] P. Boutouyrie, S. Laurent, A. Benetos, X. J. Girerd, A. P. G. Hoeks, and M. E. Safar, "Opposing effects of ageing on distal and proximal large arteries in hypertensives," *Journal of Hypertension,* vol. 10, 1992. [Online]. Available: https://journals.lww.com/jhypertension/Fulltext/1992/08001/Opposing_effects_of_ageing_on_distal_and_proximal.23.aspx.

[283] JOTEC. "E-vita OPEN PLUS Hybrid stent graft system - JOTEC." https://www.jotec.com/en/products/thoracic-stent-grafts/e-vita-open-plus.html (accessed.

[284] E. Groot Jebbink, T. G. Ter Mors, C. H. Slump, R. H. Geelkerken, S. Holewijn, and M. M. Reijnen, "In vivo geometry of the kissing stent and covered endovascular reconstruction of the aortic bifurcation configurations in aortoiliac occlusive disease," (in eng), *Vascular,* vol. 25, no. 6, pp. 635-641, 2017, doi: 10.1177/1708538117708912.

[285] J. Heaton and Y. S. Khan, *Aortoiliac Occlusive Disease*. Treasure Island (FL): StatPearls Publishing, 2020.

[286] M. J. Sharafuddin, J. J. Hoballah, T. F. Kresowik, and W. J. Sharp, "Kissing Stent Reconstruction of the Aortoiliac Bifurcation," *Perspectives in Vascular Surgery and Endovascular Therapy,* vol. 20, no. 1, pp. 50-60, 2008, doi: 10.1177/1531003507313224.

[287] M. Vértes *et al.*, "Stent Protrusion >20 mm Into the Aorta: A New Predictor for Restenosis After Kissing Stent Reconstruction of the Aortoiliac Bifurcation," (in eng), *J Endovasc Ther,* vol. 25, no. 5, pp. 632-639, Oct 2018, doi: 10.1177/1526602818794959.

[288] E. Groot Jebbink *et al.*, "Meta-analysis of Individual Patient Data After Kissing Stent Treatment for Aortoiliac Occlusive Disease," *Journal of Endovascular Therapy,* vol. 26, no. 1, pp. 31-40, 2019, doi: 10.1177/1526602818810535.

[289] P. D. Morris, J. Iqbal, C. Chiastra, W. Wu, F. Migliavacca, and J. P. Gunn, "Simultaneous kissing stents to treat unprotected left main stem coronary artery bifurcation disease; stent expansion, vessel injury, hemodynamics, tissue healing, restenosis, and repeat revascularization," (in eng), *Catheterization and cardiovascular interventions : official journal of the Society for Cardiac Angiography & Interventions,* vol. 92, no. 6, pp. E381-E392, 2018, doi: 10.1002/ccd.27640.

[290] G. Rigatelli, M. Zuin, F. Dell'Avvocata, A. Nanjundappa, R. Daggubati, and T. Nguyen, "Non-invasive Evaluation of Fluid Dynamic of Aortoiliac Atherosclerotic Disease: Impact of Bifurcation Angle and Different Stent Configurations," (in eng), *J Transl Int Med,* vol. 6, no. 3, pp. 138-145, 2018, doi: 10.2478/jtim-2018-0020.

[291] C. Chiastra *et al.*, "Computational fluid dynamic simulations of image-based stented coronary bifurcation models," (in eng), *J R Soc Interface,* vol. 10, no. 84, p. 20130193, Jul 6 2013, doi: 10.1098/rsif.2013.0193.

[292] E. Groot Jebbink, P. C. J. Goverde, J. A. van Oostayen, M. M. P. Reijnen, and C. H. Slump, *Innovation in aortoiliac stenting: an in vitro comparison* (SPIE Medical Imaging). SPIE, 2014.

[293] E. Groot Jebbink, F. A. B. Grimme, P. C. J. M. Goverde, J. A. van Oostayen, C. H. Slump, and M. M. P. J. Reijnen, "Geometrical consequences of kissing stents and the Covered Endovascular Reconstruction of the Aortic Bifurcation configuration in an in vitro model for endovascular reconstruction of aortic bifurcation," *Journal of Vascular Surgery,* vol. 61, no. 5, pp. 1306-1311, 2015/05/01/ 2015, doi: https://doi.org/10.1016/j.jvs.2013.12.026.

[294] J. S. Raben, S. Morlacchi, F. Burzotta, F. Migliavacca, and P. P. Vlachos, "Local blood flow patterns in stented coronary bifurcations: an experimental and numerical study," (in eng), *J Appl Biomater Funct Mater,* vol. 13, no. 2, pp. e116-26, Jul 4 2015, doi: 10.5301/jabfm.5000217.

[295] T. Matsuda *et al.*, "Modification of hemodynamics in basilar artery aneurysm by the single and Y stent placement," *Technology and Health Care,* vol. 25, pp. 831-842, 2017, doi: 10.3233/THC-160487.

[296] R. M. Lang, B. P. Cholley, C. Korcarz, R. H. Marcus, and S. G. Shroff, "Measurement of regional elastic properties of the human aorta. A new application of transesophageal echocardiography with automated border detection and calibrated subclavian pulse tracings," *Circulation,* vol. 90, no. 4, pp. 1875-1882, 1994, doi: doi:10.1161/01.CIR.90.4.1875.

[297] H. Zafar, F. Sharif, and M. J. Leahy, "Measurement of the blood flow rate and velocity in coronary artery stenosis using intracoronary frequency domain optical coherence tomography: Validation against fractional flow reserve," *IJC Heart & Vasculature,* vol. 5, pp. 68-71, 2014/12/01/ 2014, doi: https://doi.org/10.1016/j.ijcha.2014.10.004.

[298] S. Mujagić, "The Inner Diameter Of Arteries Of The Circle Of Willis Regarding Gender And Age On Magnetic Resonance Angiography," *Acta Medica Saliniana,* vol. 42, pp. 6-12, 11/23 2013.

[299] M. Tomaszewski, K. Sybilski, P. Baranowski, and J. Małachowski, "Experimental and numerical flow analysis through arteries with stent using particle image velocimetry and computational fluid dynamics method," *Biocybernetics and Biomedical Engineering,* vol. 40, no. 2, pp. 740-751, 2020.

[300] I. D. Johnston, D. K. McCluskey, C. K. L. Tan, and M. C. Tracey, "Mechanical characterization of bulk Sylgard 184 for microfluidics and microengineering," *Journal of Micromechanics and Microengineering,* vol. 24, no. 3, p. 035017, 2014/02/28 2014, doi: 10.1088/0960-1317/24/3/035017.

[301] R. Ponzini *et al.*, "Womersley number-based estimates of blood flow rate in Doppler analysis: in vivo validation by means of phase-contrast MRI," (in eng), *IEEE Trans Biomed Eng,* vol. 57, no. 7, pp. 1807-15, Jul 2010, doi: 10.1109/tbme.2010.2046484.

[302] M. K. Banerjee, R. Ganguly, and A. Datta, "Effect of Pulsatile Flow Waveform and Womersley Number on the Flow in Stenosed Arterial Geometry," *ISRN Biomathematics,* vol. 2012, p. 853056, 2012/11/25 2012, doi: 10.5402/2012/853056.

[303] J. E. Moore, Jr. and D. N. Ku, "Pulsatile Velocity Measurements in a Model of the Human Abdominal Aorta Under Resting Conditions," *Journal of Biomechanical Engineering,* vol. 116, no. 3, pp. 337-346, 1994, doi: 10.1115/1.2895740.

[304] K. Fraser, S. Meagher, J. Blake, W. Easson, and P. Hoskins, "Characterization of an Abdominal Aortic Velocity Waveform in Patients with Abdominal Aortic Aneurysm," *Ultrasound in medicine & biology,* vol. 34, pp. 73-80, 02/01 2008, doi: 10.1016/j.ultrasmedbio.2007.06.015.

[305] A. M. Malek, S. L. Alper, and S. Izumo, "Hemodynamic Shear Stress and Its Role in Atherosclerosis," *JAMA,* vol. 282, no. 21, pp. 2035-2042, 1999, doi: 10.1001/jama.282.21.2035.

[306] K. Luo, W. Jiang, C. Yu, X. Tian, Z. Zhou, and Y. Ding, "Fluid–Solid Interaction Analysis on Iliac Bifurcation Artery: A Numerical Study," *International Journal of Computational Methods,* vol. 16, no. 07, p. 1850112, 2019, doi: 10.1142/s0219876218501128.

[307] M. Langsfeld *et al.*, "The use of deep duplex scanning to predict hemodynamically significant aortoiliac stenoses," *Journal of Vascular Surgery,* vol. 7, no. 3, pp. 395-399, 1988, doi: 10.1016/0741-5214(88)90434-X.

[308] S. G. Yazdi *et al.*, "In-vitro particle image velocimetry assessment of the endovascular haemodynamic features distal of stent-grafts that are associated with development of limb occlusion," *Journal of the Royal Society of New Zealand,* pp. 1-14, 2020, doi: 10.1080/03036758.2020.1826988.

[309] A. Greiner *et al.*, "Does Stent Overlap Influence the Patency Rate of Aortoiliac Kissing Stents?," *Journal of Endovascular Therapy,* vol. 12, no. 6, pp. 696-703, 2005, doi: 10.1583/06-1633.1.

[310] J. García García, P. García Carrascal, F. Castro Ruiz, F. Manuel Martín, and J. A. Fernández, "Effects of bifurcation-specific and conventional stents on coronary bifurcation flow. An experimental and numerical study," *Journal of Biomechanics,* vol. 54, pp. 64-72, 2017/03/21/ 2017, doi: https://doi.org/10.1016/j.jbiomech.2017.01.043.

[311] R. J. Feezor and W. A. Lee, "Management of the Left Subclavian Artery during TEVAR," *Seminars in Vascular Surgery,* vol. 22, no. 3, pp. 159-164, 2009/09/01/ 2009, doi: https://doi.org/10.1053/j.semvascsurg.2009.07.007.

[312] A. V. Kamman *et al.*, "Impact of Left Subclavian Artery Revascularization before Thoracic Endovascular Aortic Repair on Postoperative Cerebrovascular Hemodynamics," *Annals of Vascular Surgery,* vol. 46, pp. 307-313, 2018/01/01/ 2018, doi: https://doi.org/10.1016/j.avsg.2017.06.046.

[313] C. Klonaris, G. N. Kouvelos, M. Kafeza, A. Koutsoumpelis, A. Katsargyris, and C. Tsigris, "Common Carotid Artery Occlusion Treatment: Revealing a Gap in the Current Guidelines," *European Journal of Vascular and Endovascular Surgery,* vol. 46, no. 3, pp. 291-298, 2013/09/01/ 2013, doi: https://doi.org/10.1016/j.ejvs.2013.06.006.

[314] E. Weigang *et al.*, "Should intentional endovascular stent-graft coverage of the left subclavian artery be preceded by prophylactic revascularisation?," *European Journal of Cardio-Thoracic Surgery,* vol. 40, no. 4, pp. 858-868, 2011, doi: 10.1016/j.ejcts.2011.01.046.

[315] L. Bertoglio *et al.*, "Carotid to subclavian bypass and Amplatzer vascular plug subclavian endovascular occlusion before thoracic open or endovascular repair," *Journal of Vascular Surgery,* vol. 71, no. 5, pp. 1480-1488.e1, 2020/05/01/ 2020, doi: https://doi.org/10.1016/j.jvs.2019.08.237.

[316] G. Melissano *et al.*, "Results of Endografting of the Aortic Arch in Different Landing Zones," *European Journal of Vascular and Endovascular Surgery,* vol. 33, no. 5, pp. 561-566, 2007/05/01/ 2007, doi: https://doi.org/10.1016/j.ejvs.2006.11.019.

[317] C. Lomazzi, V. Grassi, M. Domanin, C. De Vincentiis, G. Piffaretti, and S. Trimarchi, "Art of operative techniques: treatment options in arch penetrating aortic ulcer," (in eng), *Annals of cardiothoracic surgery,* vol. 8, no. 4, pp. 500-508, 2019, doi: 10.21037/acs.2019.07.06.

[318] Ö. Karabulut, K. İltimur, and M. Tuncer, "Coexisting of aortic arch variation of the left common carotid artery arising from brachiocephalic trunk and absence of the main branches of right subclavian artery: A review of the literature," *Romanian journal of morphology and embryology = Revue roumaine de morphologie et embryologie,* vol. 51, pp. 569-72, 01/01 2010.

[319] J. Dumfarth *et al.*, "Atypical aortic arch branching variants: A novel marker for thoracic aortic disease," *The Journal of Thoracic and Cardiovascular Surgery,* vol. 149, no. 6, pp. 1586-1592, 2015, doi: 10.1016/j.jtcvs.2015.02.019.

[320] J. Garcia *et al.*, "Distribution of blood flow velocity in the normal aorta: Effect of age and gender," (in eng), *J Magn Reson Imaging,* vol. 47, no. 2, pp. 487-498, 2018, doi: 10.1002/jmri.25773.

[321] J. D. Glover, C. E. McLaughlin, M. K. McFarland, and J. T. Pham, "Extracting uncrosslinked material from low modulus sylgard 184 and the effect on mechanical properties," *Journal of Polymer Science,* vol. 58, no. 2, pp. 343-351, 2020, doi: https://doi.org/10.1002/pol.20190032.